PSL
UNIVERSITÉ PARIS

THÈSE DE DOCTORAT
DE L'UNIVERSITÉ PSL
-École Normale Supérieure-

Piégeage laser d'atomes de Rydberg circulaires pour la simulation quantique

Soutenue par
Rodrigo G. Cortiñas
Le 5 Mai 2020

Ecole doctorale n° 564
EDPIF

Spécialité
Mécanique Quantique

Composition du jury :

Jean-Marc Berroir Prof. ENS, LPENS, Paris	*Président*
Isabelle Bouchoule DR CNRS, LCF, Palaiseau	*Examinateur*
Michel Brune DR CNRS, LKB, Paris	*Directeur de thèse*
Frédérik Merkt Prof. ETHZ, Zurich	*Rapporteur*
Mazyar Mirrahimi DR CNRS INRIA, Paris	*Examinateur*
Guido Pupillo Prof. UNISTRA, LPQ, Strasbourg	*Rapporteur*
Clément Sayrin MdC SU, LKB, Paris	*Membre invité*

Laboratoire Kastler Brossel
Physique quantique et applications

COLLÈGE DE FRANCE 1530

ENS ÉCOLE NORMALE SUPÉRIEURE

SORBONNE UNIVERSITÉ

cnrs

Laser trapping of cold circular Rydberg atoms for quantum simulation.

In full awareness of both the good and the harm that science can inflict on humanity, I will proceed in communion with my conscience. I will never use my skills to degrade the human body or spirit, nor the world we inhabit. Economic interest or any kind of recognition will not compromise my judgment.

In the critical spirit of science, I will use established morals only as guidance. I will not subordinate to them nor to political interests, thereby assuming personal responsibility for my own work and omissions.

Science, as one of the highest expressions of the human spirit, must take place under equal opportunities, for the benefit of humanity, and in service of world peace. I will defend these values in my practice and, in doing so, I will bring them to the attention of others.

Contents

List of Figures

List of Tables

Introduction

In this section we review state-of-the-art techniques in quantum simulation on a few predominant platforms. Depending on the application, the specific properties of each platform can be either an asset or a drawback. Different systems are thus complementary, and their simultaneous development and understanding will allow the identification of their final technological utilities.

In particular, we shall introduce our research on the Rydberg atom platform for quantum simulation. The main result of our work is the laser trapping of long-lived cold circular Rydberg atoms. For context we revisit some of the developments regarding the trapping of Rydberg atoms in the literature. This will allow us to compare our contribution to alternatives. At the end of this section we present an overview of this manuscript.

1. Foreword

There is not a single experimental observation of our world that is in disagreement with the view proposed by quantum mechanics. All experiments performed inside its well-established domain have met solid theoretical ground for almost a hundred years now. Nonetheless, even at its core, one still finds new (and old) awe-inspiring questions and the strange world that it opens for us is far from completely explored.

One of the main research efforts at present is intended to exploit the weirdness of 'the quantum' to perform useful calculations. One can motivate the interest in the following way: The differences between the classical and the quantum 'worlds' can be traced back to the validity of the logical statements one can make. The tight relation between probability theory and logic[1] suggests that the fundamental difference between 'quantum' probabilities and the 'classical' ones can be exploited to harvest computations from a completely *new logic* [3]. This has lead to the widespread belief that, soon, radically different types of computers built using quantum properties will contribute to society.

[1] Probability theory can be considered as a formalization of logical inference [1, 2].

2. Quantum simulation

An intermediate stage before a 'quantum computer' has been clearly identified: A machine able to solve a specific kind of problem that lays beyond the practical capabilities of classical supercomputers would be of use. We refer to such an intermediate computer as a quantum simulator [4, 5]. In general, an ideal quantum simulator is an analog (quantum) system which is under full experimental control and evolves under the equations of motion of a more inaccessible target (quantum) system.

In condensed matter physics or chemistry, when dealing with a large number of particles, the scope of calculations becomes limited and new approaches need to be developed. Quantum simulation reveals itself as capable of contributing to this quest. This was first noticed by Feynman in a seminal work [6] and the main argument can be reproduced as follows: Consider a microscopic cube of $10 \times 10 \times 10$ two-level atoms. The quantum mechanical description requires a Hilbert space of dimension 2^{1000}. Any computational effort to deal with any non-trivial Hamiltonian in this space is absolutely hopeless.[2] On the other hand, if one is able to build an artificial version of such a cube, the evolution will play out naturally. If, in addition, this artificial cube is built so that one can control it and measure it with sufficient precision, one can experimentally reconstruct the evolution. Physically, ones has run the Hamiltonian evolution of the original cube in the artificial one in the same way that one runs software in a programmable electronic circuit to perform a given task. This is the spirit of quantum simulation.

The quantum advantage can be identified to be the following: The amount of resources to solve the cube problem classically 'explodes' exponentially with its size when, with a quantum simulator, it only grows linearly. Heuristically, one can consider the 'classical amount of resources' needed to be given by the size of the matrix to be diagonalized (2^{1000}), while the 'amount of quantum resources' is simply given by the number of particles (1000) to be simulated.

Even if the quantum scaling is favorable, its implementation relies on technologies that we are only beginning to master. In these interesting times, the winning platform for large-scale quantum computation and simulation (if any) is still far from being identified with certainty. On the contrary, the particularities of the different proposals divide them into many complementary sets, since some are more adequate than others to address a given problem [7]. It is important to note that even when their assets overlap, the variety in their specificities provides a way to validate an otherwise untracktable calculation. The principle is that if two different systems agree in their results, one can be confident that the simulation is free of hardware artifacts and can, thus, trust the outcome.

We will now make a brief review of some promising platforms for quantum simulation, including circuits, trapped ions, cold atoms, and Rydberg atoms.

[2] To put the limitation in perspective, note that the number of protons in the universe is estimated to only be 2^{300}.

2.1 Quantum circuits

Superconducting qubits are good candidates to perform computations beyond the reach of modern supercomputers [8]. Even without error correction they are used to implement challenging quantum simulations and quantum algorithms [9].

Superconducting circuits [10] are microfabricated using aluminum or niobium. The substrate used is silicium or sapphire and are built making use of reliable techniques and materials previously developed for microfabrication [11]. They are normally encapsulated in copper or aluminum packages that provide an engineered electromagnetic environment [12–14]. Operating at frequencies from 5 to 15 GHz, they require an environment thermalized to about 15 mK. These low temperatures can be achieved with commercial dilution refrigerators.

The flexibility in the fabrication of superconducting circuits provides diverse perspectives. Certain superconducting qubit 'flavors' (transmons, charge qubits, flux qubits, phase qubits, etc.) are more suitable than others for different quantum simulations. The different qubits have built-in couplings types, commutation relationships, or decoherence channels that share intrinsic characteristics with the simulated system. Importantly, the qubits are made to have tailored frequencies and coupling strengths [15, 16]. On the downside, they are all slightly different (resonance frequency, coherence time, etc.) and they are known to age with thermal cycling [17] affecting the reproducibility of the experiments.

Superconducting devices can be used to tackle problems using directly interacting qubits or qubits coupled to a common mode in a cavity [16]. In [13], it was shown that the strong coupling regime of quantum optics experiments could be achieved in solid state systems, opening a field that has proven to be fruitful. Superconducting circuits have been used to study strongly correlated many-body systems [18] or thermalization in small quantum systems [19]. Additionally, experiments of fundamental interest in new regimes [20] and simulation of Fermionic models [21, 22] with possible technological applications in material design were made.

Experiments using a few high-quality qubits have been reported. In [23], a two-transmon system was used to efficiently simulate a Heisenberg interacting spin model using interactions that are naturally present in these qubits, while applying only resources that grow polynomially in the number of spins. In [24], a three-qubit device was used to realize synthetic magnetic fields and strong particle interactions, which are among the essential elements for studying quantum magnetism and fractional quantum Hall phenomena. Recently, a larger quantum device has been used to solve a problem that classical computers practically cannot [25]. A 52-qubit chip was used to provide the solution to a tailor-made problem (of limited practical interest) in less time than the world's fastest supercomputers.

Large numbers of qubits are interesting for quantum annealing. They could be used to provide solutions to those classically hard optimization problems that can be mapped to the problem of finding the ground state of a quantum many-body system [26, 27]. Experiments with tens to hundreds of strongly damped qubits have been reported [28, 29], but quantum speed up is an open question in dissipative systems [30]. Arrays of thousands of qubits have been built for annealing, but they have limited connectivity and it is unclear if they can deal with the level of entanglement needed to tackle the many-body problems they aim to solve [31].

2.2 Trapped ions

The first implementation of a universal quantum computer proposed trapped atomic ions as hardware [32]. This was done shortly after a clear quantum advantage was identified by the proposal of Shor's algorithm for factorization [33]. Long before these landmarks, single ions had been confined using radio frequency (RF) Paul traps [34] and proven to be of fundamental interest [35]. The observation of the first quantum jumps [36] and the first experimental studies on quantum noise [37] were done on this platform.

Trapped ions (Al^+, Ca^+, Mg^+, Sr^+, etc.) are controlled with laser or microwave drives that allow for arbitrary and high-fidelity single-qubit rotations. Arbitrary two-qubit entangling gates can also be performed with high fidelity by using the shared motional modes of two or more ions as a transfer bus. Additionally, laser cooling techniques and efficient measurement makes them a good platform for metrology [38] and quantum information. They are appealing for analog simulation [39–41], particularly for the interesting spin-boson model, but also have good performance for digital operations [42].

Qubits states can be encoded in optical or hyperfine levels. The reversible coherence of the hyperfine qubit was reported to be as long as $T_2^* = 50$ s [43]. Using dynamical decoupling techniques [44], the irreversible coherence time was reported to be $T_2 = 600$ s (10 minutes!). These coherence times are limited by dephasing due to technical field stability and are far from being limited by fundamental processes. The combined state preparation and readout fidelity was shown to be as good as 99.93% [43], making ions the leading platform in this regard. Digital operation of trapped ions has been used for the simulation of a quantum electrodynamics process [45] in a four-qubit machine and to implement Shor's algorithm [46] in a thirteen qubit machine. Even if it is, in principle, easy to scale up ion architectures in both one [47] and two dimensions [48], the historical increase in the ion number has been slow. The main problem encountered is the degradation of the system's controlability as the number of ions grows [49]. The increasing number of motional modes turns the engineering of interaction and the cooling down of the system harder to implement.

Beyond the digital approach, trapped ions are promising for analog simulations of spin arrays in the short term. Optical manipulation of common motional modes of a trapped ion chain is used to simulate a spin-spin interaction, but they are limited to long range interactions [50, 51]. Experiments demonstrating a wide variety of physics were performed including the demonstration of a quantum random walk in a spin-1/2 or spin-1 system [39, 52], the spectroscopy of spin-waves [53], many-body localization, and thermalization of quantum systems [54]. Simulations of spin-squeezing in 2D with long range interactions were also reported [55].

2.3 Cold atoms

Another platform harvesting good results in the realm of quantum simulation is that of cold atoms in optical traps [56–58]. The polarizability of the atoms, as a response to an oscillating electric laser field [59], provides the trapping mechanism. Qubit states can be cast in the occupation of the lattice sites and the coupling is provided by quantum tunneling between adjacent sites. Internal degrees of freedom are also made available

by the hyperfine structure of the participating atoms [60]. Traps forming lattices can be created by interfering laser beams. The periodic potential created imposes to the atom array a structure that simulates a magnified solid state crystal. Both Fermions and Bosons can be used to occupy the lattice sites.

A paradigmatic example of quantum simulation with cold atoms has been the study of the Hubbard model in regular lattices [61, 62]. As the simplest model for interacting particles in a lattice, it has not been solved analytically in two nor three dimensions and it is numerically resource-demanding. Controlled disorder created by a speckle pattern [63] leads to explorations of many-body localization [64] and to regimes where numerical methods quickly find their limitations. Recent advances have been made using the so-called 'atomic microscopes' [65, 66]. They consist of a cold atom sample trapped under a high numerical aperture lens (NA$\sim$0.5) that can resolve the lattice sites and detect atoms individually [65, 67, 68]. Complemented with Stern-Gerlach techniques, one can even resolve the inner state of the atoms [69].

The cold atom toolbox provides a good test bed to study electrons in solids where the charge is simulated by a Fermionic atom (many orders of magnitude bigger and heavier that the electron, thus providing a dilated timescale!) while the spin is simulated by an inner atomic two-level subspace. An example is the simulation [70] of dynamical spin-charge fractionalization [71, 72] in a 'Cheshire cat' state where the charge and the spin of a (quasi-)particle separate from each other, each traveling at different speeds. The (doped) Fermi-Hubbard model, which is expected to play an important role in the comprehension of high-temperature superconductivity [73, 74], finds a befitting simulator in atomic microscopes. The flexibility of the approach permits the measurement of complex entanglement properties [68, 75]. Experiments can now reach domains beyond the grasp of theoretical methods and classical computations [76]. The platform has also been used to simulate effective magnetic fields [77] orders of magnitude stronger than the ones that can be created in laboratories. Lattice dynamical manipulations [58, 78], or multilevel atoms [79], open the way to the simulation of gauge fields and topological phases [80–82].

However, strongly relying on tunneling (an intrinsically slow process) makes it hard for cold atom systems to follow long term dynamics like that of spin glasses. Limited by the lattice lifetime, proposals [83, 84] to reduce the inter-lattice spacing, enhancing the tunneling rate, and increasing the effective length of the simulation were made, but they have not been realized yet. Instead, polar molecules, magnetic atoms [85, 86], and highly excited atoms have been used to enhance the interaction.

2.4 Rydberg atoms

Among cold atoms, those excited to very energetic states (principal quantum number $n \gg 1$) deserve special attention [87]. The so-called Rydberg atoms [88] have long natural lifetimes (of at least a few 100's µs) and strong dipolar interactions (tens of MHz) even at large interatomic distances (a few µm). These properties make them good building blocks for a quantum simulator [89, 90]. They provide a natural platform where a 1000 qubit system capable of overcoming other platforms' limitations in scalability and dimensionality is possible [91–93]. Rydberg atoms are flexible tools since their coupling can be tuned by the inter-atomic distance, a dressing laser field [94], the relative orientation of their dipoles [95], an external directing electric (or magnetic)

field, or by varying the principal quantum number n [96]. This tunability allows one to use them as either sensors (high sensitivity to the environment) [97] or as robust qubits (low sensitivity to the environment) [98].

The assets of Rydberg atoms have been exploited for quantum simulation of many-body systems. In [99], the anti-ferromagnetic ordering in a ground-Rydberg qubit array was explored in one and two dimensions. A delay in the build-up of the correlation was observed and understood as a consequence of the finite speed of correlation propagation in a system with short-range interactions. The quantum simulations reported there used up to thirty-six Rydberg atoms. In [100], a fifty-one Rydberg atom linear system was used to prove the many-body dynamics of coupled spins. The qubit state was encoded in a ground-Rydberg two-level system. In the same work, using a thirteen Rydberg atom chain, the adiabatic preparation of an anti-ferromagnetic ground state was demonstrated and in an even shorter chain, made of nine qubits, robust many-body oscillations were observed during 1.2 µs.

A proposal to solve the 'maximal independent set problem' using ground-Rydberg qubits was also put forth [101]. This classically hard problem could, in principle, be implemented with already available Rydberg technology. The proposal relies in the tight relation between the quantum phase transition in disordered systems and combinatorial problems. The close relation to real-world problems like network design and artificial intelligence makes this proposal technologically interesting.

It is usual in Rydberg quantum information approaches to encode the qubit state in a ground-Rydberg pair of levels. The Rydberg state provides the inter-site interaction, while the ground state provides the possibility to trap the atom using cold atom trapping techniques and a direct detection method (fluorescence). In this case, the model is limited to Ising-like interactions ($\hat{\sigma}_z \otimes \hat{\sigma}_z$), since the atoms only interact when both are in the excited qubit state. The model can be extended to a more general XY Heisenberg model by encoding the qubit in two different Rydberg levels. In [102], engineered interactions of this type allowed for the first experimental observation of a symmetry-protected topological phase where interaction played a crucial role.

It is important to notice that, so far, the main advances in Rydberg atoms quantum simulation have been made in the absence of Rydberg trapping. This limits the useful time of a spin simulation to a few microseconds: the time it takes for the Rydberg-Rydberg interaction to break the crystal. Another drawback in state-of-the-art Rydberg based quantum simulations is the absence of a cryogenic environment. The large dipole matrix elements between Rydberg states makes them extremely sensitive to microwave black-body radiation. This is the limiting factor in some promising implementations. In [103], many-body interference effects were observed with Rydberg-dressed cold atoms. The Rydberg dressing provides a tunable interaction mechanism for a near-unit-filling bi-dimensional ground-state optical lattice. Coherence limitations in this experiment were attributed to black-body population transfer in the Rydberg manifold. Moreover, the process can induce an avalanche of atom loss. In [104], the related anomalous broadening in the ground-Rydberg spectral line was observed in a three-dimensional lattice. A black-body induced population in close lying Rydberg states was reported to produce a line broadening of nearly two orders of magnitude. Using a cryostat would be a solution to this problem [96, 105]. The additional benefit of improved vacuum conditions, directly increasing the lattice lifetime, would also be a positive consequence.

2.4.1 Circular Rydberg atoms

Among Rydberg atoms, 'circular' Rydberg (cRy) atoms are interesting. These are Rydberg states where the electron is in a narrow toroidal orbital. The particularities of these states allow applications of Rydberg atoms (to quantum information [105] and to quantum metrology [106, 107]) to take on a new dimension.

Recently we have proposed to encode the qubit of a Rydberg based quantum simulator in two cRy states [108]. The long lifetime of these states will allow us to follow slow quantum evolutions relevant to condensed matter problems. The free space radiative lifetime of circular levels is of a few tens of milliseconds [105] while, inside a spontaneous-emission inhibition structure and in a cryogenic environment, one expects to reach lifetimes of up to a minute for individual atoms [108, 109]. The proposal strongly relies on laser trapped cRy atoms which are expected to have negligible photionization [110] and are thus ideal for laser trapping. Spin exchange rates of tens of kHz for atoms spaced by a few micrometers account for about a hundred thousand exchange times in a 40 atom chain before the first atom is lost. The proposed system is expected to simulate XXZ Heisenberg models providing dynamic tunability of all the Hamiltonian parameters. Both circular levels forming the spin can be trapped in the same potential and in an almost level-independent trap. Importantly, a method for the deterministic preparation of a linear array of circular atoms is envisioned [111].

2.4.2 Trapping of Rydberg atoms

In general, Rydberg atom trapping for quantum simulation could be a useful tool to follow long many-body Hamiltonian evolutions, to study the build-up of correlations and thermalization of quantum systems, or to study localization phenomena.

Beyond the application to quantum simulation, Rydberg atom trapping is a useful tool for metrology. Long-lived trapped Rydberg atoms could be used to measure the Rydberg constant and the quantum defects of different species [112], or to study Rydberg molecules [113, 114]. Trapped atoms could be used to increase the interrogation time of a Rydberg based electric [115] and magnetic [107] fields sensors, to coherently manipulate the Rydberg states in place [116] or to measure local forces close to surfaces [117]. Rydberg physics effects like collisions [118], super-radiance [119], or electromagnetically induced transparency [120] could be enhanced by trapping as well.

In the last decade, some proposals and experiments regarding Rydberg atom trapping have been reported [121]. Historically, Rydberg atoms have first been trapped in high-fields (∼3 T) Ioffe-Pritchard magnetic traps [122] (see also [123]). Stark gradient Rydberg traps were also used to efficiently confine the excited atoms in a centimeter-sized region of space. In [124], cold (350 mK) Hydrogen Rydberg atoms have been trapped in two dimensions using electrostatic potentials. Before trapping, the Rydberg atoms were decelerated to zero velocity using time-dependent inhomogeneous electric fields. High densities of Rydberg atoms ($\sim 10^6$ atoms/cm^3) with a trapping lifetime of 150 µs were achieved. The lifetime was determined by a competition of black-body radiation induced processes and collisions with the background Argon gas required for the preparation of the sample. In [125], a fully electrostatic deceleration and three-dimensional trapping was demonstrated by trapping state-selected Hydrogen Rydberg atoms during ∼ 135 µs. In this experiment, the lifetime was essentially limited by the

radiative decay rate of the chosen state.

Optical-dipole traps at magic wavelengths have also been proposed [126] for ground-Rydberg qubits expecting differential trap shifts bounded by 200 kHz, but they have not been realized experimentally yet. Notably, in the context of this thesis, cRy states have no allowed optical transitions, so standard dipole trapping is not an option.

The most promising technique to trap Rydberg atoms for quantum simulation may be to use the ponderomotive energy [127] of atoms placed in an inhomogeneous laser beam. The trapping is conservative and the potential arises from the time-averaged kinetic energy of the nearly free Rydberg electron oscillating in an AC laser electric field. The much heavier atomic core is comparatively impervious to the potential and, thus, the atom as a whole responds as a dark field seeker to avoid the oscillating force on the electron. This technique would naturally allow one to make tight (tens of kHz) and almost state-independent (up to tens of Hz) traps in packed arrays (within a few µm spacing).

Experimentally, the trajectories of low-angular-momentum Rydberg atoms in one-dimensional ponderomotive optical lattices have been studied using microwave (MW) spectroscopic techniques almost a decade ago [128, 129]. Experiments were carried out at room temperature and with trapping times of ~ 20 µs.

The main result of this thesis work is the extension of ponderomotive laser trapping to cRy atoms in two dimensions and in a cryogenic environment for at least 10 ms.

Cold circular states have been trapped before. A publication in 2013 [130] reported that cRy atoms, prepared by the crossed-fields method [131], were trapped in a magnetic trap at room temperature. The population was quickly lost (160 µs) from the circular states due to black-body induced processes. The atoms were confined to about a centimeter, with a trapping frequency of $\omega < 2\pi \times 40$ Hz. In addition, the magnetic potential used was strongly level-dependent, a detrimental characteristic for the coherence of cRy atom superposition.

During the realization of our experiments, we became aware of another related experiment that was able to demonstrate the three-dimensional trapping of individual low-angular-momentum Rydberg states in optical tweezers during ~ 220 µs [132].

The accelerating advancements in this direction correspond to the identification of untrapped Rydberg atoms for quantum simulation as a bottleneck, and it reflects the importance conveyed by the community to the incorporation of this technique in the Rydberg atom toolbox.

3. This work

In this thesis we develop the theoretical ideas that led to the proposal of a new quantum simulator that can be built out of circular Rydberg atoms (which was the thesis subject of Than-Long Nguyen, [108]). Experimentally, we have made the first few steps towards its realization. We have prepared high purity ($> 91\%$) circular Rydberg atoms by a carefully designed sequence of pulses out of a cold atom cloud and we have assessed their long lifetime and coherence properties. We have also demonstrated the ponderomotive laser confinement of these atoms (to a few micrometers) for as long as ten milliseconds without signs of photoionization.

The experimental platform we exploit here has been in use by many generations of

students and continually upgraded [96, 133, 134]. Historically, the Helium-4 cryostat we use was devised to prepare and trap Rydberg atoms inside a micro structure capable of inhibiting the spontaneous decay of the excited atoms [135]. The original proposal relied on the magnetic trapping of the cold ground state atoms and the electric trapping of an individual cRy atom. The ultimate purpose of the experiment was to provide a deterministic single atom source for CQED applications [136]. Following these lines, the superconducting atom chip technology was explored, achieving BEC condensation in close proximity to superconducting structures [137]. Importantly, a cryo-compatible solution for detrimental electric field gradients close to surfaces was developed [138] and used to study the dynamics of a cold Rydberg gas close to the chip surface [139].

During this thesis work, the experimental setup has undergone upgrades with the goal to prepare and laser trap cold circular atoms. The relevant modifications are to be introduced as the manuscript develops.

3.1 Organization of the manuscript

Chapter I presents an introduction to Rydberg atoms and their properties. We convey their interest as research objects and their adequacy for quantum simulation emphasizing the physical origin of their 'exaggerated' properties (large size, long lifetime, strong interaction, etc.).

Chapter II develops the proposal to build a quantum simulator based on cRy atoms as hardware [108]. Special attention is given to the phase diagram and to the tunability of the atomic interactions that our proposal features. We present in detail the atom lifetime calculations in the many regimes relevant to us and discuss different processes limiting the usable lifetime of the cRy simulator. Finally, we discuss the trapping technique required and the deterministic preparation of a cRy atom chain. A method for single site resolution detection is proposed. The long-term goal of the proposal is a fully tunable XXZ Heisenberg quantum simulator that could operate during tens of thousands of characteristic times.

In chapter III we discuss the experimental setup and the preparation of the atomic sample. We start by discussing the ground state cold atom techniques for trapping, cooling, and imaging. We proceed to describe the successive steps towards the circular levels including the laser excitation of the ground state atoms, the electric field control, the microwave and radio frequency pulses, as well as the Rydberg detection system. We conclude with the preparation and assessment of the cold cRy states inside a cryostat.

In chapter IV we study the lifetime and the coherence of these circular states. We discuss the considerations taken into account in order to reduce the black-body radiation to increase the atomic lifetime. We find a lifetime for the $n = 52$ circular state of ~ 3.7 ms which corresponds to an effective black-body temperature of ~ 11 K. We discuss the noise mitigation techniques implemented to improve the coherence of the state. The reversible and the irreversible decoherence times are found to be ~ 35 µs and ~ 270 µs respectively. We attribute the rather short coherence time to magnetic field fluctuations in our setup that should be easily overcome with future upgrades.

Finally, in chapter V we demonstrate the trapping of the circular atoms. We introduce the spatial light modulator used to shape the light trap and explain the different calibrations made. Using low-angular-momentum Rydberg levels to make *in situ* images of the laser trap, we were able to assess the light potential at the level of the

atoms and correct for aberrations. Using a MW time-of-flight technique and relying on the Stark sensitivity of elliptical Rydberg levels, we were able to measure the thermal expansion of the cRy atom cloud in a controlled inhomogeneous electric field. We use this approach to show that our two-dimensional trap can confine the circular atoms for at least 10 ms. The mechanical frequency of the trap is measured to be $\sim$1.3 kHz. We thereby confirm the theoretical predictions that photoionization for circular states is negligible and that the trap is essentially state-independent [140].

Chapter I

Introduction to circular Rydberg atoms

Contents

Atomic physics concepts

We will start by describing the atomic physics of circular Rydberg atoms [141]. For the purpose of this manuscript, only the essential aspects of atomic physics will be discussed.

Rydberg atoms, and cRy atoms in particular, are amazing objects [142]. They have long lifetimes and large coupling both to the electromagnetic field and between themselves. This allow their use for a variety of applications, ranging from metrology [107] to quantum information [143, 144]. Most of the community is focused on low-angular-momentum Rydberg atoms. These states are directly accessible by laser excitation and do not require a cryogenic environment. Circular Rydberg atoms require, in addition, a fine-tuned preparation involving the absorption of tens of radio frequency photons in the Stark Rydberg manifold [145] and their lifetime is increased more than a 100-fold in a cryogenic environment. The experimental complications of using cRy atoms [146] are justified because their peculiar properties allow for technical applications which are out of reach for their low-angular-momentum counterparts [105, 106].

Beyond the 'exaggerated properties' of cRy atoms there is a second characteristic that deserves to be highlighted: cRy atoms are 'simple objects' and correspond to elements of the old quantum theory. The simple laws ruling their behavior allow us to build useful intuition that we will discuss in this chapter.

I.1 The Coulomb potential

The backbone of atomic physics is the analytic resolution of the Schrödinger equation for the Coulomb potential. An approach to solve this two-body problem is to consider the core-electron reduced particle [147]. This particle (essentially the electron), having a reduced mass $\mu = m_e/(1+m_e/m_{core})$ and position r, evolves under the Hamiltonian

$$\hat{H}_0 = -\frac{\hbar^2}{2\mu}\nabla^2 - \frac{q_e^2}{4\pi\epsilon_0}\frac{1}{r},$$

where q_e is the charge of the electron and ϵ_0 is the permitivity of free space. The statement corresponds to a Sturm-Liouville problem with eigenvalues (energies)[1]

$$E_{n,l,m_l} = E_n = \frac{q_e^2}{8\pi\epsilon_0}\frac{-1}{a_0 n^2} \tag{I.1}$$

and eigenvectors (wave functions) $\psi_{n,l,m_l}(r,\theta,\phi)$ that have closed-form expressions in terms of the special functions $Y_l^{m_l}(\theta,\phi)$ and $R_{nl}(r)$ given by [148]

$$\psi_{n,l,m_l}(r,\theta,\phi) = R_{nl}(r)Y_l^{m_l}(\theta,\phi),$$

$$Y_l^{m_l}(\theta,\phi) \propto e^{im_l\phi}P_l^{m_l}(\cos\theta), \text{ and}$$

$$R_{nl}(r) = \sqrt{\left(\frac{2}{na_0}\right)^3\frac{(n-l-1)!}{2n[(n+l)!]}}e^{-r/na_0}\left(\frac{2r}{na_0}\right)^l L_{n-l-1}^{2l+1}\left(\frac{2r}{na_0}\right),$$

[1] One can also introduce the Rydberg constant Ry as $E_n = -\mathrm{Ry}/n^2$.

where n, l, and m_l are integers defining unambiguously the quantum state and are collectively referred to as the 'quantum numbers'. Here $P_l^{m_l}$ and L_{n-l-1}^{2l+1} are the Legendre polynomials and the generalized Laguerre polynomials respectively. The number $n > 0$ is known as the 'principal quantum number', l is the 'angular-momentum quantum number', and m_l is the 'magnetic quantum number' that geometrically represents the projection of the angular-momentum on a quantization axis.

We note that $u_{n,l}(r) = rR_{n,l}(r)$ describes the radial motion of the reduced particle and it follows a 'one dimensional Schrödinger equation' that has, in addition to the $1/r$ potential, a centrifugal term $\propto l(l+1)$. The radial differential equation for the time independent states reads

$$\left[-\frac{\hbar^2}{2\mu}\frac{d^2}{dr^2} + \frac{\hbar^2 l(l+1)}{2\mu r^2} - \frac{q_e^2}{r}\right] u_{n,l}(r) = E_n u_{n,l}(r). \tag{I.2}$$

The presence of the centrifugal term will play a major role in the interpretation of the solutions that will interest us.

This problem statement is well-suited to address Hydrogen-like atoms: those having a single valence electron. In this thesis we have chosen to work with Rubidium-87, a species that falls into this category.

Low-angular-momentum Rydberg atoms

For low-angular-momentum Rubidium Rydberg states ($n \gg 1$ and $l < 5$), one has to take into account the penetration of the outer (Rydberg) electron into the electronic cloud of the core [88]. The screening of the nuclear charge by the inner electronic cloud is inefficient and the Coulomb potential is no longer a valid approximation. These effects lower the energy of the Rydberg state and are encompassed by the modified Rydberg formula

$$E_{n,l,j} = \frac{q_e^2/8\pi\epsilon_0 a_0}{1 + m_e/m_{core}} \frac{-1}{(n-\delta_{nlj})^2},$$

where $\delta_{nlj} > 0$ is called the quantum defect and j is the sum of the orbital and spin angular momentums. The finite electron-core mass ratio (m_e/m_{core}) has also been taken into account. The quantum defect has a phenomenological expression that reads

$$\delta_{nlj} = \delta_{lj}^{(0)} + \frac{\delta_{lj}^{(2)}}{\left(n-\delta_{lj}^{(0)}\right)^2} + \frac{\delta_{lj}^{(4)}}{\left(n-\delta_{lj}^{(0)}\right)^4} + \cdots \approx \delta_l$$

and it is only weakly dependent on n and j. One identifies a dominant contribution $\delta_{nlj} \sim \delta_{lj}^{(0)}$ and higher order corrections that become negligible for $n \gg 1$. In Table I.1 we quote the numerical values of $\delta_{lj}^{(2\times i)}$ used for Rubidium-87. Using the values from Table I.1, one can compute that, for $n \sim 50$ and $l = 0$ (S), the energy correction can be as big as 11%. For large n (~ 50 in this work), the relative correction in energy associated with j is never bigger than 10^{-3}, while the correction in energy associated with n ($\delta^{(2)}$) is never bigger than 2×10^{-7}.

The weak dependence on n (and on j) in the quantum defect δ_{nlj} reflects the fact that it is caused by the penetration of the electron orbit into the ionic core. This

Series (nl_j)	l	measured for	$\delta_{lj}^{(0)}$	$\delta_{lj}^{(2)}$
$nS_{1/2}$	0	Rb^{87}	3.131 180 4(10)	0.1787(2)
$nP_{1/2}$	1	Rb^{85}	2.654 884 9(10)	0.290 0(6)
$nP_{3/2}$	1	Rb^{85}	2.641 673 7(10)	0.295 0(7)
$nD_{3/2}$	2	Rb^{87}	1.348 091 71(40)	-0.602 86(26)
$nD_{5/2}$	2	Rb^{87}	1.346 465 73 (30)	-0.596 00(18)
$nF_{5/2}$	3	Rb^{85}	0.016 519 2(9)	-0.085(9)
$nF_{7/2}$	3	Rb^{85}	0.016 543 7(7)	-0.086(7)
nG	4	Rb^{85}	0.004 00(9)	
	> 5		$\sim 4/l^5$	

TABLE I.1 Quantum defects used for Rubidium-87. When a direct measurement of the quantity is not available in the literature, we inform the measurement made for Rubidium-85. Values taken from [149–151].

penetration is prevented by the centrifugal barrier (see eq.(I.2)), explaining the strong dependence in the orbital angular-momentum l (see Table I.1). It follows that, for high-angular-momentum Rydberg states ($n > l \gg 1$), the quantum defect correction is negligible, and the Coulomb potential gives us, to a very good approximation, the correct physics [152].

Circular Rydberg physics

Circular Rydberg states are states of maximal angular-momentum in the sense that $l = |m_l| = n-1$. No higher angular momentum is allowed by the Schrödinger equation. The observation that all three quantum numbers are large permits the applications of Bohr's correspondence principle allowing the derivation of their properties from semi-classical arguments. The full quantum calculation confirms the results.

For these states, the wave function takes a particularly simple form [141]:

$$\psi_{nc}(r,\theta,\phi) = \frac{1}{\sqrt{\pi a_0^3}} \frac{1}{nn!} \left(-\frac{r}{na_0} \sin\theta e^{i\phi} \right)^{n-1} e^{-r/na_0}. \tag{I.3}$$

The orbital is a narrow torus for large n. The angular localization of the orbit can be seen directly from the wave-function in the factor $\sin^{n-1}\theta$ which for $n > 50$ corresponds to a very narrow distribution around $\theta = \pi/2$ defining the equatorial plane. The mean value of the radius and its dispersion are

$$r_n = a_0 n^2 \quad \text{and} \tag{I.4}$$

$$\Delta r_n = a_0 n^2/\sqrt{2n}. \tag{I.5}$$

Note that as $n \to \infty$, $\Delta r/r \to 0$ (i.e: the wave function tends to be a 'one dimensional circle' with radius $r = n^2 a_0$). Under these observations we recover the Bohr atom

picture.[2]

The phase of the wave function in eq.(I.3) contains important information about the coupling to the electromagnetic field. The phase winds up $n-1$ times as it goes around the orbit and it contains the essence of the de Broglie interpretation of the Bohr quantization condition.[3] In Figure I.1 we show a pictorial representation of the wave function based on the phase of eq.(I.3). Note that, for the superposition between n and $n+1$ cRy states, there is a permanent dipole. On the other hand, for the superposition of n and $n+2$ there is only a quadrupole term in the charge distribution. The relative phase winds up two times around the orbit and the wave function no longer looks like a 'planet' rotating around the core, but now it looks like a 'dumbbell' instead. These properties rule their coupling to the radiation field (section I.2) as well as the atomic interaction in between these states (section I.3) [142].

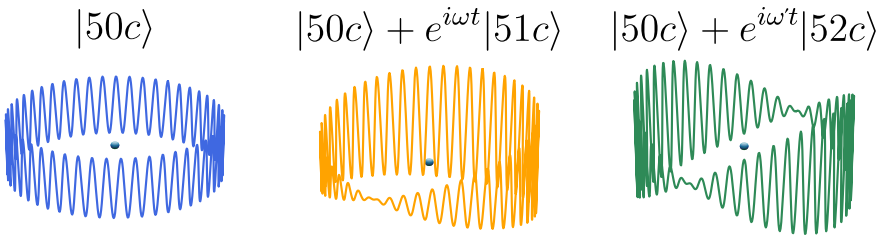

FIGURE I.1 Here we represent the cRy electron as a matter-wave. A cRy has a symmetric distribution of charge around the nucleus and presents no permanent dipole. A superposition of $|nc\rangle$ and $|(n+1)c\rangle$ creates an asymmetric electron density, which gives rise to a rotating dipole. A superposition of $|nc\rangle$ and $|(n+2)c\rangle$ regains reflection symmetry. There is no permanent dipole.

A comment on the Coulomb approximation for cRy atoms

The simplicity of the cRy states relies partly on the fact that the usual corrections to the Coulomb potential are largely negligible. This can be understood from semi-classical considerations arising from the large angular-momentum that characterizes these states.

Notably, the fine structure arising from relativistic effects is seen to be small (∼kHz for $n = 50$). Far from the core ($\gg a_0$), the circular Rydberg electron orbits at a low velocity $v_n \sim \alpha c/n$, where α is the fine structure constant [147]. The following observations are in order: i) the Darwin term vanishes since the wave function around the core is vanishingly small, ii) the spin-orbit is small since in the electron frame the field created by the core is purely electric (i.e. the components of the electromagnetic four-vector are not appreciably mixed), and iii) the kinetic energy term $\hat{p}^4/8m_e^3c^2$ is simply small with respect to $\hat{p}^2/2m_e$.

[2] For $n = 50$ we have $\Delta r_n/r_n \sim 0.05$.

[3] The quantization of angular momentum is equivalent to the quantization of the number of the matter-wave periods along the orbit: $m_e v r = n\hbar \Leftrightarrow n\lambda_{dB} = 2\pi r$.

I.2 Lifetime scaling with n

The lifetime of cRy states $|nc\rangle$'s is remarkably long for highly excited atoms. The quantum mechanical explanation for such a long lifetime lies, again, in the fact that cRy atoms have maximal angular-momentum and they can only decay by *decreasing* m_l via a microwave transition from $|nc\rangle \to |(n-1)c\rangle$. In comparison, low-angular-momentum Rydberg states have many allowed decay transitions in the optical domain. The rates of the transitions being proportional to the cube of the transition frequency explains, if only partially, the comparatively long lifetime of the circular states.

The radiative lifetime of cRy states can be semi-classically estimated [141] by noting that an atomic state emits an energy $h\nu_n$ during its lifetime τ_n. The ratio between these two quantities is the radiated power $\mathcal{P}$ which, according to the Larmor formula [153], is proportional to the square of the electron acceleration a. In the planetary picture provided by Figure I.1, the motion of a cRy electron, during a photon emission, is described by a uniform circular motion. Thus, one can write the acceleration of the trajectory as $a = (2\pi\nu_n)^2 r_n$ and one has

$$\frac{h\nu_n}{\tau_n} \sim (\nu_n^2 a_0 n^2)^2. \tag{I.6}$$

The last statement needed for the estimation is that, for large n, the transition frequency $\nu_n \sim 1/(n-1)^2 - 1/n^2$ between $|nc\rangle$ and $|(n-1)c\rangle$ can be approximated[4] by the derivative $\partial_n E_n \sim 1/n^3$. One then gets $\tau_n \sim n^5$. This is the right scaling for cRy atoms.[5] In Table I.2 we show the radiative lifetime (at 0 K) for some cRy states of relevance to this work.

nc	Lifetime (ms)
$53c$	38.4
$52c$	34.9
$51c$	31.6
$50c$	28.6
$49c$	25.8
$48c$	23.3

Table I.2 Lifetime for a few cRy of interest at 0 K.

I.3 Rydberg atoms in external fields

Due to their huge polarizability, Rydberg atoms are very sensitive to electric fields and, when promoted to high-angular-momentum levels, they also have a very strong magnetic field dependence. Moreover, because of the degeneracy in the Coulomb potential, high-l Rydberg states are only stable in non-vanishing directing fields. In this sense,

[4] This is the third Kepler law. The square of the electron period is proportional to the cube of the orbit radius $\nu_n^2 \sim r_n^{-3}$.

[5] Note that the lifetime for low-angular-momentum Rydberg states scales as n^3 [88, 142].

external fields are both a requirement and a tool for the preparation and manipulation of Rydberg states. We will now consider the modifications of the atomic Hamiltonian $\hat{H}_0$ in the presence of both electric and magnetic external fields.

First, consider an external magnetic field B_z in the z direction. This field gives rise to a Zeeman term $\hat{V}_Z$ that takes the form [147]

$$\hat{V}_Z = g_L \mu_B B_z \hat{L}_z,$$

where μ_B is the Bohr magneton, and $\hat{L}_z$ is the third component of the angular momentum operator $\hat{\mathbf{L}}$. The gyromagnetic factor of the electron is g_L. The Zeeman term degrades the symmetry of the problem from spherical to cylindrical and it shifts the energies by

$$E_{m_l} = g_L \mu_B B_z m_l.$$

In addition, an external electric field F_z in the z direction gives rise to a Stark term $\hat{V}_S$ written [147]

$$\hat{V}_S = q_e F_z \hat{z},$$

where q_e is the charge of the electron and $\hat{z}$ is the third component of the position operator $\hat{\mathbf{r}}$.

The choice of making the fields parallel to each other keeps m_l as a good quantum number while the presence of an electric field turns l into a bad quantum number. For moderate fields, the solutions to the Schödinger equation can be labeled[6] to introduce the n_1 and n_2 non-negative parabolic quantum numbers. These are related to n and m_l by $n = n_1 + n_2 + |m_l| + 1$ and, for convenience, they can be replaced by a derived quantum number $k = n_2 - n_1$. This derived quantum number permits one to write a simple expression for the Stark energy terms when developed in orders of F as $E_{n,k,m_l} = E^{(0)}_{n,k,m_l} + E^{(1)}_{n,k,m_l} + E^{(2)}_{n,k,m_l} + \cdots$. The first and second order Stark shifts in the expansion read

$$\begin{aligned} E^{(1)}_{n,k,m_l} &= \frac{3}{2} q_e a_0 n k \times F, \quad \text{and} \\ E^{(2)}_{n,k,m_l} &= \left(\frac{q_e a_0 n^2}{8\alpha c}\right)^2 (19 + 17n^2 - 9m_l^2 - 3k^2)/m_e \times F^2. \end{aligned} \tag{I.7}$$

Figure I.2 presents the diamond shaped Stark energy level structure (for $B_z = 0$ G and $F_z \gtrsim 2$ V/cm). In blue we show the result for the Coulomb potential and in red we show the structure for Rubidium-87. For the purpose of this Figure we choose $n = 52$. The main features of the Stark diamond can be understood thanks to linear Stark terms as a function of m_l and k. In the case of Rubidium one sees that, for small m_l, the levels get scrambled out of the regular spacing provided by the first order Stark shifts. This irregularity is caused by the quantum defects (see Table I.1). For $|m_l| > 4$, the blue and red levels almost completely overlap. On the inset we show the tip of the diamond where the circular level and the closest elliptical levels ($|52e^{\pm}\rangle$) lie.[7]

[6] The principal quantum number n is only approximately a good quantum number. For $n \sim 50$, at high electric fields (10 V/cm), the states are contaminated by the adjacent manifold ($\sim 1\%$).

[7] Both $k = 0$ tips of the diamond represent a circular level but with opposite projections of angular-

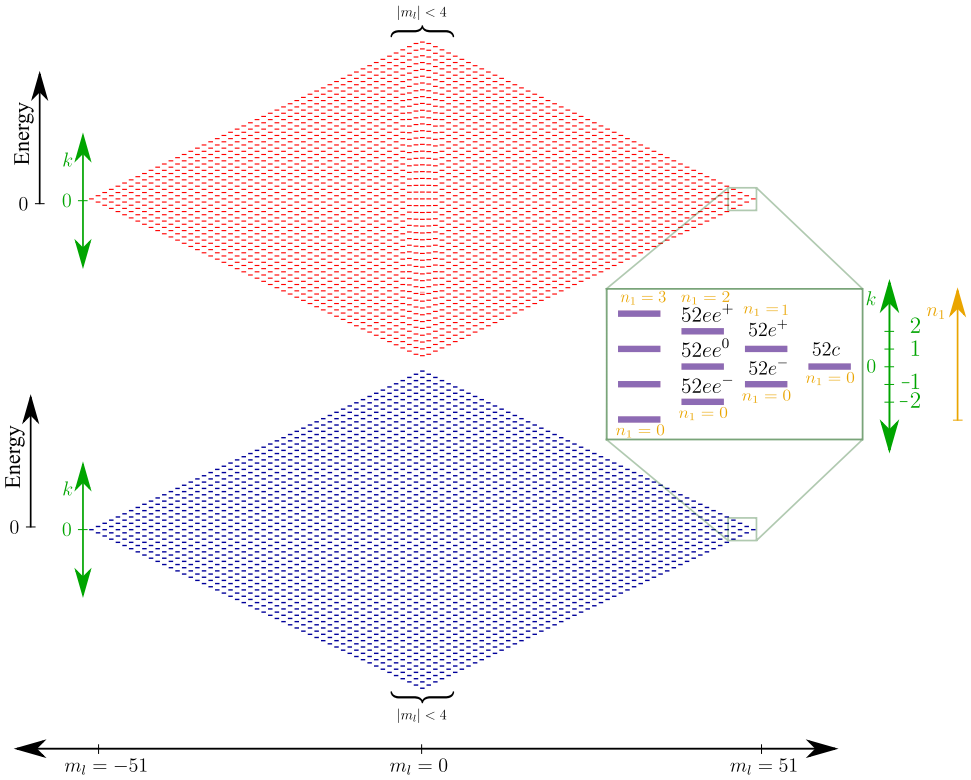

FIGURE I.2 The Stark diamond for Rubidium-87 (red) showing the quantum defects under the influence of an electric field (for $B_z = 0$ G and $F_z > 2$ V/cm) and that for the Coulomb potential (blue).

An alternative, but complementary, way to picture the relevant levels is to plot their energy as a function of the external electric field magnitude. In Figure I.3 we show the Stark map (for $B_z = 0$) for the $n = 52$ dipole accessible levels from $|52D_{5/2}, m_j = 5/2\rangle$. These are limited to $m_l = 2, 3$. We see that the quantum defect strongly shifts away the low-angular-momentum levels (D, F, and G). The stronger the shift, the weaker their electric field dependence around zero field.

I.4 The Rydberg-Rydberg interaction

Besides being very sensitive to external fields, Rydberg atoms strongly interact with each other. The dominant interaction is due to their electric dipole moment and its Hamiltonian takes the form [147]

$$\hat{V}_{dd}(R) = \frac{1}{4\pi\epsilon_0 R^3}\left[\hat{d}_1 \cdot \hat{d}_2 - 3\left(\hat{d}_1 \cdot \frac{\mathbf{R}}{R}\right)\left(\hat{d}_2 \cdot \frac{\mathbf{R}}{R}\right)\right]. \tag{I.8}$$

Here $\hat{d}$ is the dipole operator and $\mathbf{R}$ is the position vector describing the coordinates of one atom with respect to the other. One can develop the effect of this operator as a perturbative expansion taking $1/R^3$ as the expansion parameter. To make the notation

momentum m_l. The classical picture is that the electrons 'rotate' in opposite directions. [107].

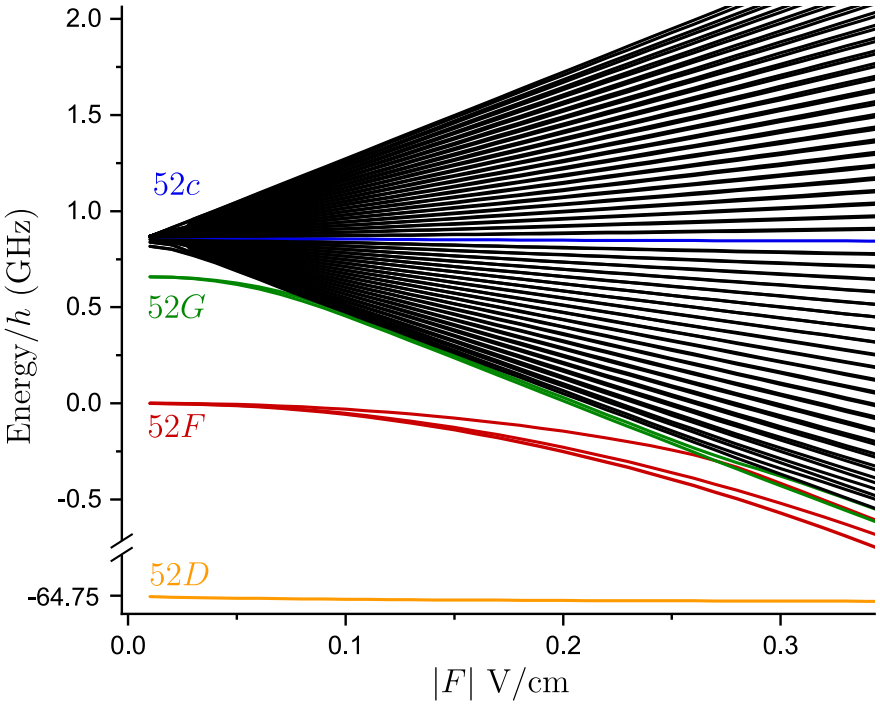

FIGURE I.3 We show the electric field dependence of the atomic levels corresponding to $n = 52$ and $l \geq 2$ for Rubidium-87. The zero of energy is taken to be the energy of state $52F, m_j = 2$ at zero electric field. At a field of ~ 0.3 V/cm the quantum defect separating the F level from the multiplicity is of the same order as Stark shift and the F level acquires a linear energy dependence with the field.

self-evident we will write the energies as

$$E = \sum_n \frac{C_{3\times n}}{R^{3\times n}}. \tag{I.9}$$

The first order term is proportional to the coefficient C_3 and it is called the 'direct dipole interaction' term. The second order term is proportional to C_6 and it is referred to as the 'van der Waals' (vdW) term. Using perturbation theory, the general expansion for *any* matrix elements V_{ab} [147] reads:

$$V_{ab}^{(1)} = \langle a_1, a_2 | \, \hat{V}_{dd}(R) \, | b_1, b_2 \rangle = \frac{C_{3,a,b}}{R^3}, \tag{I.10}$$

$$V_{ab}^{(2)} = \sum_c \frac{\langle a_1, a_2 | \hat{V}_{dd} | c_1, c_2 \rangle \langle c_1, c_2 | \hat{V}_{dd} | b_1, b_2 \rangle}{E_a + E_b - E_c - E_d} = \frac{C_{6,a,b}}{R^6}, \cdots \tag{I.11}$$

where the superindex states the order of the perturbation. Since the dipole-dipole operator does not commute with the Zeeman-Stark Hamiltonian, the interaction eigenbasis will contain states that are linear combinations of the two-atom parabolic basis.

A pair of atoms in the same state

We describe the interaction of a pair of cRy atoms by introducing a notation for the eigenstates of the full interaction Hamiltonian. We define the interaction eigenstate $|\psi_{50c,50c}\rangle$ as the state that is adiabatically coupled to the product state $|50c, 50c\rangle$ as $R \to \infty$.

This state has a well-defined energy dependence with distance that we plot in Figure I.4. Fitting this data will allow us to extract the $C_{3\times n}$ (eq.(I.9)) coefficients for the $50c$ – $50c$ interaction. The plot is made by diagonalizing the full interaction Hamiltonian (including the Stark and Zeeman terms) for each value of R. For the calculation we take the atoms to be positioned along the x direction and the fields to be along the z direction as shown on the inset. The directing fields are taken to be F_z=1 V/cm and B_z=10 G. The color code represents the proportion of the decoupled parabolic state $|50c, 50c\rangle$ in the actual eigenstates of the full Hamiltonian. The Hilbert space for the pair is truncated to 1225 states for this calculation. The basis used for the matrix diagonalization is built by taking products of parabolic states. The truncation is made by imposing limits to the span of the quantum numbers of the single atom states, taking only states with $\Delta m_l \leq 2$ and $\Delta n \leq 2$ from state $|50c\rangle$.

For as long as $|\psi_{50c,50c}\rangle \sim |50c, 50c\rangle$ we expect no direct dipole interaction since the atoms have no permanent dipole (see Figure I.1). As expected, the linear dependence in the loglog scale manifests an interaction in $1/R^6$. We then fit the energy as a function of the atomic separation by $E(R) = C_6/R^6$ (dashed black line) in the region between 5 and 20 micrometers. The coefficient associated to the eigenvalue of $|\psi_{50c,50c}\rangle$ is found to be $C_{6,50,50} = h \times 4.170$ GHz/µm^6. At $R < 3$ µm the interaction is too strong and perturbation theory to second order fails.

For a pair of atoms in state $|\psi_{48c,48c}\rangle$ the van der Waals coefficient is found to be $C_{6,48,48} = h \times 3.032$ GHz/µm^6. Note that in both cases the interaction is repulsive.

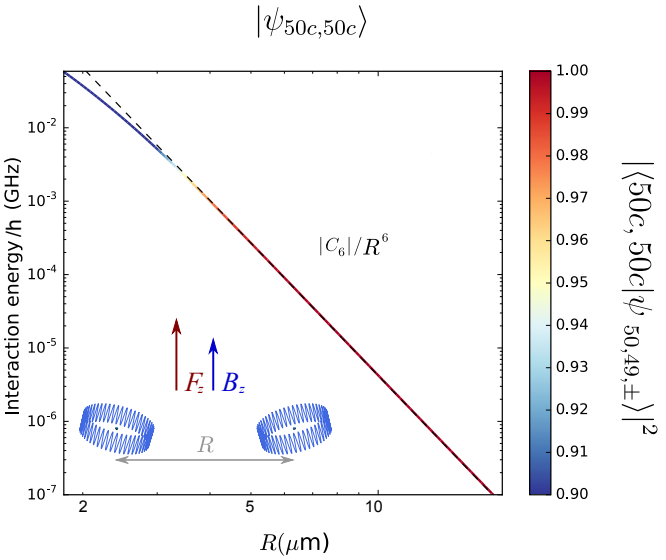

FIGURE I.4 We show the energies of pair $|\psi_{50c,50c}\rangle$ as a function of distance. The orientation of the electric and magnetic directing fields is shown by the red and blue arrows respectively.

Main contributions to the mixing

The most relevant level pairs for describing the previous van der Waals shift are the ones closest to resonance in absence of the perturbation (see eq.(I.11)). Therefore, with the help of Figure I.5 one can see that the main correction to the expansion of $|\psi_{50c,50c}\rangle$ in the parabolic basis comes from state $|ne^+, ne^-\rangle + |ne^-, ne^+\rangle$ (red level).[8] This is because circular states have no linear Stark shift ($k = 0$, see eq.(I.7) and Figure I.2) and because the pair of elliptical states in $|ne^{\pm}\rangle$ have $k = \pm 1$ so their linear Stark cancels exactly. Note that the exact resonance is nonetheless avoided thanks to the quadratic Stark shift and the linear Zeeman shift. Thus, these external fields control the level mixing. Many other close laying pairs of levels are either far off-resonant (green levels) or forbidden by the dipole selection rules (gray levels).

A semi-classical picture helps to understand the atoms' behavior when they are close together. One can picture the dipoles tilting towards each other as the inter-atomic dipolar electric field becomes relevant compared to the external directing field (see inset in Figure I.4). This explains the mixing of the parabolic basis, and at the same time suggests that stronger external directing fields will compensate for this effect. This is confirmed by the quantum mechanical picture where external fields enforcing m_l as a good quantum number mitigate level pollution caused by the m_l- mixing dipole interaction.

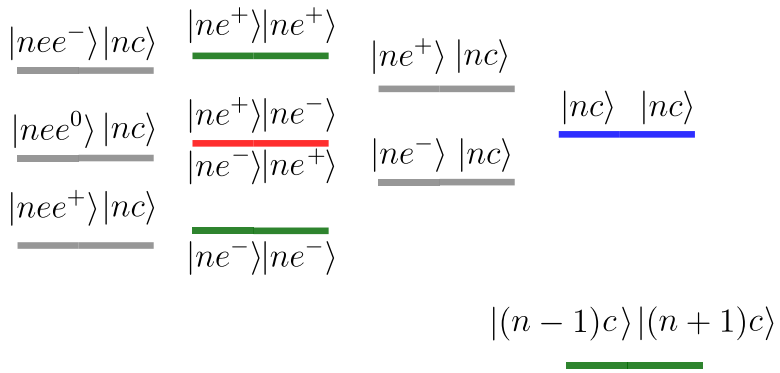

FIGURE I.5 Energy diagram of the relevant states for the interaction. The blue level represents the circular pair state. The red level provides the dominant contribution to the perturbation. The grey states are not coupled by the dipole Hamiltonian to the circular pair. The red and blue levels are drawn slightly shifted to describe the Zeeman and quadratic Stark shifts.

A pair of atoms in different states

In the case of a non-interacting pair of circular atoms with different n we have two degenerate eigenstates that we write as $|nc, n'c\rangle$ and $|n'c, nc\rangle$. The presence of the interaction breaks this degeneracy and in the limit $R \to \infty$ the eigenstates are found to be the symmetric and anti-symmetric combinations. We define then the interaction eigenstates $|\psi_{n,n',\pm}\rangle$ for all distances R as

[8] Note that interference effects eliminates the contribution of $|ne^+, ne^-\rangle - |ne^-, ne^+\rangle$

$$|\psi_{n,n',\pm}\rangle \xrightarrow{R\to\infty} \frac{1}{\sqrt{2}}(|nc, n'c\rangle \pm |n'c, nc\rangle). \tag{I.12}$$

These two eigenstates have a well-defined energy dependence with distance that one can fit to extract the $C_{3\times n}$ coefficients. In Figure I.6 (a) we show the energies dependence for $|\psi_{50,49,\pm}\rangle$ ($\Delta n = 1$). The color code represents the population of state $|50c, 49c\rangle$ at each distance R. The Hilbert space for the calculation is truncated to 2350 states defined by $\Delta m_l \leq 2$ and $\Delta n \leq 2$ now from both states $|50c\rangle$ and $|49c\rangle$.

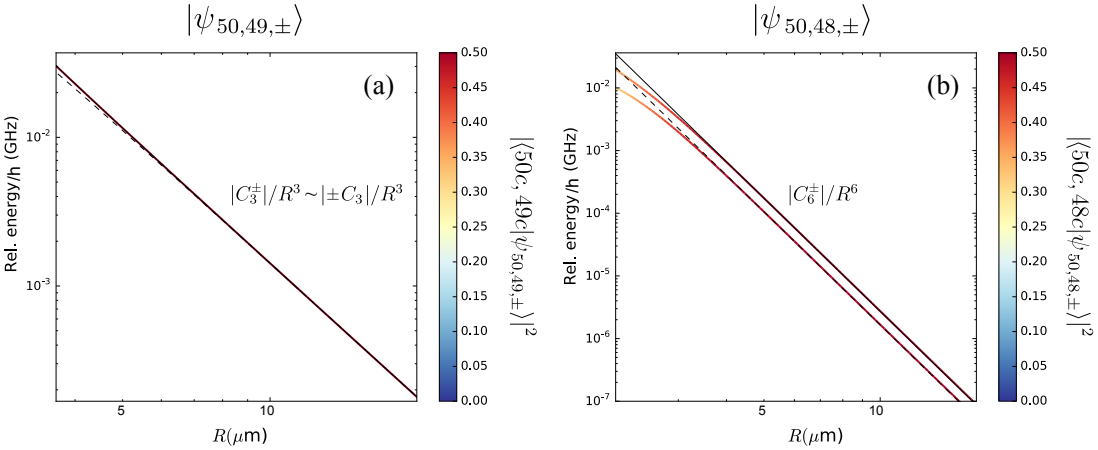

FIGURE I.6 Absolute value of the interaction energy as a function of position for interacting circular atoms. We show the energy dependence of the pair $|\psi_{50c,49c,\pm}\rangle$ (a) and $|\psi_{50c,48c,\pm}\rangle$ (b) with the interatomic distance R. The color bar represents the proportion of the product states to the eigenstate. For the pair of levels $50c$ – $49c$ ($\Delta n = 1$) the direct dipole term dominates the interaction ($1/R^3$). For the pair $50c$ – $48c$ ($\Delta n = 2$) the van der Waals ($1/R^6$) interaction dominates. In both plots (a) and (b), the solid black line fits the energy for the anti-symmetric superposition and the dashed line fits that of the symmetric superposition for $R > 5$ µm.

In contrast to the previous case study, one now expects the pair of atoms to interact via the direct dipole coupling $1/R^3$. This becomes obvious while writing the limiting state (eq.(I.12)) as

$$\begin{aligned}|50c, 49c\rangle \pm |49c, 50c\rangle = (|50c\rangle + |49c\rangle) \otimes (|50c\rangle \pm |49c\rangle) + \\ - (|50c\rangle - |49c\rangle) \otimes (|50c\rangle \mp |49c\rangle),\end{aligned}$$

as one exposes the permanent dipoles in each atom (see Figure I.1). Note also that the 'classical dipoles' are aligned or anti-aligned depending on the symmetry of the superposition. The atomic interaction is then attractive or repulsive in accordance with the classical formula.

We plot the energy dependence in Figure I.6 (a) and we fit its absolute value as a function of the atomic separation by $E(R) = |C_3^{\pm}|/R^3$ in the region between 5 and 20 micrometers. The parameters of the fit are found to be $C^{+}_{3,50,49} = +h\times 1.4236$ GHz/µm^3 (dashed line) where the (+) stands for the symmetric superposition. For the anti-symmetric superposition (−) we get $C^{-}_{3,50,49} = -h \times 1.4267$ GHz/µm^3 (solid black line).

In Figure I.6 (b) the pair states we consider is $|50c\rangle$ and $|48c\rangle$. Again, after the pictorial representation in Figure I.1, one expects no permanent dipole interaction. We fit the energy as a function of the atomic separation by $E(R) = C_6^{\pm}/R^6$ in the region between 5 and 20 micrometers.

In this case, the fit parameters are found to be $C^{+}_{6,50,48} = h \times 1.635$ GHz/µm^6 where the (+) stands for the symmetric superposition (dashed black line). For the anti-symmetric superposition (−), we get $C^{-}_{6,50,48} = h \times 2.435$ GHz/µm^6 (solid black line). Both superpositions interact repulsively.

I.5 Conclusion

In this chapter we developed a theoretical framework to study cRy atoms using elementary atomic physics. A short review of some simple effects that give the cRy atoms their exaggerated properties was presented. We focused our attention on cRy atoms with principal quantum number around $n \sim 50$, and we introduced some scaling rules that allow us to calculate, if not exactly [154], the expected behavior for other circular states. The intuition we tried to transmit will prove useful as one progresses in the present manuscript.

Circular Rydberg atoms have a millisecond range lifetime at cryogenic temperatures and interact very strongly with each other (tens of MHz), even at distances of a few micrometers. These properties make them, themselves, fascinating research objects, but together with state-of-the-art experimental techniques, their exaggerated properties are promoted to technological tools. In the following chapter we will turn to defend the claim that a promising quantum simulator can be built using cRy states.

Chapter II

Towards quantum simulation with Circular Rydberg atoms

Contents

II.1 Principle of the proposed simulator

Many-body physics has proven to be very demanding. The field has developed rapidly and many experimental and theoretical advances have been made in the last years [155]. Nonetheless, open questions still remain and they have pushed the field in new directions. Problems related to slow dynamics and disorder are at the center of this discussion and, even if some very powerful and helpful approximations provide insight, there is still room beyond them for research.

Atomic physics provides us with a toolbox of highly controllable and versatile quantum objects out of which one can engineer artificial systems [156]. We will discuss a new paradigm for quantum simulation of a spin-chain using cRy atoms. Our proposal promises unprecedented flexibility during long timescales and, with it, the possibility to explore domains which have remained out of reach so far.

The proposed quantum simulator relies on the laser trapping of cRy atoms and it is sketched in Figure II.1. The deterministic preparation of a cRy atom chain inside a spontaneous emission inhibiting structure complemented by single site resolution will provide the hardware [108]. The very challenging steps to achieve such an experimental landmark are discussed in this chapter.

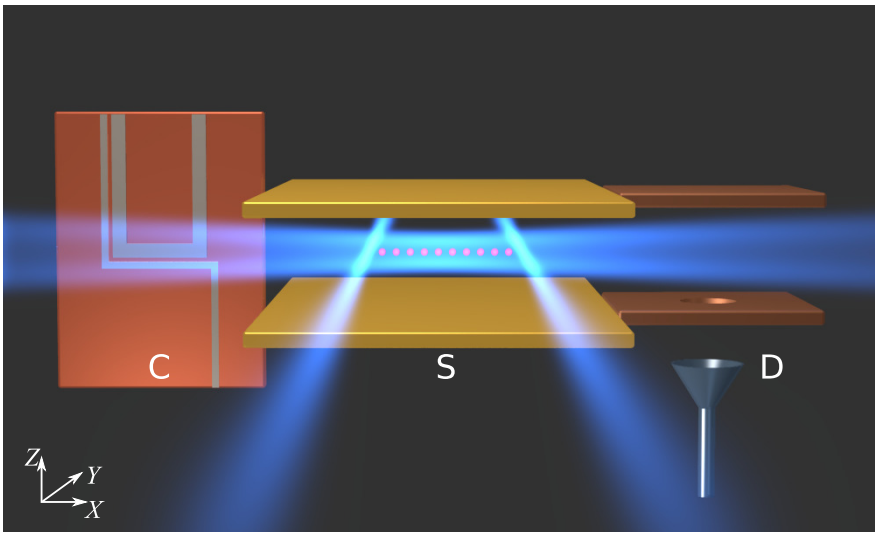

FIGURE II.1 Sketch of the proposed simulator. An atom-chip (C) will be used to prepare cold atoms, a chain of Rydberg atoms will evolve under a capacitive structure in the science (S) region. The Rydberg atoms are to be detected (D) with single site resolution.

II.1.1 The emulated XXZ model

It is well-known that spin physics is responsible for magnetic phenomena in matter. Even though the magnetic spin-spin interaction of a pair of electrons at 0.1 nm from each other is about 1 K, the ferromagnetic properties of, say, magnetite persist beyond 800 K. This is strong evidence suggesting that magnetism is hardly related to the magnetic dipolar interactions in matter [157]. Actually, the origin of magnetism is to be tracked back to the interplay between fermionic spin statistics and the Coulomb

interaction. The Coulomb energy depends only on the relative distance between the two charged particles in question but, due to the anti-symmetrization postulate, the position of a pair of indistinguishable electrons is strongly correlated to their spin wave function. It is this correlation that permits us to cast the relevant interaction in the language of spin [158].

In this thesis we will be concerned with a Heisenberg Hamiltonian that takes the form

$$\begin{aligned}\frac{\hat{H}}{h} =& \frac{\Delta}{2}\sum_{j=2}^{N-1}\hat{\sigma}_j^z + \frac{\Omega}{2}\sum_{j=1}^{N}\hat{\sigma}_j^x + \\ &+ \sum_{j=1}^{N-1}\left[J_z\hat{\sigma}_j^z\hat{\sigma}_{j+1}^z + J\left(\hat{\sigma}_j^x\hat{\sigma}_{j+1}^x + \hat{\sigma}_j^y\hat{\sigma}_{j+1}^y\right)\right],\end{aligned} \tag{II.1}$$

where $\sigma_j^{x_i}$ is the x_i Pauli operator of the jth spin of an N spin chain.

This Hamiltonian describes anisotropic magnets where two spin components are coupled with the same strength J, while a third direction labeled z couples spins with an independent coupling constant J_z.[1] The one-particle terms correspond to external magnetic fields in x and z directions with magnitudes Ω and Δ respectively. The phase diagram in Figure II.2, allows us to motivate the flexibility and variety of phases that can be achieved in a simulation of this Hamiltonian.

II.1.2 Phase diagram

The phase diagram in Figure II.2 shows the magnetic phases for different values of the Hamiltonian parameters and $\Delta = 0$. Four main areas are separated by the type of correlations found in the ground state of the chain. The fact that it is possible to theoretically understand the behavior of the system's ground state is of great importance and will provide a way to benchmark our simulator.

We start discussing the phase diagram by referring to the biggest area in the plot (green). It corresponds to the situation in which the magnetic field along the x direction is dominant over the interaction ($\Omega \gg J, J_z$). The Hamiltonian can then be seen as $\hat{H}/h \sim \Omega\sum_{j=1}^{N}\hat{\sigma}_j^x/2$ and the ground state is, naturally, polarized along the x direction. The ground state is then $\otimes^N(|\uparrow\rangle - |\downarrow\rangle)/\sqrt{2}$ and the phase is 'paramagnetic' (P_x).[2] This phase is separated from the rest by critical (algebraic) Ising transitions as shown by the red lines in Figure II.2.

In the limit of a vanishing transverse magnetic field ($\Omega = 0$) we find three symmetry-breaking phases that correspond to the purely XXZ model with no external magnetic field. For $J_z < -J$ the system presents ferromagnetic ordering (F), a gapless Luttinger liquid critical phase shows up for $-J < J_z < J$, and a gapped Néel phase in the z direction appears for $J_z > J$. The ferromagnetic and the Néel phases (N_y and N_z) have doubly degenerate ground states (in contrast with the paramagnetic phase) and break the Z_2^z symmetry. The Néel phase also breaks the translational symmetry.

[1] In particular this Hamiltonian describes the physics of the Cs_2CoCl_4 [159, 160] or $BaCo_2V_2O_8$ [161] quantum magnets.

[2] The terminology of Ferromagnet is reserved for spins that are aligned due to their interaction.

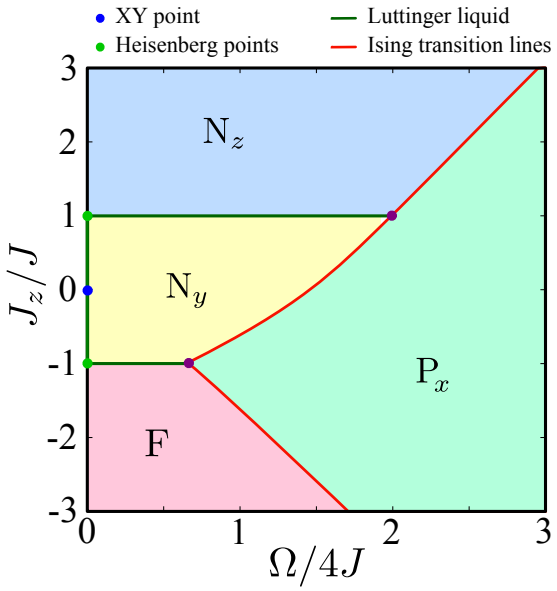

FIGURE II.2 Sketch of the phase diagram of the Hamiltonian eq.(II.1) for $\Delta = 0$. The reconstruction is based on the results of Figure II.3 and from [162]

If a transverse magnetic field is applied ($\Omega > 0$), these two gapped phases are stable until the gap closes at the Ising transition line, at which the system enters the paramagnetic phase. For the Luttinger liquid phase, a non-zero transverse field immediately opens a gap. The associated broken symmetry is Z_2^y, corresponding to a Néel ordering in the y direction. This order is eventually destroyed by the transverse field through an Ising transition towards the paramagnetic phase.

The boundaries between the ferromagnetic phase and the two Néel phases emerge from the Heisenberg points $J_z = \pm J$, and $\Omega = 0$. The upper line $J_z = J$ corresponds to the Heisenberg model under an external field [163, 164], for which a Luttinger liquid phase survives up to the critical field $\Omega/4J = 2$, at which a commensurate-incommensurate transition occurs [165, 166]. The line $J_z = -J$ is subtle since it does not correspond to the Heisenberg model as the Hamiltonian cannot be cast as a scalar product. A pertinent transformation ($\hat{\sigma}_z \to (-1)^j \hat{\sigma}_z$) however, permits the treatment in terms of a Heisenberg model with a staggered external field [166, 167].

This spin-1/2 model presents other remarkable features. The integrability of the model is an essential feature to discuss relaxation and thermalization (non integrable models are chaotic). The model is integrable by the Bethe ansatz when $\Omega = 0$ and on the critical lines emerging from the Heisenberg points. In particular, $\Omega = J_z = 0$ corresponds to the XY model that maps onto free fermions (via a Wigner-Jordan transformation) [168]. In the $J = 0$ limit, the model maps onto the anti-ferromagnetic Ising model in a transverse field, which is also equivalent to free fermions [169], and is thus integrable. Away from these limits, the model is non-integrable.

The quantitative plot of Figure II.2 is supported by numerical results based on matrix-product state (MPS) simulations [170–173] that are shown in Figure II.3. We define the average magnetization along the different axis as

$$\mathcal{M}_{x_i} = \frac{1}{N}\sum_{j=1}^{N}\langle\hat{\sigma}_j^{x_i}\rangle.$$

For symmetry reasons, $\mathcal{M}_{y,z}$ must be zero on non-degenerate finite-sized ground states. Therefore, the ordering of the spins is better captured by order parameters defined from correlations as

$$\mathcal{O}_{x_i} = \text{sign}\,(C_{x_i})\,\sqrt{|C_{x_i}|} \text{ with } C_{x_i} = \left\langle \hat{\sigma}_{N/2}^{x_i}\hat{\sigma}_{N/2+r}^{x_i}\right\rangle.$$

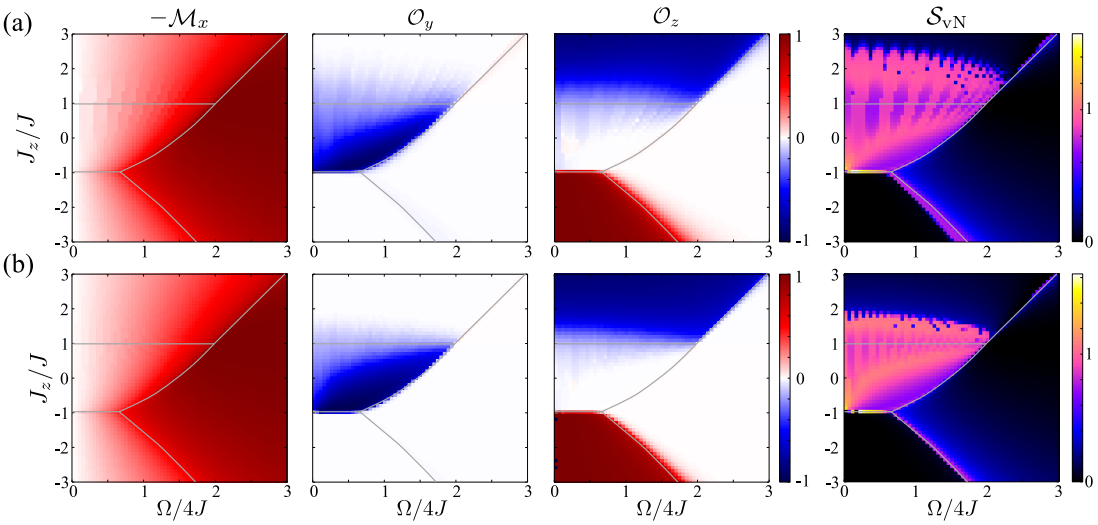

FIGURE II.3 (a): MPS results for the order parameters (see definitions in main text) for an open chain with $N = 40$ spins. (b): Same for a $N = 90$ open spin chain. The order parameters are computed with $r = 17$ for $N = 40$ and $r = 31$ for $N = 90$. Red regions represent ferromagnetic ordering while blue ones represent anti-ferromagnetic (Néel) ordering. The gray lines are guides to the eye for the quantum phase transition lines. The horizontal lines can be computed analytically, or inferred from symmetry arguments.

The magnetization and order parameters along the three spin axes as a function of $\Omega/4J$ and J_z/J for (a) $N = 40$ and (b) $N = 90$ spin chains are shown. The first column shows that, as expected, the magnetization $\mathcal{M}_x$ increases steadily with $\Omega/4J$. The region with a large $\mathcal{M}_x$ value corresponds to the paramagnetic phase. Along the $J_z = J$ line and for $N = 40$, we observe magnetization plateaus, corresponding to a succession of ground states with fixed total magnetization along x. These finite-size effects are gradually smoothed out away from this line [162, 174].

The order parameters $\mathcal{O}_y$ and $\mathcal{O}_z$ show the strength of Néel and ferromagnetic ordering across the phase diagram. While most phase transitions are rather steep, the transition at $J_z = J$ is much smoother due to strong finite-size effects. In this region, the gaps are indeed the smallest (the Luttinger liquid to Néel transition is of the Berezinskii-Kosterlitz-Thouless type [175–177]).

The features of the phase diagram and its finite-size effects are also evident when plotting the von Neumann entropy

$$S_{vN} = -\mathrm{Tr}\left[\hat{\rho}\log\hat{\rho}\right],$$

where $\hat{\rho}$ is the reduced density-matrix of the first $N/2$ spins. Along the critical lines, one expects [178, 179] a logarithmic divergence of the entropy $S_{vN} \sim c/6\log[N]$ with $c = 1$ for Luttinger liquid phase and $c = 1/2$ for Ising transitions. In the gaped phases, the entropy remains finite, and decreases when the gap increases. It displays plateaus along the $J_z = J$ line reminiscent of the magnetization plateaus.

Figure II.3 shows that this spin chain Hamiltonian exhibits a wide variety of interesting behaviors. It also shows that, in most regions, finite size effects are not too large, since a good approximation of the thermodynamical limit can be reached with 40 atoms only. The observation of this phase diagram would be an excellent benchmark for the operation of the simulator where many clear theoretical claims are still awaiting experimental confirmation. Success in such a preliminary experimental stage will give one confidence in the simulation. One will then be able to trust the results that the simulator provides in more demanding regimes. This will pave the way to study more challenging dynamical experiments or even disordered systems where interesting questions are still open.

II.1.3 The role of the circular Rydberg atoms

In what follows we derive the emergence of this spin Hamiltonian from the underlying atomic physics of the actual system used to build the simulator. The spin will be encoded in a two-level system made of two cRy states. The van der Waals atomic couplings between the atoms give rise to the spin coupling terms proportional to J and J_z. A MW dressing of the atom chain will give rise to single atom terms that are identical to those appearing for a single spin in an external magnetic field.

The van der Waals interaction

A pair of circular Rydberg atoms in the same state $|nc\rangle$ and at a distance of $R \gg n^2 a_0$ interact via the fluctuations of their electronic wave function (see chapter I). This is known as the van der Waals ($\sim 1/R^6$) interaction and corresponds to a second order process mediated by the dipole-dipole interaction. The model Hamiltonian for the interaction between neutral atoms is given by eq. (I.8) and we rewrite it here in terms of the spherical tensor operators [148]. Taking the quantization axis orthogonal to the axis connecting the pair of atoms, we get

$$\hat{V}_{dd}(R) = -\frac{q_e^2}{3\epsilon_0 R^3} r_1 r_2 \left[\hat{Y}_1^0\hat{Y}_1^0 + \frac{1}{2}(\hat{Y}_1^{+1}\hat{Y}_1^{-1} + \hat{Y}_1^{-1}\hat{Y}_1^{+1}) - \frac{3}{2}(\hat{Y}_1^{+1}\hat{Y}_1^{+1} + \hat{Y}_1^{-1}\hat{Y}_1^{-1})\right]. \tag{II.2}$$

From this notation, the allowed dipole transitions are explicit since the rank and the component of the involved operators are exposed. The selection rules arise straightforwardly from the Wigner-Eckart theorem.

Considering now an atomic pair of different states $|nc\rangle\,|(n+1)c\rangle$ at distances of

$R \sim$5 µm (much bigger than the atom size) one obtains first-order exchange interactions that scale as $V_{dd} \sim 1/R^3$. This will lead to trivial dynamics since these terms will dominate the evolution. Having Hamiltonian terms of the same order of magnitude (all $\sim 1/R^6$) will allow us to fully exploit the richness of our simulator. This is the case if we explicitly take as the pair of states $|nc\rangle$ and $|(n+2)c\rangle$.

Using the parabolic basis, we can write the Hamiltonian restricted to the two-atom two-level subspace $\{|nc\rangle|nc\rangle, |nc\rangle|(n+2)c\rangle, |(n+2)c\rangle|nc\rangle, |(n+2)c\rangle|(n+2)c\rangle\}$ as

$$\hat{V}_{vdW} = \frac{1}{R^6}\begin{pmatrix} C_{6,n,n} & 0 & 0 & 0 \\ 0 & C_{6,n,n+2} & A_{6,n+2,n} & 0 \\ 0 & A_{6,n+2,n} & C_{6,n+2,n} & 0 \\ 0 & 0 & 0 & C_{6,n+2,n+2} \end{pmatrix}. \tag{II.3}$$

The matrix elements can be written as

$$V^{(2)}_{ab} = \sum_{|c\rangle} \frac{\langle a|V_{dd}|c\rangle\langle c|V_{dd}|b\rangle}{E_a + E_b - E_c - E_d} = \begin{cases} A_{6,a,b}/R^6 & \text{if } a \neq b \\ C_{6,a,b}/R^6 & \text{if } a = b \end{cases} \tag{II.4}$$

where both a and b stand for two-atoms states.

The central 2×2 matrix can be diagonalized. The eigenvalues are found to be $C'_{6,\pm} = C_6 \pm A_6$, where we have used the fact that $C_{6,n,n+2} = C_{6,n+2,n} = C_6$ and done analogously for A_6. The $\pm$ subindex corresponds to the symmetric and anti-symmetric superposition of states.

The Feynman-like diagrams shown in Figure II.4 are useful to understand the terms in the Hamiltonian (II.3). The C_6 coefficients are known as the self-interactions (diagonal) and the A_6 coefficients are known as the exchange coefficients (off-diagonal) and represent flip-flops between the basis states.

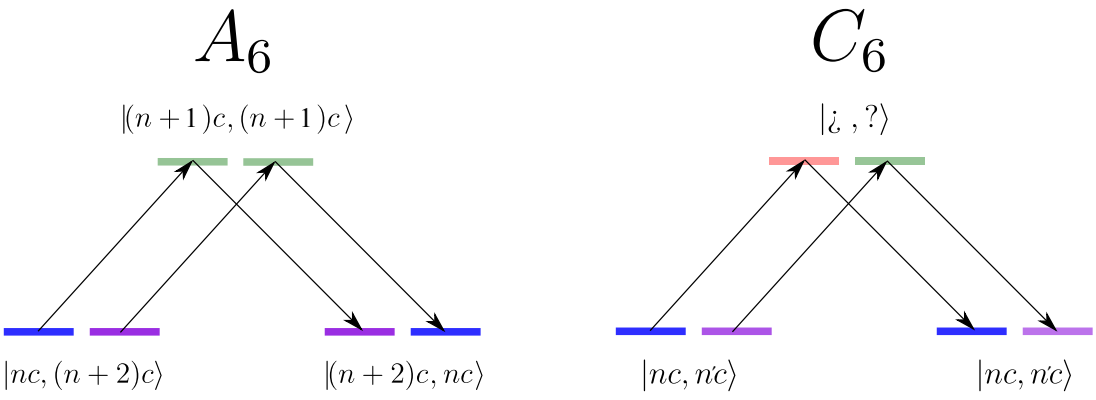

FIGURE II.4 We show a graphical interpretation of the physical processes giving rise to the van der Waals interaction eq.(II.3) between cRy atoms. The state labeled with question marks represent anyone of the many states contributing to the process.

A convenient rewriting of this interaction Hamiltonian can be done in terms of the Pauli matrices. Projecting $\hat{V}_{vdW}$ in the base that one can construct out of $\hat{\sigma}^i \otimes \hat{\sigma}^j$ where $i, j \in \{0, x, y, z\}$, $\hat{\sigma}^0$ is the 2×2 identity operator and the other three indices designate the three Pauli matrices, the new expression reads

$$\hat{V}_{vdW} = \delta E_0 \hat{\sigma}_1^0 \hat{\sigma}_2^0 + \frac{\delta\zeta}{2}\left(\hat{\sigma}_1^z \hat{\sigma}_2^0 + \hat{\sigma}_1^0 \hat{\sigma}_2^z\right) + J_z \hat{\sigma}_1^z \hat{\sigma}_2^z + J\left(\hat{\sigma}_1^x \hat{\sigma}_2^x + \hat{\sigma}_1^y \hat{\sigma}_2^y\right), \tag{II.5}$$

where the subindex labels the atom, and the tensorial product notation has been dropped. The coefficients introduced are given by the atomic interaction parameters as

$$\begin{aligned} \delta E_0 &= \frac{C_{6,n,n} + 2C_{6,n,n+2} + C_{6,n+2,n+2}}{4R^6} \\ \delta\zeta &= \frac{C_{6,n,n} - C_{6,n+2,n+2}}{2R^6} \\ J_z &= \frac{C_{6,n,n} - 2C_{6,n,n+2} + C_{6,n+2,n+2}}{4R^6} \\ J &= \frac{A_{6,n,n+2}}{2R^6}. \end{aligned} \tag{II.6}$$

If the motional degrees of freedom are completely frozen, the δE_0 term is constant and nothing but an energy offset that we will omit from now on.

The expression in eq.(II.6) is to be compared with eq.(II.1). One notices that, in our derivation, we have an extra term $\delta\zeta/2(\hat{\sigma}_1^z + \hat{\sigma}_N^z)$ which keeps track of the finite size of the chain. It originates from the fact that the first and last atom have only one neighbor and thus their energies are shifted by half of the interaction. This makes the atoms in the tips of the chain different from the inner atoms and represents an imperfection in the simulation of the standard XXZ Heisenberg Hamiltonian. Note, however, that it is an asset or a drawback depending on the purpose of the quantum simulator. For instance, the local symmetry breaking field is an asset while entering a ferromagnetic phase. It creates a perturbation that naturally triggers the build-up of the order parameter. Also note that, for large enough chains and in gapped phases, these edge effects are relevant only over the correlation length. The physics of the model can still be captured in the bulk of the chain. If the end atom asymmetry shows to be a limiting factor, a spatial light modulator can be used to design periodic chains [180]. Another solution is to prepare the end atoms in far lying cRy levels. The exchange interaction would then be negligible for the end atoms, but they will still shift the energy of their neighbor and compensate for $\delta\zeta$. The flexibility and control that state-of-the-art techniques provide make these challenging perspectives a possibility.

In comparing eq.(II.6) with eq.(II.1), one also notices that the single spin terms are missing. These are reproduced by a MW dressing that we introduce next.

The single-atom terms

A single two-level atom defined in the space spanned by $\{|(n+2)c\rangle, |nc\rangle\}$ has a Hamiltonian given by

$$\hat{H}_0 = \frac{h\nu_0}{2}\hat{\sigma}^z,$$

where the energy difference $h\nu_0$ is computed from eq.(I.1). The ground state is trivially found to be $|nc\rangle$ but by turning on a MW coupling, the dynamics are very much enriched. In the interaction picture, under the rotating wave approximation [141], the

single-atom Hamiltonian now presents two non-commuting terms

$$\hat{H}_0 = \frac{\hbar\Delta}{2}\hat{\sigma}^z + \frac{\hbar\Omega}{2}\hat{\sigma}^x, \tag{II.7}$$

and directly maps into the external fields to be simulated (eq.(II.1)). Here Δ is the detuning between the MW field and the atomic transition and Ω is the Rabi frequency of the dressing. We note that this dressing does not change the interaction terms.

By adding up the interaction terms (eq.(II.5)) and the single atom terms (eq.(II.7)), and by summing over all the N atoms in the chain, the formal analogy between the simulated system (eq.(II.1)) and the cRy atom simulator is complete.

II.1.4 Tunability

We see from Figure II.2 that the relevant thermodynamic ratio is J_z/J. By being able to tune it from $J_z/J < -1$ to $J_z/J > 1$ one is able to access all the available phases. Remarkably, we have found that the atomic interaction is tunable at will by controlling the electric and magnetic field over the atoms. We show this in Figure II.5 (a) and (b). The points in the graphs each correspond to the full diagonalization of a two-atom Hamiltonian. The basis used is defined, as before, to contain states differing by $\Delta n \leq 2$, $\Delta m_l \leq 2$ from each level in the considered pair. Many choices on the spin encoding into cRy levels are shown.

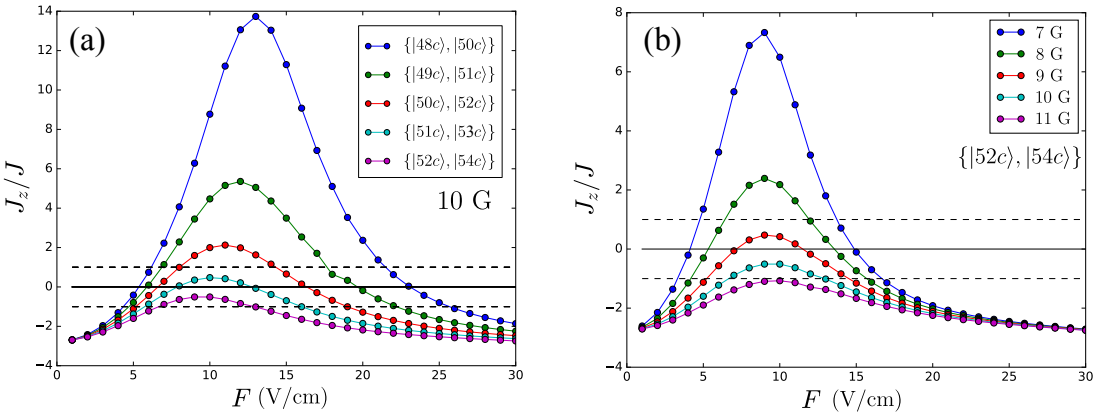

FIGURE II.5 On the left we show the J_z/J ratio for $\{|nc\rangle, |(n+2)c\rangle\}$ pairs. The plot is done for $B = 10$ G and as a function of the electric field F. Atoms are 5 µm apart. Note that for $n = 52$ the ratio is always negative. On the right we show, as an illustration of the flexibility provided by the magnetic field, that by reducing the magnetic field, the $J_z/J \to -1, 1$ tunability with F is regained for $n = 52$.

The exchange characterized by J is proportional to the van der Waals exchange term $\sim A_6$ (see eq.(II.4) and Figure II.4) and it is found to depend only weakly on the electric field. We understand this using the analytic expression coming from perturbation theory: The only way a pair of atoms can flip in a Föster-like energy transfer $|nc\rangle\,|(n+2)c\rangle \to |(n+2)c\rangle\,|nc\rangle$ is via the intermediate pair $|(n+1)c\rangle\,|(n+1)c\rangle$ as shown in Figure II.4. Effectively, the A_6 depends only quadratically on the electric field because the intermediate pair $|(n+1)c\rangle\,|(n+1)c\rangle$ has a quadratic Stark shift to leading order.

The parameter J fixes the typical time constant for the simulation. For a pair of interaction atoms in $|50c, 48c\rangle$ at distance of $R = 5$ µm from each other, and under external directing fields of $F = 2$ V/cm and $B = 12$ G, we find a numerical value of $J \sim h \times 17$ kHz. Note that its strong dependence on distance ($1/R^6$) allows for a large tunability of this characteristic timescale.

On the other hand, the magnitude of the electric field has a strong effect on the value of J_z. Once more, this can be understood using the diagrams in Figure II.4. Since the self-coupling $|nc\rangle\,|n'c\rangle \rightarrow |nc\rangle\,|n'c\rangle$ can be achieved in a back and forth manner by a two-photon process, any pair of levels directly coupled to the circular state will contribute. A dependence on the electric field is imprinted by intermediate levels with a linear Stark shift. This differential sensitivity to the electric field between J and J_z provides the tunability of our simulator.

Since J and J_z have different scaling with n, we can choose a range of n and a set of external fields so that their ratio spans the region of interest. In Figure II.5 (b), we show the ratio of J_z/J for different qubit spaces and different magnetic fields B as a function of the electric field F.

The edge term $\delta\zeta$ varies only slightly with the electric field. For $R \sim 5$ µm, $B > 10$ G, and 2 V/cm$< F <$12 V/cm, we have $\delta\zeta/J \sim 2$. We note that since the diagonal mechanical repulsion, and not only the transition 'planetary' dipole, is involved in the expression of $\delta\zeta$, its dependence with distance presents a contribution in $1/R^3$ arising from the 'permanent' electric dipole induced by the directing electric field.

Regarding the tunability of the single atom terms, we will simply state that by changing the frequency of the MW dressing field and its amplitude one can change them completely within a few nanoseconds. This is much faster than any other timescale of the Hamiltonian evolution.

II.2 Atomic lifetime

We now turn to the study of the preservation of the atomic state in our quantum simulator. We review some standard techniques from cavity QED and tailor them to our purposes in order to stop the natural decay of cRy states.

Charged particles are coupled to the electromagnetic 'vacuum' field in a fundamental and inescapable way. The decay of excited electronic states is a direct consequence. Quantum mechanically, the origin of spontaneous emission is partly due to the vacuum fluctuations in the modes resonant with the transition in question [109, 181].[3] This section focuses on the fact that even if one cannot escape this fundamental coupling, one can engineer the vacuum where an atoms sits so to interrupt its 'natural' evolution. An inhibiting structure will be reviewed here since it will be used to reduce the density of modes and, with them, suppress the decay rate in the experiment we envision.[4]

[3] We will also remark here that the spontaneous emission rate is proportional to the density of resonant modes, the density of off-resonant modes provoke a level's shift of the same kind as those produced by the Stark shift of off-resonant light on an atom. This vacuum shift is known as the Lamb shift and was known well before the actual light shifts we just used as an explanation. Also note that, if this energy shift has a noticeable gradient, an atom will feel a force proportional to it. This force is known as the Casimir force [141, 182–184]. All these effects share a common origin.

[4] We will mention that the converse is also true and historically was the first of the two phenomena

II.2.1 Atoms in free space

The identification of three processes i) (spontaneous) decay, ii) (stimulated) emission, and iii) absorption, is enough to compute the lifetime of an atomic state [186].

If we consider an atom in an initial state $|i\rangle$, the decay rate towards a final state $|f\rangle$ is given by

$$\Gamma_{i\to f}^{spont} = \frac{4\alpha\omega_{if}^3}{3c^2}|\langle i|\hat{r}|f\rangle|^2 = \frac{2\omega_{if}^3}{3\epsilon_0 c^3 h}|d_{if}|^2, \tag{II.8}$$

where α is the fine structure constant, ω_{if} is the frequency of the transition, c the speed of light, and $\hat{r}$ is the position operator, and where we have defined the dipole operator $\hat{d}$. It is implicit in the above equation that the initial state is the more energetic of the two, $E_i > E_f$.

The presence of black-body photons opens other channels via which the atomic state can be lost. The rate of loss through these channels is proportional to the mean number of thermal photons and thus a function of the temperature. The respective loss rates are

$$\Gamma_{i\to f}^{stim} = n_{th}(\omega_{if}, T)\frac{4\alpha\omega_{if}^3}{3c^2}|\langle i|\hat{r}|f\rangle|^2, \tag{II.9}$$

$$\Gamma_{i\to f'}^{abs} = n_{th}(\omega_{if'}, T)\frac{4\alpha\omega_{if'}^3}{3c^2}|\langle i|\hat{r}|f'\rangle|^2. \tag{II.10}$$

Where $E_{f'} > E_i$ and $n_{th}(\omega, T) = 1/(e^{\hbar\omega/k_B T} - 1)$ is the mean number of resonant thermal photons per mode for a given black-body temperature T. In the case that more than one final state is allowed, one obtains the total rate of depopulation of state $|i\rangle$ by summing over all final states

$$\Gamma_i = \sum_{f<i}\left(\Gamma_{i\to f}^{spont} + \Gamma_{i\to f}^{stim}\right) + \sum_{f'>i}\Gamma_{i\to f'}^{abs}, \tag{II.11}$$

where the sum index is just a reminder on the energy condition for each process.[5] The incoherent sum of terms comes from the fact that each loss channel has a different final state f (f') and thus they interfere not.

In Figure II.6 we show the light-atom processes giving rise to Γ_i. For the sake of clarity, we choose to describe the physics around the decay of the $n = 52$ circular state. Note the difference in order of magnitude for the dipole matrix elements for transitions towards the upper multiplicity. This is respected in general for any $n \gg 1$ where $|d_{\sigma^+}| \gg |d_\pi| \gg |d_{\sigma^-}|$. One can estimate that the σ^+ transition is ~ 50 stronger than the next leading process (π).

The strong dependence on temperature is captured in Figure II.7 for a few cRy levels. The basis to calculate the lifetime of each of them is built by taking neighboring states that differ from it by $\Delta n \leq 2$ and $\Delta m_l \leq 2$ (35 states). The rate is computed by adding the independent transitions rates towards each state of the basis (eq.(II.11)).

to be identified [185]. If one increases the density around one mode, the spontaneous emission in this mode gets enhanced. This is known as the Purcell effect.

[5] We note that these rates are often times cast in terms of the 'Einstein's A and B coefficients' instead.

The dashed lines are guides to the eye. As we will develop in the following sections, the dependence in n and T found in this plot can be understood using the simple scaling rules developed in chapter I.

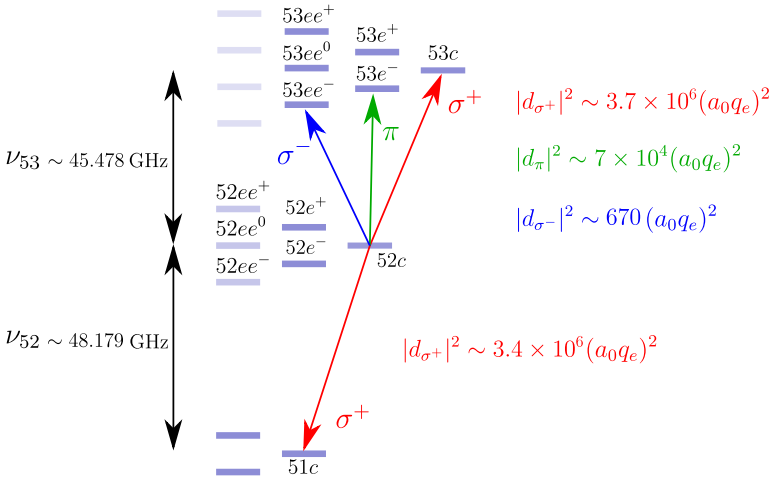

FIGURE II.6 Main transitions responsible for the decay of level $52c$. Note that $|d_{\sigma^+}| \gg |d_\pi| \gg |d_{\sigma^-}|$. The ordering is in general true for all cRy levels n and it is a consequence of the scaling laws.

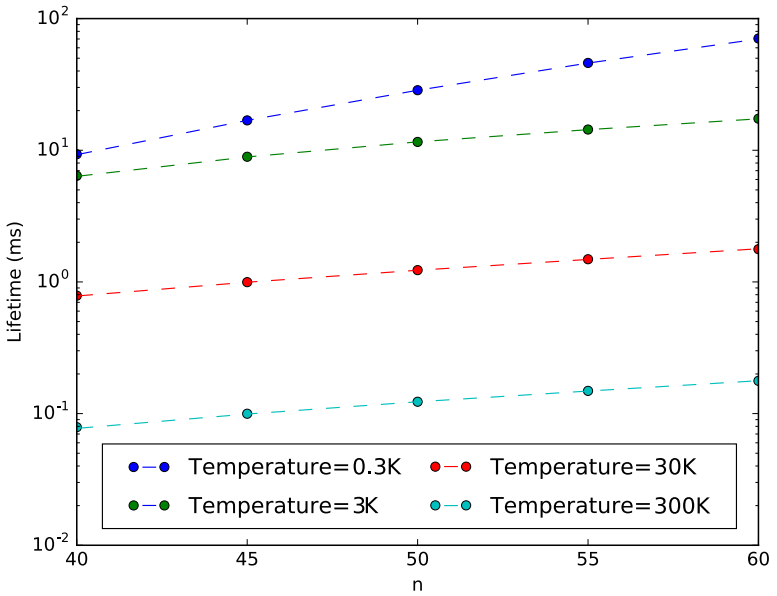

FIGURE II.7 Lifetime in free space as a function of the principal quantum number for a few temperatures. The dashed lines are guides to the eye. At low temperatures, spontaneous emission is dominant and the scaling is n^5. At 'high temperature' ($T \geq 3$ K), stimulated emission is dominant and the decay rate is suppressed by a factor of $n_{th} \sim n^3$. The scaling becomes n^2 producing the parallel lines in the plot.

II.2.2 Atoms inside an ideal capacitor

The decay channel for circular states around $n \sim 50$ has a wavelength of $\lambda \sim 5$ mm. If the circular state is placed between two conducting planes spaced by a distance $L \sim \lambda$, the density of modes will be heavily modified. The calculation is elementary and can be performed in many equivalent ways using classical arguments. A quantum treatment can be found in [183, 184].[6] The modes with polarization parallel to the surfaces are affected differently than those with perpendicular polarization. Since in the proximity of a conducting surface the electric field is normal to it, it is natural to define the quantization axis also in that direction. In general, the σ modes (polarization parallel to the surface) are inhibited as one can guess from elementary electrostatics, and the π modes (polarization normal to the surface) are enhanced. The modification shows up as multiplicative factor C_ϵ ($\epsilon \in \{\sigma, \pi\}$) in the free space density of modes and it modifies the loss rates towards state $|i\rangle$ to become $\Gamma_i = C_\epsilon \Gamma_0^i$, where Γ_0^i is the decay rate in free space. For an atom placed at z in between a pair of infinite and perfectly conducting plates, the correction factors are computed to be

$$C_\sigma = \sum_{n=0}^{[2L/\lambda]} \frac{3\lambda}{4L} \left[1 + \left(\frac{n\lambda}{2L}\right)^2\right] \sin^2\left(\frac{n\pi z}{L}\right), \tag{II.12}$$

$$C_\pi = \frac{3\lambda}{4L} + \sum_{n=1}^{[2L/\lambda]} \frac{3\lambda}{2L} \left[1 - \left(\frac{n\lambda}{2L}\right)^2\right] \cos^2\left(\frac{n\pi z}{L}\right). \tag{II.13}$$

The sum is to be understood as running over n for as long as $n\lambda < 2L$. In Figure II.8, we plot the wavelength dependence of the C_ϵ factors at $z = L/2$. The cut-off at high wavelength in C_σ is the feature that we will use to enhance the lifetime of our quantum simulator. These effects have been observed before [109], but never during the timescale that would be available if one used cold laser-trapped cRy atoms.

The physical interpretation of such an effect is that there is no long-wavelength fluctuation of the vacuum field parallel to the mirrors, so no atomic decay can take place. From a classical point of view one can think of this as an impedance divergence that 'reflects' back into the atom any tentative of photon emission. We note that the peaks in Figure II.8 are Purcell resonances [141].

Note that the relevant limit for us will be $L/\lambda < 1$. Here the expressions $C_\sigma = 0$ and $C_\pi = 3\lambda/4L$ are exactly valid.

The method of images helps us to understand the nature of the inhibition as an interference process between the emitter and its successive reflection (separated a distance equivalent to few $\sim L$). In the inset of Figure II.8, we depict the images of dipoles to help understand both the inhibition of the σ polarization and the enhancement of the π polarization at long wavelengths. For a dipole parallel to the surface, the image dipole orientation is opposed (conjugated). In the limit where $L \ll \lambda$ the interference is destructive in the far field since dipoles radiate in phase-quadrature with sub-λ, separation. For a dipole normal to the surfaces, the image dipole is identical

[6] It must be noticed that all these effects can be understood via classical arguments. The modification of the density of modes is a purely classical effect. If one computes the emission of a classical dipole close to a surface, one finds the quantum mechanical result.

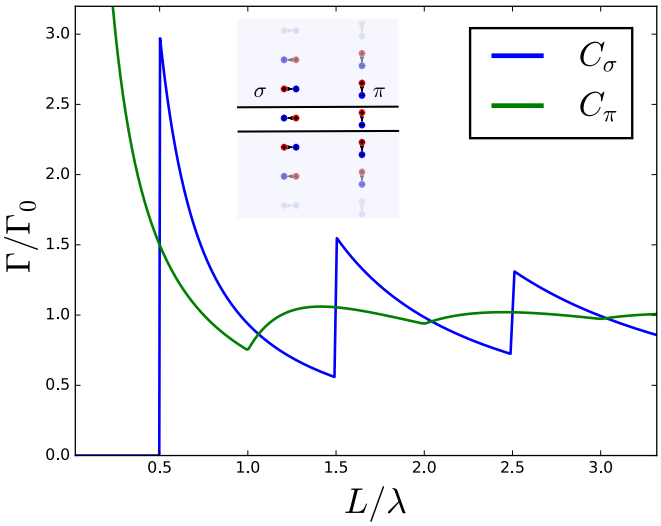

FIGURE II.8 Inhibition (or enhancement) of an ideal capacitor. We show the modification of the spontaneous emission rate by an infinite and perfectly conducting capacitor of gap L. Below cut-off, π polarization is enhanced ($C_\pi > 1$) and σ polarization is completely inhibited ($C_\sigma = 0$). Above cut-off, both polarizations oscillate in between enhancement and inhibitions. The inset of the figures shows the electric image picture as responsible for the classical effect.

(parallel) to the dipole. In the regime where $L \ll \lambda$, the interference is constructive since it corresponds to many copies of the dipole radiating in phase. The emission is then enhanced.

The cRy states offer an ideal platform to study these effects. They have only one decay channel, which is inhibited (σ^+) and lies in the MW domain [105, 109]. These states already have a considerably long free space lifetime and the millimeter sized capacitor needed for inhibition still allows access to the atoms with free-space lasers.

II.2.3 Single cRy atom lifetimes

The individual loss rates of a state can be written as

$$\Gamma_{i\to f} = C_\epsilon \frac{4\alpha}{3c^2}\omega_{if}^3 |\langle f|\mathbf{r}\cdot\epsilon|i\rangle|^2(\delta_{i\to f} + n_{th}(\omega_{if}, T)). \tag{II.14}$$

In this expression, ϵ defines the polarization of the transition $\sigma^\pm$ or π, $\omega_{if} = |E_i - E_f|/\hbar$ and we have introduced the function $\delta_{i\to f}$ which differentiates emission processes from absorption ($\delta_{i\to f} = 1$ if $E_i > E_f$ and $\delta_{i\to f} = 0$ if $E_i < E_f$).

In Figure II.9 we show a numerical calculation of the radiative lifetime of some cRy states in free space (left) and inside an ideal 2 mm capacitor (right) as a function of temperature.

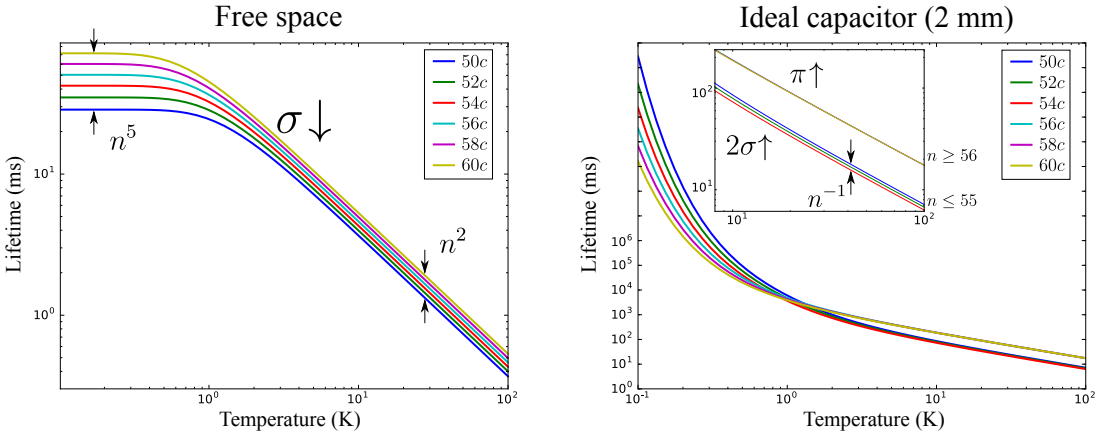

FIGURE II.9 Left: Lifetimes are ordered by n since the lifetime in free space always follows a scaling law with a positive power of n. The dominant transition is $\sigma\downarrow$ and the spread in the lifetimes changes from $n^5 \to n^2$ due to thermal population of the mode. At high temperature, the linear dependence with slope one in the loglog scale corresponds to the Rayleigh-Jeans limit $n_{th} \propto T$ where the losses are thermally dominated. At low temperatures $n_{th} \ll 1$, there is no temperature dependence. Right: Idealized radiative lifetime in an infinite capacitor. In the low temperature regime the Wien's law applies and smaller n have bigger lifetimes. The quantity of black-body photons decreases with frequency (for $\nu_n < 50$GHz) so the enhanced $\pi\uparrow$ transition rules the lifetime. At high temperatures, two different behaviors are observed. For $n < 55$ the $|nc\rangle \to |(n+2)e\rangle$ transition (named here $2\sigma\uparrow$)is not inhibited and dominates the lifetimes. For $n > 55$ the $2\sigma\uparrow$ transition is inhibited and the $\pi\uparrow$ transition dominates. In the latter case the rate is almost independent of n at high temperatures.

An elegant interpretation of the results can be given using the scaling laws for the physical quantities involved: the loss rates eq.(II.14) present a competition between the dipole moments d_n^2, the black-body photons n_{th}, and the density of modes $\propto C_\epsilon \nu_n^3$ ($C_\epsilon = 1$ in free space). We proceed to analyze the results.

A single cRy in free space

The dominant transition is the downwards σ^+ transition to the lower circular (see Figure II.6). We introduce the notation $\sigma\downarrow$ for this transition. The general tendency of the decay rates can be condensed in the expression $\Gamma_{nc} \propto C_\epsilon(\delta_{nc\to f} + n_{th})d_n^2\nu_n^3$. Knowing that [142, 187] the dipole scaling is $d_{n\sigma} \sim q_e r_n \propto n^2$ (see eq.(I.5)) and that $d_{n\pi} \propto n^{3/2}$, one can use Kepler's third law $\nu_n \propto 1/n^3$ to analyze the temperature dependence using only the n scaling laws.

In the **low temperature limit** ($k_B T \ll h\nu_n$) there are almost no black-body photons. The losses are dominated by spontaneous emission and scale as

$$\Gamma_{nc} \propto d_n^2 \nu_n^3 \propto n^{-5}$$

in accordance with the semi-classical argument given in chapter I.

The **high temperature limit** ($k_B T \gg h\nu_n$) is valid here for $T \gg 1$ K, and $n > 50$ ($\nu_n < 50$GHz). The Rayleigh-Jeans limit of the Plank law is then applicable ($n_{th} \sim k_B T/h\nu_n$) and we have

$$\Gamma_{n\sigma\downarrow} \propto n^{-2}T \quad \text{and,} \quad \Gamma_{n\pi\uparrow} \propto n^{-3}T.$$

In free space the $\pi\uparrow$ process is only a correction since $|d_{n\pi}| \ll |d_{n\sigma^+}|$ and can be neglected in the qualitative interpretation of Figure II.9 (left). We notice that the spread of the curves is reduced as the number of photons grows. This is but a reflection of scaling law for Γ_n transiting from $n^{-5} \to n^{-2}$. In both the high- and low-temperature limit, negative powers of n in the decay rates guarantee a bigger lifetime for higher lying cRy levels.

Note that these scaling laws are also apparent in Figure II.7. From the slope we see that, at 0.3 K, lifetime scales as n^5. In this plot it is evident that the high-temperature limit is already attained for $T \geq 3$ K, making all lifetimes scale as n^2 and the lines in the plot parallel to each other.

A single cRy atom inside an ideal capacitor

The situation concerning the infinite ideal capacitor is radically different and it is shown on the right of Figure II.9. The main $\sigma\downarrow$ transition is inhibited ($\Gamma_{n\sigma\downarrow} = 0$) for $n > 50$ in a 2 mm capacitor completely changing the behaviour of the atoms. Two other competing transitions take the relay and dominate the losses. Both correspond to photon absorption but at very different frequencies so a strong dependence on temperature is expected. The involved transitions are shown in Figure II.10. We will split the analysis in low and high temperature limits.

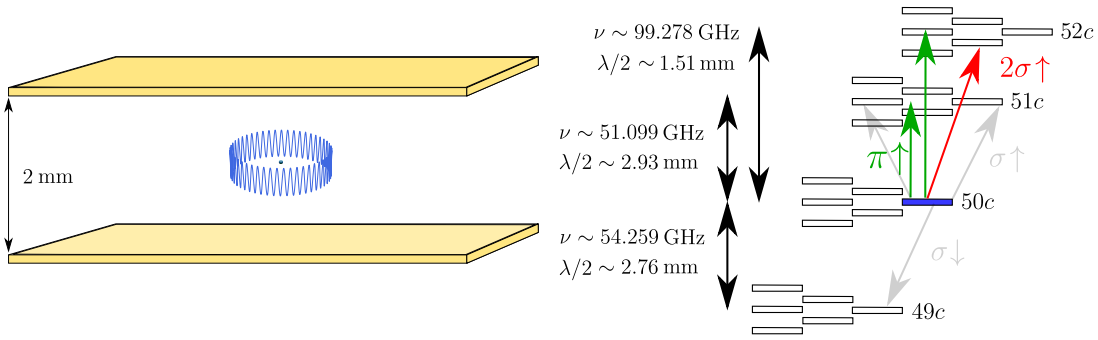

FIGURE II.10 Dominant transition involved in the lifetime of single atom in the cavity. The shaded arrows are inhibited by the capacitor.

We begin with the case of the **high temperature limit**. In this limit we see that there is a different behaviour for levels with principal quantum number either above or below $n = 55$. This is because the non-linear response of the inhibition rate to frequency (see Figure II.8) changes the dominant transition as a function of n. The analysis can still be done in the simple mind frame provided by the scaling rules.

In the Rayleigh-Jeans limit and below cut-off ($\lambda/2 >$2 mm), for the $\pi\uparrow$ transition we find ,

$$\Gamma_{n\pi\uparrow} \propto n^0 T.$$

We have that $C_{n\pi} \sim \nu_n^{-1}$ and thus $\Gamma_{n\pi} = cte$; effectively independent of n. This remarkable cancellation implies that, for as long as these transitions remain below the cut-off, the lifetime is independent of n at high temperatures. This explains the behavior for $n \geq 56$ states.

In the case of $n \leq 55$, at high-temperatures, the transition that dominates the decay is the $2\sigma\uparrow$ transition ($\Delta n = 2$, Figure II.10). In contrast to the $n \geq 56$ case, this transition is not inhibited and it is actually enhanced by the capacitor ($C_\sigma > 1$).[7] From eq.(II.12), the capacitor correction to the density of modes is exactly $C_\sigma \sim (\nu - \nu_L)^{-1}$ (for $0.5 < L/\lambda < 1.5$), where $\nu = c/\lambda$ is the frequency of the transition and ν_L is a constant that depends on the capacitor gap size L. We get

$$\Gamma_{2n\sigma\uparrow} \propto \frac{n^{-2}T}{\nu_n - \nu_L} \sim nT + \cdots$$

We take note that, at high temperatures, for $n \leq 55$ circular states the lifetime *decreases* with n (since $C_\sigma\Gamma_{2\sigma\uparrow}$ is dominant), but that for $n \geq 56$ the lifetime is *independent* of n (since $C_\pi\Gamma_{\pi\uparrow}$ is dominant). These are both in striking contrast with the free space behaviour where the lifetime *increases* with n (for all n since $\Gamma_{\sigma\uparrow}$ is dominant).

In the **low temperature limit**, more microwave photons are present for smaller frequencies (in the range < 50 GHz). This makes the $\pi\uparrow$ ($\Delta n = 1$, now dependent on n) dominant in front of the $2\sigma\uparrow$ ($\Delta n = 2$) process and lower n are blessed with higher radiative lifetimes. In this limit, the lifetime of all cRy states *decreases* with n, again in stark contrast with the free space behavior. Since the computed values are unrealistically high, the relevant physical statement is that, at low temperatures, the *single atom radiative lifetime* will not be the limiting factor in an efficient inhibition structure. The single atom lifetime of cRy states will then be limited by other processes (collisions with the background gas, etc) and will essentially be n independent.

II.2.4 The finite size effects and the conductivity of mirrors

In the case of mirrors with finite conductivity, the reflected waves have an attenuated (and phase-shifted) amplitude. The modified inhibition rates differ from the ideal ones in that all the sharp features of C_ϵ as a function of frequency ($\nu \sim L/\lambda$) are smoothed out. The smoothing out of the Purcell resonances reflects the spectral broadening of a bad cavity. The boundary condition is no longer sharply imposed, bringing along a low finesse. More importantly, the inhibition no longer goes to zero abruptly. Instead, C_σ approaches zero as a Lorentzian for $L \lesssim \lambda/2$. For large wavelengths ($L/\lambda \ll 1$), the dissipation caused by the finite conductivity of the mirrors diverges for both polarizations as they are efficiently damped by the plates. This means that making smaller capacitors no longer improve the inhibition [183].

To take into account the finite conductivity of the mirrors and their finite size, we ran CST-studio simulations to evaluate the situation within the relevant experimental conditions. For this exposition, we chose to discuss the scenario where the quantum simulator is built out of the $|48c\rangle$ and $|50c\rangle$ circular states [96]. For this purpose, we have run the calculations corresponding to a classical dipole source placed normal

[7] The wavelength for $|55c\rangle \to |57e^-\rangle$ is $\lambda/2 = 2.0004$ mm and limits of the inhibited transitions.

(π) and parallel (σ) to the mirrors at the center of a cavity made of gold at 1 K ($4.55 \times 10^9 \Omega$/m for gold at 1 K at 50 GHz). The calculations were done by taking the ratio of the radiated power by both the dipole in the cavity and in free space. The CST results are shown in Figure II.11. In the left we plot the CST calculation for the dipole placed orthogonal (σ) to the plates. The capacitor is taken to have square plates of size a spaced by a distance L. The dipole emission frequency chosen for this plot is that of the transition dominating the atomic population losses in free space ($\nu_{48c\to47c}$ =61.407 GHz). The vertical dashed line corresponds to $L = c/2\nu_{48c\to47c}$. The white dot at a =13 mm and L =2 mm represents the choice for the experimental realization. On the right we show the CST calculation (dashed lines) done as a function of frequency for the chosen capacitor size together with the analytic result (full lines) for the ideal plates.

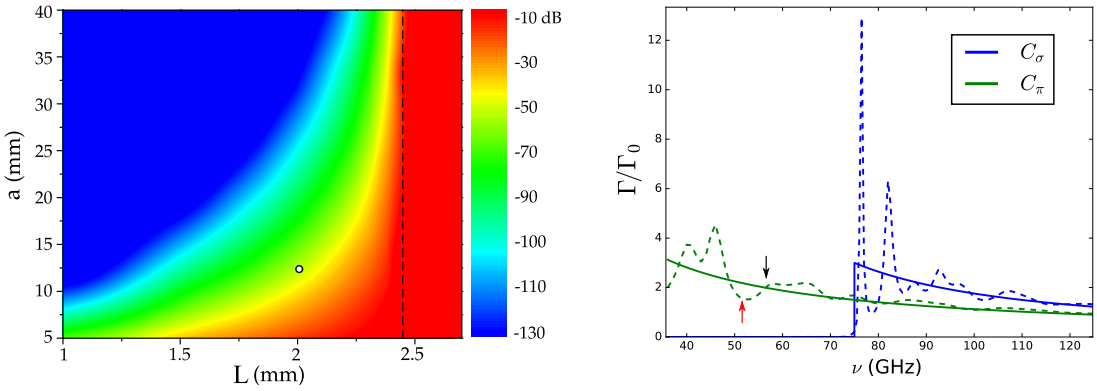

FIGURE II.11 On the left we plot the CST calculation for the inhibition of the real capacitor. On the right we plot the power ratio as a function of frequency for both dipole orientations for the chosen capacitor geometry. The full lines correspond to the ideal capacitor and the dashed lines correspond to the CST calculation. The dominant transition frequencies are marked with arrows. The black arrow corresponds to the frequency of the $n = 48, \pi\uparrow$ (57.69 GHz) transition and the red arrow corresponds to the frequency of the $n = 50, \pi\uparrow$ (51.099 GHz) transition.

We find that the now limiting transition ($n = 48, \pi\uparrow$ at 57.69 GHz) has an inhibition factor which is identical to the ideal capacitor case (black arrow). Regarding level $|50c\rangle$, the inhibition for the $\sigma\downarrow$ is even more efficient than for level $|48c\rangle$ since $\nu_{48c\to47c} > \nu_{50c\to49c}$. The next leading transition ($n = 50, \pi\uparrow$ at 51.099 GHz) is actually less enhanced (red arrow) for the resistive capacitor. This is due to resonances arising from its finite size. Then, the lifetime estimate turns out to be longer using the more realistic capacitor. As a pessimistic approximation, we have focused our analysis on the ideal capacitor. The estimation for the radiation lifetime of a single $|48c\rangle$ atom at 0.4 K is then $\sim$ 2500 s.

II.2.5 Lifetime for a pair of cRy atoms

We have so far addressed the cRy lifetime in the case of non-interacting atoms. In the case of the quantum simulator we discuss, the atomic interaction is important. We now develop the considerations made to assess how the lifetime of the cRy atoms in the linear chain is modified in the presence of the levels mixing due to their interaction.

We study the effect in the case of a single pair of interacting atoms. The classical picture is that the pair of dipoles lose the alignment with the quantization axis imposed by the external field. By tilting towards each other, they couple their radiation to allowed modes in the capacitor. The quantum picture is that the mixing induced by the interaction opens new decay channels.

Here, we work out an estimation of the expected lifetime in the quantum picture. Let $\{|b\rangle\}$ be an eigenbasis of the two-atom Hamiltonian

$$\hat{H}_{tot} = \frac{\hat{p}^2}{2m_e} + \hat{V}_C + \hat{V}_S + \hat{V}_Z + \hat{V}_{vdW},$$

with energies E_b. Here the C, S and Z operators stand for the Coulomb, Stark, and Zeeman terms respectively. The decay rate of any other state $|\psi\rangle$ is then computed as

$$\Gamma_\psi = \sum_b |\langle b|\psi\rangle|^2 \Gamma_b \tag{II.15}$$

where

$$\Gamma_b = \sum_c \Gamma_{b\to c},$$

and both sums run over the steady states of $\hat{H}_{tot}$.

Since we are considering two atom processes here, the loss rates take the form

$$\Gamma_{b\to c} = (\delta_{b\to c} + n_{th}(\omega_{b\to c}, T))\frac{4\alpha}{3c^2}\omega^3_{b\to c}|\langle c|C_{\epsilon_1}\mathbf{r_1}\cdot\epsilon_\mathbf{1} + C_{\epsilon_2}\mathbf{r_2}\cdot\epsilon_\mathbf{2}|b\rangle|^2.$$

This study will be numerical and, for the sake of clarity, we will discuss the particular case of $n = 50$. A pair of atoms that are in state $|50c, 50c\rangle$ at infinite distance are adiabatically coupled to state $|b\rangle = |\psi_{5050}\rangle$ as they are brought together (see chapter I). The sum in eq.(II.15) has then only one term.

The lifetime calculated per atom is shown in Figure II.12. The interatomic distance for the calculation was chosen to be $R = 5$ µm. The basis used is defined, as before, to contain states differing by $\Delta n \leq 2$, $\Delta m_l \leq 2$ from each level in the considered pair. The electric field F and the magnetic field B are parallel to each other and orthogonal to the line connecting the center of mass of the atoms (see Figure). One sees that, for higher fields, the lifetime improves even though, in the chosen range, the dependence on the magnetic field is weaker. The fact that the lifetime increases with the magnitude of the directing fields is explained by the fact that the atoms regain their circular character (mixing in the parabolic basis is reduced) as the external fields dominate over the dipolar interaction. The classical picture is that the external field realigns the atomic dipole with the inhibited mode of the capacitor.

State $|\psi_{50c,50c}\rangle$, although different, is very similar to the non-interacting product $|50c, 50c\rangle$. For fields such that $F >2$ V/cm and $B >10$ G (this is the range of interest for the tunability of the simulator) the state is approximately (see Figure I.5)

$$|\psi_{50c,50c}\rangle \sim \alpha_{50,50}\,|50c,50c\rangle + \alpha_{+,-}\frac{|50e^+,50e^-\rangle + |50e^-,50e^+\rangle}{\sqrt{2}} + \\ + \alpha_{51,49}\frac{|51c,49c\rangle + |49c,51c\rangle}{\sqrt{2}} + ... \tag{II.16}$$

with $|\alpha_{50,50}|^2 > 0.995$, $|\alpha_{+,-}|^2 < 10^{-3}$ and $|\alpha_{51,49}|^2 < 5 \times 10^{-5}$. This is reflected in the opacity of the levels in Figure II.12. Note that polluting elliptical states have two harmful transitions that are not inhibited by the capacitor. A first π transition to the $|(n-1)c\rangle$ level and a σ^+ transition towards the $|(n-2)c\rangle$ level having a wavelength above cut-off. Using a smaller gold capacitor that would also inhibit this transition is unrealistic in terms of optical access.

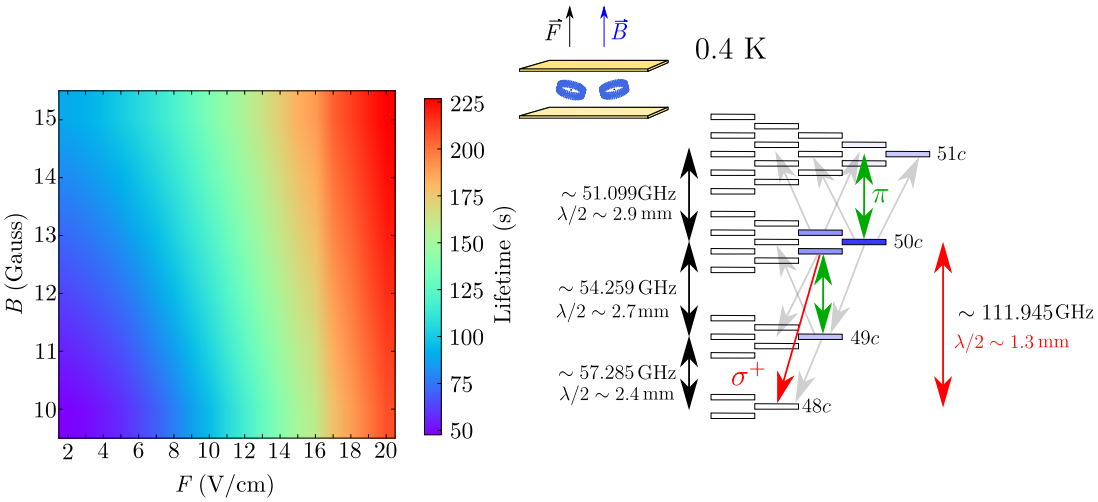

FIGURE II.12 The lifetime per atom is calculated inside an ideal inhibiting capacitor at 0.4 K. The plot is done for a pair of $|50c\rangle$ atoms at a 5 µm distance as a function of the electric and magnetic fields. The individual atom populations is schematically represented by the opacity in the level drawn in the diagram on the right. The colored arrows depict the main transition limiting the lifetime in the capacitor. The light gray arrows show some relevant σ transitions that are suppressed by the capacitor. Absorption of photons with $\Delta n = 2$ are negligible at low temperatures.

We extend the two-atom result to an N-atom chain by considering the time it takes to lose the first atom as the lifetime of the whole chain. This occurs at a rate N times larger than for a single atom. Note that microwave superradiance [188] does not contribute to a lifetime reduction since it is the emission of the first photon that starts it. The lifetime of a 40 atom chain is then estimated to be >80 s/40∼2 s for external directing fields of $B > 12$ G and $F > 6$ V/cm. The lifetime reduction caused by the vdW interaction is estimated to be as big as all the other limiting processes put together [96].

II.2.6 The asset of our simulator

Let us now summarize the assets of the quantum simulator discussed so far. Two main assets make our simulator stand out: i) We have complete control over the Hamiltonian parameters and ii) a comparatively long lifetime. We illustrate this in Figure II.13 where we show the interplay between the tunability and the lifetime. The yellow regions are guides to the eye and correspond to the single atom lifetime for each set of fields.

At 12 G (green dots) the J_z/J ratio can be tuned from -1 to 1 in the region where the lifetime per atom is > 80 s. At $R = 5$ µm from each other and for a qubit in $\{|48c\rangle, |50c\rangle\}$, we have $J \sim h \times 17$ kHz. A few tens of hundred thousands characteristics times will pass before the chain loses the first atom. These long timescales and controllability are unprecedented assets of our proposal and they open perspectives in a new regime.

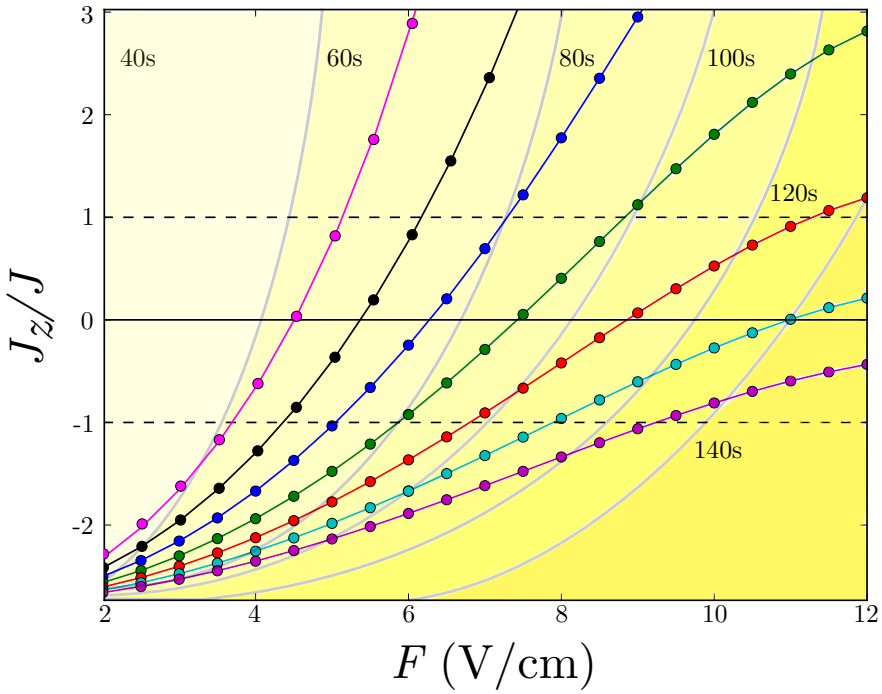

FIGURE II.13 The dependence of the ratio J_z/J as a function of the electric field F as we change the magnetic field B. Dots result from the numerical diagonalization of the complete atomic Hamiltonian for B = 9, 10, 11, 12, 13, 14, and 15 Gauss (magenta, black, blue, green, red, cyan, and purple dots, respectively). The colored lines are a guide to the eye.

In order to be able to contribute to the quest of quantum simulation of Heisenberg chains it is mandatory[8] for us to trap the atoms and to build the atom-chain in a deterministic way. This can be achieved thanks to the state-of-the-art laser-trapping techniques and thanks to a tailor-made chain preparation process that we will discuss in the next section.

[8]It must be noted that, at these timescales, even falling due to the action of gravity is a problem.

II.3 Trapping and chain preparation

To benefit from the long lifetime of the cRy atoms in the study of spin chains, it is necessary to trap them. We envision coupling constants of several kilohertz but, for untrapped atoms, the interaction produces an explosion of the cloud, breaking-down of the frozen gas approximation, in a few microseconds only [139]. Laser trapping of cRy atoms will provide a tunable coherence-preserving confinement compatible with the Hamiltonian evolution which interests us here. We have chosen to study the chain of atoms in the presence of a Laguerre-Gauss ($p = 0, l = 1$) laser mode (LG_{01}) providing the collective harmonic confinement in the transversal direction. An additional standing wave provides an optical lattice which further traps each atom in the longitudinal direction.

We will lay down the principle of the laser trapping of cRy atoms. On the one hand, cRy atoms have no optical transition available and standard dipole trapping techniques cannot be used. On the other hand, for $n \gg 1$ the electron remains far from the nucleus and reacts to external oscillating fields to some extent as a 'free electron' would [189]. The associated kinetic energy of the movement provides a method for trapping [108]. If a single electron is surrounded by a barrier of light and sits in the dark center of a hollow beam, no energy is available to intrude on the region where strong oscillation is required. The electron is then confined by a conservative potential. If the electron is the valence electron of a cold cRy atom, the atom itself will be trapped since the electron is bounded to the core. The details of the trapping are to be discussed in what follows.

An electron of mass m_e and charge q_e in a monochromatic (ω_L) laser field has a ponderomotive energy given by [88]

$$\mathcal{E} = \frac{q_e^2}{2m_e\epsilon_0 c\omega_L^2} I, \tag{II.17}$$

where c is the speed of light, ϵ_0 is the permittivity of free space, and I is the beam intensity. For an LG_{01} beam the intensity takes the form

$$I = I_{LG} = \mathcal{P}\frac{4\rho^2}{\pi w^4(x)}\exp\left\{-\frac{2\rho^2}{w^2(x)}\right\}. \tag{II.18}$$

The variables ρ and x are polar coordinates, $w(x)$ is the beam waist, and $\mathcal{P}$ is the laser power. The maximum of intensity is at $\rho = w(x)/\sqrt{2}$ and takes the value $I_{\max} = 2\mathcal{P}/e\pi w^2(x)$.

From eq.(II.17) we see that the ponderomotive potential depends on the inverse of the mass of the charged particle. The Rubidium ionic core is tens of thousands of times heavier than the electron and thus the potential effectively acts only on the single Rydberg electron.

A Taylor expansion of the ponderomotive potential around the center ($\rho \sim 0$) gives

$$\mathcal{E} = \frac{2q_e^2\mathcal{P}}{\pi m_e\epsilon_0 c\omega_L^2}\left(\frac{\rho^2}{w^4(x)} - \frac{2\rho^4}{w^6(x)} + \mathcal{O}(\rho^6)\right).$$

The harmonic frequency associated with small atomic oscillation in the z and y directions around the equilibrium position is

$$\omega_{z,y} = \frac{4}{\omega_L w^2(z)} \sqrt{\frac{\alpha \hbar \mathcal{P}}{m_e m_{Rb}}}, \tag{II.19}$$

where α is the fine structure constant. This potential describes a bidimensional radial (ρ) trapping with the atoms being free to move along the axial (x) direction. In Figure II.14 we show (a) the waist of the 1064 nm LG_{01} beam. The plot corresponds to a LG_{01} with a 7 µm waist and a power of 0.5 W. In these conditions the radial trap frequency is $\omega_z = \omega_y = 2\pi \times 12.17$ kHz, and the height of the light barrier is > 200 µK. The necessary axial confinement for the chain of cRy atoms is obtained by a pair of almost collinear Gaussian beams that form a standing light wave as shown in Figure II.14 (b) (green). Changing the small angle between the crossing beams tunes the distance between longitudinal wells and, with them, the inter-atomic interaction strength. An inter-well distance of 5 µm can be obtained with angles of $\pm 5.7°$ with respect to the y axis. The Gaussian beams are taken to have a waist of $w_z = 7$ µm along the z direction and $w_x = 200$ µm along the x direction. Using a power of 1.45 W per beam, the axial trap frequency is $\omega_x = 2\pi \times 24$ kHz and a trap depth of 200 µK. An angle of $\pm 4.1°$ and a power of 2.8 W per beam make an inter-well distance of 7 µm maintain the same trap frequency and depth.

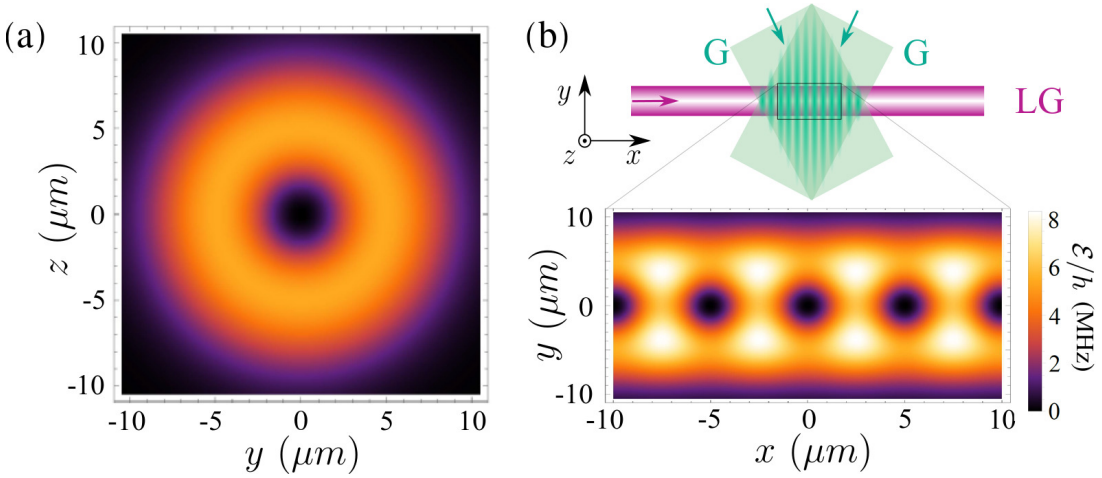

FIGURE II.14 (a) The intensity in a transversal cut of a LG_{01} laser beam of 7 µm waist. In (b), the intensity along the axial direction of the LG trap is shown. A standing wave formed by counterpropagating Gaussian beams (green). The weaker trap wall is > 4 MHz corresponding to 200 µK.

II.3.1 Some considerations regarding the laser trapping of cRy atoms

Photoionization and elastic scattering

The photoionization of cRy atoms is negligible and we will limit ourselves to mention the intuitive argument that sustains the claim. We refer the reader to [96, 108] and references therein where the technical details are given.

The photoionization rate is proportional to the square of the matrix element of $\hat{A} \cdot \hat{p}$ between the free electron state $|p_e\rangle$ of momentum p_e and the cRy state which reads

$$|\langle p_e|\,\hat{A}\cdot\hat{p}\,|nc\rangle\,|^2 \propto p_e^2|\langle p_e|nc\rangle|^2.$$

It is thus proportional to the overlap of the initial atomic cRy state and that of a final state corresponding to an energetic free electron. The analysis is most obvious when done in terms of the wave function in momentum space $\langle p|nc\rangle = \hat{\psi}_{nc}(p)$. The cRy electron wave function only has components at low momentum ($p \sim \alpha m_e c/n$, where α is the fine structure constant, c is the speed of light, and $n \gg 1$) while the free electron is a narrow peak at a relatively high momentum p_e. Thus, the overlap is $\hat{\psi}_{nc}(p_e) \sim 0$ to a very good approximation.

We remind the reader that it is the high angular momentum that keeps the electron at low speed. Highly energetic Rydberg states with low-angular-momentum l have considerable components at high momentum $\hat{p}$ providing a coupling to the continuum. Their contribution to the ionization probability is then non-negligible. In the semi-classical 'planetary' picture, the explanation is that, during the 'perihelion apsis', the electron goes extremely fast and may then escape the orbit [110].

Nonetheless, Compton elastic scattering may transfer the electron into another quantum state (an elliptical level) by imprinting a momentum kick to the electronic wave function. This is a limiting factor to the coherence and for the useful lifetime of the atom in the simulator. The diffusion cross-section can be evaluated with the classical Thompson diffusion model. A worst case estimate gives a lifetime of $\tau_{Compton} \sim 575$ s to the LG trap alone and of $\tau_{Compton} \sim 180$ s to the three trapping beams together.

Trap perturbation to the wave function

The trap can be considered as only a small perturbation to the electron wave function if the ponderomotive energy $\mathcal{E}_{\max}$ is much smaller than the Coulomb energy V_C. The ratio of these two quantities is evaluated for a laser power of $\mathcal{P} = 0.5$ W and for a trapping wavelength of 1064 nm focused to $w_0 = 7$ µm focus of the LG_{01} beam to be $\mathcal{E}_{\max}/V_C \sim 3\times10^{-8}$. Thus the electronic wave function is unaffected by this potential.

Anharmonicity induced decoherence: a single-atom effect

We choose a LG_{01} because, around the center ($\rho \sim 0$), the intensity grows quadraticaly with distance, thus providing a harmonic trap for the atoms. The anharmonicities should be avoided because they induce decoherence in the spin chain as we now explain.

Consider the center of mass of the atom to be at position $\mathbf{R}$ and the relative position of the electron to be $\mathbf{r}_e$. For a harmonic trap one can expand the potential as

$$\mathcal{E} \propto \langle(\mathbf{R}+\mathbf{r}_e)^2\rangle = \langle\mathbf{R}^2+\mathbf{r}_e^2+2\mathbf{R}\cdot\mathbf{r}_e\rangle \sim R^2 + a_0^2 n^4$$

where the average is taken over the electron orbit. One notices that the energy regarding the center of mass of the atom is only shifted by a constant term (independent of R) so the trapping force ($-\nabla\mathcal{E}$) is independent of n, i.e. the trap is state independent.

Considering now higher order corrections to the potential ($\delta\mathcal{E} \propto \langle(\mathbf{R}+\mathbf{r}_e)^4\rangle$), one finds non-vanishing terms introducing a dependence in n for the trapping ($\sim n^4R^2$). The center of mass evolution still undergoes a harmonic evolution but conditional to the

cRy state of the atom, thus producing spin-motion entanglement. The state dependent LG trap frequency is $\omega_n = \omega_z + \delta\omega_n$ where

$$\delta\omega_n = \frac{2n^2 q_e a_0}{\omega_L w^3(z)} \sqrt{\frac{6\mathcal{P}}{\pi m_{core} m_e \epsilon_0 c}}.$$

To estimate the associated decoherence in the cold atom limit, where the atom is in the fundamental state of the trap, we consider the trap ground state wave function $\phi_n^0(x)$ conditional to the electronic state $|nc\rangle$. For a power of 0.5 W in the LG_{01} beam and for a waist of 7 µm, ($\omega_z \sim 2\pi \times 12$ kHz) the differential frequency is $\delta\omega_{50c} - \delta\omega_{48c} \sim 2\pi \times 45$ Hz. Assuming a superposition qubit in state

$$|\psi\rangle = \frac{1}{\sqrt{2}} \left(|48c\rangle_s \, |\phi_{48}^0\rangle_x + |50c\rangle_s \, |\phi_{50}^0\rangle_x \right)$$

we compute the overlap of the $n = 50$ and $n = 48$ ground states to be

$$|\langle \phi_{48}^0 | \phi_{50}^0 \rangle| = \frac{\sqrt[4]{\omega_{50}\omega_{48}}}{\sqrt{(\omega_{50} + \omega_{48})/2}} \sim 1 - (8 \times 10^{-7}), \tag{II.20}$$

value which is independent of the laser power and accounts for a small amount of entanglement between the electronic state (spin, s) and the position (x) of the atom. We thus neglect the effect.

Coupling to phonons: a multi-atom effect

Even in the state-independent harmonic-trap approximation, the interaction between the atoms can induce spin-motion entanglement washing away the spin coherence. If the two-atom recoil due to the spin-flip interaction is strong enough to kick the atoms away from the trap ground state, the spin system will be open to the phonon environment. This is another reason to avoid the direct dipole-dipole interaction ($\sim 1/R^3$) and to use the weaker van der Waals interaction instead [187].

We estimate that for a pair of Rubidium-87 atoms in circular state $n = 50$ and $n = 48$ in a pair of traps of frequency $\omega_x \geq 2\pi \times 24$ kHz, at $R \geq 7$ µm from each other, and with exchange interaction bounded by $A_{6,48,50} \leq h \times 0.53$ GHz µm^6 (exchange rate $J < 2.3$ kHz) the systems are with probability > 0.9995 in a product state of spin and the motional ground state [108]. The intuitive argument is that the magnitude of the atomic displacement from the center of the trap after a spin-flip is much smaller than the extension of the ground state wave packet. Thus, the spin and the phonons remain decoupled in this regime and there is no associated entanglement induced decoherence.

II.3.2 Deterministic preparation of the chain

We have devised a method to prepare a chain of cRy atoms deterministically and close to the ground state of the trap. The calculations are based on a one dimensional Newton's cradle classical model and the investigation of the process in the quantum regime is being carried out [111]. Here, we discuss the classical model only.

The deterministic preparation of the cRy atom chain is a strong point of our simulator proposal since building up a many-body system is usually a quite inefficient

probabilistic process [69]. The method is reminiscent of the common place evaporative cooling used in cold atomic physics. Although here, instead of the contact interaction used to evaporate ground state atoms, we will use the van der Waals repulsion as the cRy atom expulsion mechanism.

The departing point of the preparation is an ultra cold cloud of ground state atoms. They must be brought to the inside of a parallel plate capacitor that will later inhibit the spontaneous emission of the cRy states. This can be done using a red trap for the ground state atoms as it is standard in cold atoms experiments. Once in the capacitor, an excitation laser excites up to ~ 100 atoms into the low Rydberg states which are circularized immediately to $|50c\rangle$. The ground state atoms can be pushed away using a resonant beam if needed. The LG_{01} beam is turned on and cRy atoms are now trapped in two dimensions. A sketch of the process starting with the cRy atom trapping is shown in Figure II.15. Plug beams (dark blue in the Figure) are used to confine the chain in the axial direction. The separation between these two plug beams is named L.

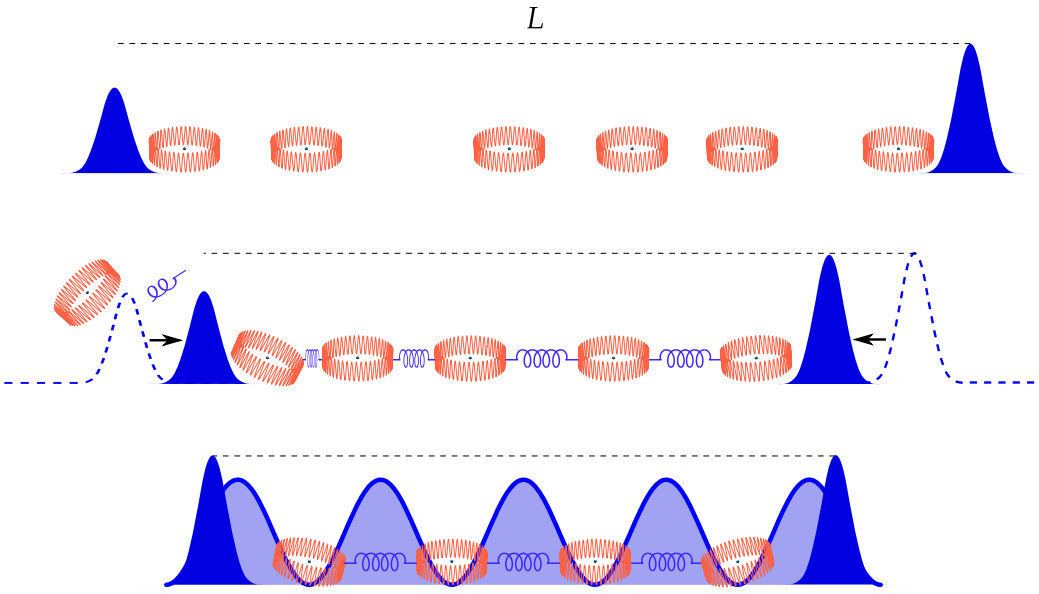

FIGURE II.15 Chain preparation protocol. An LG beam traps a linear chain of atoms while a pair of plug beams (blue Gaussians in this figure) compresses the chain by reducing their relative distance L. At some point the interaction energy of the atoms is bigger than the lower plug and the end atoms jump over taking away energy and cooling down the chain. Once the desired number of atoms is reached, the compression stops and a standing wave is turned on. In this pictorial representation we show the end atoms affected by the fact that they have only one neighbor. Note also that the electron orbit penetrates in the light potential. The different penetration of different n will be a source of decoherence.

The plug beams are brought together slowly and the atoms begin to interact. The repulsive van der Waals energy keeps the atoms apart. As the interaction increases, the end atoms climb the plug barriers and, at some point, the closest one to the weaker plug is ejected. Tailoring the way in which this ejection is made, one can see from the simulation that the ejected atom takes away energy, cooling down the chain. The tailored timing of the process involved in the chain preparation is shown in Figure II.16.

During stage I in Figure II.16 the LG_{01} is switched on in combination with two plug beams to trap the cRy atoms. The 1064 nm Gaussian plug beams have a large waist of 30 µm that will permit smooth evaporation later on. The initial separation of the plug beams is 1 mm (a) and the initial number of cRy atoms is taken from a Poissonian distribution of mean value 100. The height of the barriers are 3 and 4 MHz (b). In stage II the ejection of the atoms can be seen in (d) where the individual atom trajectories are plotted. A deterministic number of atoms can be prepared in about a second. One can see that during the evaporation, the kinetic energy of the chain decreases as shown by the red curve in (e). The blue curve in (e) is the interaction energy. The distance L is then slightly adjusted in stage III to provide a final interatomic distance of 5 µm. In stage IV the standing wave produced by the interference of counter propagating beams is turned on adiabatically forming a light comb. It is critical to match the minima of the comb with the target atomic position to avoid heating.

In Figure II.17 we show an average of 100 realizations of the evaporation. The final atom number N is determined by the power in the weak plug beam and by the final value of L. We see from the numerical simulation that this process can be very efficient. We see also that, by the time the number of atoms is ~ 40, the preparation is deterministic (the number of atoms has null variance).

The residual motion in the trap is an important parameter [129]. We find that for 14 atoms, the residual longitudinal motion is ∼65 nm. This corresponds approximately to one quantum of oscillation. For 40 atoms, about four quanta are expected. Considering the final ground state extension, the coherence time is limited to $\sim$ 160 ms for a 40-atom chain due to the exploration of the anharmonicities of the trapping potential. We have checked, with 3D simulations of the dynamics, that the position dispersion in all directions is of the same order of magnitude.

We note that the process is lengthy and the capacitor inhibition is vital. A high electric field is to be applied during the evaporation to increase the atomic lifetime and preserve the chain.

II.3.3 Detection scheme

The ejection of the atoms heavily used for the cool-down of the chain provides, in itself, a detection method. The ejected atoms are channeled by the LG beam into an ion counter where we perform standard state-selective field-ionization. The detection is then a lengthy process and the way to preserve the quantum state of the chain in the meantime, is to transfer one of the two cRy levels out of the qubit space to freeze the evolution. For the sake of clarity, consider as a qubit space the $\{|50c\rangle, |48c\rangle\}$ space and a flipping of $|48c\rangle \rightarrow |46c\rangle$. The exchange between the remaining $|50c\rangle$ and $|46c\rangle$ atoms is in the millihertz range and the spin evolution is frozen while the repulsive van der Waals interaction is nearly unchanged. The evaporation can then be resumed and, if the lower plug beam is placed in the direction of an ion counter, standard field ionization detection [88] can be performed one atom at a time (see Figure II.1).

The velocity of the ejected atoms in the guiding LG beam is determined by the height of the weak plug, and it is computed to be 16 cm/s for a 3 MHz lower plug beam. The atoms thus reach the detection region, about 2 cm away, after a 125 ms delay which is much shorter than their lifetime.

This scheme reads out the spin states in the new 'up-down' ($\{|50c\rangle, |46c\rangle\}$) basis.

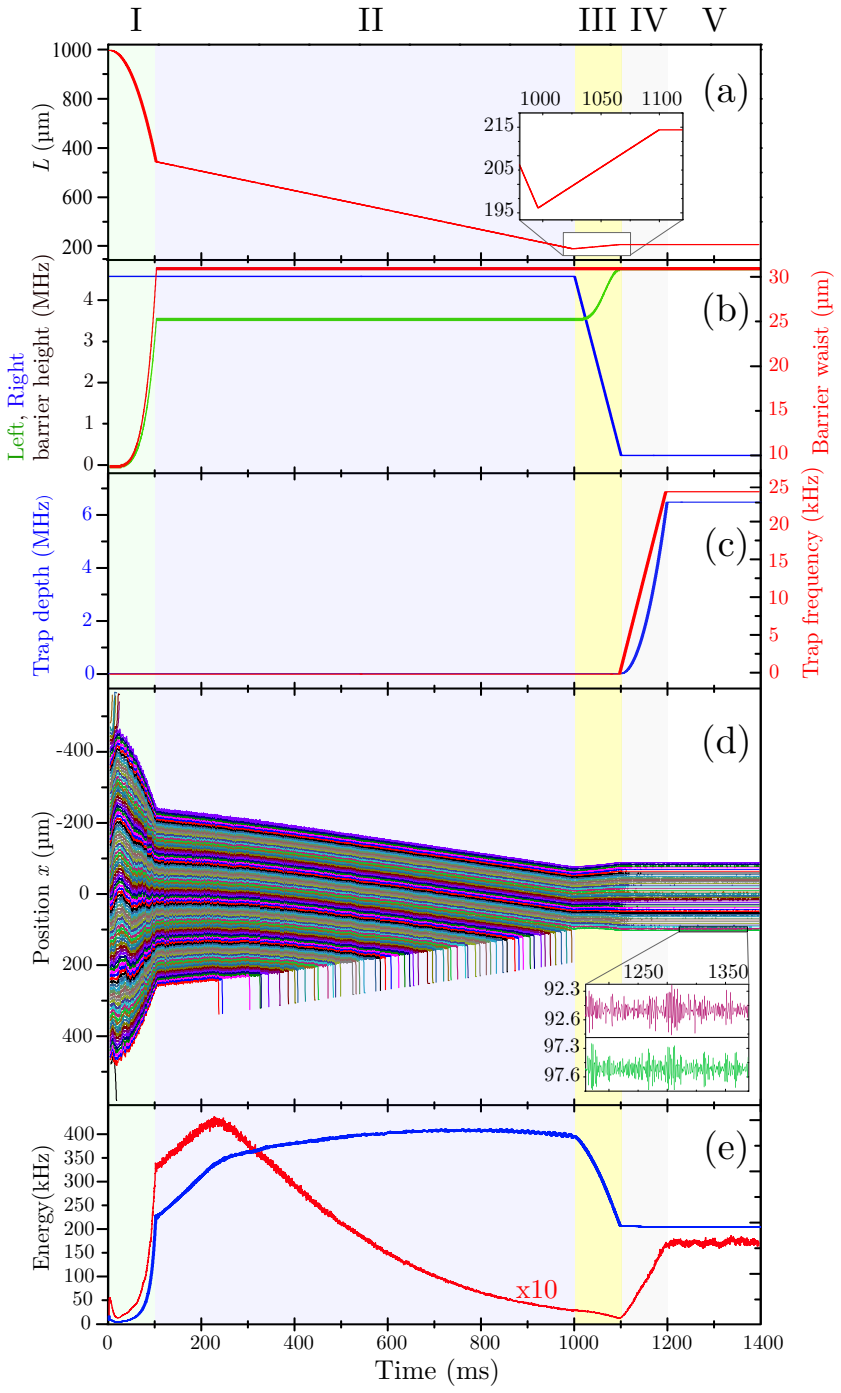

FIGURE II.16 Four phases are apparent. In I, during the installation of the plug beams and the fast compression, rapid atomic escapes occur from both sides while the plugs are still weak. This initial evaporation stops after approximately 100 ms. The chain is then compressed slowly in phase II. Atoms escape the chain during the compression taking away kinetic energy (red in (e)). In III the plugs are separated to bring the atoms to the target distance. In IV trap is tightened. In V the chain is prepared. We show a detail of the residual atomic motion.

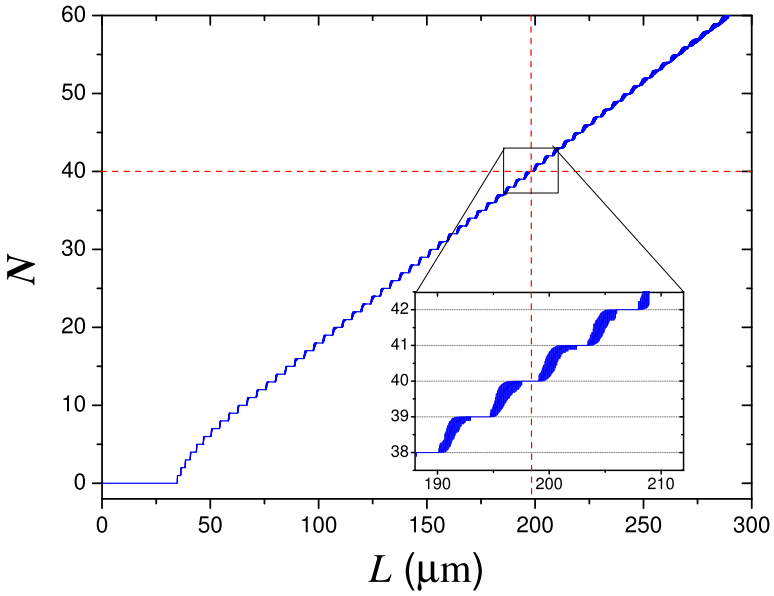

FIGURE II.17 Number of cRy atoms in the chain as a function of the inter-plug distance L. Stopping L at the right moment, a chain of ~ 40 atoms can be prepared in a deterministic way.

Adding a hard microwave pulse before freezing the interaction, we can rotate the spin at will and, thus, detect any single spin observable. This provides access to all the correlation functions of the chain shown in Figure II.3.

II.4 Conclusion

In this chapter we have developed the theoretical ideas that motivate our quantum simulator proposal. The unprecedented tunability, together with their long lifetime make cRy atoms a unique platform to study long-lived strongly-interacting Heisenberg chains.

The tunability of the Hamiltonian will allow us to explore a rich phase space [108]. The remarkable lifetime of cRy atoms can be further enhanced by a spontaneous-emission inhibiting structure. This is again a particularity of the cRy levels having only one dominant decay channel that can be inhibited in a millimeter-sized conducting structure. Using state-of-the-art techniques, single atom lifetimes in the order of seconds, and even minutes, are available. This would be a remarkable experimental observation.

Further perspectives can be envisioned. In a chain of only a few atoms living during many tens of $1/4J$ periods, one starts to explore the regime in which the next nearest neighbour interaction can no longer be neglected, enriching the evolution. The observation of these effects does not require a long atom chain, nor a spontaneous emission inhibiting structure, and it could be studied in free space optical tweezers using the ponderomotive potential [132].

Until that stage is achieved, the nearest neighbour model can be studied with our system. This simpler model is very rich and the deep understanding developed by the solid state physics community deserves experimental validation. Beyond that, lies unexplored ground related to dynamics, thermalization, and disorder.

In the following chapter we will develop the experimental setup where we have prepared cold cRy atoms and performed the first few experimental steps towards these challenging perspectives.

Chapter III

Cold circular state preparation

Contents

In this chapter we will discuss our experimental setup and the preparation of the cold circular Rydberg states. As developed in chapter II, Rydberg atoms are very sensitive to microwave fields and 300 K black-body radiation is detrimental. A cryogenic environment greatly suppresses the mean number of thermal photons and is a requirement adding complexity to our setup. The first part of this chapter deals with the details of the cold-atom preparation inside the cryogenic environment.

A second part is devoted to the Rydberg atom preparation. The excitation and manipulation of the Rydberg atoms take place in an electric field control electrode structure that is also used for detection by field ionization. Here, we discuss several experimental protocols including the detection by field ionization, the careful calibration of the RF field used in the preparation of cRy atoms, and the MW spectroscopy used to assess the circular state preparation.

III.1 Cold atoms in a cryogenic environment

In this section we discuss the peculiarities of the cold experimental setup permitting the study of cold long-lived cRy atoms. Our cryogenic environment does not allow for a stable vapor pressure of Rubidium in order to load a MOT and, thus, the source of atoms needs to be external. A 2D-MOT setup produces an atomic beam that enters the cryostat providing the atom flux that feeds the main atomic cloud. The atomic beam is stopped by a 3D mirror-MOT configuration in the cold core of the experiment. The atomic cloud is further cooled down with optical molasses before being ready for the Rydberg excitation and circularization. The tools needed are introduced in what follows.

III.1.1 The cryostat

In Figure III.1 we show the cryostat providing the environment for our experiments. A liquid Helium-4 reservoir (orange in Figure III.1 (a)) keeps the environment at 4 K. It is in turn thermally shielded from 300 K black-body radiation by a 77 K screen thermalized to liquid Nitrogen (violet). The cryogenic screens are mounted inside an external 300 K vacuum chamber. In Figure III.1 (b) we show a horizontal cut, at the level of the heart of the experiment, of the three screens. A layer of lead, which becomes superconducting below 7 K, is installed around the inner wall of the Helium shield and helps in screening external magnetic field fluctuations. Additionally, the lead shield reduces Eddy currents that would otherwise be formed in the outer copper screen due to the fast variation of magnetic fields needed for our cold atom experiments. The Helium shield is sufficiently large to accommodate the electrodes needed for electric field control (red, blue and orange in Figure III.1 (c)), the magnetic bias coils (black), as well as the Rydberg detection system (green). The coils for magnetic field control are all superconducting to prevent heating. Several optical ports are opened on the cryostat screens. The size of these windows limits the solid angle for optical access, but large windows expose the Rydberg atoms directly to the 300 K black-body radiation. Therefore, the windows are chosen to be 6 cm in diameter and copper flanges with a $\sim$2 cm opening cover the windows of the Helium-4 screen.

The cryostat is an important tool to fully exploit the Rydberg properties. On the

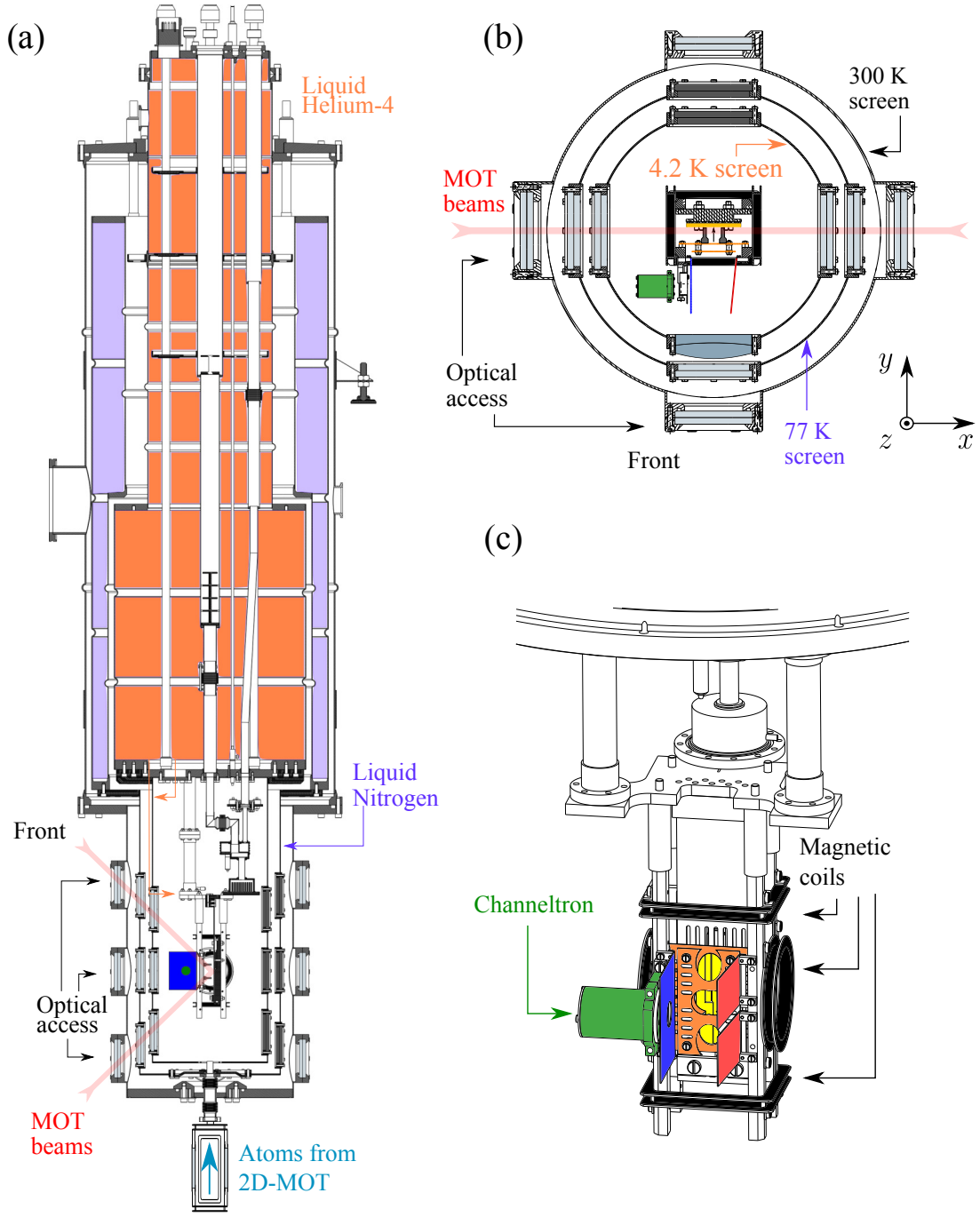

FIGURE III.1 (a) Side view of the cryostat as a whole. (b) Top view of the heart of the experiment. (c) A close-up of the heart of the experiment featuring the main electrodes and the magnetic coils. The channeltron is shown in green and the electrodes are shown in blue, orange, and red.

one hand, the use of the cryostat puts some constraints on optical access as well as on the complexity of experimental operation. On the other hand, it helps to have a high vacuum without much effort. Residual gases are strongly absorbed on cold surfaces. A pressure smaller than 10^{-10} mbar can be obtained without baking [134]. It is this cryopumping that imposes the need of an external atom source that we now describe.

III.1.2 Atom source

In Figure III.2 a sketch of the 2D-MOT atom source is shown. It is a commercial device designed and fabricated by the SYRTE laboratory and described in detail in [190]. Its purpose is to provide the first cooling stage for a hot gas ($\sim$ 50°C) coming from a Rubidium cell. Three pairs of 780 nm wavelength laser beams and four rectangular magnetic coils (with a current I circulating in each) are used to create a jet of thermal atoms that feeds the main atom cloud. The quarter-wave plates are used to turn the polarization of the beams so as to have the correct polarization after their reflection in the mirrors. The laser beams intersect in three regions where the atoms are cooled down in the horizontal plane. In these regions, three elongated cold atom clouds (cyan in Figure) are aligned along the vertical direction and feed each other. The final result is the collimation of the Rubidium gas. The beam goes up (and down) with a mean velocity of 13 m/s into the cryogenic environment. The dispersion in velocity is 10 m/s and the maximum atom flux is 10^{10} atoms/s.

The ultra-high vacuum in the main chamber is necessary for our atomic experiments while the 2D-MOT needs a considerable Rubidium vapor pressure to maintain a high flux of atoms. The 2D-MOT atom source and the cryostat are therefore linked by a 1.5 mm hole to allow for a differential Rubidium pressure. The vacuum in the 2D-MOT chamber is $\sim 10^{-8}$ mbar and it is maintained by two ion-pumps.

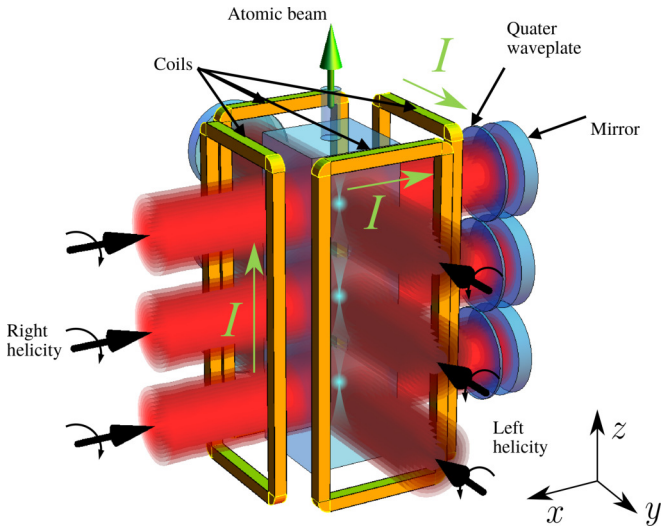

FIGURE III.2 Drawing of the 2D-MOT. The (bi-dimensional) cold atoms are shown in cyan.

III.1.3 3D-MOT and Optical Molasses

The main cold-atom cloud of our experiment is produced by a MOT in between the magnetic coils. The corresponding MOT cooling beams are featured in Figure III.3 and a side and a top view of these same laser beams can be found in Figure III.1 (a) and (b). A Rubidium-coated mirror (yellow in Figures III.1 and III.3) is used to reflect [191] the pair of lasers entering through the front windows.[1] The laser frequencies needed to operate the cold atoms are shown in Figure III.3. The MOT cooling beam cycles population in the $D2$ transition $|5^2S_{1/2}, F = 2\rangle \rightarrow |5^2P_{3/2}, F' = 3\rangle$ but a non-negligible fraction of the atoms decays to state $|5^2S_{1/2}, F = 1\rangle$ instead. To avoid the accumulation of population in this state, a 're-pumper' beam addresses the transition $|5^2S_{1/2}, F = 1\rangle \rightarrow |5^2P_{3/2}, F' = 2\rangle$ and recycles the population to $|5^2S_{1/2}, F = 2\rangle$.

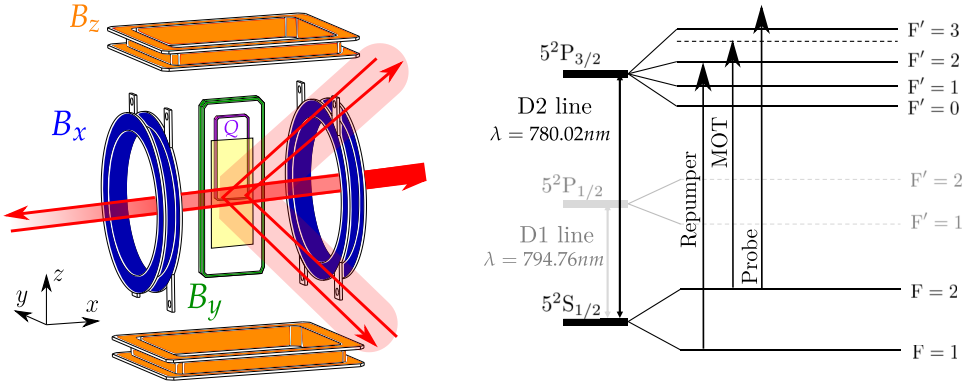

FIGURE III.3 Left: Scheme of the mirror-MOT configuration. The magnetic coils (orange, blue, green, and purple) are also shown in black in Figures III.1. Right: Level scheme displaying the hyperfine structure of Rubidium-87. The relevant laser frequencies are indicated with arrows.

The magnetic field gradients are created by the quadrupolar coil Q shown in Figure III.3 (purple) and the bias fields are created by the coils around. The atom cloud is close to the lower side of Q, where the lasers cross. The bias coils produce a nearly homogeneous magnetic field at the scale of the atom cloud in the x (blue), y (green), and z (orange) directions. These fields permit the displacement of the MOT cloud as they change the position of the trap minimum. To further reduce the atomic temperature a molasses stage is needed and a careful transition must be put in place not to lose the trapped atoms.

A typical cold-atom experimental sequence is shown in Figure III.4.[2] A few seconds are needed to fully load the 3D-MOT. The initial amount of atoms is determined by this waiting time. Next, a gentle ramp-down of the laser detuning cools the atoms further down. The detuning is measured in units of the natural line-width of the cooling transition $\Gamma = 2\pi \times 6.065$ MHz [193]. To go from the MOT to optical molasses, we abruptly turn off the magnetic fields and ramp-down the detuning to go from high

[1] The mirror structure inside the cryostat is a superconducting atom-chip [138, 192]. Since the advantages of the atom-chip are not necessary for our current purposes, the chip will play the role of a mundane mirror. The atom-chip technology has been explored and reported elsewhere [137].

[2] The exact values for the parameters in the sequence are subject to daily optimization procedures to compensate for various experimental drifts.

capture velocity to low temperature [186]. During this ramp-down the cooling laser power is gradually reduced and its detuning is increased further from resonance. During the optical molasses stage the applied magnetic fields are used to cancel the magnetic field at the position of the atoms. The atom cloud can be held in place for up to a second, while the number of atoms decreases exponentially with a half-lifetime of a few hundreds of milliseconds. The atoms undergo a slow diffusion under the strong viscosity of light until a new sequence needs to be started due to a lack of atoms. A full Rydberg sequence, from excitation to detection, takes up to a few milliseconds, and during the molasses stage a few hundreds of them are played. A dense and long-lasting atom cloud is then an asset permitting a high repetition rate of the experiments.

The assessment of the cold-atom cloud is done using cameras to image the atoms, measure their temperature, and tune there position. We will next develop the imaging system in our experiment.

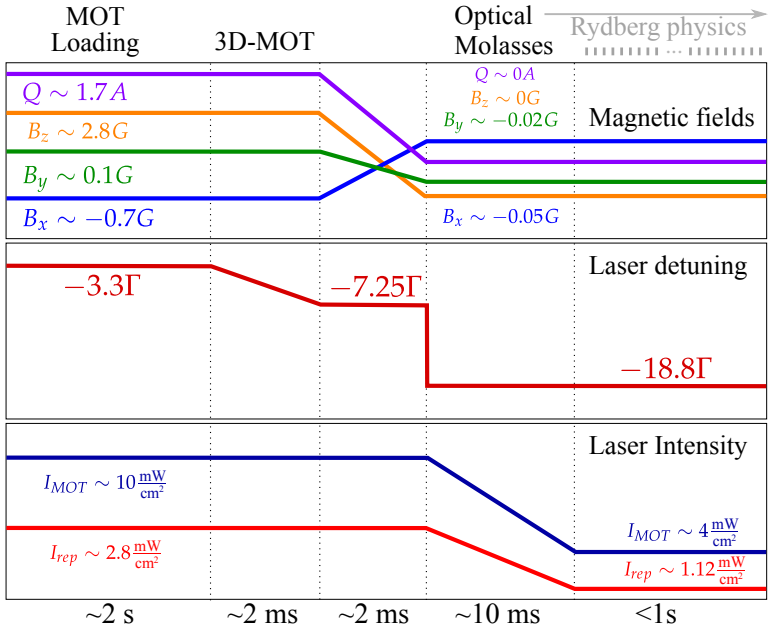

FIGURE III.4 A typical cold atom sequence. The color code for the current/field trajectories in the first panel corresponds to the color code of the coils in Figure III.3.

III.1.4 Imaging System

The imaging setup, together with the cooling lasers and the Rydberg excitation system, is shown in Figure III.5. The 'front' and 'side' probe beams (violet) are used for imaging the atom-cloud when the atomic-absorption technique is needed. The probe lasers are at a 780 nm wavelength ($|5^2S_{1/2}, F = 1\rangle \rightarrow |5^2P_{3/2}, F' = 3\rangle$) as one can see from the level diagram in Figure III.3. Two cameras, one from the side and one from the front, take images during the cool down of the atoms. These images allow us to set the position of the cloud, to measure the number of atoms, and to optimize the loading time, the size and the lifetime of the atomic cloud [139].

A side view of the molasses is shown on the left of Figure III.6. The image of the

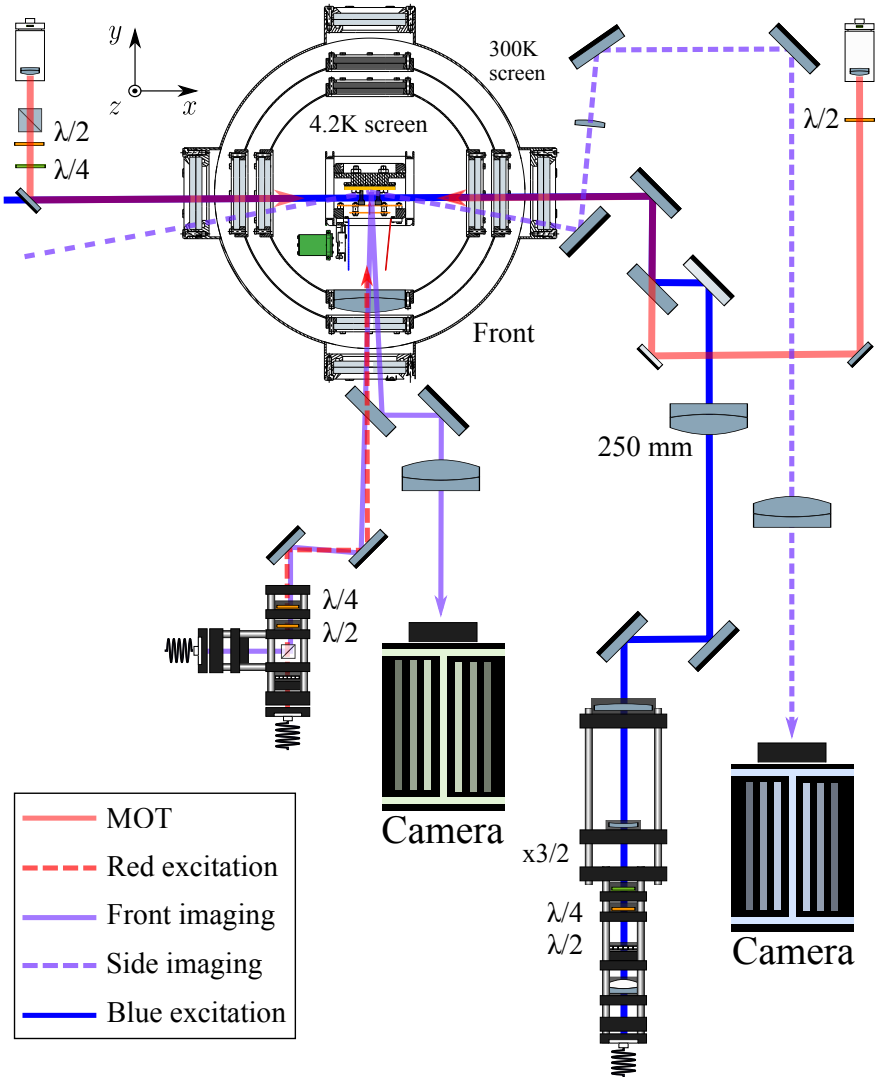

FIGURE III.5 A top view of the cryostat and the available lasers. The laser path for absorption imaging, Rydberg excitation, and atom cooling is shown.

cloud is taken by absorption. The rightmost cloud corresponds to the reflection on the mirror as one can see from the inset. Using simple geometric arguments, the distance between these two images gives the distance between the cloud and the mirror surface [139]. For a separation greater than 2.5 mm, the reflection cannot be seen and the distance to the mirror cannot be measured in this way. For fast diagnosis, fluorescence images can be taken live and are used for the coarse tuning of the cold-atom parameters. The fluorescence of the MOT cloud as seen from the front window is shown on the right of Figure III.6. Both absorption and fluorescence images can be taken using the side and front cameras. These two points of view provide complementary information. The structure visible in the background depicts the superconducting atom-chip wires that are used to calibrate the magnification of the picture. The white arrows setting the scale correspond to the xz mirror plane.

Time of flight measurement sequences are done to access the momentum distribution

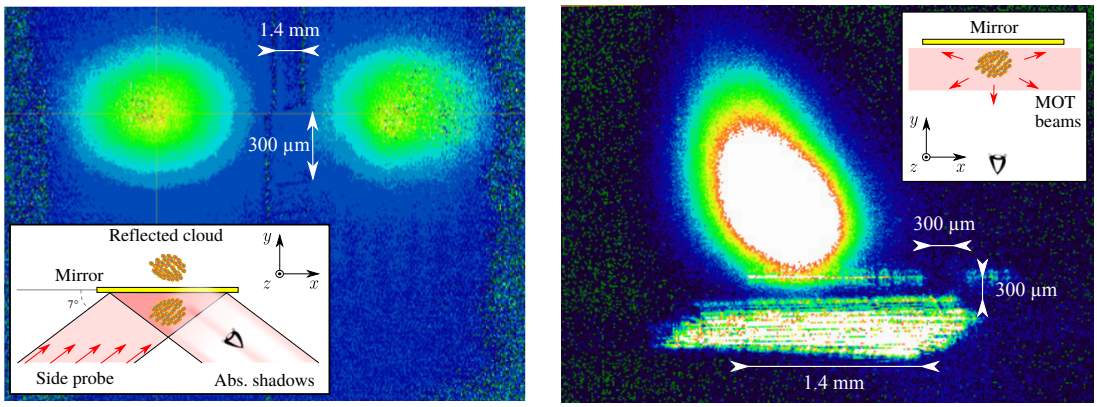

FIGURE III.6 Left: Side *absorption* image of the cold atom cloud and its reflection in the mirror. Right: *Fluorescence* image taken from the front. The insets schematize the imaging technique used.

of the atom gas. They consist of measuring the size of the cloud as a function of time during free expansion. In Figure III.7 we show the width of the atom cloud as a function of time t. The data is taken using the front camera for absorption imaging after the molasses stage. The temperature of the atoms is computed by fitting the expansion to

$$\sigma(t) = \sqrt{\sigma_0^2 + \frac{k_B T}{m_{Rb}} t^2}, \tag{III.1}$$

for the x and z directions. Here T is the atomic gas temperature, k_B the Boltzmann constant, σ_0 is the initial size of the cloud and m_{Rb} the mass of Rubidium-87. The fit assumes independent distributions in each direction.

The temperature of the MOT is about 200 µK and the number of atoms saturates for long loading times (∼2 s) to $\sim 10^8$. The molasses are typically at a temperature of 15 µK and they are formed by $N \sim 10^6$ atoms. The typical volume of our molasses is about $(300\ \mu m)^3$.

III.2 Rydberg atoms

We will now focus on the Rydberg atoms that are to be excited from the cold atom cloud. In the preparation of cRy atoms, two main stages can be identified: A first stage where energy is pumped into the atom using optical photons and a second stage where angular momentum is pumped into them. This second stage is the circularization process and it consists of a multi-photon RF adiabatic passage. An intermediate MW passage is needed to bring the laser-excited atoms to a state that will allow for the adiabatic circularization to take place. These steps, together with the detection mechanism, will now be developed.

III.2.1 Laser excitation of low-angular-momentum Rydberg atoms

After the molasses stage, the atoms are found in their ground state $|5S_{1/2}\rangle$. A two-photon transition is used to excite the fraction of atoms in $|5S_{1/2}, m_F = 2\rangle$ to the

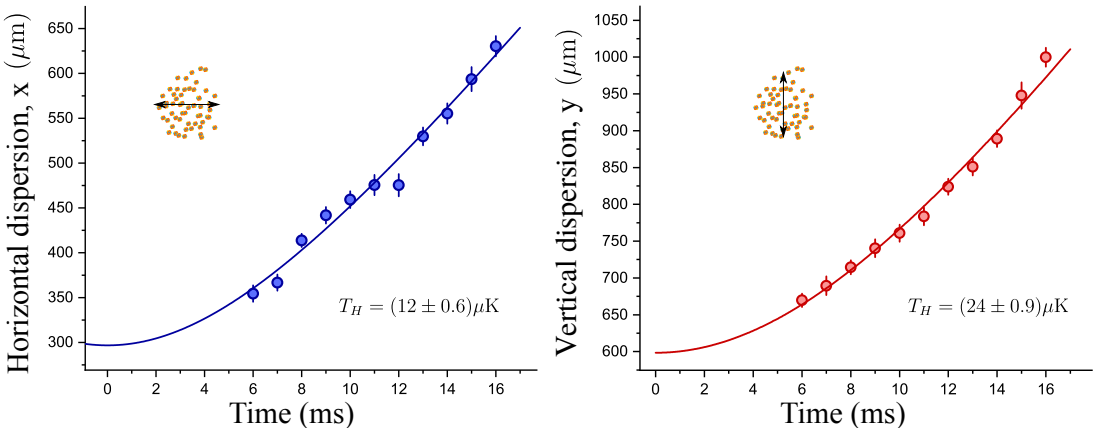

FIGURE III.7 Time of flight temperature measurement. The data corresponds to an absorption picture taken from the front optical port of the cryostat after a molasses stage. The inset represents an 'expanding' atomic cloud.

$|52D_{5/2}, m_j = 5/2\rangle$ Rydberg level. On the left of Figure III.8 the laser excitation scheme used is shown. The intermediate level providing the coupling is $|5P_{3/2}\rangle$ and it is reached off-resonantly by a 780 nm wavelength red excitation laser. The second photon is provided by a 480 nm wavelength blue laser. The $|52D_{5/2}, m_j = 5/2\rangle$ Rydberg level is chosen because it allows coupling to both the intermediate level $|5^2P_{3/2}, F = 3\rangle$ and to the $|52F, m_j = 2\rangle$ level, which will be the next target involved in the circularization process.[3]

The optical setup allowing for the Rydberg experiments can be seen in Figure III.5. The blue laser is tightly focused (∼10 µm waist) at the level of the atoms. A cage mount holding optics gives us the freedom to change its diameter and its polarization before the 250 mm lens that focuses it into the cryostat. An elongated Rydberg atom cloud is produced where the blue laser crosses the much bigger red excitation laser (∼100 µm waist). The red laser is σ^+ polarized and the polarization of the blue laser is linear and parallel to the MOT-mirror plane. The Stark separation of the levels allows us to discriminate them in energy and select the transition by choosing the blue laser frequency.

The detection of the Rydberg atoms is done by field-ionization. It consists of stripping the Rydberg electron from the atom using a strong electric field and collecting the ionic core. The ground state atoms do not react to strong electric fields applied and only atoms in Rydberg states produce ion counts. The spectrum shown on the right of Figure III.8 corresponds to the average amount of Rubidium core-ions detected by the Channeltron (green in Figure III.1 (b) and (c)) as a function of the two photon detuning δ. The separation of the peaks is due to a Stark shift caused by a 0.36 V/cm electric field along the y direction during the laser pulse. The higher peak corresponds to $|52D_{5/2}, m_j = 5/2\rangle$, which has the biggest Stark shift. The other two peaks correspond to $m_j = 3/2$ and $m_j = 1/2$.

[3]Note that for strong enough electric fields, state $|52F, m_l = 2\rangle$ is adiabatically coupled to the state $|n = 52, k = -47, m_l = 2\rangle$. In an abuse of notation we will continue to refer to it as the '$52F$ level' regardless of the field in which the atom finds itself.

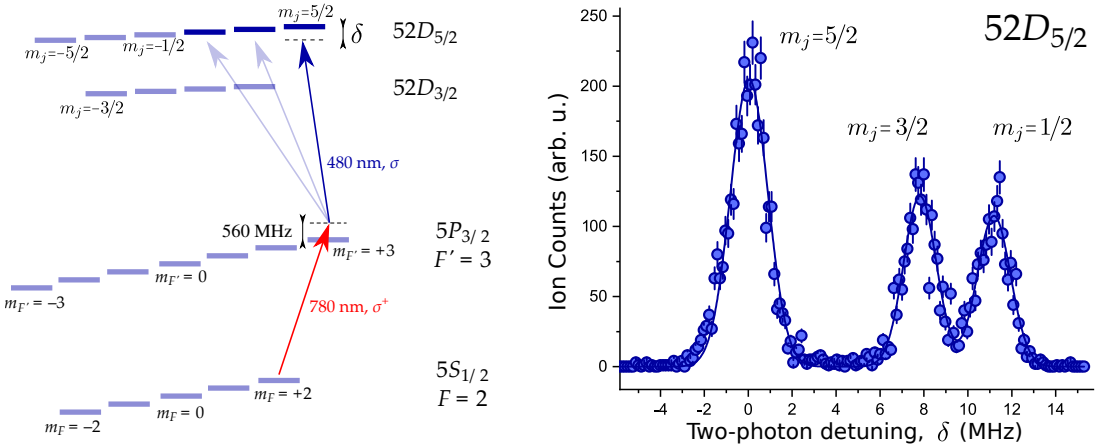

FIGURE III.8 Laser excitation diagram up to Rydberg levels (left) and laser spectroscopy of the $52D_{5/2}$ Rydberg levels (right). The blue laser frequency is scanned changing the two-photon detuning δ. The three spectral lines (right) correspond to the three dark blue levels in the diagram (left). The frequency offset is ∼624 THz.

After the laser excitation, the simple ion counting technique no longer suffices for our studies. For Rydberg states manipulation, a way to discriminate the ions coming from different Rydberg states is needed.

III.2.2 State selective field-ionization spectroscopy

Our Rydberg discrimination mechanism consists of progressively applying an electric field ramp on the atoms and recording the field at which each ion count arrives. Keeping track of the ionization field allows us to discriminate different classes of Rydberg states.

The electrodes

In Figure III.9 we show the experiment's electrodes (see also Figure III.5 (c)). These electrodes are used to extract and guide the ions to the detector.

In our setup, a pair of electrodes named 'Stark electrodes' (orange in Figure) are used to determine the quantization electric field orthogonal to the MOT-mirror during Rydberg manipulation and also to provide the ionization voltage for detection. In the experiment, we introduced a home-made commutation box acting on the Stark electrodes voltage in order to isolate the high-voltage electrical line used for ionization from the low noise electrical line needed for Rydberg control.

The flat electrodes colored in red are the 'deflection electrodes' to channel ions into the (green) Channeltron ion counter (KBL10RS-EDR). The blue colored electrode shields the high voltage needed to operate the Channeltron and has a hole to let the ions pass through. The hole is covered by a thin copper mesh (80 lines per inch, filling factor 20%, wires diameter of 3-5 µm). The Channeltron operates at 40 K and the mesh acts as mirror for the MW protecting the atoms from the associated black-body radiation. The voltage in this mesh is also a parameter used to direct the ions. The dashed line in Figure III.9 represents the ionic trajectory towards the Channeltron.

The cylindrical rod electrodes (grey in Figure) are arranged in a 2 cm sized square. They carry individual DC voltages that permit us to control the electric field in the x and z directions and also give us control over the electric field gradients of the experiment.

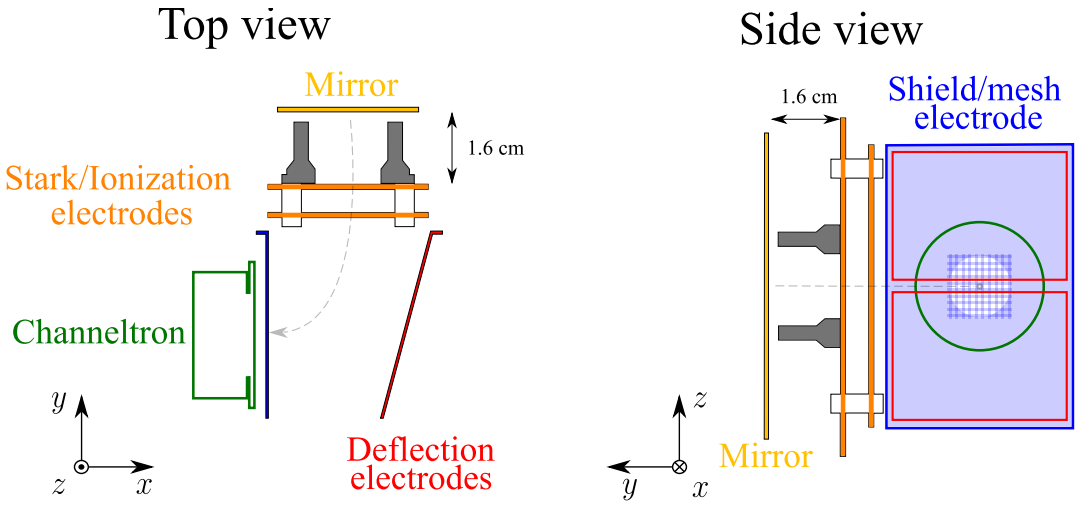

FIGURE III.9 The electric field control structure is shown. The four 'cylindrical' rods (gray) are the RF circularization electrodes. The Stark electrodes (orange) are also used to control the electric field normal to the MOT-mirror and the ionization field. The two twin flat electrodes (red) are the deflection electrodes, the Shield electrode (blue) screens the Channeltron's (green) high voltage. The flat mirror (yellow) is the superconducting atom-chip. The dashed line shows the trajectory of the ions.

The arrival time signal

The ionization voltage, applied to the Stark electrodes, is lifted in ∼200 µs from 0 V to 450 V to ionize all the levels of interest. This ramping up of the electric field, together with a time resolved detection of the ions, provides what we refer to as the 'arrival time signal' that we use to perform state-selective field-ionization spectroscopy. In Figure III.10, two ionization signals after a Rydberg excitation laser pulse are shown. The voltage on the Stark electrode is a known function of time and it is used to map the arrival times to a corresponding ionization voltage. In Figure III.10 (blue) we show an arrival time signal for a high number of Rydberg atoms prepared by tuning the blue laser frequnecy to the $|52d_{5/2}, m_j = 5/2\rangle$. By collision among Rydberg atoms, higher angular-momentum states are populated [88, 194]. Even if the many-body processes involved in the collisional transfer to high-l are very rich in atomic physics [88], we will, in this thesis, focus mainly on studying one-atom effects. The proliferation of interactions is avoided by working with a small enough number of atoms. The number of atoms is controlled by the length and power of the blue laser pulse. The data in red in Figure III.10 corresponds to a 2 µs long laser excitation using 1 mW at 480 nm, and 65 µW at 780 nm. In these conditions we can identify a single ionization peak that we identify with the preparation of $|52D_{5/2}\rangle$.

Once an ionization line has been found, one can define a time window associated

to the level of interest and consider the integral of ion counts therein as the number of atoms detected. But since many Rydberg states share the same ionization threshold, the method by itself is not sufficient for unequivocal level identification. For example, all m_j sublevels of the $|52D_{5/2}\rangle$ states have overlapping ionization spectra and cannot be distinguished by their ionization threshold alone. The solution is to complement the technique with laser or MW spectroscopy towards a level ionizing at a different field.

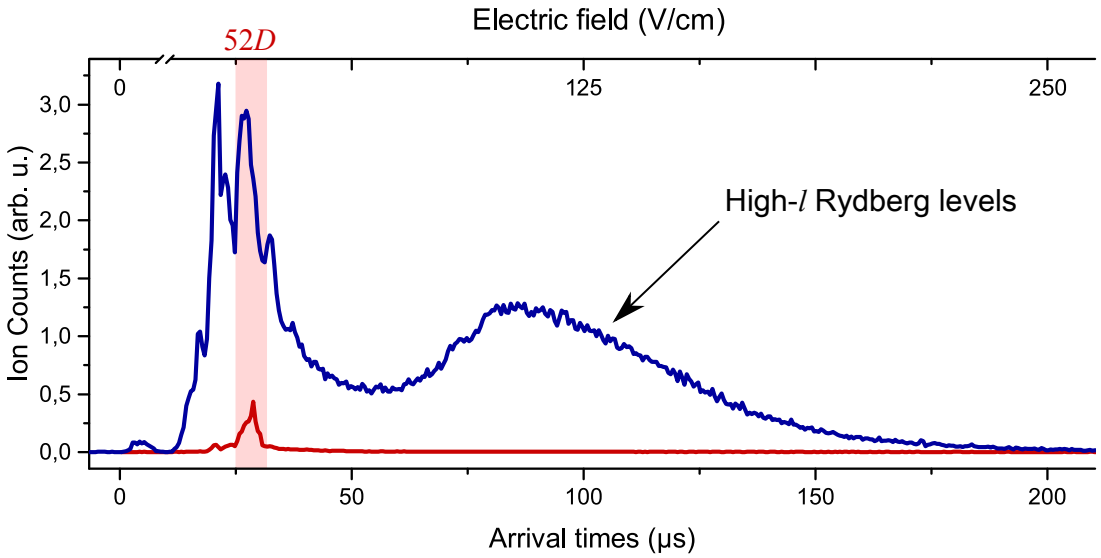

FIGURE III.10 Arrival time signals after laser excitation. A high power laser excitation (blue) gives rise to collisions populating high-l Rydberg levels. A low power laser excitation and frequency selection provides a clean ionization spectrum for $|52D_{5/2}, m_j = 5/2\rangle$. The shaded area shows the time window associated with $|52D_{5/2}\rangle$.

III.2.3 The MW $52D$-$52F$ transition

Level $|52D_{5/2}, m_j = 5/2\rangle$ cannot be used as a starting point for the RF circularization since it suffers from a large quantum defect (see Figure I.3). To circumvent this, an intermediate MW pulse to $|52F, m_l = 2\rangle$ is needed in between the laser excitation and the RF circularization.

The microwave used for the D-F transfer is generated by an ANAPICO APSYN420. The signal is amplified by a fourth-harmonic generation amplifier (Millitech AMC 314) permitting us to attain the desired frequency range and gated by pin diodes controlled by computer generated TTL signals. The output of the amplified fourth-harmonic generator is a free space waveguide. It is connected directly to the cryostat by a layer of glue (Araldite). The Araldite is transparent for the MW and provides a good vacuum seal. The signal travels through the Helium reservoir in a tube soldered to the base of the Helium reservoir, where a small hole with a 2 mm radius connects it to the main vacuum. Next, a bent copper tube with a radius of (2.00±0.05) mm working as a MW guide brings the field directly 2 cm above the atom cloud. Note that this copper tube puts a cut-off of (44±1) GHz in the MW transmission of the line.

At zero electric field, one finds the D-F transition at a frequency of ∼64.75 GHz (see Figure I.3) and the arrival time signal for the field ionization before (red) and after

a highly optimized MW transfer (blue) is shown in Figure III.11. The shaded areas represent the time window associated with each of the excited quantum states.

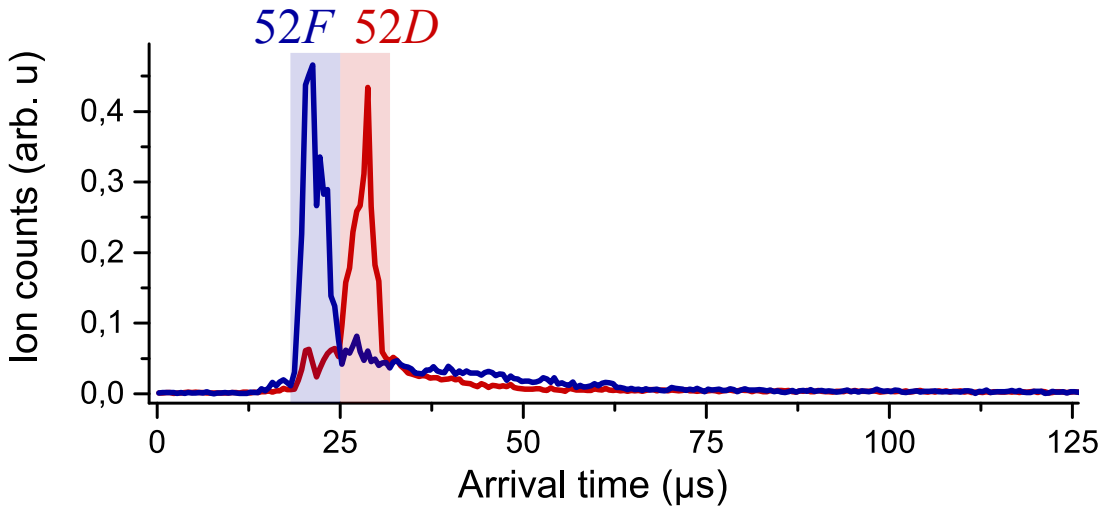

FIGURE III.11 The arrival time signal provides a field ionization spectroscopy for Rydberg levels. In red we show the ionization spectrum after a laser excitation to level $|52D_{5/2}\rangle$. In blue we show the ionization signal after MW transfer of the D level to the $|52F, m_l = 2\rangle$ level.

Calling n_D and n_F the average number of counts in each detection window, we write the transition probability from state D to state F as $n_F/(n_D+n_F)$ which quantifies the efficiency of the level transfer. In Figure III.12, we can see the D-F MW spectroscopy line at zero field (blue dots) and at 0.67 V/cm (red dots). Three $52F$ projections of angular momentum ($m_l = 1, 2, 3$) are resolved.

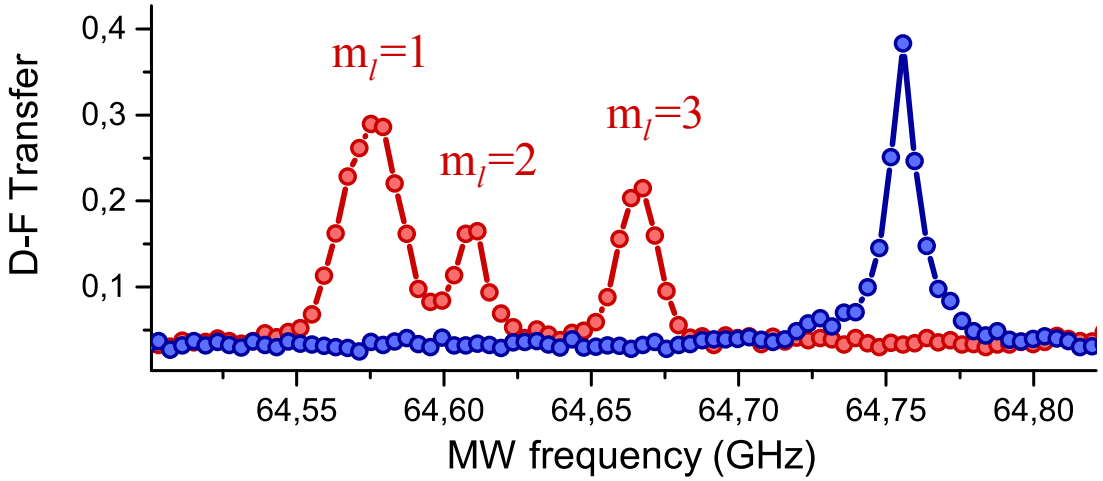

FIGURE III.12 MW spectroscopy from $|52D_{5/2}\rangle$. In blue, the three $52F$ lines collapsed into one at zero electric field. Excitation is done from the laser accessible level $|52D_{5/2}, m_j = 5/2\rangle$. At an electric field of ∼0.67 V/cm we see that the three lines are resolved (red).

The adiabatic passage

To optimize the D-F transfer, a MW adiabatic passage is used. We have devised a rather peculiar method to perform the D-F transfer which relies in the particularities of the home-made commutation box controlling the Stark electrodes voltage. The commutation box introduces a non-linearity in between the input voltage signal V_S, generated by a wave form generator (Agilent 33250A), and the electric field at the level of the atoms. In Figure III.13 we show the response of the electrodes in two different regimes: a steady state and a dynamical evolution of the Stark electrodes voltage. Using spectroscopic data like the one in Figure III.12, we map the electric field seen by the atoms to the V_S signal. For the measurements in Figure III.13 (a) we waited for the electrodes to reach a steady state voltage in order to disregard the time constants of the system. The non-linearity (the plateau) corresponds to the voltage drop in a diode (ON-GA-1N 4007-1816) inside the home-made box.

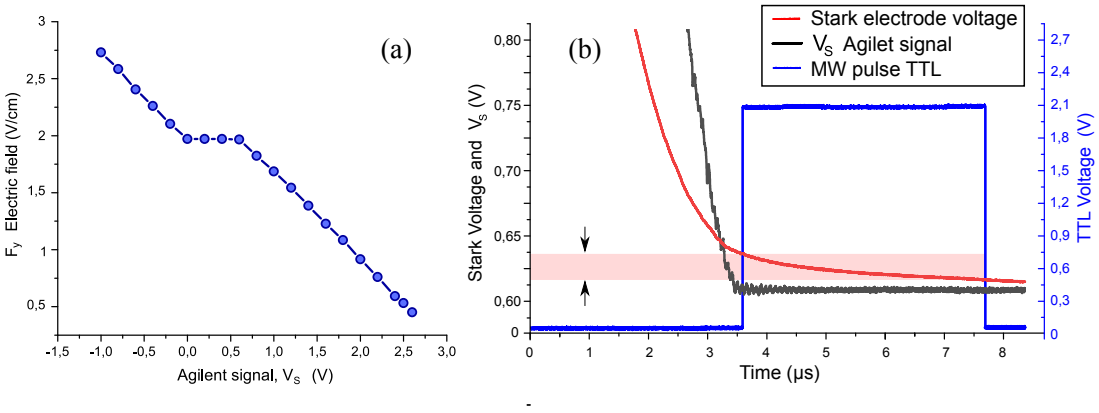

FIGURE III.13 Non-linear voltage-field relationship through the commutation box. Left: The static relationship between the input voltage V_S and the electric field at the level of the atoms. Right: The dynamical electrode voltage at the timescale of the experiment as seen in an oscilloscope plugged to the Stark electrodes directly. The D-F MW pulse is also shown.

Moreover, the dynamical response of the system is what allows us to make an efficient D-F adiabatic passage. In Figure III.13 (b) we show the time dependent signals involved in the D-F adiabatic transfer as seen in an oscilloscope. To achieve it, the input signal V_S is ramped linearly (black in Figure) from 2.1 V (providing the field during laser excitation) to 0.6 V in 2.5 µs. The signal seen by the atoms is filtered by the commutation box and, as an output, a noiseless decay on the Stark electrode voltage is obtained (red in Figure). During this smooth and comparatively small electric field scan, the MW pulse is on (blue in Figure) to produce the adiabatic transfer. The black arrows show the voltage scan made by the Stark electrodes during the MW pulse. We note that the magnitude of the scan made (red band) is of the order of the noise in the Agilent signal (black) justifying the approach: it is this level of precision in the electric field control that improves the adiabatic passage.

In Figure III.14 we show the response of the atoms to the MW frequency of the pulse. The middle peak corresponds to the transfer to the $|52F\rangle$ level which is achieved with an efficiency of $> 80\%$.

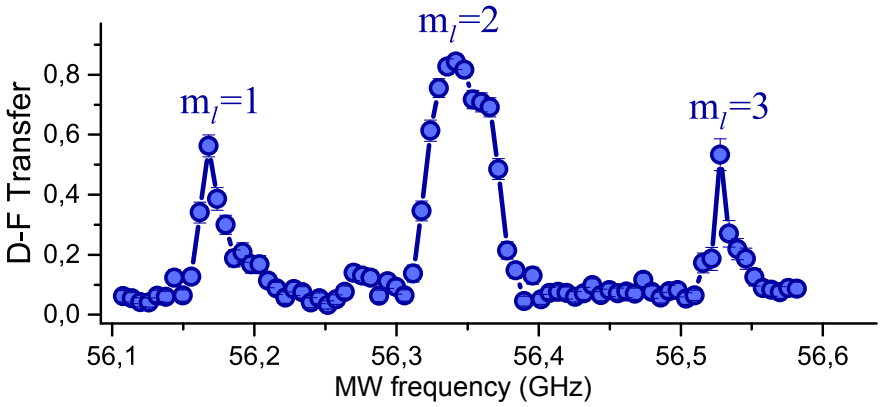

FIGURE III.14 The D-F adiabatic transfer. The broad microwave line provides a robust and efficient population transfer method.

III.2.4 RF circularization

The circularization process [195] essentially consists of pumping angular momentum into the already very energetic $|52F, m_l = 2\rangle$ state. The anguar momentum comes from a RF field that dresses the atom and couples different parabolic eigenstates of the bare atomic Hamiltonian. To achieve the circularization, σ^+ a polarized RF field must be produced. One can picture the atom climbing a σ^+ ladder of angular momentum as shown in Figure III.15 to the circular level. Due to degeneracy in the atomic levels, a non-polarized field couples the ladder states to spurious levels (dashed arrow in Figure III.15) and useful population is lost. We will discuss in what follows the techniques used for the circularization of cold Rydberg atoms.

The RF circuit

The RF circuit used to produce the polarized RF field is schematized in Figure III.16. A 230 MHz RF signal is created by a PCI card (Acquitek Synth-300) with two independent outputs. The software allows us to set both frequencies and to fix the relative phase between the channels. Each channel is split in two by a 3dB RF splitter (PULSAR P2-08-411) and the four signals are sent to the four circularization rod electrodes (see Figure III.9). After the RF splitters, dephasers (PULSAR ST-H85-444A) are used to control the relative phase between the two channels. Each RF line has three mixers (PULSAR X2L-06-411) that allow us to control the RF amplitude, via an analogue channel. The first mixer is used as a power regulator to compensate for the power imbalance between the four channels and the subsequent pair is used to make a time envelope for the signal. The power regulator mixer is controlled by filtered DAC cards (low-pass 1.4 kHz). The RF envelope is generated by an arbitrary wave-function generator (Agilent 33521A) and it is a smooth bell curve turning on and off the field adiabatically. The RF signals are then amplified (Mini-Circuits ZHL-2-12 and ZHL-1-2W+) and sent to RF circulators (HYTEM 09-02-57) to avoid unwanted reflections entering back into the amplifiers. Four polarization-T (PULSAR BT-20-411) are used to mix the RF signals to DC fields used to manage potential offset of the rod electrodes. During optimization, the rod electrodes DC voltages are controlled by a DAC card. For

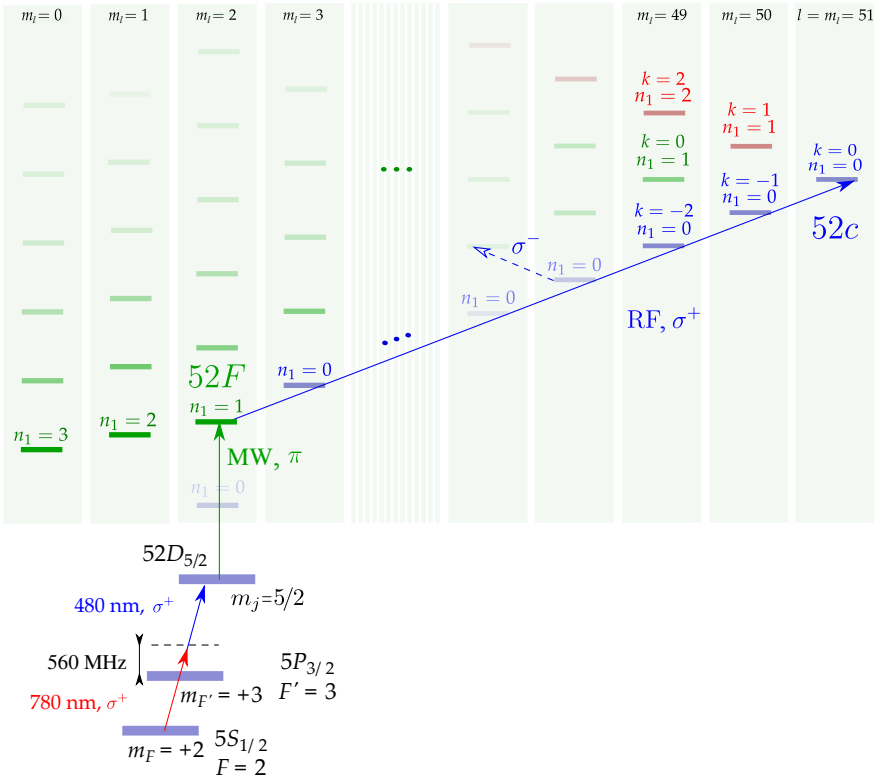

FIGURE III.15 The circularization process starting in the ground state. Laser photons excite the Rubiduim-87 atom to the $n = 52$ Rydberg state. The adiabatic MW passage brings the population to the F level. The population can then be adiabatically transferred to the circular state by a RF multi-photon adiabatic passage. The notation for the quantum number used in this plot was introduced in Chapter I.

applications requiring low noise (Chapter IV), a home-made box containing a set of batteries is used to provide a noiseless reference.

Polarization adjustment

One can optimize the polarization of the RF by optimizing the circular state purity. This is performed on a daily basis. But in order to find an initial circularization signal, the setting of the polarization requires a more refined technique that we will now develop.

In Figure III.17, we show the level structure around the $|52F\rangle$ level for the circularization Stark field (a) and for an auxiliary Stark field used to do the initial RF optimization (b). Since the ladder states ($n_1 = 0$) in $n = 52$ manifold have a differential Stark shift of 99.8 MHz/(V/cm), the adiabatic passage must be done around 2.31 V/cm where the 230 MHz RF resonance condition is met. At this circularization field (a), the level $|52F\rangle$ is coupled to the circular state via the ladder (shown in red here). At 1.76 V/cm (b) the $|52F\rangle$ state has an energy difference of 230 MHz only to state $|n = 52, n_1 = 3, m_l = 1\rangle$ and the coupling requires a single σ^- photon. The red levels in Figure III.17 (b) form an isolated two-level system. Under a σ^- RF dressing field the eigenstates are $|\pm\rangle = |52F\rangle \pm |n = 52, n_1 = 3, m_l = 1\rangle$. At resonance, the

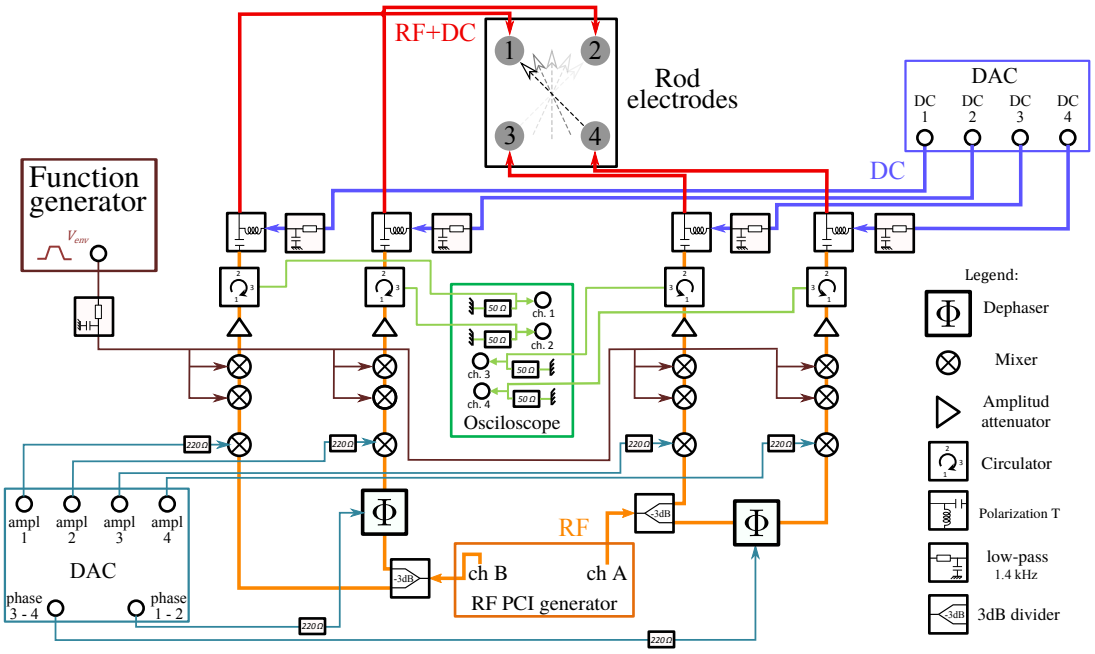

FIGURE III.16 The RF circuit used for circularization. The four RF powers and the three relative phases of the rod electrodes (see Figure III.9) can be controlled independently. The dashed arrow represents the σ^+ RF field created by the rod electrodes.

energy splitting is exactly the Rabi frequency Ω_- of the RF field component at σ^- polarization. This is known as the Autler-Townes (AT) splitting [106] and provides a tool to measure the power in the σ^- field component.

Experimentally, if a σ^- RF coupling field is turned on diabatically over atoms in state $|52F\rangle$, the population is projected equally into the $|\pm\rangle$ states. Microwave spectroscopy to an auxiliary level $|n = 51, n_1 = 2, m = 1\rangle$ is used to reveal the AT-splitting of the lines (green arrow in Figure III.17). The electrode geometry is such that the RF field is almost completely in the xz plane so that the π polarization component of the RF field (along the y direction) is small. The maximal AT splitting is achieved for optimized σ^- polarization and it is a measure of the RF power that can be shone on the atoms. The polarization optimization consists of measuring and eliminating the splitting while all four electrodes are on by tuning the relative phases and powers.

The first step in the optimization is to tune the RF power of the electrodes individually to achieve a comparable AT splitting. Next, two neighboring electrodes are turned on simultaneously and the relative phase (and power) is tuned so that the two AT lines collapse to a single one. In Figure III.18 we can see the AT splitting revealed by the MW spectroscopy (blue dots). In the same graph we show the product of the compensation (red dots). Once this is achieved, one has produced mainly σ^+ polarization. The same is done for the other pair of electrodes.

Finally, all four sinusoidal RF signals are turned on together and the relative phase between the optimized pairs is used to maximize the power of the σ^+ field. Even if using the four electrodes together improves the spatial homogeneity of the polarization,

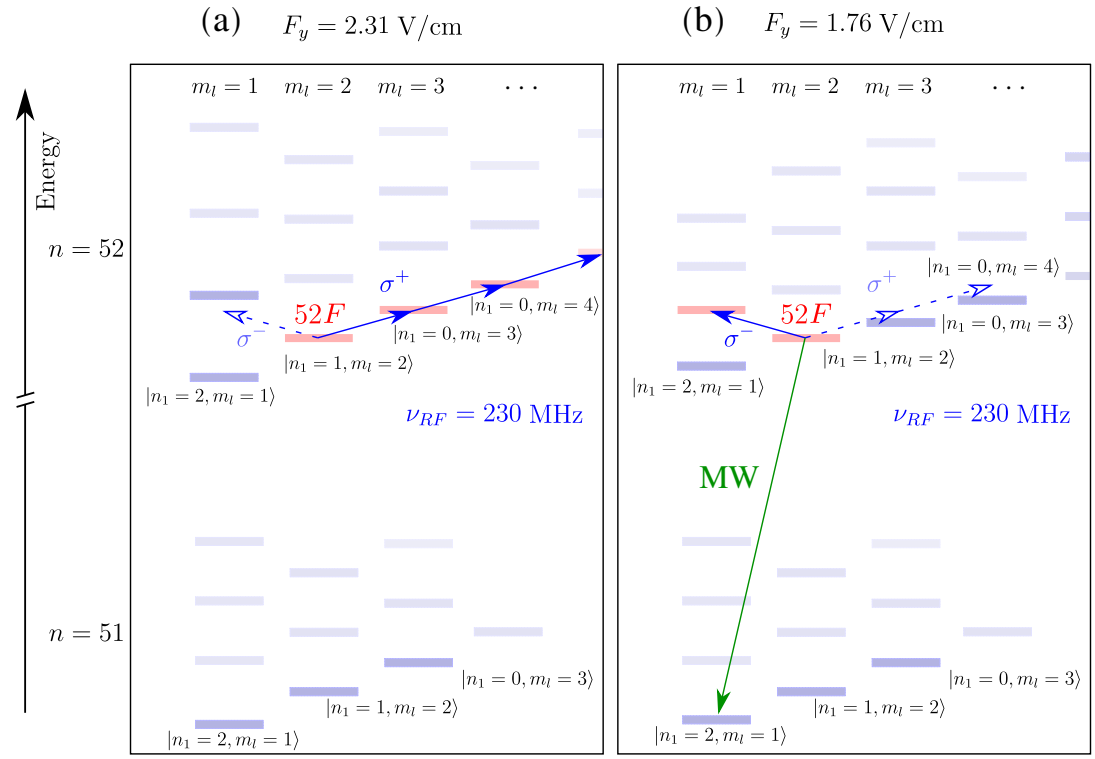

FIGURE III.17 Diagram of the Autler-Townes procedure for polarization optimization. Panel (a) shows the level scheme at the circularization field. Panel (b) shows the structure of levels at an auxiliary electric field used for polarization optimization.

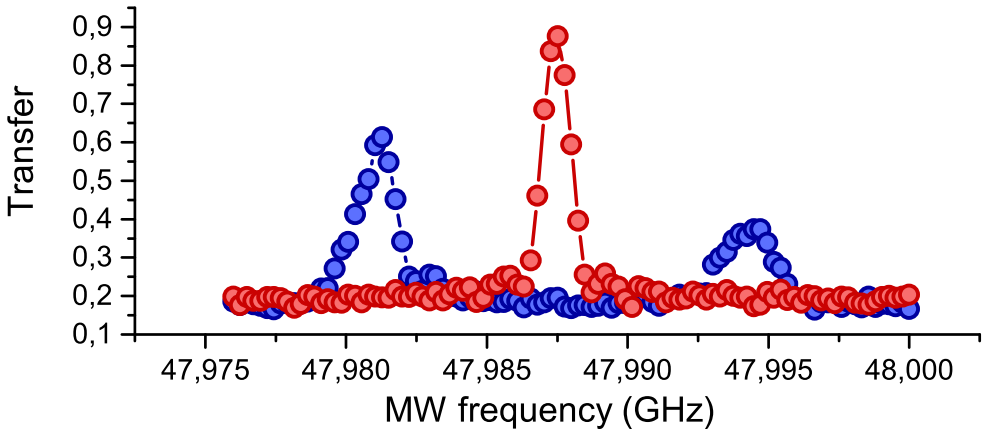

FIGURE III.18 Autler-Towns splitting and recombination. The σ^- RF field splits energies of the $|\pm\rangle$ states (blue dots). Tuning the electrodes phases to turn the polarization of the field into σ^+ recombines the peaks into one single line (red dots).

for the experiments in this thesis, we prepared the circular states using only two circularization rods alone. The improvement supposed by the four rod approach is marginal and requires time-consuming calibrations on a daily basis.

Multi-photon adiabatic passage

The pure RF polarization decouples the bigger part of the multiplicity isolating a subspace of almost equidistant levels, as shown in Figure III.15 ($n_1 = 0$ ladder in blue). At ∼2 V/cm the Stark term in the atomic Hamiltonian becomes dominant with respect to the energy shifts due to the quantum defect and all levels ($l > 2$) have a linear energy dependence with the electric field (see Figure I.3). As a consequence, the energy gap between the first level of the circularization ladder and the next is approximately equal to that of all the rest (see eq.(I.7)) [106]. Then, by turning on a σ^+ 230 MHz field and scanning the electric field through the ladder resonance, an adiabatic transfer from level $|52F\rangle$ to the circular states is achieved.

It is illuminating to think of the adiabatic circularization in the dressed atom picture. In Figure III.19 we draw the associated diagram. In the first panel we see the Stark energies for the $n = 52$ Rydberg manifold (see also Figure I.3). In the middle panel we show the energies of the atomic levels dressed by the RF field. The notation for the joint quantum states used here is $|k, N\rangle$ and refers to the atomic states in the $n_1 = 0$ ladder by their parabolic quantum number k while N stands for the Fock state of the RF field. In this diagram we consider the energies to be additive and each line is displaced by N times the photon energy ($h\times$230 MHz). The level crossing is produced in 'resonance' where neighboring bare states are spaced by the photon energy. If the RF is applied over the atoms, a multi-photon avoided crossing appears. We show this in the last panel of Figure III.19. By scanning the electric field under the RF coupling (as shown in the inset), we adiabatically couple the $|52F\rangle$ state to the $|52c\rangle$ state producing an effective absorption of 49 RF photons, each providing a quantum of angular momentum. The green arrow in the picture shows the evolution of the atomic state during the passage.[4]

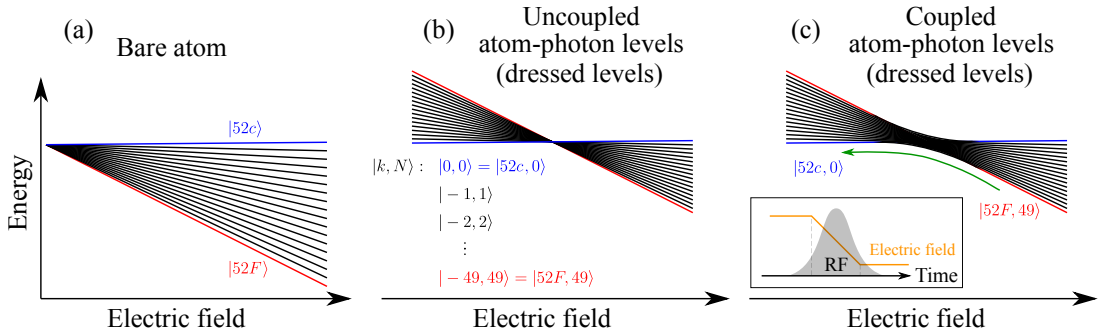

FIGURE III.19 Adiabatic circularization in the $n = 52$ manifold in the dressed atom picture. In (a) we show the bare energy levels ($n_1 = 0$) that take part in the circularization. In (b) the energy of the joint atom-photon states in absence of coupling are seen to cross. In (c) the atom-photon coupling makes an anti-crossing appear.

[4]Experimentally we use a classical RF field $|\alpha\rangle$ (coherent, $\langle N\rangle = |\alpha|^2 \gg 1$) and the photon number states considered in the dressed atom picture must be understood as its components in the Fock basis. In full rigor the state evolution is the coherent superposition of all N contained in $|\alpha\rangle$ undergoing $|52F, N \sim |\alpha|^2 + 49\rangle \rightarrow |52c, N \sim |\alpha|^2\rangle$ where we use that $|\alpha|^2 + 49 \sim |\alpha|^2$. Note that the coupling (the gap at the anti-crossing) is actually proportional to $\sqrt{N+1}$ [141].

Preparation of circular states

The full Rydberg sequence allowing for the excitation, circularization, and detection of Rydberg atoms is shown in Figure III.20. This sequence is played repeatedly during the molasses in the cold atoms sequence (see Figure III.4).

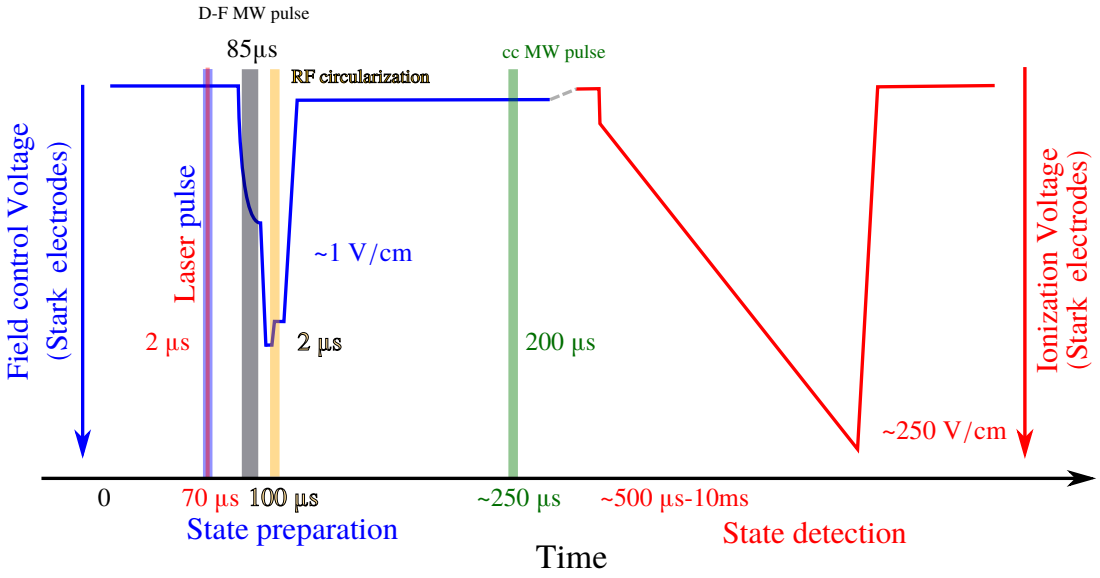

FIGURE III.20 Rydberg atom preparation and detection timing. The preparation of the circular Rydbergs is done in a few tens of microseconds. The shaded rectangles represent the different pulses (laser, MW and RF) used for the manipulation of the atomic state. The blue curve depicts the Stark electrodes voltage evolution. The red curve shows the ionization voltage applied to the Stark electrodes for detection. The dashed line between the Stark voltage and the ionization voltage represents a variable waiting time that can vary from 0 to 10 ms. The ionization ramp-down is done in ∼200 µs.

Right after the laser excitation pulse (blue and red bars in Figure III.20) and the *D-F* adiabatic passage (black bar in Figure III.20), the Rydberg atoms are ready for circularization. The multi-photon RF adiabatic passage is done by scanning the electric field during a RF pulse (yellow bar in Figure III.20) as illustrated by Figure III.19 (c). The electric field is linearly scanned from 2.6 V/cm to 2.25 V/cm in 2 µs. The benchmarking of the circularization is done here by probing the population distribution using MW spectroscopy (green bar in Figure III.20) towards the $n = 51$ adjacent manifold at an electric field of $F \sim 1.55$ V/cm.

In Figure III.21 we show the ionization signal after an RF adiabatic passage done using the phase optimization provided by A-T spectroscopy. We address a MW probe pulse to different high-l levels to assess the efficiency of the cRy atom preparation. The population of elliptical states is a signature of low circularization efficiency. The number k designates the $|n = 52, k, m_l = n - k - 1\rangle \rightarrow |n = 51, k, m_l = n - k - 1\rangle$ transitions between the high-l levels (see Chapter I). We show the ionization signal for the MW pulse addressing some of the high-l transitions close to the $|n = 52c\rangle \rightarrow |n = 51c\rangle$ transition frequency. Note that we have changed the slope of the ionization voltage with respect to Figure III.11 to have improved resolution on the high-l section of the ionization spectrum. The shaded blue area corresponds to the ionization time window

for high-l $n = 52$ levels and the red shaded area corresponds to the high-l $n = 51$ levels. The ionization peaks in the blue shaded area correspond to low-purity circular levels. The many peaks in the red area correspond to pure levels selected with a MW transition. The ionization peak for the elliptical levels ($|k| \gtrsim 0$) greatly overlap with that of the circular level ($k = 0$) and between themselves. We also note that, for higher parabolic quantum number k, the ionization peak slightly shifts to higher voltages.

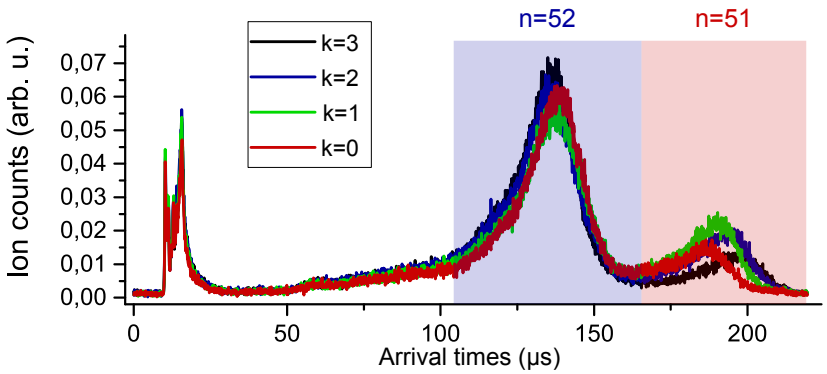

FIGURE III.21 Ionization signal corresponding to the different transitions seen on the blue colored spectrum in Figure III.22. The shaded blue area corresponds to the ionization time window for high-l $n = 52$ levels and the red shaded area corresponds to the high-l $n = 51$ levels.

In Figure III.22 we show the MW spectrum found after the A-T polarization optimization (blue dots). Sub-optimal polarization brings the population out of the $n_1 = 0$ ladder and, with enough power, the population is pushed against the boundary of the multiplicity along the upper diagonal ($k > 0$, see Figure III.15 and Figure III.22). Since the $|52, k\rangle \rightarrow |51, k\rangle$ transition is shifted by an amount directly proportional to k from the circular to circular transition (see eq.(I.7)), we conclude that the blue spectrum in Figure III.22 is a consequence of too much RF power and slightly elliptical RF polarization. This explains the elliptical peaks on the right of the circular to circular transition. A pure polarization with not enough power would populate the $n_1 = 0$ levels close to the circular, and these spectroscopic peaks would appear to the left of the circular one ($k < 0$).

The red spectrum in Figure III.22 corresponds to the fine tuning of the RF phases and powers over this signal. The transfer rate of the circular to circular line ($k = 0$) is an indirect measure of the purity of the preparation.

III.2.5 Circular to circular transitions

Other circular levels in the surroundings of the $n = 52$ circular state are also available via MW transitions. In Figure III.23, the available circular levels prepared in this way are shown. The ionization spectrum starts 330 µs after circularization. The shaded rectangles delimit the level identification. Note that the ionization spectrum is asymmetric. Note also that the ionization spectrum for each circular level overlaps with that right next to it on the lower field side.

We remark that, to access level $|54c\rangle$ from $|52c\rangle$, a pair of photons at 44.4 GHz

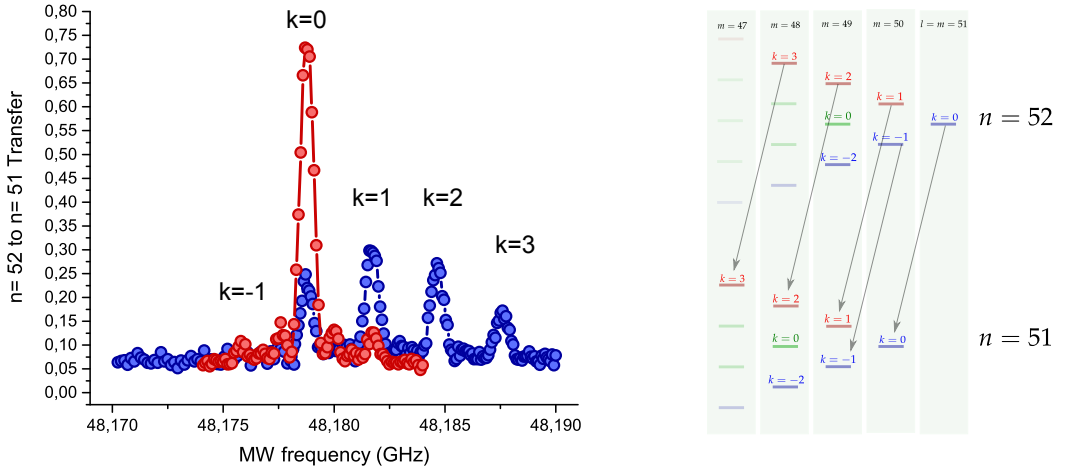

FIGURE III.22 High-l Rydberg MW lines. Before the fine RF tuning (blue dots), several elliptical states are populated. The red dots correspond to the optimized circularization. The level identification of the elliptical to elliptical transitions close to the circular to circular line is made possible thanks to the right panel.

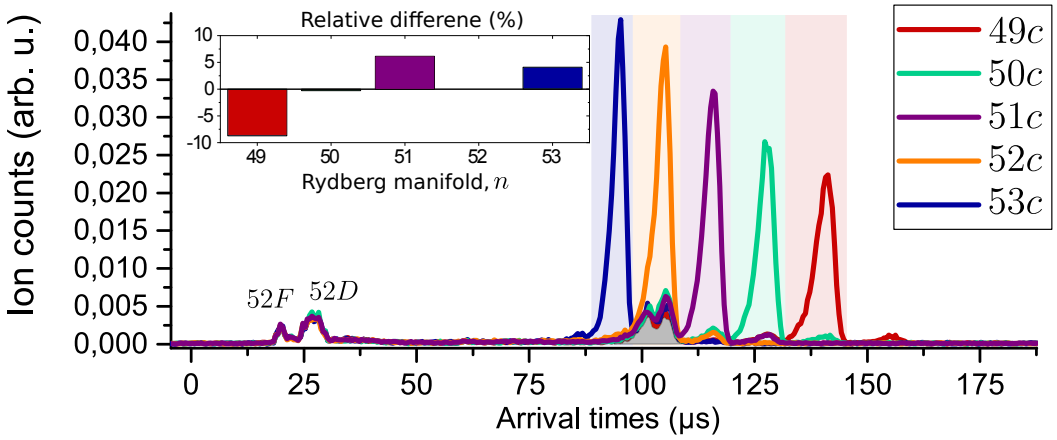

FIGURE III.23 Ionization signal for MW available circular states from $|52c\rangle$. The inset is the relative detection efficiency per circular level.

(see eq.(I.1)) is required. This transition cannot be accessed in our setup because the corresponding frequency is below cut-off for our MW waveguide. On the other hand, the transition $|52c\rangle \rightarrow |48c\rangle$ can be obtained only with very bad state purity since such a four-photon transition requires too much power and the line gets polluted by spurious transitions that are off-resonantly excited.

The double-peak structure left after the MW transfer pulses (shaded gray in Figure III.23) corresponds to residual elliptical population after the circular state preparation. Note also that in Figure III.22 the spectrum colored in red has small peaks at $k = \pm 1$. These two experimental signals share a common origin: an imperfect circularization. Nonetheless, by applying a MW pulse from $n = 52$ circular state to another circular level, we purify the state preparation by selectively only transferring the circular atoms.

The inset of Figure III.23 represents the differential level-dependent detection efficiency in these experiments. Since each cRy level ionizes at a different electric field, the trajectory of the core ions towards the channeltron is also different. The efficiency thus depends on the deflection voltages and on the position the atoms are ionized. The voltages of the ion-deflection electrodes are tuned to get a total number of counts independent (up to 8%) of the level preparation intended.

Purity of the cRy preparation

We assess the purity of the optimized preparation for the $|52c\rangle$ state by performing MW spectroscopy on the $|52c\rangle$ to $|50c\rangle$ transition. In Figure III.24, we show the circular to circular MW line at its highest. The spectroscopy is plotted as a function of the MW detuning δ_{mw}. The solid black trace is a squared cardinal sinus fitted to the data. The MW pulse is 1.4 µs-long. In an applied electric field of 0.8 V/cm, this transition is separated by 2.7 MHz from the nearest transition starting from the $n = 52$ populated elliptical states. The $> 91\%$ transfer from $|52c\rangle$ to $|50c\rangle$ at resonance is a lower-bound estimation of the purity of $|52c\rangle$.

Note that using a two-photon, instead of a one-photon, transition is beneficial in that no direct thermal transfer affects the final level, providing a cleaner background. Moreover, the absence of a permanent dipole (see Figure I.1) makes the interaction negligible by limiting the number of excited Rydberg atoms.

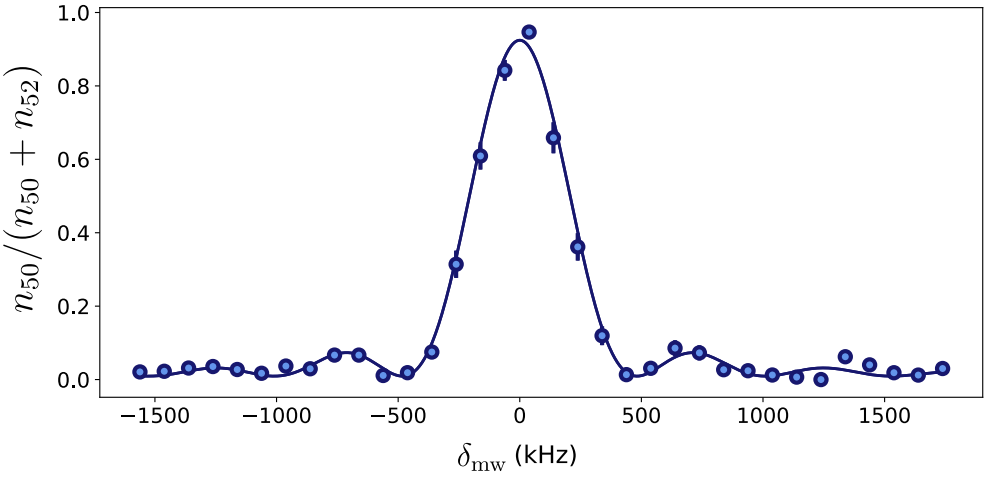

FIGURE III.24 Microwave spectroscopy of the two-photon $|52c\rangle$ to $|50c\rangle$ (MW_S) transition. The frequency offset is 99.2786 GHz.

As explained before, one is to avoid the proliferation of interactions since population losses induced by Rydberg-Rydberg collisions become a limiting factor for the purity of the state preparation. We have measured the purity of the circular state preparation as a function of the total number of cRy atoms detected. We measure the maximal MW transfer from state $|52c\rangle$ to $|50c\rangle$ as we vary the blue laser excitation power and we plot the results in Figure III.25. We see that in these detection conditions, and under an electric field of 0.74 V/cm during the circular state manipulation, up to an average number of counts of $n_{50}+n_{52} \sim 0.4$, the purity is not affected by density effects.

This threshold depends strongly on the directing electric field. As a general rule, the stronger the electric field, the bigger the number of atoms one can excite without seeing losses in the population (see chapter II and IV).

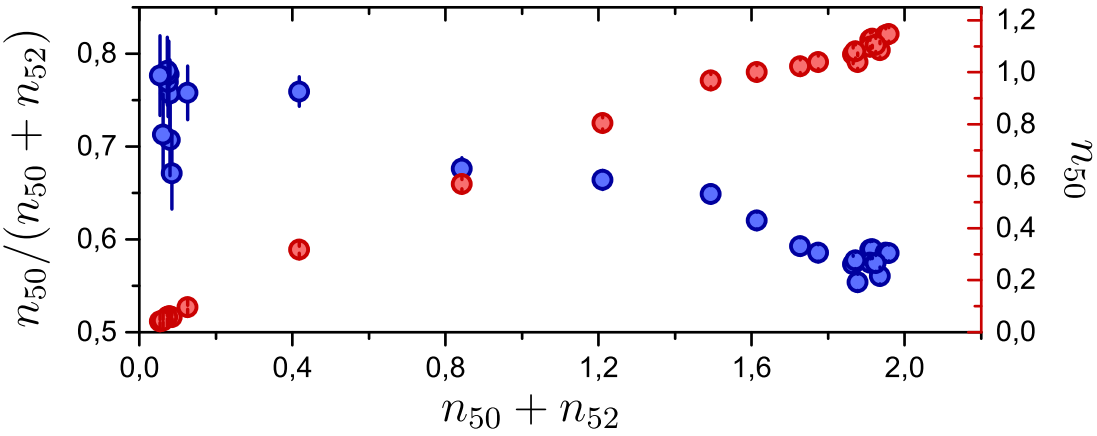

FIGURE III.25 Purity of the $|52c\rangle$ preparation as a function of the total number of circular levels prepared. The blue dots represent the maximal transfer from state $|52c\rangle$ to $|50c\rangle$ after a MW pulse. The blue excitation laser power is varied to increase the number of Rydberg excitations. The red dots represent the quantity n_{50} of $|50c\rangle$ states prepared from a MW pulse from $|52c\rangle$.

III.3 Conclusion

In contrast to other cold atom experiments, our atom manipulation happens inside a Helium-4 cryostat. The optical table containing the cold atom lasers, the imaging system, and the Rydberg excitation lasers have been introduced. Using these tools, we are able to prepare and optimize optical molasses ($\sim$ 15 µK) in the cryogenic environment. The accomplishment of the cold atom cloud marks the starting point for the Rydberg excitation.

We have achieved a high purity preparation of circular states. The excitation from ground to cRy is done using an orchestrated combination of electric field, laser, MW, and RF pulses. Furthermore, we have shown the capability of transferring the circular states from one manifold to another: a competence that will prove to be a necessary utility.

The tools introduced in this chapter will be used heavily in the rest of this work. They all converge in the preparation and manipulation of the cRy atoms, which are the main object of study in this thesis. In the following chapters we discuss the lifetime of the cRy states and their coherence in our setup (chapter IV), as well as the laser trapping techniques we implemented (chapter V).

Chapter IV

Lifetime and coherence measurement of circular Rydberg atoms

Contents

As discussed in the previous chapters, intense black-body radiation is a drawback for Rydberg states physics. Preparing these states in a cryogenic structure therefore provides an advantage. In this chapter we will study the lifetime and coherence of the cold cRy states prepared in our cryostat.

In the first part of this chapter we deal with the lifetime of the circular states. The walls of the cryostat are at ∼4 K, while the black-body radiation entering through the windows, as well as the presence of the heated Channeltron ion counter, rise the electromagnetic temperature seen by the atoms. We find that, in our cryostat, the mean number of photons is compatible with the one predicted by the Plank law for a temperature $T = (11 \pm 2)$ K. The corresponding lifetime of state $|52c\rangle$ is then of (3.7 ± 0.1) ms.

In the second part of this chapter we deal with the coherence of the superposition of $|50c\rangle$ and $|52c\rangle$. We measure the response to MW excitation of the atoms by making spectroscopy over two different transitions sensitive to either magnetic or electric field variations. In this way, we identify and correct for possible sources of decoherence. We find that the frequency spread of the circular to circular transition is dominated by technical magnetic field noise. Finally, we assess the coherence of these states by measuring the reversible (∼ 35 µs) and irreversible (∼ 270 µs) decoherence times directly, and a simple model is introduced to fit the data.

IV.1 Lifetime (T_1)

The mean number of thermal photons at 50 GHz goes from about a hundred at 300 K, to about one at 4 K. This implies a 100-fold increase in the $n \sim 50$ cRy lifetime. It is in our interest to thermalize the radiation temperature to the liquid Helium temperature. For this purpose we have i) reduced the optical access of our cryostat to shield the atoms from the 300 K external black-body radiation, ii) installed a mesh to block the 40 K radiation emitted by the Channeltron ion counter, and iii) installed a MW absorber to get rid of any residual hot radiation in the cryostat. In this section, we first detail the upgrade of the experiment performed in order to reduce the MW black-body radiation. We then present a measurement of the lifetime of the $|52c\rangle$ level from which we deduce the electromagnetic temperature in our cryostat.

IV.1.1 Reducing the effective MW temperature

Experimental upgrades

The windows in our cryostat are effectively transparent to the MW radiation and a first attempt to reduce the black-body temperature inside the cryostat is to reduce their aperture. In Figure IV.1 (a) we show a picture of the Helium shield with irises made of copper installed on its windows. Different windows have different holes corresponding to the minimal aperture needed for laser access and imaging of the atom cloud.

Secondly, a thin mesh (see Figure III.9) was installed in the hole of the shield electrode to block the radiation coming from the channeltron, which is heated to 40 K. The mesh acts as a mirror for the millimeter-wave radiation. The aperture and the almost invisible copper mesh are shown in Figure IV.1 (b) (also see Figure III.1 and III.9). The mesh is glued to the electrode shielding the channeltron voltage using

silver paint (Electrolube SCP03B). It turns the whole plane of the electrode into an equipotential. The hole in the electrode originally played the role of an ion lens to focus the ions in the counter. Supressing this effect in the current experimental setup severely degrades the detection efficiency.

Finally, 355 cm^2 of radar absorbing material was installed in the interior of the cryostat and thermally anchored to the Helium shield using a cryo-compatible glue (Stycast). Its purpose is to thermalize the MW field to 4 K. In Figure IV.1 (c) we show a picture of the installation. Due to differential thermal contraction, and in order to reduce mechanical constrains, the MW absorber is cut in blocks of 1 cm $\times$ 1 cm and glued to a copper foil that is in turn cut in 1 cm $\times$ 15 cm strips. The metal strips also help reduce the eddy currents when we tune the magnetic field during the cooling sequence. In the picture, one block was removed to show the design. The blue surface is the Stycast glue.

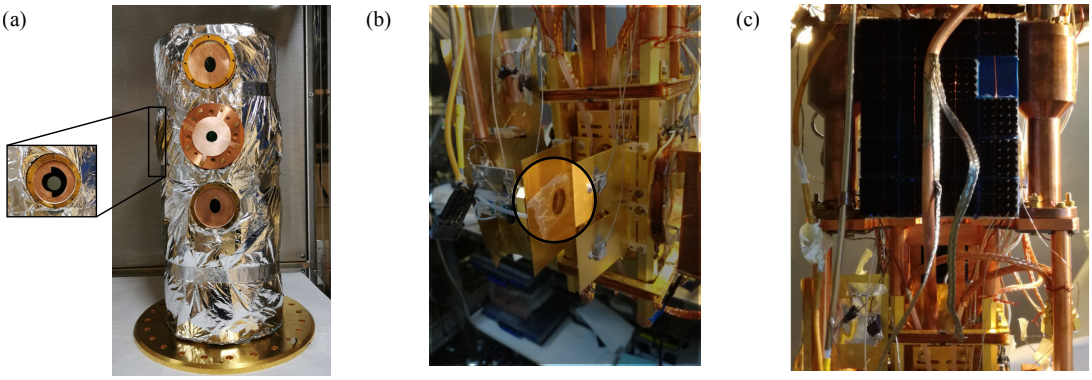

FIGURE IV.1 In (a), the Helium screen is shown where the copper irises are installed. In (b), the hole in the shield electrode covered with the thin mesh is show. In (c),we show a photograph of the MW absorber installation.

IV.1.2 Measurements

We measure the lifetime of $|52c\rangle$ cRy atoms by measuring the population of the different circular states using field ionization after a variable time τ. The timing of the sequence is shown in Figure IV.2 (a). Time $t = 0$ is taken at the end of the circularization. The ionization signals obtained for different values of τ are shown in Figure IV.2 (b). We see how the population, initially concentrated in $|52c\rangle$, distributes into the neighboring levels as time elapses. Note that the residual population in levels $|52D\rangle$ and $|52F\rangle$, significant at $t = 0$, quickly disappears. This is a striking manifestation of the improvement that using cRy brings. The lifetime of these levels, even in a cryogenic environment, is in the range of 100 µs, two orders of magnitude smaller than that of the circular states at zero temperature.

The dots in Figure IV.2 (c) correspond to the integration of ion counts in each of the detection windows (corrected by a small offset of $\sim 8 \times 10^{-4}$ counts/µs introduced by dark-counts) and describes the population diffusion among the circular levels.

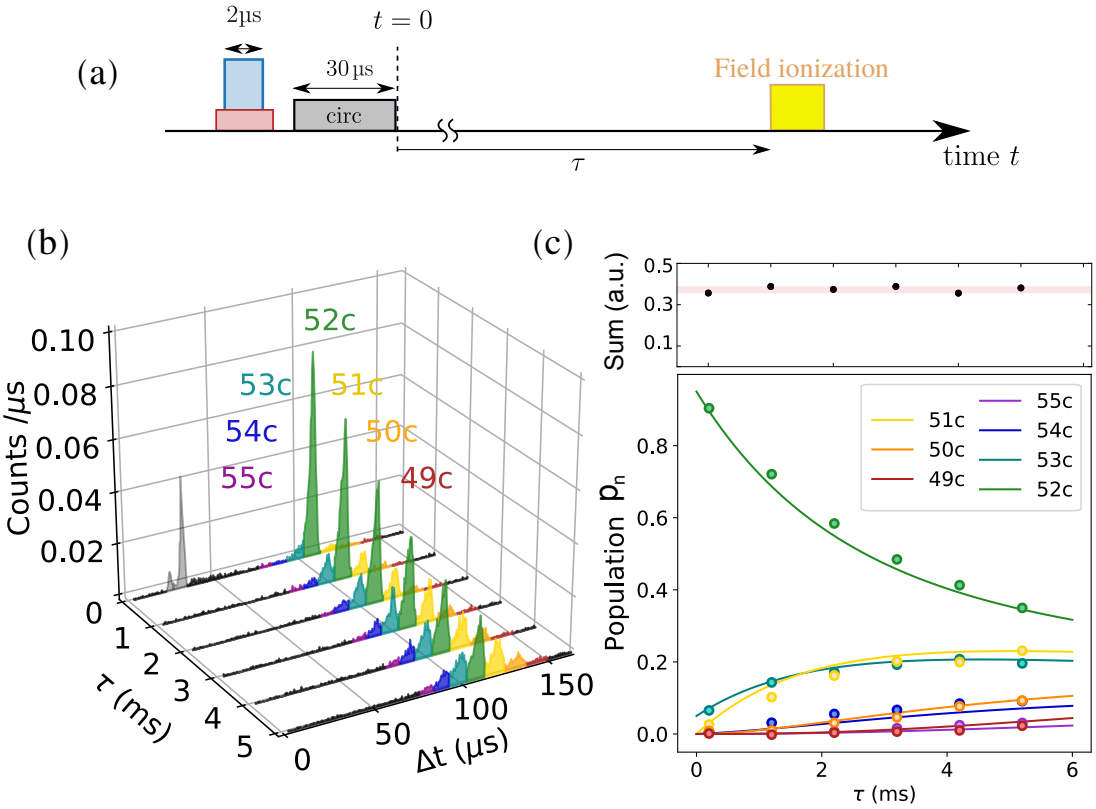

FIGURE IV.2 Atoms prepared in $|52c\rangle$ redistribute into the neighboring circular states. In (a), we show the timing of the experimental sequence. In (b), we show the measured field ionization signal for different delay times τ. In (c), the dots represent the measured circular level population as a function of time. The solid lines are a fit using a rate equation model where the temperature is the only fit parameter. The temperature is measured to be $T = (11 \pm 2)$ K.

IV.1.3 Data analysis

In free space, and at non-zero temperature, atoms prepared in cRy states have only a few relevant loss channels. The jumps towards the neighboring cRy states are the dominant ones (see eq.(I.6), Figure II.6 and II.9). For circular states with $n \sim 50$, the ratio of the dominant absorption rate (σ^+ : $|nc\rangle \rightarrow |(n+1)c\rangle$) and the next leading one ($\pi \uparrow$: $|nc\rangle \rightarrow |(n+1)e\rangle$) is $\Gamma_{n\sigma}/\Gamma_{n\pi} \sim 50$ and scales like $n^{-1/2}$ (see Chapter II). Thus, in a time span which is much smaller than a few tens of lifetimes, the population evolution is confined to the circular ladder.

We will model the population diffusion seen in Figure IV.2 (c) by an incoherent rate equation. The rates involved will be the free space decay rates $\Gamma_{i\rightarrow f} = \Gamma(i, f, T)$ defined in Chapter II (see eq.(II.14)) and the only free parameter is the electromagnetic temperature T entering the equation via Planck's black-body law $n_{th}(\omega_{if}, T)$. In doing so, we also make the assumption that all modes are equally thermalized. At $\tau = 0$ the only populated circular state is $n = 52$.

The rate equation that we consider reads

$$\begin{aligned}\dot{p}_n(\tau) = \Gamma(n+1,n,T)\; p_{n+1}(\tau) + \Gamma(n-1,n,T)\; p_{n-1}(\tau) + \\ - \left(\Gamma(n,n-1,T) + \Gamma(n,n+1,T)\right) p_n(\tau),\end{aligned} \tag{IV.1}$$

where p_n is the population of state $|nc\rangle$. This equation reproduces a one-dimensional inhomogeneous random walk in the circular state ladder. In Figure IV.3, a sketch of the jumps of the atoms is shown.

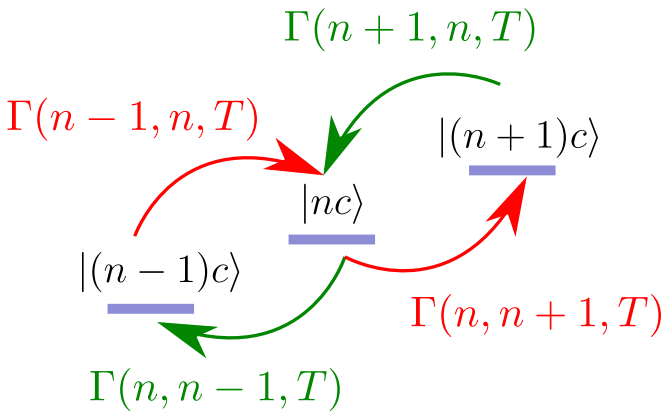

FIGURE IV.3 Population is lost from state $|nc\rangle$ after jumping towards the neighboring circular states.

Some modifications to this simple model are made to account for known imperfections in the experiment. Due to the asymmetric shape of the ionization spectrum (see Figure III.23), we include a 5% leakage of population in the model from state $|nc\rangle$ into the detection window of state $|(n+1)c\rangle$. Also, we note that the purity of the cRy levels used for these measurements was $\sim 80\%$ and close neighboring elliptical levels spuriously prepared by the circularization imperfections thus participate in the population evolution. The population in those elliptical levels ($m_l \lesssim l$) does not modify the simple model since those elliptical levels have similar decay rates to that of the circular level with the same n. In Table IV.1, we show the dipole elements involved in the population evolution. We thus treat, in this context, elliptical levels as if they were circular levels with the same n.

The set of coupled equations defined by $49 \leq n \leq 55$ is solved numerically. The cut-off in n is justified by the fact that the population in $|49c\rangle$ and in $|55c\rangle$ states are measured to be $p_{49},\ p_{55} \ll 1$ at all times. The fit in Figure IV.2 (c) (solid lines) is done by iterating over the temperature and minimizing the mean square distance to the data. The fit is in good agreement with the experimental data and yields a black-body temperature of $T = (11 \pm 0.4)$ K. The remarkable observation of (3.7 ± 0.1) ms lifetime for the circular states is due to the efficient thermalization of the radiation inside the cryostat. Previous experiments in this setup measured black-body temperatures close to 40 K in low-l Rydberg experiments [139]. At 40 K, $n = 52$ cRy atoms barely live one millisecond. One can estimate the black-body temperature in the new setup as an average of 4 K and 300 K, while using, as weights, the areas of the cold radar

Transition	Type	d_{if}^2/a_0^2
$\|50c\rangle \leftrightarrow \|49c\rangle$	σ^+	2.91×10^6
$\|50c\rangle \leftrightarrow \|51c\rangle$	σ^+	3.15×10^6
$\|50c\rangle \leftrightarrow \|51e\rangle$	π	63×10^3
$\|50e\rangle \leftrightarrow \|49e\rangle$	σ^+	2.79×10^6
$\|50e\rangle \leftrightarrow \|51e\rangle$	σ^+	3.03×10^6
$\|50e\rangle \leftrightarrow \|51ee\rangle$	π	61×10^3
$\|50e\rangle \leftrightarrow \|49c\rangle$	π	59×10^3

TABLE IV.1 Square of dipole elements between high-l Rydberg levels. Circular and close lying elliptical levels ($m_l \lesssim l$) have similar decay rates.

absorbing material (355 cm^2) and of the irises (15 cm^2) connecting the experiment to the room temperature environment. The average is computed to be 17 K, in qualitative agreement with our measurement.

Our observations are compatible with the rates calculated in free space for the relevant transition, where frequencies are in the range of 40 to 60 GHz.[1] We nonetheless remark that a modification to the free space density of modes due to the surrounding electrodes may affect the validity of the free space assumption. The main consequence of this effect is the modification of the transition rates $\Gamma_{i\to f}$ and, thus, a bias is introduced in our temperature measurement. Taking the modification in the mode density caused by the closest electrode (the MOT-mirror, $z \sim 3$ mm away from the atomic sample) as representative of the effect of all the electrodes together, we can compute a bound for the rate modification. We model the surface of the MOT-mirror as an infinite ideal mirror and analytically compute the associated loss rate modifications for the cRy population. The analytic expression is simply obtained by taking $L \to \infty$ in equation eq.(II.12). The resulting multiplicative factors for each polarization are

$$\begin{aligned} C_\sigma &= \frac{3}{2}\left\{\frac{2}{3} - \frac{\sin 2kz}{2kz} - \frac{\cos 2kz}{(2kz)^2} + \frac{\sin 2kz}{(2kz)^3}\right\}, \\ C_\pi &= 3\left\{\frac{1}{3} - \frac{\cos 2kz}{(2kz)^2} + \frac{\sin 2kz}{(2kz)^3}\right\} < 2, \end{aligned} \tag{IV.2}$$

where $k = 2\pi\nu_n/c$. We show in Figure IV.4 the analytic decay rate modification (C_σ) for the involved circular to circular transition frequencies. The dashed line is the free space value. Note that π transitions, having couplings tens of times weaker than the σ^+ transitions (see Table IV.1), remain negligible even if their loss rates are enhanced, since we note that $C_\pi < 2$. We see a modification of, at most, $\pm 20\%$ (at $z \sim 3$ mm) in the loss rates. Taking this magnitude ($\pm 20\%$) as an upper bound for the modification of all transitions, we find a satisfactory fit to the data with $T = (11 \pm 2)$ K.

We note that this measurement approach could allow us to measure *in situ* the absolute temperature of the black-body radiation. This could be an important tool for

[1] Since state $|52c\rangle$ is the initial state, we are most sensitive to the mean number of photons inducing transitions towards $|51c\rangle$ and $|53c\rangle$.

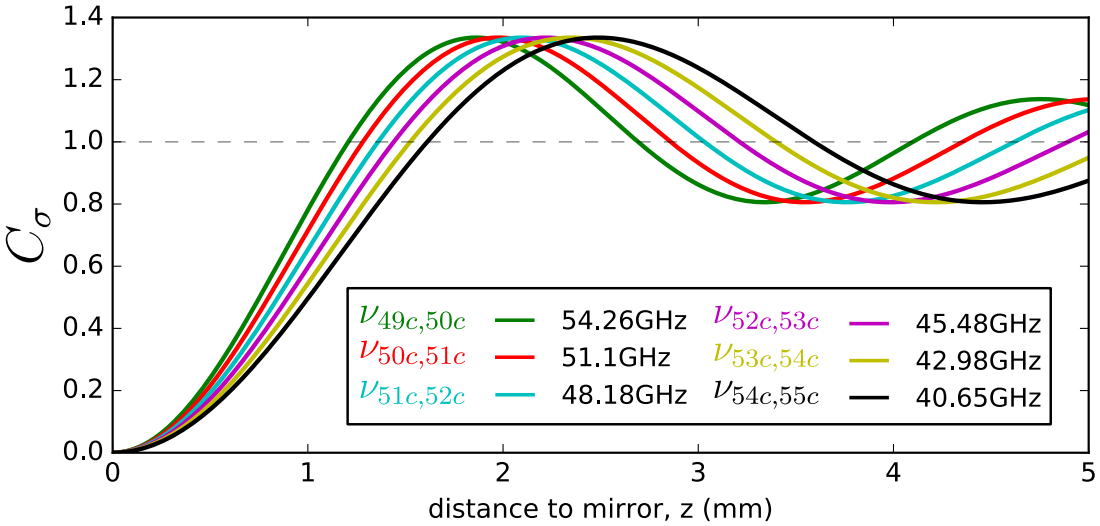

FIGURE IV.4 Inhibition factor affecting the free space MW transition decay rates of Rydberg atoms. The analytic calculation corresponds to an infinite and perfectly conducting mirror. The dashed line is the free space value.

metrology, particularly in the field of atomic clocks, in which the black-body radiation-induced shifts significantly contribute to the uncertainty budget [196, 197].

The long lifetime of the cRy atoms is a technological asset that could provide enhanced sensitivity to cRy-based sensors [106, 107] and the grounds to build a quantum simulator capable of studying 'slow' dynamics relevant to many-body physics. Moreover, the fact that the lifetime of the cRy states is related to the black-body temperature in such a simple manner can be regarded as a direct measurement of the photon number distribution at the level of the atoms. In our present setup, assuming a mean photon number distribution given by a single free parameter T suffices.

IV.2 Dephasing (T_2^* and T_2)

In this section we study the coherence of the circular state superposition and the limitations that need to be surpassed in order improve our experimental conditions. On the basis of the quantum simulator proposal developed in Chapter II, we take states $|50c\rangle$ and $|52c\rangle$ as a qubit basis. We measure the reversible and irreversible single qubit coherence times to be $T_2^* \sim 35$ µs and $T_2 \sim 270$ µs after a spin-echo sequence. Here, we discuss how we dealt with the frequency shifts (either from Stark or Zeeman drifts) during the data acquisition. They remain the limiting factor for our atomic coherence.

On the one hand, the circular to circular qubit line has a linear sensitivity to the magnetic field. This implies an associated linewidth of $2\mu_B \delta B$, where μ_B is the Bohr magneton and δB is the magnetic field fluctuation. On the other hand, the qubit line also has a quadratic sensitivity to the electric field. To estimate the electric field contribution to the coherence of the circular state superposition, we consider the electric field in the experiment to be expressed as $F = F^{(0)} + \delta F$, where the electric field varies around a mean field $F^{(0)}$, an amount δF due to either a temporal electric field noise or because of static electric field gradients over the atomic cloud. The contribution to

the qubit transition linewidth is then estimated as 534.89 kHz/(V/cm)$^2 \times 2|F^{(0)}||\delta F|$, where the numerical value is the differential quadratic shift between the qubit states.

The transition from the MOT to the molasses involves a rapid switch-off of the magnetic fields right before the Rydberg atom preparation. The associated electromotive force creates eddy currents in the electrodes. The dissipation of these eddy currents produces a time dependent Zeeman shift of the $|52c\rangle \rightarrow |50c\rangle$ two-photon transition that one must avoid. In this section we first report on the measurement of the characteristic timescale of this magnetic field drift in our experiment. Next, we discuss the electric field contribution to the qubit coherence and we evaluate it to be small. We then show the measurements of the coherence time of our qubit superposition and, by the end of the chapter, a simple model for the dephasing is introduced to analyze the data.

IV.2.1 Magnetic field drift measurement

The biggest current loops in our experiment are those created in the copper Helium screen surrounding the core of the experiment. However, a layer of superconducting Lead covers the inner part of the screen and it is supposed to prevent the MOT magnetic field from leaking out. We have found that, due to bad thermalization of the shield, the screening was not perfect. Holding a magnetic Hall probe close to the external vacuum chamber, we were able to measure a strong magnetic field variation due to the MOT-molasses cycle ($\Delta B \sim 150$ mG). This was solved by pumping on the Helium-4 reservoir to ensure the superconducting state of the shield. By reducing the temperature of the Helium bath from 4.2 K to 3.6 K, the screening factor was seen to increase by a factor of 100.

To measure the magnetic field inside the experimental chamber, we measure the transition frequency of the $|52c\rangle \rightarrow |50c\rangle$ line as a function of the time delay T after the magnetic field ramp triggered at the end of the MOT stage (see Figure III.4). We show the timing of the experimental sequence used in Figure IV.5 (a). We perform circular to circular MW spectroscopy using 200 µs long MW pulses. The Fourier limit for the frequency determination is 800 Hz. They are applied 65 µs after circularization (see Figure III.20) and the electric field is $F^{(0)} \sim 1.5$ V/cm. For each value of the delay T, the transfer rate is calculated by averaging the data corresponding to Rydberg atom samples detected in a time window width of 50 ms (open blue dots) or 25 ms (solid blue dots). In this way we are able to get information about the magnetic field variation at these time scales.

For each time delay T, the frequency of the MW pulse is scanned and a Gaussian fit of the resonance line determines the line center. Figure IV.5 (b) presents the variation of the measured transition frequency as a function of T. The data is fitted by an exponential having a decay time of 54 ms (solid blue line). After a delay of 250 ms we analyze the data by subdividing it in sets of 25 ms. The inset of the Figure shows the spectroscopic lines taken for $T >$250 ms with their respective Gaussian fits. We find that, for all the lines in Figure IV.5, the $\sim 2 \times 49.638985$ GHz two-photon transition frequency has stabilized to $< 2 \times 0.5$ kHz up to the fit precision. This is negligible with respect to the linewidth.

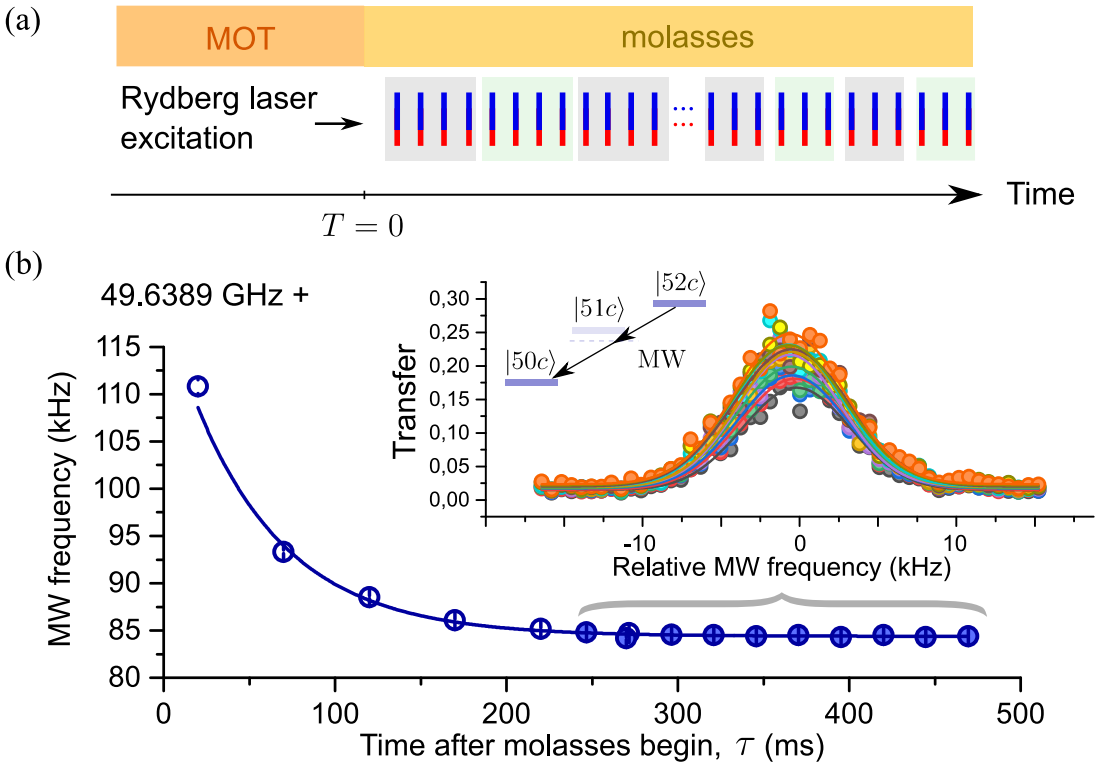

FIGURE IV.5 In (a), we show the data acquisition timing for the measurement of the magnetic field drift measurements. In (b), we show the stabilization of the line center. After 250 ms the line is stable well below its linewidth. The frequency axis corresponds to the MW drive. In the inset we show the MW two-photon lines.

The Gaussian line width (standard deviation, $\sigma_E/h = 2 \times \sigma_{cc}$) of the two-level energy is (7.0 $\pm$ 0.2) kHz, where σ_{cc}^2 is the fitted Gaussian variance of the circular to circular spectroscopy and the factor 2 comes from the fact that it is a two-photon transition. This is compatible with a current noise of $\sim (0.16 \pm 0.2)$ mA in the MOT magnetic coils producing a magnetic field noise with standard deviation $\sigma_B \sim 2.5$ mG. In Figure IV.6 we show a single $|52c\rangle \rightarrow |50c\rangle$ narrow line. The linewidth is fitted to be $\sigma_E/h = 2 \times \sigma_{cc} = (7.13 \pm 0.13)$ kHz. The data collection starts 250 ms after the switching MOT-molasses transition and it is integrated during 250 ms. The electric field is of $F^{(0)} \sim 1.5$ V/cm.

IV.2.2 Electric field drift

Short timescale drift

The manipulation of cRy states requires a fast dynamical control of the electric field (1-100 µs). The bandwidth for the manipulation of the electric fields is limited to the timescales imposed by the parasitic inductance and capacitance present in the voltage control lines. Charging of the electrodes due to proximity effects can also limit the timescale at which one can control the electric fields in the experiment. To study the electrode charging and discharging times in our experiment, we perform MW spectroscopy on the $|52c\rangle \rightarrow |53e^-\rangle$ (see Figure I.2 and Chapter II for level diagram)

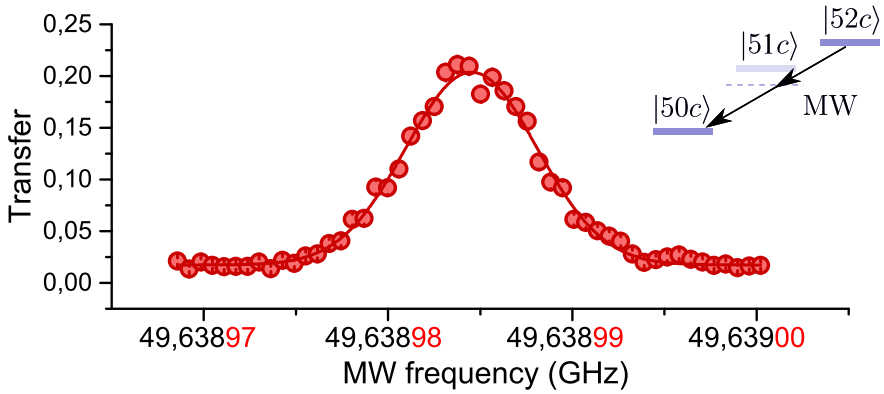

FIGURE IV.6 Narrow circular to circular line. The one-photon standard deviation is fitted to be $\sigma_{cc} = (3.57 \pm 0.07)$ kHz. Assuming the broadening is only of magnetic origin, the linewidth corresponds to ∼2.5 mG spread in the magnetic field.

transition which is extremely sensitive to the electric field (~ -101.7 MHz/(V/cm)) and has no first order magnetic field dependence ($\Delta m_l = 0$).

After circularization, the field is switched to a lower value to perform spectroscopy. We now measure the time needed for electric field stabilization after this change. Being able to pinpoint the center of the line to a few kHz gives us a way to precisely measure the electric fields at the level of the atoms. In Figure IV.7 (a), we show the experimental sequence used for this calibration. In Figure IV.7 (b), we show the circular-elliptical line for different waiting times after the adiabatic circularization field ramp. The mean value of the electric field is $F^{(0)} \sim 1.475$ V/cm and the circular to elliptical MW pulses are 10 µs long. In Figure IV.7 (c), we plot the line center (blue dots) and the linewidth (red dots) as a function of the delay τ' after circularization.

The observed mean Stark shift first decays by 300 kHz between 40 and 90 µs, corresponding to a field variation of 3 mV/cm. The field then stabilizes with a residual drift of 0.7 mV/cm in 200 µs, which is the duration of MW pulses used to characterize the magnetic field above. The width of the $|52c\rangle \rightarrow |53e^-\rangle$ is measured here to be $\sim$ 130 kHz to the experimental precision and corresponds to electric field fluctuation of $\delta F \sim$1.3 mV/cm on the 10 µs timescale.

In the search for optimal operation conditions during our coherence measurements, we now turn to study the long term drifts of the electric field. In the following section we discuss the electric field stability at the timescale of the data averaging (1-100 ms).

Long timescale drift

A few hundred successive Rydberg electric field sequences like the one in Figure IV.7 (a) are needed to gather statistics. They are played consecutively during the molasses stage (see Figure III.4 and IV.5 (a)). If the sequence is not repeated in an identical manner each time, effective decoherence may degrade the measurements. Due to electrodes charging, the first few sequences are not identical to the rest and they need to be discarded. This is done by blocking the excitation laser and triggering many Rydberg sequences before finally unblocking them. We refer to those electric field sequences as 'Fake' sequences. Since 250 ms are needed to stabilize the magnetic field of the

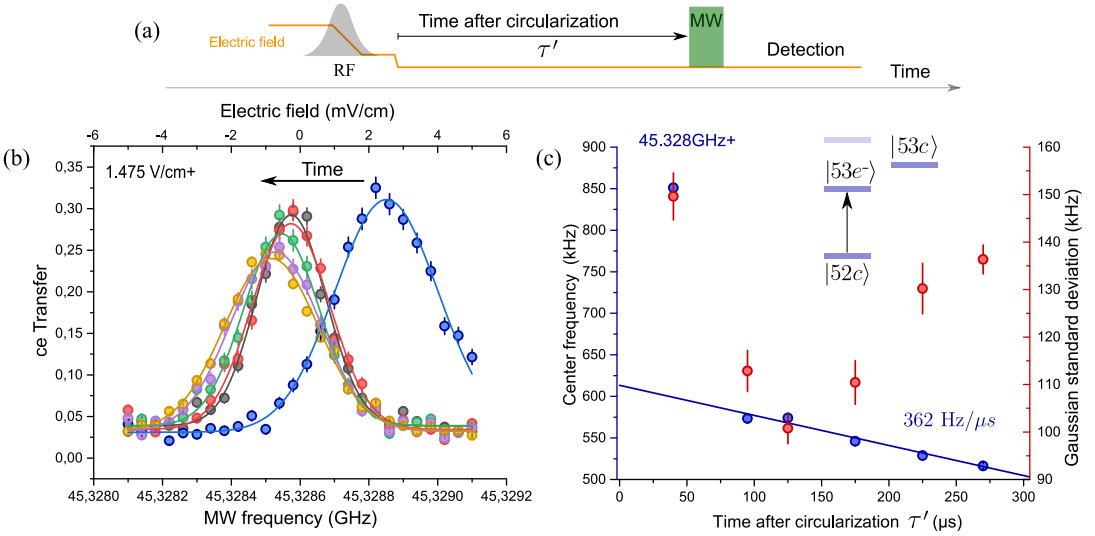

FIGURE IV.7 In (a), the time sequence for the electric field stability measurement is shown. In (b), we show the circular elliptical spectroscopy for different time delays after circularization. The lines are Gaussian fits. In (c), we show the fit parameters, center (blue dots), and width (red dots) of the lines as a function of the MW pulse delay with respect to the circularziation field ramp. After the circularization electric ramp, the electric field drifts due to charge effects. Without taking into account the first of the blue dots, we fit a linear function to the time dependence of the line center.

experiment we use this time to trigger Fake electric field sequences before the data collection. We now check that this duration is long enough so that the electric field is stable. In Figure IV.8 (a), we show the timing of the sequence where Rydberg electric sequences (duration 750 µs) are triggered during 250 ms before the laser excitation starts. The mean electric field was $F^{(0)} \sim 1.47$ V/cm, while the MW pulse was 10 µs long and they were applied 50 µs after the adiabatic circularization electric field ramp (see Figure IV.7).

Blocking the excitation laser during the first 250 ms, we gather statistics during the following 230 ms. We subdivide the data into smaller sets to confirm the electric field stabilization. The procedure consists of averaging over 23 ms of the collected spectroscopic data and then plotting the results as a function of the central time for each data set (see shaded areas in Figure IV.8). The spectroscopy and the result of Gaussian fits are shown in Figure IV.8 (b) and (c) respectively. The Gaussian standard deviation of the MW $|52c\rangle \rightarrow |53e^-\rangle$ line is constant to the experimental precision and it is fitted to be (132±4) kHz. We plot the fitted standard deviation in (c) (red dots). The center frequency of the MW line is also seen to be constant up to the experimental precision (±5 kHz). We plot the fitted center (blue dots) as a function of time in (c).

By triggering Fake Rydberg electric sequences during the magnetic field relaxation, the electric field in the experiment stabilizes. We find that 230 Fake sequences are enough to stabilize the electric field. We keep this number fixed independently from the duration of the Rydberg sequence. The duration of the ensemble of the Fake sequences is also changed accordingly. Note that, since the ground state atoms are impervious to the electric field, one can start the Fake sequences before the end of the

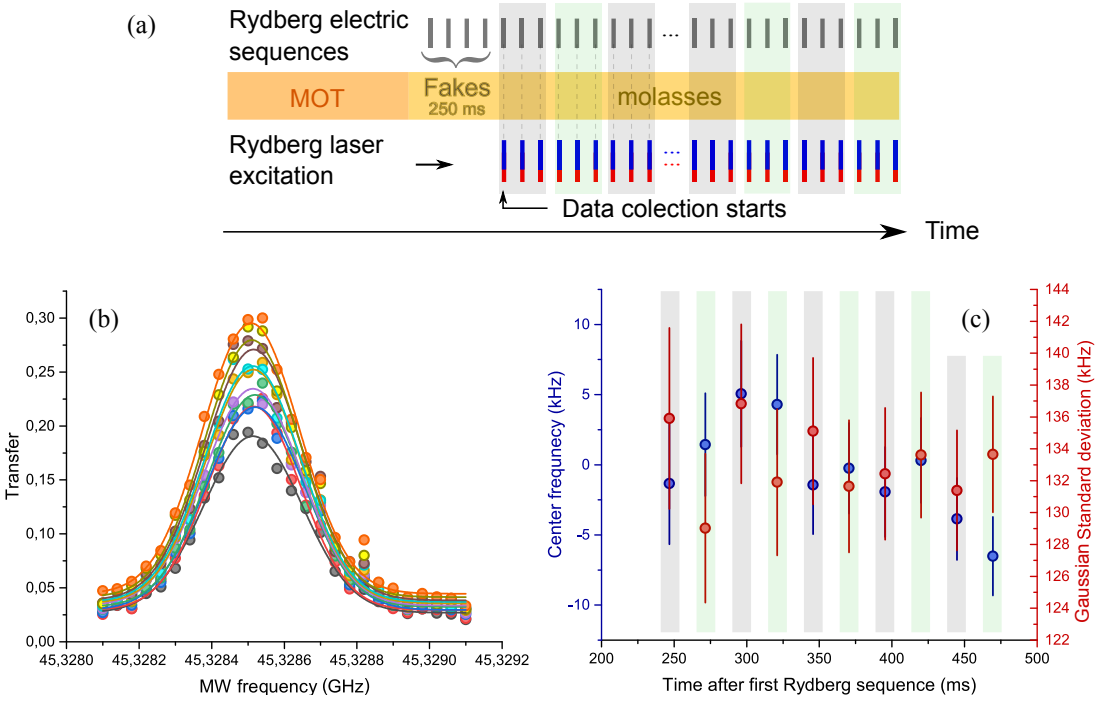

FIGURE IV.8 (a) Timing of the sequence. The short bars represent Rydberg sequences. We have depicted the electrical sequences (short black bars) and the laser excitation pulses (short red and blue bars) separately. (b) Circular-elliptical line taken after 250 ms of Fakes. The frequency offset in (b) is 45.328 GHz. In (b) and (c) we show the stability of the electric field after 250 ms of Rydberg electric sequences before starting the Rydberg laser excitation. In (e) the frequency offset is 45.328515 GHz.

MOT if needed.

As a final calibration, we measure the electric field gradients in our setup. Static (DC) electric field gradients may contribute to the linewidth of the $|52c\rangle \rightarrow |53e^-\rangle$ transition frequency. Ultimately, they will manifest as effective (reversible) decoherence in the data averaging. We now turn to discuss how one can measure and optimize the spatial variation of the electric field in our experiment.

Gradients

We turn to the task of studying the spatial electric field dependence. For this purpose we move the excitation lasers to displace the excitation volume. This volume is determined by the overlap of the blue and red excitation beams and it has a cigar-shape with a typical dimension along the x, y, and z directions of (200 µm×20 µm×20 µm). We then perform laser spectroscopy on the ground-Rydberg ($|52D_{5/2}, m_j = 5/2\rangle$) line to measure the static electric field gradients over the atom cloud. The position of the laser beams is tracked by measuring their position in a CCD camera.

In Figure IV.9 (a), (b), and (c), we show the laser displacement we perform in order to displace the excitation volume in the x, y, and z directions respectively. The yellow pad represents the surface of the MOT-mirror. The red circle represents the front view of the red excitation laser on the mirror plane and the blue taper represents the focused

blue excitation laser.

We first cancel the electric field gradients at the field of the Rydberg laser line ($F \sim 0.3$ V/cm). The blue dots in Figure IV.9 (d) represent the mean electric field seen by the atom cloud at different positions along the y direction, previous to the gradient optimization. The slope of the linear fit gives the gradient in that direction and it is measured to be $\partial_y F = (900 \pm 10)$ mV/cm^2.

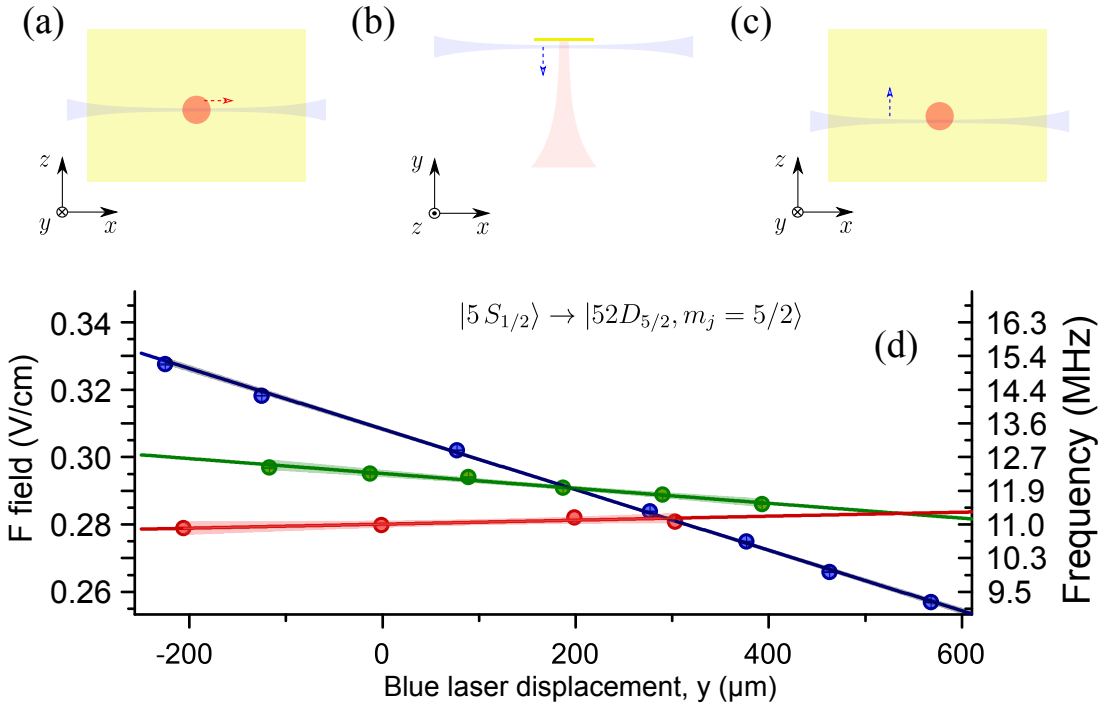

FIGURE IV.9 Measurement sequence for the electric field as a function of the laser displacement of the Rydberg cloud. In (a), (b), and (c), we show the laser beam displacements performed to measure the electric field as a function of position. By changing the electrodes' voltages, one can change the gradients in the experiment. In (d), we show the gradients in the y direction, before and after compensation.

The reduction of electric field gradients is made possible by the presence of the rod RF electrodes (see Figure III.9). In Figure IV.10, we show a front view of the Stark electrode and of the four circularization rod electrodes. The four electrodes give us four degrees of freedom to tune the electric field in the experiment. The degrees of freedom can be the individual V_i voltages with $i \in \{1, 2, 3, 4\}$ or any other linear combination of them. We prefer to work with the transformation given by

$$\begin{pmatrix} V_x \\ V_y \\ V_z \\ V_+ \end{pmatrix} = \begin{pmatrix} 1 & -1 & 1 & -1 \\ 1 & 1 & 1 & 1 \\ 1 & 1 & -1 & -1 \\ -1 & 1 & 1 & -1 \end{pmatrix} \begin{pmatrix} V_1 \\ V_2 \\ V_3 \\ V_4 \end{pmatrix}, \tag{IV.3}$$

since it defines new voltages with a simple physical interpretation. On this basis we have access to four parameters that essentially tune the electric field in the three spatial directions (V_x, V_y, and V_z) and still allow the tuning of a quadrupolar term of the field

(V_+) as depicted in Figure IV.10. In Figure IV.10, we show the configuration, colored in red, where the rod electrodes are held to a positive voltage and, in blue, where they are held to the opposite voltage value. The black arrows show the main component of the electric field created by each configuration.

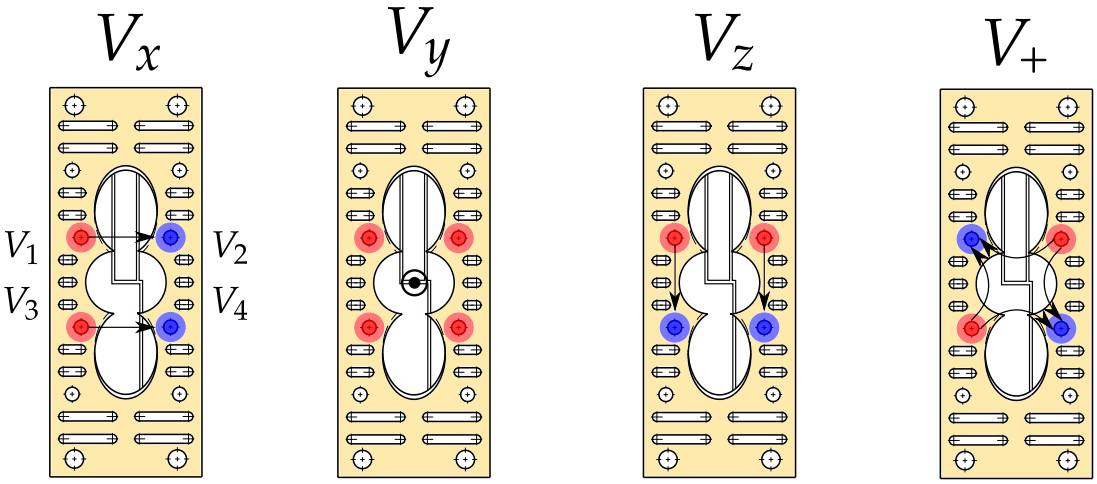

FIGURE IV.10 The rod electrodes permit a directional gradient at the level of the atoms. Red symbolizes a positive voltage and blue symbolizes a negative voltage. The black arrows show the electric field produced by different configuration of voltages.

Iterating over these values and the Stark electrode (orange in Figure IV.10) voltage allows us to improve the electric field homogeneity for a fixed average electric field. The green dots in Figure IV.9 show an intermediate step in the iteration. The optimization converges to $F_y^{(0)} = (280 \pm 6)$ mV/cm (red dots in Figure IV.9) over a half a millimeter. The gradients in the three directions are measured to be, after optimization, $\partial_x F \sim 170$ mV/cm^2, $\partial_y F \sim 80$ mV/cm^2 and $\partial_z F \sim 100$ mV/cm^2.

We observe a degraded purity of the cRy states at ~ 0.3 V/cm with respect to that found in higher directing electric fields. The observation is attributed to Rydberg-Rydberg interactions occurring at high excitation rates (see Chapter III). Note that high directing electric fields preserve the purity of the circular states even at moderate excitation rates, but a too high electric field would limit the coherence of the superposition. We decide to work in an electric field of ~ 0.46 V/cm as a compromise (Stark electrode voltage set to V_S=2.00 V, purity $> 80\%$).

We note that MW measurements of transitions frequencies provides more reliable information on the gradients than our laser line, which is broaden due to our laser linewidth. We thus directly optimize, in place (for a fixed position of the excitation lasers), the width of the $|52c\rangle \rightarrow |53e^-\rangle$ line to minimize the gradients at $F^{(0)} \sim 0.46$ V/cm. The MW pulse duration is 10 µs and was applied 50 µs after the circularization pulse as above. We present the result in Figure IV.11. The data coloured in red corresponds to the circular-elliptical line before re-optimization of the gradients at $F^{(0)} \sim 0.46$ V/cm. The blue dots, correspond to the optimization. The improvements achieved by the control of the rod electrodes voltages have reduced the standard deviation of the circular-elliptical line to $\sigma_{ce} = (72 \pm 4)$ kHz. The associated electric field variation is $\delta F \sim 0.7$ mV/cm. The observed residual shift of the resonance

frequency ($\sim$ 700 kHz) is due to a 7 mV/cm shift in the mean field due to the optimization procedure. The final electrode configuration for the rod electrodes is found to be $V_1 = 3.271$ V, $V_2 = 2.181$ V, $V_3 = 2.728$ V, and $V_4 = 1.818$ V.

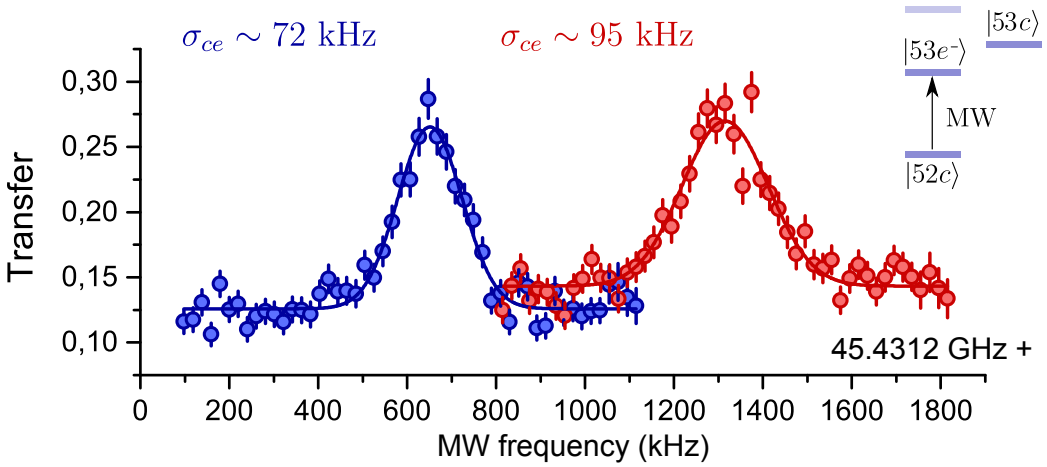

FIGURE IV.11 Optimization of the circular elliptical linewidth ($|52c\rangle \rightarrow |53e\rangle$). The solid lines are Gaussian fits. The standard deviation of the line was reduced from 95 kHz to 72 kHz by optimizing the electric field gradients. The mean electric field is $F^{(0)} \sim 0.46$ V/cm.

The electric field fluctuation causing the finite width of the circular-elliptical line is $\delta F = \sigma_{ce}/101.7$ MHz/(V/cm)$\sim$ 0.7 mV/cm. The electric field variation measurement bounds the reversible coherence to 4.7 ms, which is beyond the lifetime of the qubit state in our cryostat.

IV.2.3 Ramsey interferometry

In this section, we will discuss the measurement of the qubit decoherence times for the superposition of the $|52c\rangle$ and $|50c\rangle$ states. The working electric field was chosen to be $F^{(0)} \sim 0.46$ V/cm. To ensure an optimal working condition, the Helium-4 reservoir was pumped (temperature of 3.6 K) during the coherence experiments and 230 Fake Rydberg electric field sequences are played (with a duration of 1050 µs each) before data collection. Also, a 50 µs delay is introduced after circularization to operate the MW pulses controlling the qubit in optimal field conditions.

To quantify the coherence time, we measure the damping of a Ramsey signal in a superposition of the $|52c\rangle$ and $|50c\rangle$ states: The initial state $|52c\rangle$ is rotated by a first $\pi/2$ 'Ramsey' pulse (R1) and then measured by ionization after a second $\pi/2$ Ramsey pulse (R2). Both MW pulses are in phase. The R1 pulse prepares the superposition. After free evolution, the R2 pulse mixes the two-states again and the state is detected, by field ionization, in the $\{|52c\rangle, |50c\rangle\}$ basis. By operating the Ramsey pulses detuned by an amount $\Delta_0 = 2\nu_{MW} - (E_{52c} - E_{50c})/h$ from the atomic transition resonance we witness oscillations of the transfer from $|52c\rangle$ to $|50c\rangle$ as a function of the time delay between the two Ramsey pulses ($\tau_{1,2}$). To efficiently fit the data, we make the detuning big enough so that many oscillations can be seen before the damping time has elapsed ($\Delta_0 > 1/T_2^*$), but small enough with respect to the Fourier limited width of the hard pulses ($\gtrsim 1$ µs) used to prepare the state.

Rabi oscillation

The preparation and detection of the superposition relies on the efficiency of the Ramsey pulses one is able to perform. The coherent MW manipulation is performed by submitting the atoms to a MW field for a given amount of time during which they perform a Rabi oscillation. Setting the time of the driven evolution, one can rotate the state in the Bloch sphere by an arbitrary angle.

In Figure IV.12 we show a Rabi oscillation used to prepare the atomic superposition used for the coherence experiments. The blue dots correspond to a Rabi oscillation driven at resonance and the red dots correspond to a drive detuned by $\Delta_0 \sim 2\pi \times 60$ kHz. For the detuning Δ_0, the π and $\pi/2$ pulses correspond to the durations of $\Delta t_\pi = 3.2$ µs and $\Delta t_{\pi/2} = 1.8$ µs respectively. The finite transfer efficiency is explained by a finite purity of the $|52c\rangle$ state preparation ($\sim 80\%$).

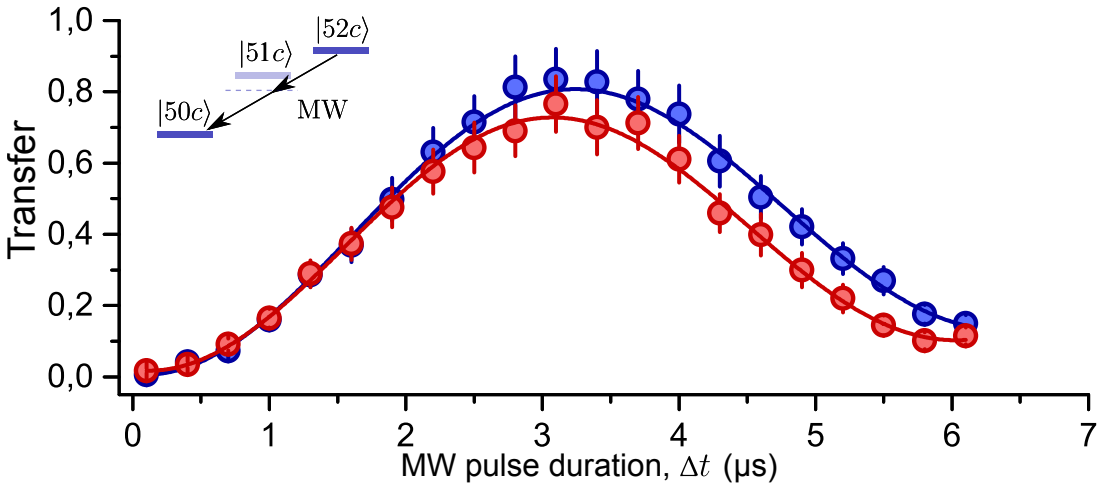

FIGURE IV.12 The first cycle of a Rabi oscillation. In blue, we show a resonant MW drive. For the red dots, the driving is detuned by $\Delta_0 \sim 2\pi \times 60$ kHz.

Ramsey fringes

To measure the Ramsey coherence time T_2^*, we scan the time in between the first Ramsey pulse and the second Ramsey pulse ($\tau_{1,2}$), and measure the transfer probability from state $|52c\rangle$ to $|50c\rangle$ as a function of $\tau_{1,2}$. We show the experimental result in Figure IV.13 and, in the inset of the Figure, we show a scheme of the sequence. The first Ramsey pulse is performed 50 µs after circularization.

The transfer data from $|52c\rangle$ to $|50c\rangle$ is fitted by a sine with a Gaussian envelope as

$$T_{52c-50c}\,(\tau_{1,2}) = Ae^{-\frac{1}{2}[\tau_{1,2}/T_2^*]^2}\sin(\Delta_0\tau_{1,2}+\theta)+c \qquad \text{(IV.4)}$$

The fit yields an oscillation frequency $\Delta_0 = 2\pi \times (59 \pm 0.2)$ kHz and a T_2^* time of (45 ± 7) µs ($A = 0.69 \pm 0.02$ and $c = 0.41 \pm 0.1$).

We remark that the Ramsey damping time and the qubit linewidth transition do not fulfill the Fourier relation for Gaussians, but instead respect the bound $\sigma_E T_2^* > \hbar$.

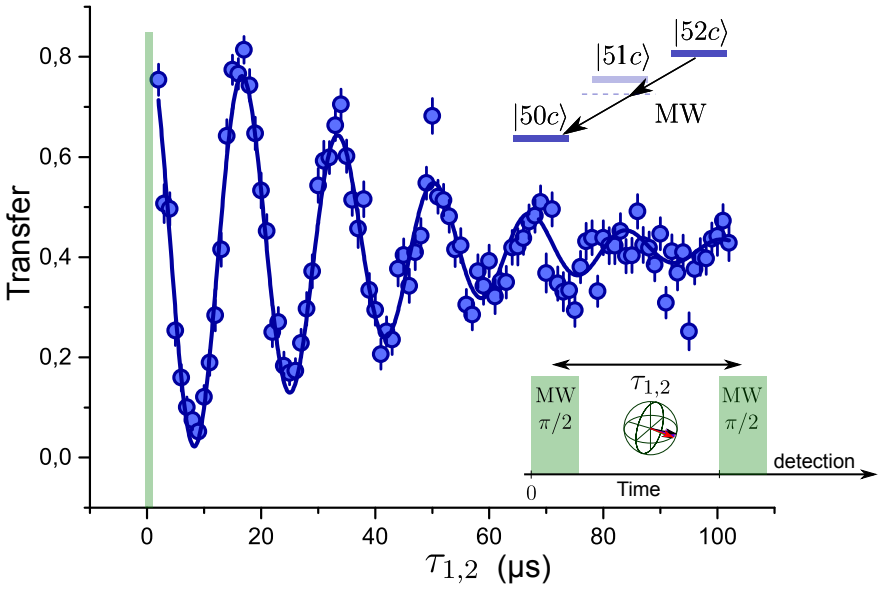

FIGURE IV.13 Ramsey oscillation for the transfer $T_{52c-50c}$ between the $|52c\rangle$ state to the $|50c\rangle$ state.

This is typical of time-dependent noise to which Rabi and Ramsey sequences have different sensitivities [198].

IV.2.4 Spin-echo

The response function of the Ramsey sequence is maximal for DC noise [199], but the spin-echo sequence is actually immune to it. Slowly varying temporal noise, as well as strictly static frequency gradients over the sample, is completely canceled by this technique. One thus expects an extended coherence time for the state superposition.

In Figure IV.14, we show an example of a echo experiment. The sequence simply consists in introducing a MW-π pulse (orange), at time t_π after the first $\pi/2$ Ramsey pulse. In this example, the π pulse is performed at $t_\pi \sim 100$ µs and the time interval in between the two Ramsey pulses ($\tau_{1,2}$) is scanned. We see that before the π pulse is applied ($\tau_{1,2} < t_\pi$), the evolution is that of the Ramsey oscillations. The Bloch sphere picture in the inset helps to understand the dephasing process. After the π pulse ($\tau_{1,2} > t_\pi$), the phases of the superposition are transformed in such a way that a 'spin-refocusing' is observed some time after. The oscillation revival product of the spin refocusing happens at time t_E, where the sub-index E stands for 'echo'. This data has a good signal to noise ratio because it has been taken with a large number of Rydberg atom excitations per laser pulse. An improved initial contrast is obtained by reducing the laser excitation power.

The reduced contrast of the echo with respect to the initial Ramsey is the signature of the dephasing, which has not been reversed by the spin-echo sequence. By measuring the maximal contrast of the echo as a function of time, we quantify the 'irreversible' decoherence[2] processes and measure the T_2 decoherence time. In Figure IV.15, we

[2]We use the word irreversible here in the context of the simple spin-echo technique. More elaborated

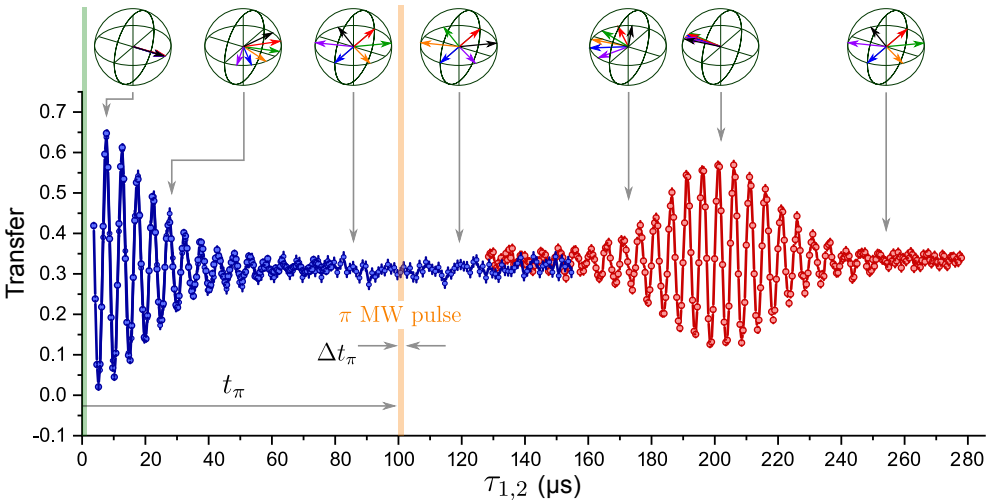

FIGURE IV.14 A spin-echo sequence. Applying a π pulse before the second Ramsey pulse produces a revival of the oscillations.

plot a few oscillations close to the center of the echo envelope for different t_π times. The data is taken at a low counting rate to avoid the initial contrast reduction due to Rydberg-Rydberg interactions. We measure the echo maximal contrast by fitting a sine with a Gaussian envelope to the oscillations. The expression used is

$$T_{52c-50c}\left(\tau_{1,2}\right) = Ae^{-\frac{1}{2}[(\tau_{1,2}-t_E)/T_2^*]^2}\sin(\Delta_0(\tau_{1,2}-t_\theta)) + c. \tag{IV.5}$$

We fit all the data using this function and sharing the parameters Δ_0, c and T_2^*. For this data, we find $\Delta_0 = 2\pi \times (57.7 \pm 0.2)$ kHz and $T_2^* = (36 \pm 2)$ μs ($c = 0.42 \pm 0.01$). The fit is in good agreement with the data.

In Figure IV.16 (a), we show the fitted Gaussian amplitude A as a function of the experimentally controlled parameter $2\times t_\pi$ (dots). In Figure IV.16 (b), we plot the fitted echo (revival) time t_E as a function of $2\times t_\pi$. The red dashed line in the (b) corresponds to the identity line. Note that, even if the effect of the spin-echo is to completely reverse the DC noise at $2 \times t_\pi$, the maximal contrast of the oscillation is measured at $t_E < 2\times t_\pi$. The reason is that the contribution of the high frequency noise permanently accumulates and the optimal phase compensation is achieved before the DC component gets to be fully reversed. This effect is intrinsic to spin-echo spectroscopy.

The solid lines in Figure IV.16 (a), and (b) correspond to a dephasing model we develop in the next section.

IV.2.5 A model for dephasing

To gain some insight into the decoherence process involved– beyond the quantitative measurement provided by the Gaussian fit– we introduce here a simple model.[3]

dynamic decoupling techniques can reverse different components of the noise spectrum [199].

[3] After developing the model to explain our experimental data we found similar theoretical work done by Klauder and Anderson [200].

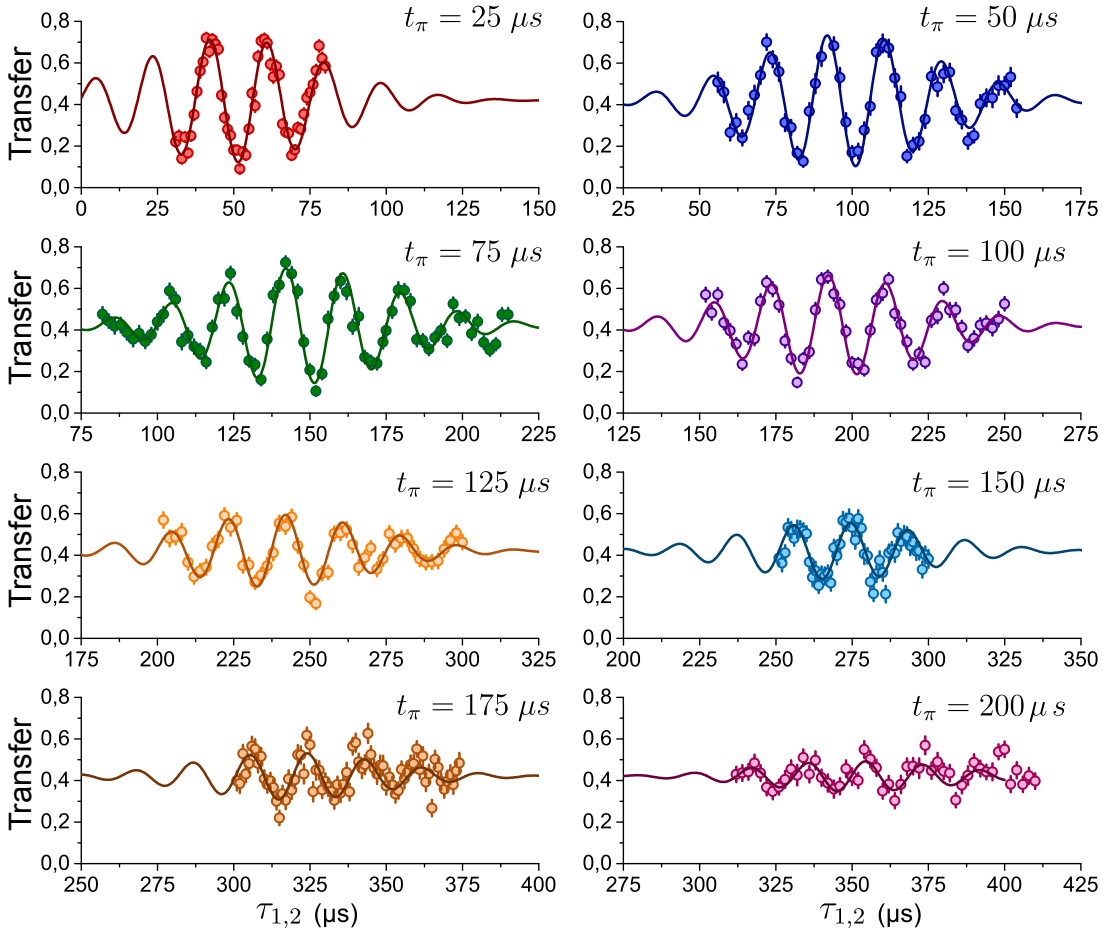

FIGURE IV.15 Spin-echo. Transfer rate from $|52c\rangle$ to $|50c\rangle$ as a function of time. The envelope of the fit is given by a sine with a Gaussian envelope.

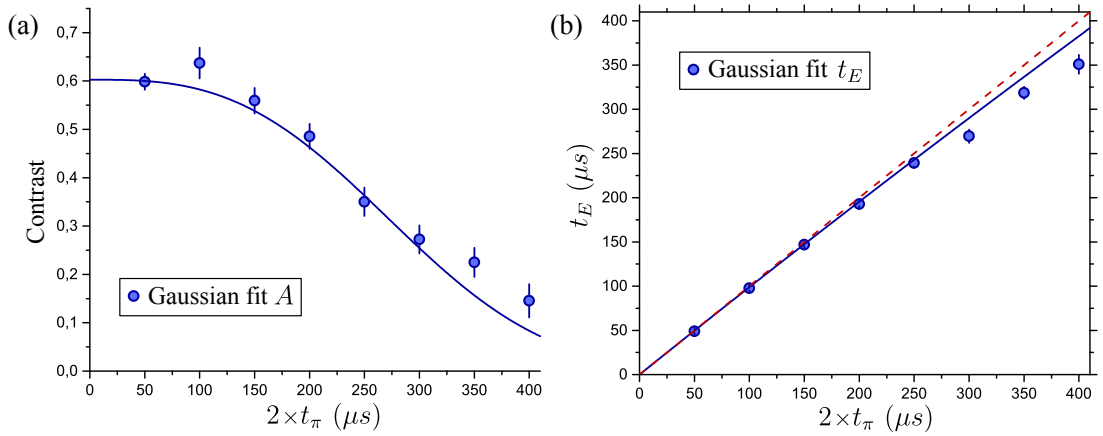

FIGURE IV.16 In (a), we plot the Gaussian amplitude A (dots) as a function of $2 \times t_\pi$. Physically, A represents the contrast of the oscillation at time t_E. Note that the measured t_E is smaller than $2 \times t_\pi$ (b).

We reproduce the dephasing in the $|52c\rangle + e^{i\varphi(t)}|50c\rangle$ superposition seen in the experiment by working out a stochastic equation for the relative phase $\varphi(t)$ as a function of time.

Ramsey oscillations

Temporal noise in the external fields can be considered as a time dependent Hamiltonian evolution. In the rotating frame at two times the MW drive frequency ($2\nu_{MW}$), the Hamiltonian reads $\hat{H}_j(t') = \hbar\omega_j(t')\,|52c\rangle\langle 52c|$, where $\omega_j(t') = -\Delta_0 + \Delta_j(t')$ is the two-level detuning as a function of time in the jth realization of the noise. To capture the essence of the dephasing, we model the noise in the experiment by a filtered white noise. We use an exponential function with a time constant τ_φ to obtain the expression

$$\Delta_j(t') = \int_{-\infty}^{t'} W_j(t'')\frac{e^{\frac{t''-t'}{\tau_\varphi}}}{\tau_\varphi}dt''.$$

Here, $W_j(t'')$ stands for a Gaussian white noise process with $\langle W_j(t'')\rangle_j = 0$, where $\langle\cdot\rangle_j$ stands for the ensemble average over the noise realizations. The white noise is determined by $\langle W_j(t_1'')W_j(t_2'')\rangle_j = D_\varphi\delta(t_1'' - t_2'')$ which is the two-point correlation function of W_j. Here $\delta(t'')$ is the Dirac distribution. By averaging the white noise using an exponential time window, we have enforced on $\Delta_j(t')$ a Lorentzian noise spectrum defined by the noise amplitude D_φ and the correlation time τ_φ.

Taking as the initial condition

$$|\psi_j(t=0)\rangle = (|52c\rangle + |50c\rangle)\sqrt{2},$$

the integration of the Schrödinger equation yields a time dependent state in the form

$$|\psi_j(t)\rangle \sim |52c\rangle + e^{-i\varphi_j(t)}|50c\rangle,$$

where the phase as a function of time is given by the frequency integral

$$\varphi_j(t) = -\Delta_0 t + \int_0^t \Delta_j(t')dt'.$$

These expressions correspond to the quantum evolution of the qubit state after a first (perfect) $\pi/2$ Ramsey pulse.

The construction leads to a Gaussian distribution for the phase random variable φ_j for all times t and, thus, its distribution is completely determined by its two first central moments. They mean value is computed to be

$$\langle\varphi_j(t)\rangle_j = -\Delta_0\, t.$$

For the sake of simplicity we will set, for now, explicitly $\Delta_0 = 0$ to substract the deterministic drift of the phase and concentrate in the stochastic process. This simpler treatment directly yields an expression for the envelope of any 'carrier' signal at the arbitrary frequency Δ_0. One can then compute the variance of the random variable to be

$$\sigma_\varphi^2(t) = \langle \varphi_j^2(t) \rangle_j = D_\varphi \left(t + \tau_\varphi (e^{-\frac{t}{\tau_\varphi}} - 1) \right).$$

Intuitively, the oscillation is damped by the time this variance is $\sigma_\varphi^2(t) \sim \pi^2$ since the phase variable is no longer well-defined. Using the Gaussian character of the phase random variable, one can readily compute the contrast as a function of time to be $C(t) = \langle \mathbb{R}e\{e^{-i\varphi_j(t)}\} \rangle_j \equiv e^{-\frac{1}{2}\sigma_\varphi^2}$. This expression provides the envelope for the Ramsey experiments. Note that the expression justifies the Gaussian fit in Figure IV.13 and in Figure IV.15 if $t \ll \tau_\varphi$. Then $\sigma_\varphi^2(t) \sim t^2 \times D_\varphi / 2\tau_\varphi$. As we will discuss next, this condition corresponds to our experimental situation.

Echo experiments

To extend this result to spin-echo experiments, we consider an infinitely short and perfect π pulse applied at time t_π. For $t > t_\pi$, the phase random variable (denoted now with a tilde) reads

$$\varphi_j(t) \to \tilde{\varphi}_j(t) = -\int_0^{t_\pi} \Delta_j(t')dt' + \pi + \int_{t_\pi}^{t} \Delta_j(t')dt'.$$

The second moment of the new Gaussian distribution can be calculated directly and the new expression for the variance is

$$\sigma_{\tilde{\varphi}}^2 / D_\varphi = t_\pi + \tau_\varphi (e^{-\frac{t_\pi}{\tau_\varphi}} - 1) + (t - t_\pi) + \tau_\varphi (e^{-\frac{t - t_\pi}{\tau_\varphi}} - 1) + \tau_\varphi [e^{\frac{t_\pi}{\tau_\varphi}} - 1][e^{\frac{-t}{\tau_\varphi}} - e^{\frac{-t_\pi}{\tau_\varphi}}].$$

Everything taken into account, the envelope for the Ramsey and the echo oscillation is directly given by

$$C(t) = \begin{cases} e^{-\frac{1}{2}\sigma_\varphi^2(t)} & \text{if} \quad t < t_\pi \quad \text{(Ramsey)} \\ \\ e^{-\frac{1}{2}\sigma_{\tilde{\varphi}}^2(t)} & \text{if} \quad t > t_\pi \quad \text{(Spin-echo).} \end{cases} \tag{IV.6}$$

To include the oscillating character (the 'carrier' signal) in a detuned reference frame, we need to consider a non zero frequency Δ_0 in the model. The calculation can be resumed in a similar manner. The expression for the transfer probabilities as a function of $\tau_{1,2}$ simply reads

$$T_{52c-50c}\,(t) = C(t) \cos(\Delta_0 (t + t_\theta)). \tag{IV.7}$$

The model now describes the data in Figure IV.13, IV.14, and IV.15. One can use eq.(IV.7), instead of eq.(IV.5), to fit the damped oscillations in Figure IV.15 if one allows for an offset c' and a global amplitude A' to take experimental imperfections into account.

The new fit is shown in Figure IV.17 and yields a noise correlation time constant of $\tau_\varphi = (2.1 \pm 0.3)$ ms and a noise amplitude of $D_\varphi = (3.8 \pm 0.8) \times 10^6$ s^{-1} (with $A' = 0.60 \pm 0.10$ and $c' = 0.420 \pm 0.002$). Since $\tau_{1,2} \ll \tau_\varphi$, the analytic expression for the Ramsey coherence time (defined as a Gaussian standard deviation) reads
$T_2^* = \sqrt{2\tau_\varphi / D_\varphi} = (34 \pm 2)$ µs.

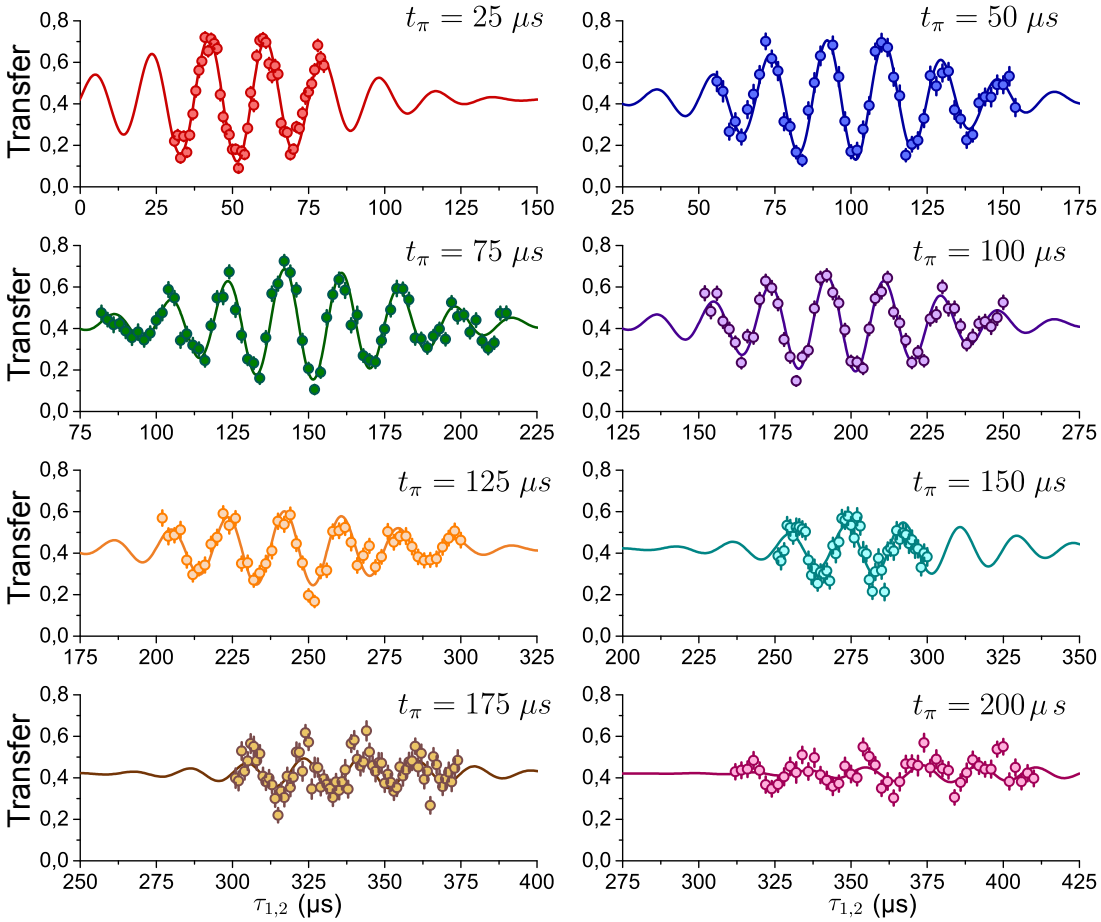

FIGURE IV.17 Spin-echo. Transfer rate from $|52c\rangle$ to $|50c\rangle$ as a function of time. The data is the same as was presented in Figure IV.15. The oscillations are now fitted by the model eq.(IV.7).

The fitted noise parameters can be translated to the width of the Lorentzian noise spectrum as $\Gamma_\varphi \equiv 1/2\pi\tau_\varphi = (75 \pm 6)$ Hz.

The noise energy dispersion can also be computed from the fit parameters to be $\sigma_E/h = \sigma_\Delta/2\pi = \sqrt{D_\varphi/2\tau_\varphi}/2\pi = (4.8 \pm 0.2)$ kHz and, assuming that the dispersion has magnetic origin only, it corresponds to a magnetic field dispersion of $\sigma_B = \sigma_\Delta/2\mu_B$ of $< (1.70 \pm 0.4)$ mG. This is compatible with a current noise of $\sim (0.11 \pm 0.03)$ mA in the MOT magnetic coils.

To get the functional form for the data in Figure IV.16 (b), we work out an analytic expression for the echo (revival) time t_E. The condition is $\partial_t C(t)|_{t_\pi} = 0$ (with $t > t_\pi$) and yields

$$t_E = \tau_\varphi \ln(2e^{\frac{t_\pi}{\tau_\varphi}} - 1) < 2 \times t_\pi. \tag{IV.8}$$

We use this expression and apply the fitted value $\tau_\varphi = 2.1$ ms to trace the solid line in Figure IV.16 (b). Finally, one can write an expression for the maximal echo contrast as a function of the echo time t_E.

The solid line traced in Figure IV.16 (a) is obtained by evaluating eq.(IV.6) at

$t = t_E(t_\pi)$ to get a model prediction for the contrast C at t_E as a function of t_π. We further introduce a factor of 2 to be able to plot the expression as a function of $2 \times t_\pi$. The model parameters are fixed to $\tau_\varphi = 2.1$ ms and $D_\varphi = 3.8 \times 10^6$ s^{-1} in agreement with the fit of the oscillations. Furthermore, it is easy to simplify the expression to get rid of the experimentally controlled parameter t_π and to express the contrast as a function of the measured parameter t_E. The expression for the maximal contrast of the echo oscillation as a function of the echo t_E time reads

$$C(t_E) = e^{-D_\varphi \left[t_E/2 - \tau_\varphi \tanh\left(\frac{t_E}{2\tau_\varphi}\right)\right]}. \tag{IV.9}$$

In Figure IV.18, we plot the measured Gaussian amplitude A again, now as a function of the echo time t_E. The solid line is directly the model eq.(IV.9) taking $\tau_\varphi = 2.1$ ms and $D_\varphi = 3.8 \times 10^6$ s^{-1}.

The model is in good agreement with the data and the early revival of the oscillations $t_E < 2t_\pi$ finds a formal explanation. The irreversible decoherence time T_2 for the spin-echo sequence is defined as $C(T_E = T_2) = C(0)/2$ and it is graphically found to be of $T_2 \sim 270$ µs. Note that since $t_E \ll 2\tau_\varphi$ in our experiment, we have from eq.(IV.9)

$$C(t_E) \sim \exp\{-t_E^3 \times D_\varphi / 24\tau_\varphi^2\}.$$

The irreversible decoherence time is then $T_2 \sim \sqrt[3]{\ln(2) \times 24\tau_\varphi^2/D_\varphi}$, and yields a numerical value of $T_2 = (268 \pm 5)$ µs when evaluated in the parameters extracted from the fit in Figure IV.17.

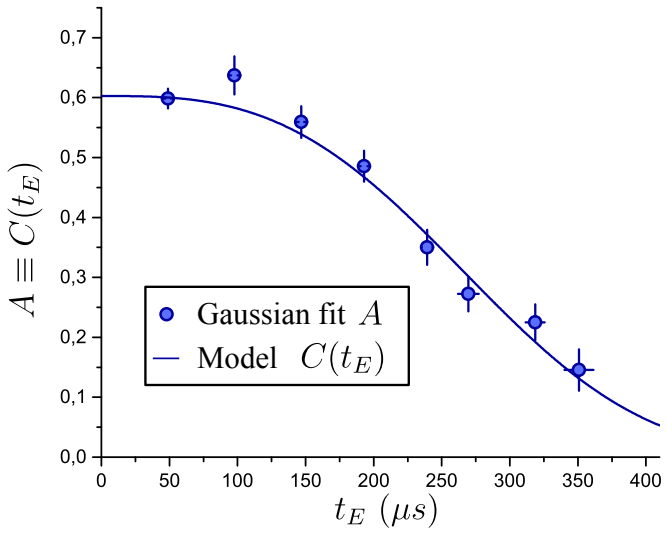

FIGURE IV.18 The maximum contrast of the revival oscillation as a function of the echo (revival) time t_E. The irreversible decoherence at $C(0)/2$ is found to be $T_2 \sim 270$ µs.

IV.3 Conclusion

We used a cold cloud of cRy atoms to measure the spontaneous and black-body radiation losses from circular states. This provides an experimental demonstration of the simple evolution of the cRy state population damping processes. The cRy states in our cryostat are found to have a lifetime of $T_1 = (3.7 \pm 0.1)$ ms, corresponding to an effective black-body temperature $T = (11 \pm 2)$ K.

We have studied the coherence properties of these atoms and we have measured the T_2^* and T_2 times to be ~ 35 µs and ~ 270 µs respectively. We have identified the limiting factor to be magnetic field noise of about $\delta B \sim 2$ mG of a purely technical nature. A simple model based on correlated noise fits the data fairly well. Solutions to this limitation are on their way; they consist of filtering the lines that bring the signals down into the cryostat, the implementation of more stable current sources, and the installation of a mu-metal screen under the 300 K screen to prevent the penetration of external magnetic field noise.

Having measured the lifetime and coherence of cold circular atoms, we now turn to discuss their laser trapping. This is the topic of the next and last chapter and the main result of this thesis.

Chapter V

Laser Trapping

Contents

In the present chapter, we demonstrate the laser trapping of circular Rydberg atoms. This is the main result of this thesis. To achieve the trapping, a 1064 nm laser is introduced to provide a ponderomotive potential. As discussed in Chapter II, it is to be shaped as a hollow Laguerre-Gauss (LG) mode. This is done in the updated experimental setup depicted in Figure V.1. The circular Rydberg atoms are repelled by the laser-induced potential and transversally confined in the light tube for times up to 10 ms. The trapping frequency is measured to be 1.3 kHz. We check that the lifetime and the coherence of the trapped atoms are not sensibly affected by the trapping light, as expected for levels insensitive to photoionization and for a nearly n-independent trapping potential.

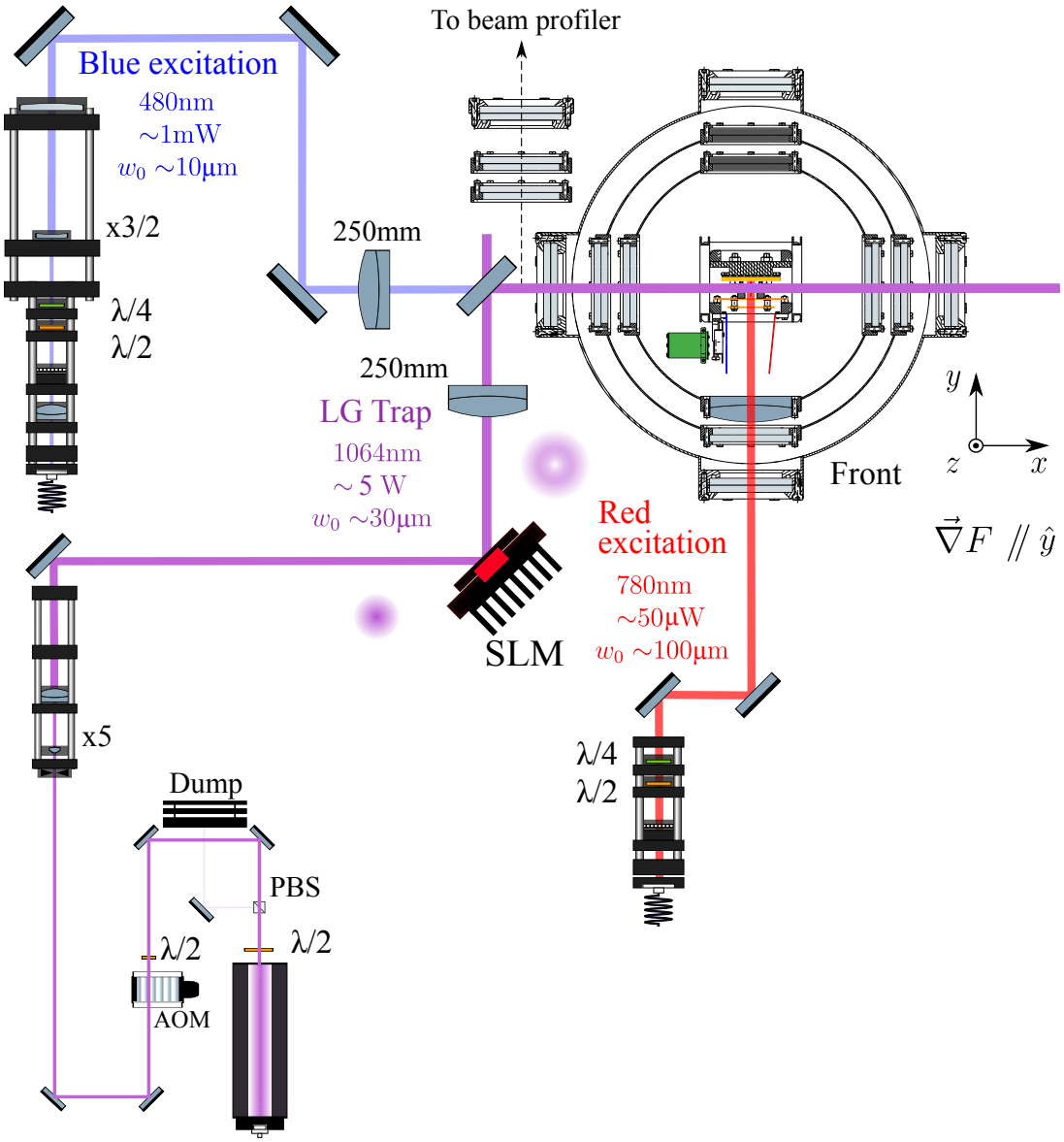

FIGURE V.1 The cryostat and the optical table as used for the cRy trapping experiments.

V.1 Laser control

We shape the 1064 nm laser into a LG_{01} beam with a dark spot in the center. The shaping and alignment of the trap is done using a Spatial Light Modulator (SLM) that we show in Figure V.1. The trap is produced by a fiber laser capable of providing up to 10 W. The choice of wavelength λ_L =1064 nm is a good compromise regarding the different experimental constraints. On the one hand, one knows from eq.(II.17) that the ponderomotive potential $\mathcal{E} \sim \lambda_L^2$ increases with wavelength for a given power. On the other hand, a far infrared field (say, 10 µm) would be completely absorbed by our cryostat windows. Our windows are transparent to the chosen wavelength and reliable powerful lasers are easily available on the market.

A few mirrors are used to prepare the laser before the beam shaping in the SLM. A polarizing beam splitter (PBS) is used to filter the polarization and coarsely tune the power with the help of a half-wave plate. A beam dump is used to absorb the unwanted laser power. In order to turn the trap on and off at microsecond timescale, the 1064 nm beam is gated using an AOM. The high power order zero of the AOM (not shown) is also sent to the beam dump.

The blue laser has been moved with respect to previous experiments (see Figure III.5) and now enters the cryostat through the same window as the LG beam. Having their propagation vectors parallel to each other makes it easier to align the two lasers. The excitation volume must coincide with the trap to capture all of the created Rydberg atoms. The alignment with the blue excitation beam is critical. Both beam profilers external to the cryostat and the response of the atoms providing an *in-situ* imaging technique are needed to optimize and tune the SLM parameters and, with them, the shape of the trap.

V.1.1 The SLM for beam shaping

The SLM device consists of a mirror covered with transparent pixels (1272×1024) that can be programmed independently to add a local phase shift from 0 to 2π (8 bits) to any reflected wave. This allows us to shape the reflected beam almost arbitrarily. The SLM is computer controlled by a custom software that acts on each pixel in a manner analog to the intensity control of a normal Liquid Crystal Display (LCD) screen. The 250 mm focal length lens in the path of the 1064 nm beam (see Figure V.1) performs the optical Fourier transformation of the incident waveform near its focal plane [201]. The diffraction in the SLM is used to imprint a phase pattern that will be transformed, by the lens, into the desired trap.

In Figure V.2 (a), we show a phase mask that gives a turn of 2π for any fixed radius. This phase pattern is known as 'phase vortex'. The imprinted phase is encoded in the gray-level of the figure with black corresponding to zero. The phase singularity (discontinuity) at the center ensures that the reflected beam will have a hole: the only way the phase condition can be fulfilled is if the amplitude of the field is zeroed in the center. Imprinting this phase on a Gaussian beam produces the LG_{01} trap in the Fourier plane of the lens.

The phase modulation by the SLM is not perfect, and a fraction of the light is reflected without acquiring the intended phase shift. Thus, for the mask in Figure V.2 (a), the light diffracted in the first order (the trap) overlaps with the order zero.

To get rid of this spurious undiffracted beam, a grating is added to the vortex phase pattern. We show the corrected phase mask in Figure V.2 (b). The diffracted LG emerges now with a finite angle and it is spatially separated from the zeroth order. Figure V.2 (c) is the measured intensity in the Fourier plane. The diffracted LG beam can be identified by its characteristic 'doughnut' shape, while the Gaussian spot is the undiffracted zeroth order. The waist of the Gaussian beam used to produce this image is 11 µm.

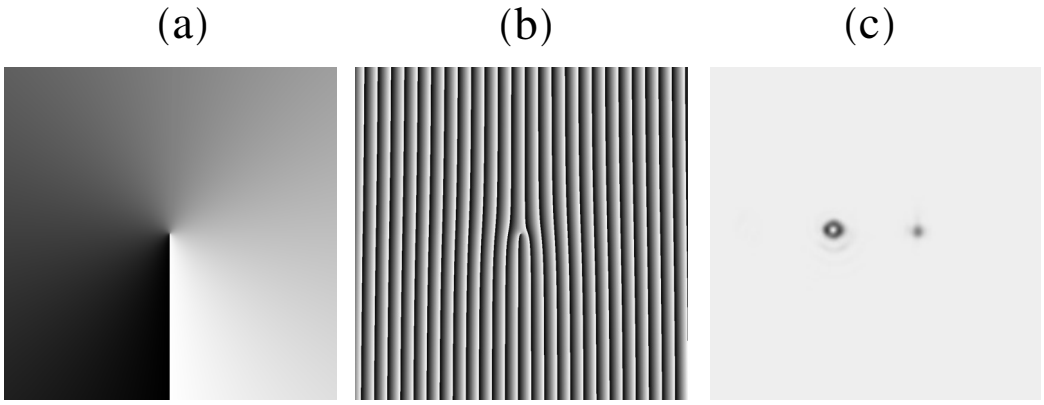

FIGURE V.2 (a): A 'vortex' phase singularity. (b): A grating is added to the singularity. This displaces the whole diffracted beam. (c): The intensity profile of a Gaussian beam reflected on (b). The measurement of intensity is done with a beam profiler in the focal plane of a focusing lens.

The picture in Figure V.2 (c) was taken with a beam profiler in a simplified calibration setup. We have found that, in the actual experimental situation depicted in Figure V.1, detrimental aberrations introduced by the necessary optical elements destroy the LG profile. Imperfections in an optical system add an unwanted phase pattern to the wavefront. Thus, one can compensate for them by using the SLM. It suffices to add the opposite phase pattern to subtract the aberrations.

The phase masks corresponding to the dominating aberrations found in typical optical systems and their effect over the trap are shown in Figure V.3. The phase masks added to the ideal displaced vortex of Figure V.2 (xgb) are shown in the upper panels. In the lower panels, we show the diffracted intensity pattern at the focus of an imaging lens. The reference panel corresponds to an LG beam of waist 11 µm, the same as in Figure V.2 (c). In the subsequent panels, aberrations with different orders of symmetry are shown.[1] The aberration known as 'coma' has a symmetry of order one in the sense that a full rotation is needed to recover the same phase pattern. The astigmatism possesses a symmetry of order two in that a π rotation recovers the phase pattern. In general, a symmetry of order n corresponds to a phase mask that is invariant under a $2\pi/n$ rotation. The Trefoil and Quadrafoil correspond to symmetries of order three and four respectively. The characteristic effect of the different orders of aberrations makes it possible to identify the imperfection affecting the beam and allows us to correct for them.

[1] We use the basis of Zernike polynomials [202–204] to correct for our aberrations. In Figure V.3 we represent the 'primary' Zernike polynomials of each order.

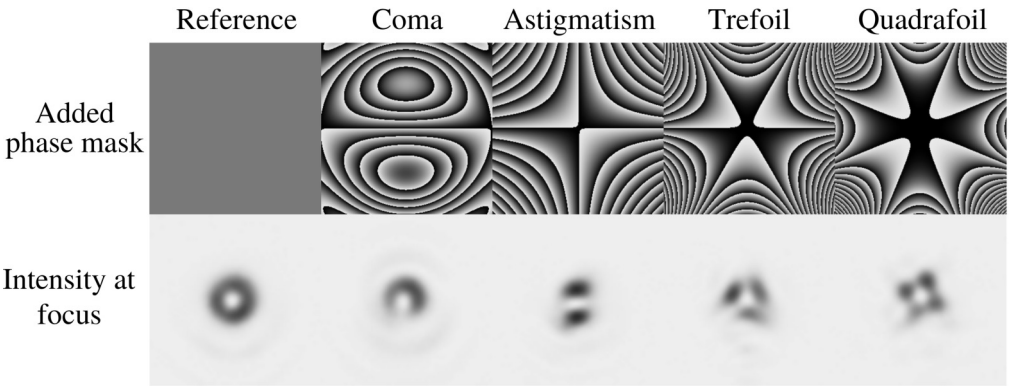

FIGURE V.3 The phase mask added on top of the displaced LG mask (Figure V.2 (b)) is an example of the typical aberration that will need to be corrected. Their isolated characteristic effect can be identified.

V.1.2 The aberrations in the experiment

In our experiment, the many lenses, mirrors, and three successive thick glass windows on the cryostat thermal shields introduce unwanted distortion in the wave front. In Figure V.4 (a), we show the intensity pattern in the Fourier plane of the 250 mm lens focusing the 1064 nm beam. The optical path for the imaging is marked by the dashed line in Figure V.1. A flip-flop mirror (not shown) allows us to switch the LG beam between the optical imaging configuration and the trapping configuration. Note that three identical windows to the ones in the cryostat have been placed in the imaging path to mimic the aberrations suffered by the beam on its way towards the atoms. One recognizes the main aberrations to be 'diagonal astigmatism' (two lobes), and 'diagonal coma' (affected reflection symmetry). Once the main aberrations have been identified, one can perform a manual correction. The product of the optimization is shown in Figure V.4 (b) together with the required phase mask. From a fit to this optimized profile, we find the waist of the LG_{01} beam to be $\sim$30 µm.

One experimental consideration deserves to be mentioned. The high power of the 1064 nm beam is able to heat up the SLM screen and distort the beam over a timescale of minutes. It takes about one hour of operation for it to reach a steady state. Only after such a time lapse, permanent corrections to the beam profile can be made. Moreover, calibration experiments like those in Figure V.4 need to be done using the same duty cycle as the ones to be used during the actual trapping experiments. If necessary, the 1064 nm beam is turned on during the loading of the MOT (see Figure III.4) to dissipate, on average, the same amount of power in the SLM during all relevant sequences. With this consideration taken into account, the image in the beam profiler is stable in time and can be used to align the LG relative to the blue excitation beam.

V.1.3 Coarse alignment of the trap on the blue beam

The LG trap and the blue laser are mixed with a dichroic mirror as shown in Figure V.1. The much less demanding blue Gaussian beam is shaped using standard lenses to have a waist of about 20 µm. The flip-flop mirror allows us to make a beam-profiler

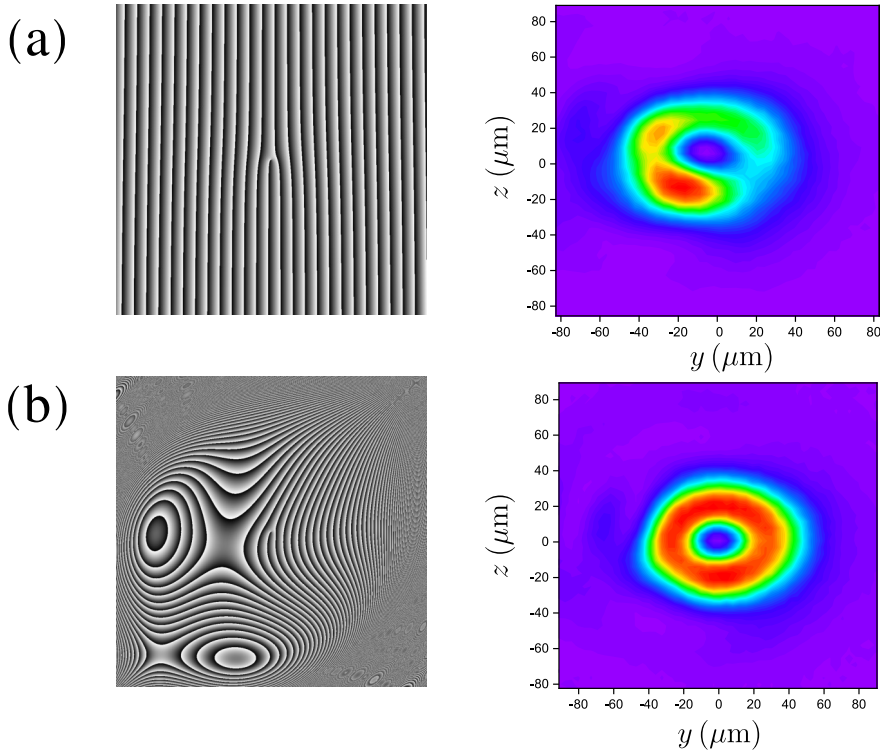

FIGURE V.4 (a): Displaced vortex mask (left) and intensity distribution (right) in the focal plane of the 250 mm lens on the 1064 nm path. (b): Manual optimization by subtraction of aberrations. The phase mask (left) correcting for the optical aberrations produces the intensity distribution of a proper LG trap (right) in the focal plane.

image of both lasers simultaneously. Taking images in this way allows us to make a preliminary alignment of the beams relative to each other.

The blue beam focus is displaced by moving its 250 mm lens and its mirrors. Its position is chosen to optimize the Rydberg signal. The LG beam focus is then brought to that same position using the SLM alone. The LG beam focus can be displaced in the longitudinal direction introducing the circular phase pattern of a (Fresnel) lens in the SLM. By setting the pitch of the phase grating in the SLM, one can also move the beam in the transversal direction. With this method the resolution of the LG displacement is better than 1 µm and it is completely reversible. We can move the beam ±1 mm in any direction without appreciable distortion. The criterion to perform this first alignment is to overlap the blue and the LG beam in the plane conjugated to the position of the atoms with respect to the flip-flop mirror where the beam profiler is placed. The longitudinal alignment consists of making the LG beam the smallest possible at the level of the camera.

Nonetheless, the profile of the beam at the level of the atoms is found to be sub-optimal. The techniques described so far are not enough to compensate for the aberrations introduced by the actual cold cryostat windows and only give a qualitative insight into the intensity distribution at the location of the atomic cloud. An approach relying directly on the wave front, as seen by the atoms, is mandatory to evaluate and optimize the trap. We have successfully developed such a technique.

V.2 Low-l Rydberg atoms as a beam profiler

We probe the trap beam intensity profile by measuring the light-shifts it induces on the $|5S_{1/2}\rangle \rightarrow |52D_{5/2}\rangle$ ground-Rydberg two-photon transition. Getting laser spectra for several positions of the trapping beam with respect to the blue beam, we reconstruct the LG intensity distribution as seen by the atoms themselves. We use this information to optimize the LG beam-shape, with the SLM correcting the aberrations introduced by the cryostat windows. Finally, we extract quantitative parameters for the trap using a simple model to fit the data. The LG beam is found to have waists of 35 and 41 µm along the z and y axes, respectively. The peak laser intensity is measured to be 6.6×10^4 W/cm^2 (total power 4 W) corresponding to a 80 µK trap depth, much larger than the initial ~ 15 µK atomic temperature.

V.2.1 Light shifts of the ground state to Rydberg transition

In order to efficiently reconstruct the intensity profile of the LG trapping beam, we record the laser excitation spectrum of the $|5S_{1/2}, F = 2\rangle$ to $|52D_{5/2}, m_J = 5/2\rangle$ ground-Rydberg two-photon transition while shining the trapping light on the atoms. The trapping laser light shifts both the ground- and the Rydberg-state energy levels proportionally to the local intensity I by $h\beta_{\mathrm{G}}I$ and $h\beta_{\mathrm{Ry}}I$, respectively. Here h is the Planck constant and β_i is a state-dependent constant. From the $[h\,(\beta_{\mathrm{Ry}} - \beta_{\mathrm{G}})I]$-light shift of the transition, we infer I at the position of the Rydberg atoms. The measurement requires the *a priori* calculation of the pre-factors β_i to transform the measured AC-Stark shift into the corresponding light intensity.

From Chapter II, the ponderomotive energy shift of the Rydberg energy levels reads

$$\mathcal{E} = h\beta_{\mathrm{Ry}}I = \frac{q_e^2}{2m_e\epsilon_0 c\omega_L^2}I, \tag{V.1}$$

where q_e is the electron charge, m_e its mass, ϵ_0 the vacuum permittivity, c the speed of light and ω_L the trapping laser angular frequency. Note that this formula now applies to the laser-accessible $|52D_{5/2}\rangle$ Rydberg level, when it was discussed for circular levels in Chapter II. Neither the interpretation nor the formula requires modifications [88].

The scalar polarizability of the $|5S_{1/2}\rangle$ ground state at a 1064 nm-wavelength has been calculated [205] to be

$$\alpha_{\mathrm{G}} = 4\pi\epsilon_0 \times 693.5(9)\, a_0^3, \tag{V.2}$$

where a_0 is the Bohr radius. The light shift of the ground state is then given by

$$\mathcal{E}_{\mathrm{G}} = h\beta_{\mathrm{G}}I = -\alpha_{\mathrm{G}}\,\frac{I}{2\epsilon_0 c}. \tag{V.3}$$

Numerically we find

$$\beta_{\mathrm{Ry}} = 2.56 \times 10^{-5}\,\frac{\mathrm{MHz}}{\mathrm{W/cm^2}}, \tag{V.4}$$

$$\beta_{\mathrm{G}} = -3.25 \times 10^{-5}\,\frac{\mathrm{MHz}}{\mathrm{W/cm^2}}, \tag{V.5}$$

and for the total light-shift of the ground-Rydberg transition we get

$$\Delta\nu = (\beta_{\mathrm{Ry}} - \beta_{\mathrm{G}})\, I = \beta_{\mathrm{tot}} I \approx 5.81 \times 10^{-5}\,\mathrm{MHz}\,\frac{I}{\mathrm{W/cm^2}}. \tag{V.6}$$

Spectroscopy in presence of the 1064 nm beam

The measurement of the light-shift provides the intensity of the LG beam as seen by the atoms. Laser spectroscopy of the $|52D_{5/2}, m_j = 5/2\rangle$ line is now done in the presence of the 1064 nm beam. In Figure V.5, we show the blue laser excitation spectroscopy in the absence of 1064 nm light (blue dots, $F = 0.8$ V/cm), together with light-shifted spectra with the 1064 nm beam on. The expected light-shift is observed. The green dots correspond to the 1064 nm beam shaped in a Gaussian mode and the red dots correspond to the light shaped as the LG beam. The Gaussian beam shifts much more strongly the frequency of the atoms since its intensity is at its maximum in the region where we prepared the Rydberg atoms. The LG beam has a zero of intensity in that volume, but the finite size of the blue excites atoms in the twilight around the center. The blue and the 1064 nm beams are aligned by maximizing the light-shift produced by the Gaussian 1064 nm light.[2]

Because ground-state atoms are attracted towards the high-intensity ring of the LG beam, the light-shift must be produced by a 'short' light pulse to keep a homogeneous atom density during the light-shift probe. We then let the trapping laser on only for 15 µs starting 7 µs before the laser Rydberg excitation (2 µs).

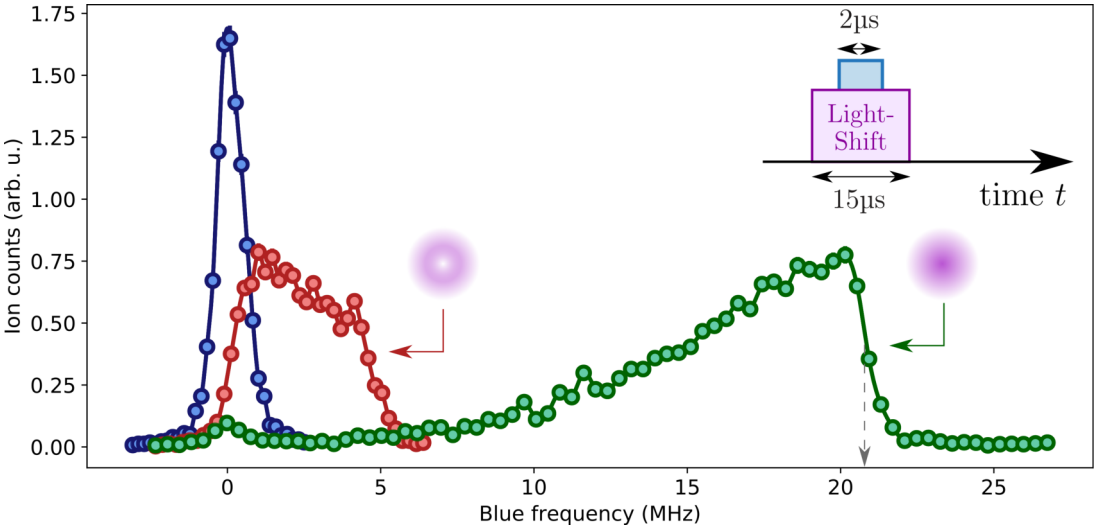

FIGURE V.5 Rydberg ($|52D_{5/2}\rangle$) two-photon laser spectroscopy at 0.8 V/cm in the absence of 1064 nm light (blue dots), together with light-shifted spectra corresponding to the aligned 1064 nm beam shone as a Gaussian (green dots) and as a LG (red dots). The inset defines the timing of the laser pulses.

To get a quantitative measurement of the trap profile, a model considering the finite waists of the two beams and the different atomic frequencies involved in the spectroscopy is needed. We now turn to discuss the *in-situ* assessment of the LG trap.

[2] Applying the vortex phase mask does not shift the center of the beam.

V.2.2 Trap alignment and optimization

In order to precisely center and optimize the LG beam at the level of the Rydberg atoms, we use the SLM. We name the position of the focal point of the 1064 nm beam (x_{LG}, y_{LG}, z_{LG}) and we will experimentally define the origin of coordinates *a posteriori* as the position at which it is centered on the Rydberg excitation volume.

First, we will discuss the alignment in the *longitudinal* direction along the coordinate x. By measuring the light-shift produced by the Gaussian 1064 nm beam on the atoms, one can bring the 1064 nm focus into the excitation region. The optimal x position for the 1064 nm laser focus is mainly set by the red excitation beam (see Figure V.1). By changing the 1064 nm focal point, we optimize the maximal light shift, defined as the mid-point of the sharp edge of the ionization spectrum (dashed line in Figure V.5).

As mentioned before, the longitudinal beam displacement is done by introducing the phase mask of a (Fresnel) lens in the SLM. For different positions of the 1064 nm focus, two-photon laser spectroscopy is performed and the maximal light-shift is extracted from the data. The position $x_{LG} = 0$ is defined as the point at which this *maximal light-shift* is at its *maximum value*. In Figure V.6, we show the data allowing the determination of the origin of the x coordinate. The fit is a Lorentzian, as one would expect from a Gaussian beam $I_{\max} \sim 1/w^2(x)$ (where $w(x)$ is the Gaussian waist along the propagation axis). The Rayleigh length is extracted from the fit to be ~ 3.3 mm, in agreement with values expected from the beam shaping procedure.

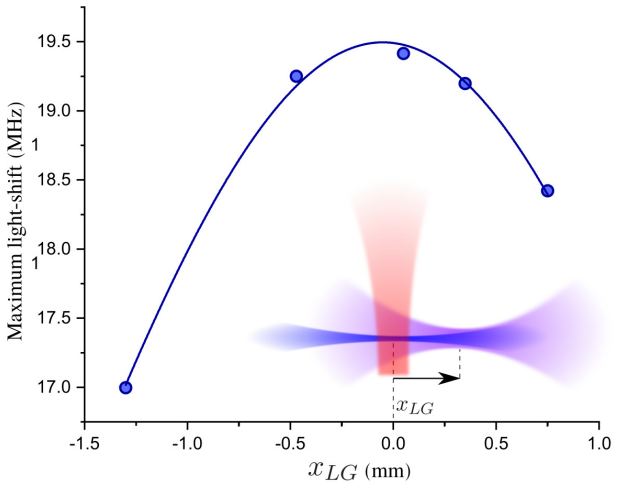

FIGURE V.6 Maximum light-shift measurement as a function of the focal point of the 1064 nm beam (violet in Figure). The red and blue beam represent the Rydberg excitation beams.

With the longitudinal alignment made, the blue and the 1064 nm beams can then be aligned in the *transversal* direction defined by coordinates y and z. For this, we fix the two-photon detuning δ between the free-space atomic transition frequency ν_0 and the blue laser drive at ν_B to $\delta = 4.5$ MHz, addressing atoms close to the maximal LG light shift (see Figure V.5). In Figure V.7, we plot the number of atoms detected in the $|52D_{5/2}\rangle$ level as a function of the LG transverse beam position. The data reveals the intensity regions where the atoms are light-shifted by the LG beam into the spectral range of the blue laser ($\beta_{\text{tot}} I_{LG} \sim \delta \pm \gamma$, where γ is the linewidth). We

identify here the two maxima defining the LG trap. The red dots correspond to a sub-optimal trap, resulting from uncompensated astigmatism that comes from the cryostat windows. Imperfections in the LG beam intensity at the level of the atoms are identified and corrected for by adding correction phase masks on the SLM as explained in the previous section. The blue dots provide the picture of the trap after optimization. The solid lines in Figure V.7 are the sum of *ad-hoc* Gaussian peaks. The ratio between the height of the pair of fitted peaks increases from 0.76 to 0.98. The improvement is evident. The placement of the LG beam focus at the coordinates' origin is achieved at the point in which we find the valley between the two peaks in the distribution. Naturally, scans in both the y and z directions are needed.

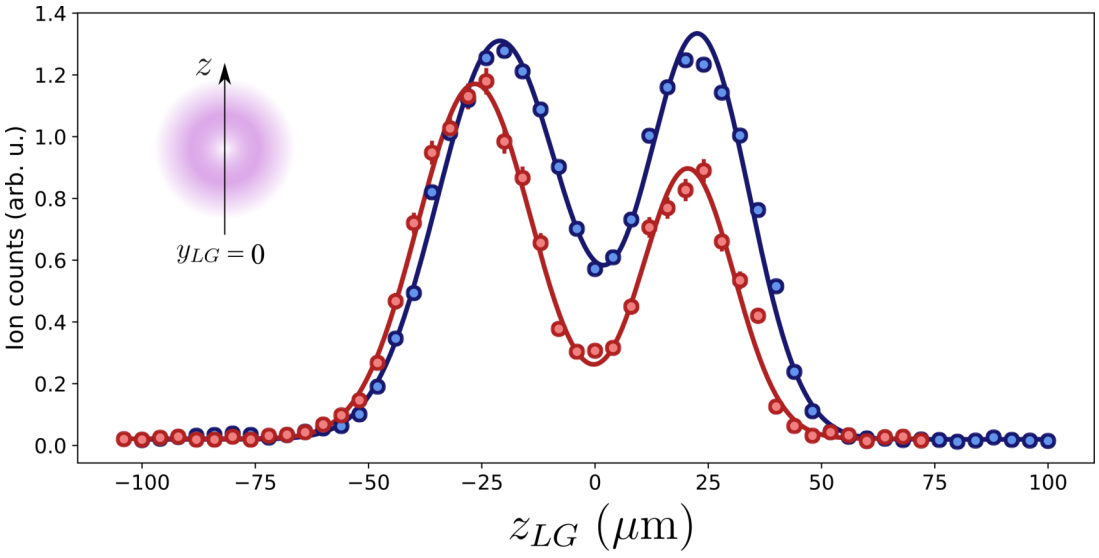

FIGURE V.7 *In-situ* reconstruction of one transversal cut the trapping beam using light-shift measurements.

The methods discussed above allow us to align and optimize the shape of the beam. Having developed the experimental techniques to access the information about the LG beam as seen by the atoms, we now present the analysis that allows for the extraction of the trap parameters.

V.2.3 The shape and depth of the trap

In order to make a quantitative analysis of the data taken as a response to the atomic cloud to the 1064 nm beam, we need to further model the excitation. First we assume a Gaussian line-shape for the laser spectrum in the absence of 1064 nm light-shift (blue dots in Figure V.5) given by

$$\Gamma_{\mathrm{B}}(\delta) = \sqrt{\frac{2}{\pi\gamma^2}} \exp\left(-\frac{2\delta^2}{\gamma^2}\right), \tag{V.7}$$

of FWHM $\gamma\sqrt{2\ln(2)}$. To take into account the elliptical shape of the LG profile, a product of uncompensated residual astigmatism, we model the trap with an intensity

distribution given by

$$I_{\mathrm{LG}}(y,z) = \mathcal{P}\frac{4}{\pi\, w_y\, w_z}\left(\frac{y^2}{w_y^2}+\frac{z^2}{w_z^2}\right)\exp\left[-2\left(\frac{y^2}{w_y^2}+\frac{z^2}{w_z^2}\right)\right], \tag{V.8}$$

where $\mathcal{P}$ is the power of the LG beam and w_y and w_z are the beam waists along the two directions. In the expression for I_{LG} we assume that the axis of the elliptical Gaussians are along y and z and that there is no dependence on coordinate x. These assumptions simplify the data analysis and the interpretation of the model. We note that, in our experiment, the Rayleigh lengths of the blue ($z_R = 2.6$ mm) and LG beams ($z_R = 3.3$ mm) are large with respect to the Rydberg cloud size (∼100 µm) and, thus, we neglect the intensity variations along the propagation axis x.

The peak intensity of the LG beam is then

$$I_{\max} = \frac{2\mathcal{P}}{\pi e\, w_y\, w_z}. \tag{V.9}$$

With these formulas at hand, the number $n(y,z)$ of excited atoms at a position (y,z) after integration in x is

$$n(y,z) = n_0 \times \Gamma_{\mathrm{B}}\left[\delta - \beta_{\mathrm{tot}} I_{\mathrm{LG}}(y-y_{\mathrm{LG}}, z-z_{\mathrm{LG}})\right] \times I_{\mathrm{B}}(y,z), \tag{V.10}$$

where n_0 is a normalization factor and $I_{\mathrm{B}}(y,z)$ is the blue laser intensity. The intensity profile of the blue beam reads

$$I_{\mathrm{B}}(y,z) = I_{\mathrm{B}}^{(0)} \exp\left[-\frac{2(y^2+z^2)}{w_{\mathrm{B}}^2}\right], \tag{V.11}$$

where w_{B} is the waist of the blue laser and $I_{\mathrm{B}}^{(0)}$ is its peak intensity. Note that the red excitation laser waist is bigger than that of all the other beams and, thus, it will not be considered in the model.

The Γ_{B} term in eq.(V.10) represents the response of the atoms to the excitation *frequency*. It encodes the probability of exciting an atom, placed in (y,z), which has resonance frequency $\nu_0 + \beta_{\mathrm{tot}} I_{\mathrm{LG}}(y,z)$ while driving its transition at frequency $\nu_B \equiv \nu_0 + \delta$. The second term ($I_{\mathrm{B}}$) represents the sensitivity to the excitation *intensity*. It corresponds to the statement that the probability of exciting a Rydberg atom is proportional to the local blue beam intensity. Note that we have assumed that we excite far away from saturation and that the spatial variation of the density in the cold-atom cloud (n_0) can be neglected.

Integrating over the cloud, we can compute, out of these quantities, the number of excited atoms as a function of the two-photon detuning and of the LG center coordinates. The result reads

$$N(\delta, y_{\mathrm{LG}}, z_{\mathrm{LG}}) = \iint n(y,z)\,\mathrm{d}y\,\mathrm{d}z + N_0, \tag{V.12}$$

where N_0 accounts for a small offset in the experimental data. The free parameters of the model are n_0, w_{B}, w_y, w_z, $I_{\max}$, and N_0. The blue laser linewidth γ is measured independently of the LG presence and it is an input parameter of the model.

By fixing the two-photon detuning and taking data as a function of the LG *position* (y_{LG}, z_{LG}), we were able to obtain important information about the *shape* of the trap at the level of the atoms (see Figure V.7). This information was used to manually correct for the aberrations and to optimize the trap geometry.

On the other hand, by fixing the two-photon detuning, the measurement is 'blind' to atoms light-shifted several γ away from δ. Complementary information can be obtained by taking data as a function of the two-photon *detuning* δ for a given position of the LG beam. In this way, one gets the local *intensity distribution* and eventually a reliable measurement of the trap depth. We discuss next the measurements performed to quantitatively evaluate the LG trap parameters.

Measurements and analysis

We are now in position to measure the laser intensity seen by the atoms in a space- and frequency-resolved way. The ground-Rydberg transition for several positions of the LG trap with respect to the blue laser is recorded. In Figure V.8 (a), we plot the corresponding laser-excitation spectra with and without trapping light. The spectral width associated with the blue beam without light-shift (violet, first panel) is fitted to be $\gamma = (1.41 \pm 0.04)$ MHz.

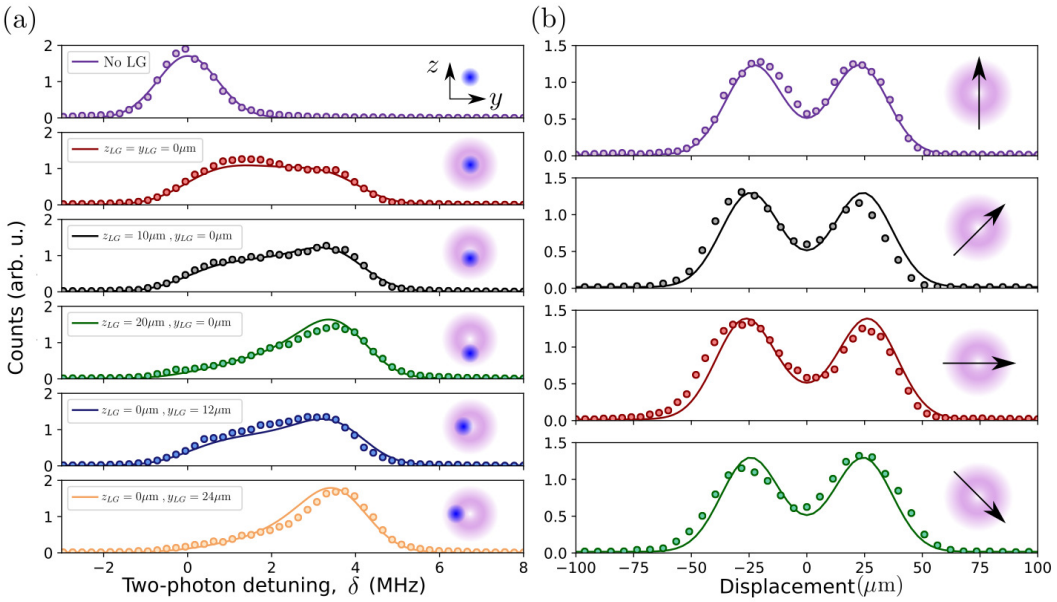

FIGURE V.8 (a) Curves of excitation spectra of the Rydberg transition as a function of the blue laser detuning δ for several positions of the trapping laser with respect to the blue laser. In (b), we fix the detuning to 4.5 MHz and scan the position of the blue laser focus. The direction of the scan for each curve is shown schematically on the insets.

The second panel in Figure V.8 (a) corresponds to the LG beam on and aligned with the blue beam, while the four remaining panels correspond to the excitation spectrum when the LG beam is displaced out of the beam x-axis, either along the y- or the z-axis. Slightly off-centering the LG beam shifts the excitation spectrum to higher

frequencies until the maximum is reached. In Figure V.8 (b), we plot the number of atoms detected in $|52D_{5/2}\rangle$ as a function of the LG beam position for a fixed two-photon detuning of $\delta = 4.5$ MHz. As before[3], we choose the two-photon detuning to be close to the maximum measured light-shift of the ground-Rydberg transition. In these experiments, the LG beam is scanned through the blue laser beam along four different directions. These are the y- and z-axes as well as the two diagonals tilted by $\pm 45°$.

We fit all the light-shifted data in Figure V.8 simultaneously by eq.(V.12), but we allow for different values of n_0 for Figure V.8 (a) and Figure V.8 (b), taking into account the different mean number of excited atoms in the two experiments. The other parameters are shared. We obtain good agreement with the experimental results for a maximum light-shift of $\beta_{\text{tot}} I_{\text{max}} = (3.81 \pm 0.06)$ MHz and a diameter of (21.9 ± 0.8) µm for the blue laser. The waists of the LG beam are found to be $w_y = (41 \pm 3)$ µm and $w_z = (35 \pm 1)$ µm.

The distribution of light-shifts observed corresponds to $I_{\text{max}} = 6.6 \times 10^4$ W/cm^2 and a trap depth of 80 µK. Given the fitted LG beam, we predict an oscillation frequency (see eq.(II.19)) at the bottom of the trap of (1.12 ± 0.08) kHz for the movement in the y direction and of (1.33 ± 0.05) kHz in the z direction. We estimate a total power of (4.0 ± 0.3) W of trapping light in fair agreement with the measured (4.3 ± 0.3) W power of the beam that exits the cryostat.

Optimized LG beam shape

The data extracted from the experiment and the analysis we have made allow us to get a picture of the trap inside the cryostat and of the Rydberg cloud.

A beam profiler picture of the LG beam after the *in-situ* optimization is shown in Figure V.9 (a). As expected, the wavefront looks far from ideal. To picture the trap inside the cryostat, one can gather the data in Figure V.8 (b) in a 2D picture like we show in Figure V.9 (b). We have used a simple interpolation to fill the plane for the reconstruction.

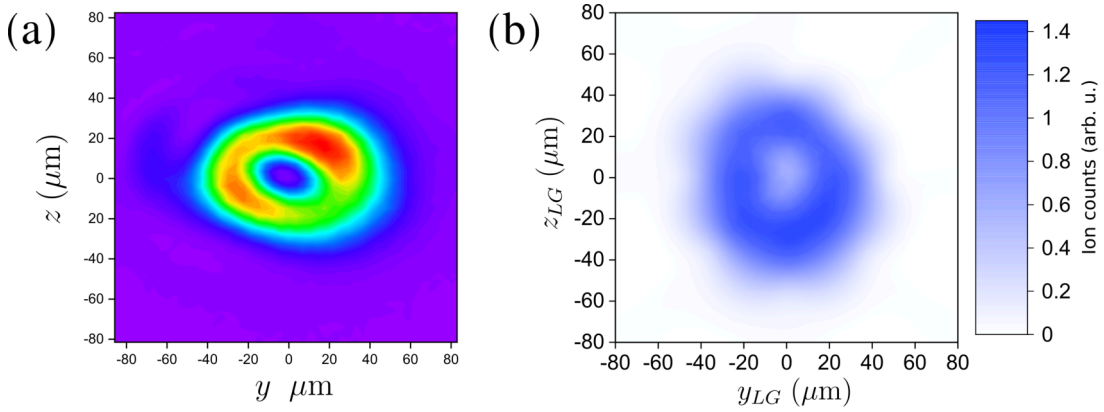

FIGURE V.9 (a) The beam profiler picture of the LG beam after the atomic optimization. In (b), a 2D atomic picture of the LG trap is done by interpolating the data of Figure V.8.

[3]Note that the blue dots in Figure V.7 correspond to the data in the first panel of Figure V.8 (b).

Rydberg distribution in the trap

Our model allows us to predict the spatial distribution of atoms excited by the blue laser. The expression in eq.(V.10) gives us the density of Rydberg atoms. With the fits done on the data, the free parameters of the trap model are now known and one can draw the expected distribution of excited atoms in space. As an example, in Figure V.10, we show the distribution of cRy atoms when the LG beam is aligned with the blue laser ($y_{\mathrm{LG}} = z_{\mathrm{LG}} = 0$) with $\delta = 0.5$ MHz and when the LG beam is displaced with respect to the blue laser ($y_{\mathrm{LG}} = 0$ and $z_{\mathrm{LG}} = 12\,\mu\mathrm{m}$) and $\delta = 4.5\,\mathrm{MHz}$. By integrating over the y direction we find that the diameter of the excited Rydberg cloud, in both cases, measures $\sim$ 10 µm. These two excitation conditions will prove useful in the demonstration of the trapping.

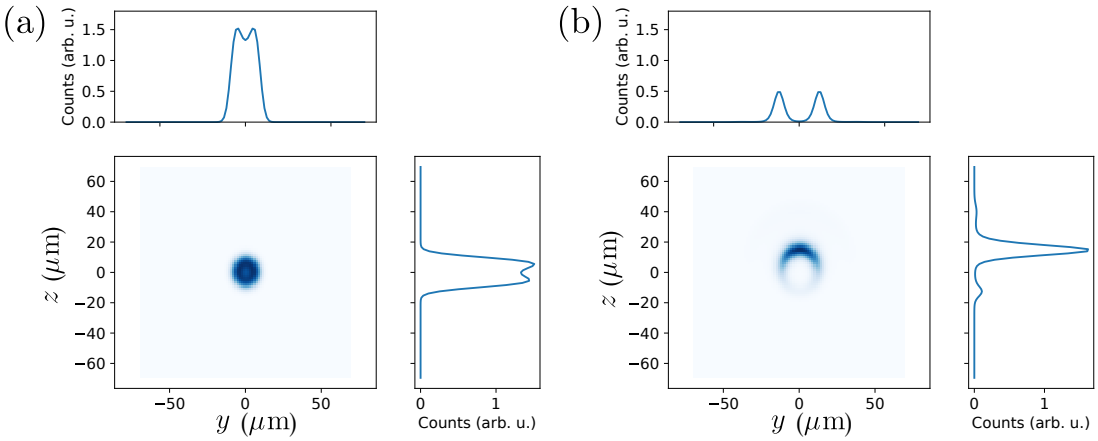

FIGURE V.10 Calculated atomic distribution for two different positions of the LG and two different detunings of the blue excitation. (a): The LG beam is aligned with the blue laser and $\delta = 0.5\,\mathrm{MHz}$. (b): The LG beam is displaced with respect to the blue laser ($y_{\mathrm{LG}} = 0$ and $z_{\mathrm{LG}} = 12\,\mu\mathrm{m}$) and $\delta = 2.1$ MHz.

V.3 Trapping of circular states

Having used the low-angular-momentum Rydberg atoms to prepare and calibrate the LG beam, we proceed to circularize them for trapping. To exhibit the trapping, we will show how the presence of the LG beam stops the thermal expansion that the cRy atoms undergo otherwise. One is able to measure the spatial extension of the Rydberg cloud using MW spectroscopy if the atoms sit in a spatially varying electric field. Due to inhomogeneous Stark shifts, the width of the line encodes the size of the cloud. A circular-elliptical transition, which experiences a large linear Stark shift, will then allow us to make a MW time of flight image of the cloud while it expands in free space. We show that the presence of the LG trap forbids this expansion in the radial direction. We also measure the frequency of the trap and we check that the circular to circular transition, while trapped, is not sensibly affected.

Since we expect to probe the trapping of the cRy atom cloud during a few milliseconds, the lifetime of the atoms plays a role. The black-body transfer will distribute the population initially in the $|52c\rangle$ state into the neighboring circular states

and spectroscopy towards these manifolds will thus be degraded by a time dependent background. We now explain the method developed to get rid of this background.

First, we need to identify the elliptical level to measure the cloud extension using MW spectroscopy. Because the dipole selection rules forbid any circular-elliptical transition downwards in n, and because the $|52c\rangle \rightarrow |54e\rangle$ transition is already below cut-off for our MW guide (so are all others transitions towards $n > 54$, see Chapter III), far lying elliptical levels whose detection windows remain empty during the experiment are all out of reach. The only possible solution then is to perform a partial ionization ramp to clean up the background counts in the accessible detection windows before performing spectroscopy.

Since levels with higher principal quantum number n ionize at lower voltages (see Figure III.23), the natural choice would be to ionize the circular levels with $n \geq 53$ and then practice circular-elliptical spectroscopy for the $|52c\rangle \rightarrow |53e\rangle$ line. Again, a more complicated scenario is required since we find that practicing an efficient ionization up to the level of the $|53e\rangle$ ($|(n+1)e\rangle$) detection window is detrimental for the $|52c\rangle$ ($|nc\rangle$) level.

All things considered, in order to deal with the black-body transfer in the presence of the MW cut-off, we perform a partial ionization ramp after having applied a shelving two-photon pulse (MW_S) from $|52c\rangle$ to $|50c\rangle$ in order to protect the useful population. The partial ionization ramp is then able to get rid of the background up to the $|52c\rangle$ detection window without adversary effects. Finally, we probe the extension of the cRy cloud by performing spectroscopy on the $|50c\rangle \rightarrow |52e^-\rangle$ transition.

V.3.1 The partial ionization ramp

In Figure V.11, we demonstrate the operation of the partial ionization. In (a), we show an ionization signal that corresponds to the preparation of state $|50c\rangle$. The state is prepared by circularization in the $n = 52$ manifold and a subsequent MW transfer (MW_S) to $|50c\rangle$ is applied 300 µs after circularization. The ionization ramp (yellow) starts 850 µs after the RF circularization, allowing for some thermal transfer to take place. The zero of time for this plot is taken where we start counting ions. It corresponds to 330 µs after circularization. Here, for reference, no partial ionization ramp is applied. In the zoom-in (b), we show the detection windows of the $|52c\rangle$ and $|50c\rangle$ states by the red and blue shaded regions respectively. We emphasize that the ionization signal has a pedestal corresponding to the presence of thermal population of neighboring levels. The pedestal is modest here, but it dominates the signal after a few milliseconds (see Chapter IV). Moreover, in this example we see the remaining population at the level of the $|52c\rangle$ detection window, which is a signature of low circular purity. In the blue colored signal in (c), we show the effect of applying a partial ionization ramp (R1) that stops at the ionization voltage of $|51c\rangle$. In doing so, we ionize all the residual lower-ionizing states. We see that after partial ionization, the time window corresponding to $|52c\rangle$ is clear of counts, and it is emphasized in the zoom-in, in (d). The red signal corresponds to a π-pulse from $|50c\rangle$ back to $|52c\rangle$ between the partial ramp and the final full ionization (R2). To apply the MW pulse, a > 200 µs waiting time is needed after R1 to let the electric field relax after the partial ionization ramp. Note that, in order to leave the population in $|50c\rangle$ unaffected, we

choose not to completely ionize the population in the $|51c\rangle$ level. Note also that the 'shelving pulse' is a 'selection pulse' too, in the sense that it selectively addresses the circular levels. The partial ionization, then, does not only solve the black-body transfer problem, but it also acts as a state-purification mechanism ionizing all impurities left up to the $|52c\rangle$ detection window.

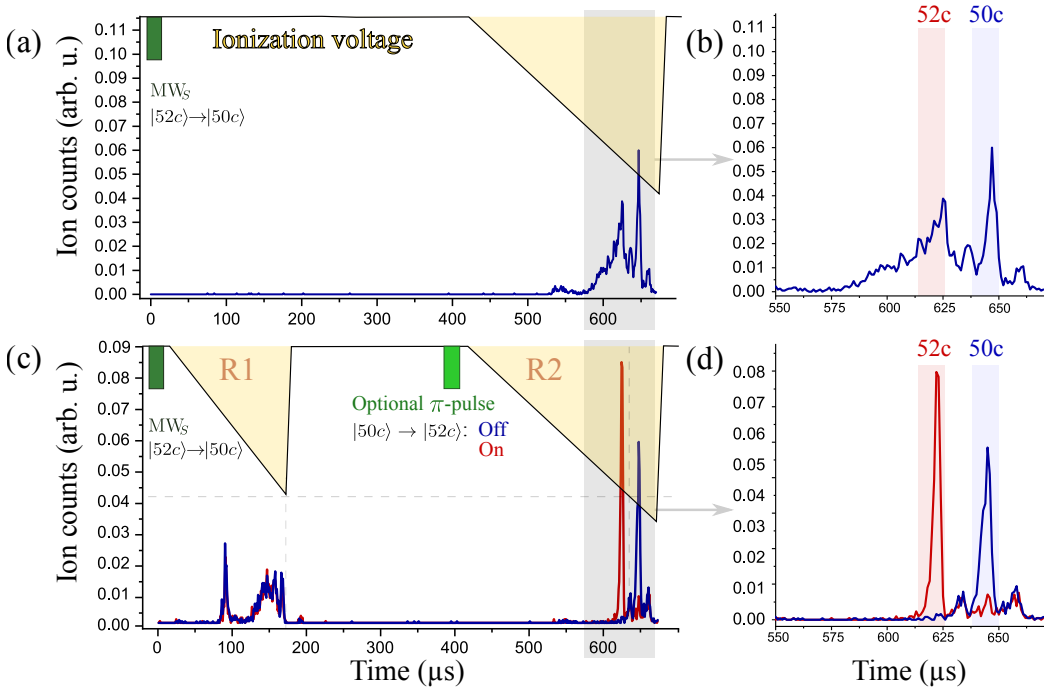

FIGURE V.11 The partial ionization technique. The ionization voltage is shown by the yellow shaded area. In the upper panel, we show the ionization-signal corresponding to the preparation of $|50c\rangle$ state (a) and a zoom to the interesting area (b) for a high number of Rydberg atoms. The lower panel (c) shows the action of the partial ionization with (red) and without the action of a π pulse from $|50c\rangle \rightarrow |52c\rangle$. A zoom to the interesting area is shown in (d).

V.3.2 Timing of the experiment

With the partial ionization tool at hand, we are able to develop the explanation of the trapping sequence. The timing of the experiment is sketched in Figure V.12. To prepare the cRy atoms at the bottom of the trap, we perform the Rydberg excitation in presence of the trapping beam. The trapping beam is switched on for 15 µs around the 2 µs excitation pulse. The electric field during the excitation is set to $F = 0.8$ V/cm. Setting $\delta = 0.5$ MHz, the excitation selects only atoms close to the center of the LG beam. This excitation condition corresponds to the atomic distribution in Figure V.10 (a). We switch off the 1064 nm beam and, in in about 30 µs, perform the transfer to the $|52c\rangle$ circular state, completed at time $t = 0$.

As explained in the introduction to this section, we measure the spatial extension of the cRy atom cloud using a $|50c\rangle \rightarrow |52e^-\rangle$ MW pulse (MW$_P$ in Figure V.12). The spectrocopy is done at a variable time τ after circularization unveils the thermal expansion of the cRy cloud.

To get rid of the thermal background, we selectively transfer at time $\tau - 600$ µs all $|52c\rangle$ atoms (irrespective of their position) into $|50c\rangle$ by a 'hard' 0.8 µs-long π-microwave selection pulse MW_S and ionize all states with $n > 51$. The partial ionization ramp used in the trapping sequence is shown as the first yellow rectangle (R1) in the top timeline found in Figure V.12. It is applied 150 µs after the shelving pulse and it lasts 160 µs. We then wait for an additional 288 µs delay, letting the field relax to $F = 1.46$ V/cm before applying a 1.8 µs MW_P probe pulse used to measure the expansion. Finally, a full ionization (R2) is used to make the measurement.

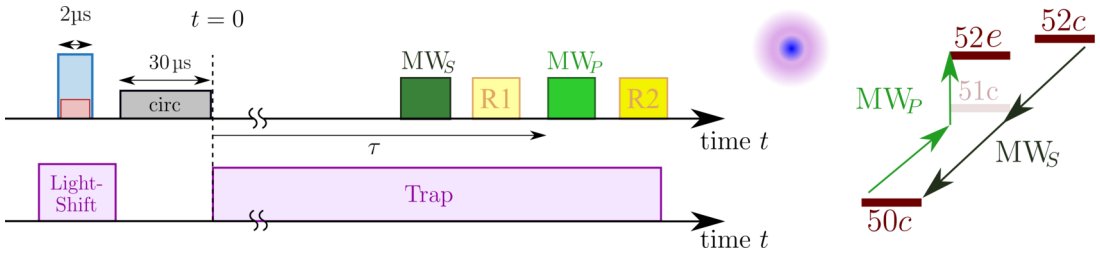

FIGURE V.12 Left: Timing of the experiment (not to scale). In the top timeline, from left to right, we have the laser excitation (blue/red), circular state preparation (grey), selection pulse $\mathrm{MW_S}$ (dark green), partial ionization (light yellow), probe pulse MW_P (light green), and field ionization (dark yellow). In the lower timeline, the trapping laser timing is shown. Right: Partial diagram of the Stark levels in the $n = 50$ and $n = 52$ manifolds. The arrows represent the microwave transitions MW_S (level selection) and MW_P (probe). The two-photon transition is done with two MW photons of equal frequency despite the length difference of the arrows in the drawing.

In order to make the MW measurement most sensitive to the spatial expansion of the cloud, we use the rod electrodes to apply, at $\tau - 200$ µs (not shown), a strong electric field gradient along the z-axis while keeping the gradients in the other direction much smaller. The gradients are measured by moving the excitation volume (see Chapter IV) along the three spatial directions and performing circular-elliptical spectroscopy to measure the mean Stark shift. The dominant gradient is measured to be $\partial_z F = 0.56$ V/cm^2. The gradients in the other directions are $\partial_x F = -0.18$ V/cm^2 and $\partial_y F = 0.10$ V/cm^2. The low gradient configuration in these experiments corresponds to rod electrode voltages set to (see Chapters III and IV) $V_1 = 3.27$ V, $V_2 = 2.181$ V, $V_3 = 2.728$ V, and $V_4 = 1.818$ V. The high gradient configuration in these experiments corresponds instead to $V_1 = 1.271$ V, $V_2 = 0.181$ V, $V_3 = 4.728$ V, and $V_4 = 3.818$ V. The Stark electrode voltage was set to $V_S = 1$ V in both cases.

Along the z-axis the cloud is confined by the ponderomotive trap and a difference in the circular-elliptical MW linewidth is expected for the trapped and untrapped scenarios. The expansion rate of the linewidth depends on the temperature of the cloud, the electric field gradients, the initial size of the cloud, and the electric field sensitivity of the chosen probe transition to $|52e^-\rangle$. These parameters are brought together in a simple expansion equation that we introduce in the next section.

V.3.3 Experimental results

Under optimal circularization conditions (purity >91%, see Chapter IV) and making use of the partial ionization, we take the spectroscopic data that we show in Figure V.13. We plot the recorded spectra for $\tau = 2.8$ ms with (blue dots) and without (red dots) trapping light. We see here that the untrapped cloud is clearly wider than the trapped cloud and that the background remains small. A Gaussian fit to the spectrum of this probe transition determines its linewidth, defined by the Full With Half Maximum (FWHM) σ_{p}. We find, for the data in Figure V.13, $\sigma_{\mathrm{p,\ no\ trap}} = (0.83 \pm 0.04)$ MHz and $\sigma_{\mathrm{p,\ trap}} = (0.33 \pm 0.02)$ MHz. The data and the analysis of the linewidth as a function of time will be now presented.

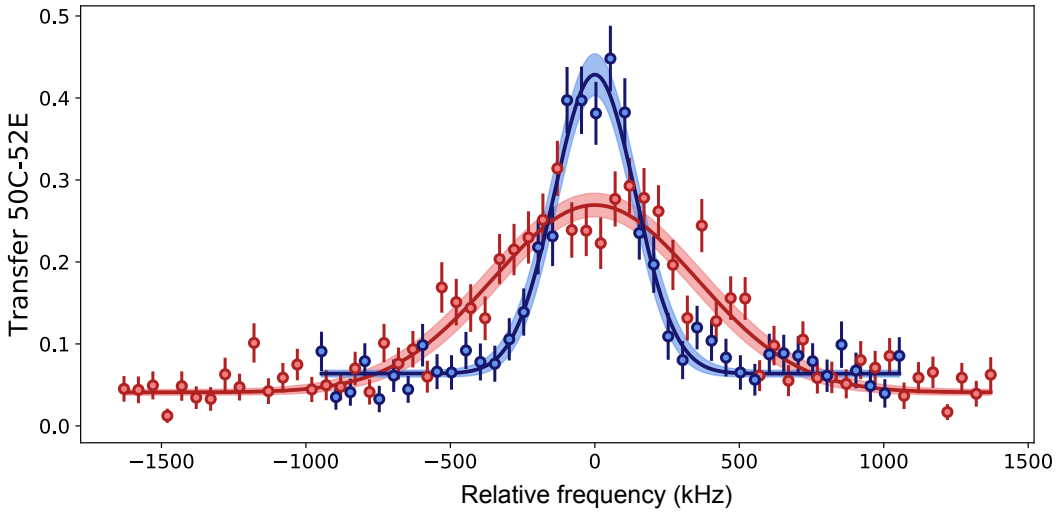

FIGURE V.13 MW_P Spectroscopy after partial ionization. The MW pulse is performed at τ =2.8 ms delay to probe the cloud expansion. The spectroscopy is done with (blue dots) and without (red dots) the trap.

Cloud expansion

In Figure V.14, we show the data illustrating the expansion and trapping. We present σ_{p} as a function of τ with (blue points) and without (red points) the trapping beam. To study the role of cRy density effects, we repeat our experiments with two average atom numbers. The initial sample has an average number of atoms $\bar{N}$ (full symbols) and a second test sample contains $\approx \bar{N}/2$ (empty symbols).[4] The density of Rydberg atoms is controlled by changing the duration of the two-photon laser excitation.

Without trapping light, the Rydberg cloud expands because of its finite temperature. When turning on the trapping laser, the linewidth remains basically constant (blue points). We only observe a slow broadening at long times resulting from the motion of the atoms along the unconfined x-axis.

[4]The calibration of detection efficiency is unknown and we restrict ourselves to inform the average number $\bar{N}$ of detected ions. This quantity represents a measurement, in arbitrary units, of the total number of Rydberg atoms prepared.

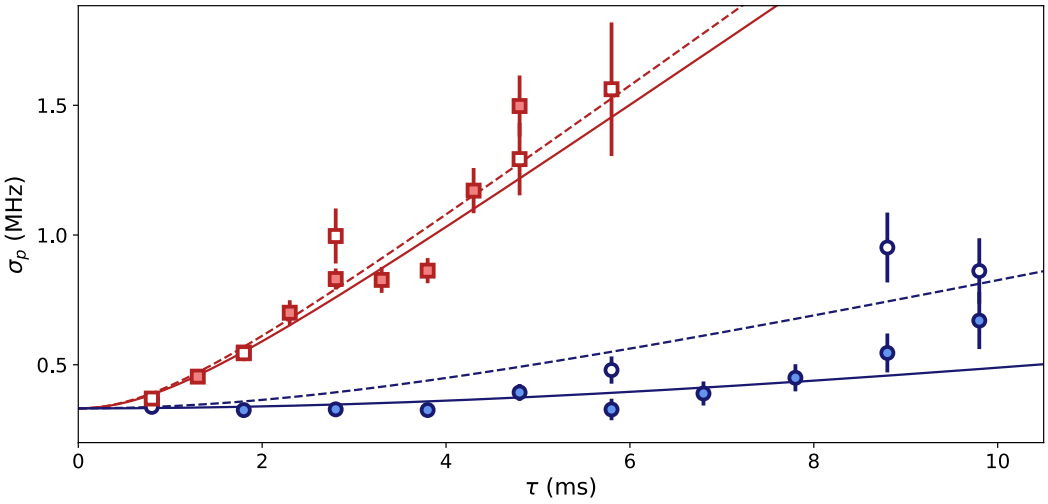

FIGURE V.14 Laser trapping. (a) FWHM σ_p of the probe transition as a function of the delay time τ for untrapped (red rectangles) and trapped (blue circles) atoms. The lines result from a classical model of the Rydberg cloud expansion for untrapped (red) and trapped (blue) atoms. Full symbols correspond to an average atom number $\bar{N}$. Open symbols correspond to measurements with about $\bar{N}/2$ atoms.

We now analyze the data with a simple thermal expansion model. Assuming an initial Gaussian spatial distribution for the Rydberg cloud, we can write that, after a free expansion of duration τ, the spatial extension is

$$\langle x_j^2 \rangle(\tau) = \langle x_j^2 \rangle_0 + \frac{k_B T}{m_\mathrm{Rb}} \times \tau^2, \tag{V.13}$$

where $x_j \in \{x, y, z\}$ and T is the temperature of the gas, k_B is Boltzmann's constant, and m_Rb is the mass of the Rubidium-87 atom. Having eq.(V.13), we can now compute the expected linewidth in presence of the gradients. When the Rydberg cloud is freely expanding, the expected FWHM of the $\mathrm{MW_P}$ spectrum reads

$$\sigma_{\mathrm{P,\ no\ trap}}(\tau) = \sqrt{\sigma_0^2 + 8\ln 2 (\beta_\mathrm{Stark} |\boldsymbol{\nabla} F|)^2 \frac{k_\mathrm{B} T}{m_\mathrm{Rb}} \times \tau^2}, \tag{V.14}$$

where $|\boldsymbol{\nabla} F|^2 = (\partial_x F)^2 + (\partial_y F)^2 + (\partial_z F)^2$, σ_0 is the FWHM at time $\tau = 0$, β_Stark =-99.8 MHz/(V/cm) is the linear Stark shift of $|52e^-\rangle$, and the $8\ln 2$ factor accounts for the difference between standard deviation and the FWHM of a Gaussian profile.

When we shine the trapping laser, atoms can only move along the x-axis. In this case, the FWHM of the $\mathrm{MW_P}$ spectrum reads

$$\sigma_{\mathrm{P,\ trap}}(\tau) = \sqrt{\sigma_0^2 + 8\ln 2 \left(\beta_\mathrm{Stark} \partial_x F\right)^2 \frac{k_\mathrm{B} T}{m_\mathrm{Rb}} \times \tau^2}. \tag{V.15}$$

To fit the data, we allow for different values of T for each data set and we take σ_0

to be a global fit parameter. We find:

- $\sigma_0 = (0.32 \pm 0.01)$ MHz,
- $T = (14.6 \pm 2.2)$ µK for untrapped atoms with $\bar{N} = 0.08$ (open red rectangles),
- $T = (12.8 \pm 0.9)$ µK for untrapped atoms with $\bar{N} = 0.18$ (solid red rectangles),
- $T = (14.4 \pm 3.2)$ µK for trapped atoms with $\bar{N} = 0.08$ (open blue circles),
- $T = (3.5 \pm 1.2)$ µK for trapped atoms, with $\bar{N} = 0.18$ (solid blue circles).

The number of detected atoms at $t = 0$ is $\bar{N} = 0.08 \pm 0.01 \approx \bar{N}_0/2$ for open symbols and $\bar{N} = \bar{N}_0 = 0.18 \pm 0.01$ for solid symbols. All but one of the temperatures found by these spectroscopic measurements are in fair agreement with the one measured by the absorption imaging time-of-flight. A much smaller temperature is found for the high number of cRy atoms when trapped. It is likely that this is an indication of the interactions in the trap. Since the atoms are trapped in a 1D-tube, the probability that two atoms come close and undergo a decircularizing collision is larger than in free space.

Lifetime in the trap

In Figure V.15, we plot the total number of detected atoms in $|50c\rangle$ (N_{tot}) before $\mathrm{MW_P}$ for trapped (blue dots) and untrapped (red dots) atoms. In both cases, the population decay reflects the thermal transfers from the initial $|52c\rangle$ state, to neighboring circular states. We observe no significant modification of the atomic lifetime when the trap is on. This shows that photoionization is quite negligible over this timescale, as expected [108]. The lines correspond to an exponential fit with a single decay time of $(4.6 \pm 0.3$ ms$)$.[5] Note that any kind of trap-induced decircularization towards other manifolds can also be neglected. Such a process would manifest itself as a modification in the expected lifetime and Figure V.15 presents no hint of it.

Population preservation in the trap

Furthermore, we check that the purity of the circular states is not appreciably affected by the trapping. To this end, in Figure V.16 we plot the total number of atoms A_p which undergo the probe microwave transition as a function of τ, with (blue dots) and without (red dots) trapping light. Experimentally, A_p is the area under the MW line. Since high-l elliptical states and the circular state ionize in the same detection window, the effect of decircularization into the same manifold would manifest itself as a reduced A_p value. Thus, the number of atoms A_p measures the purity of the circular levels, independently of their position in the electric field gradient.

[5] The time constant associated with the exponential fit is longer than the ~ 3 ms lifetime found in Chapter III due to the replenishment of $|52c\rangle$ from the neighboring levels.

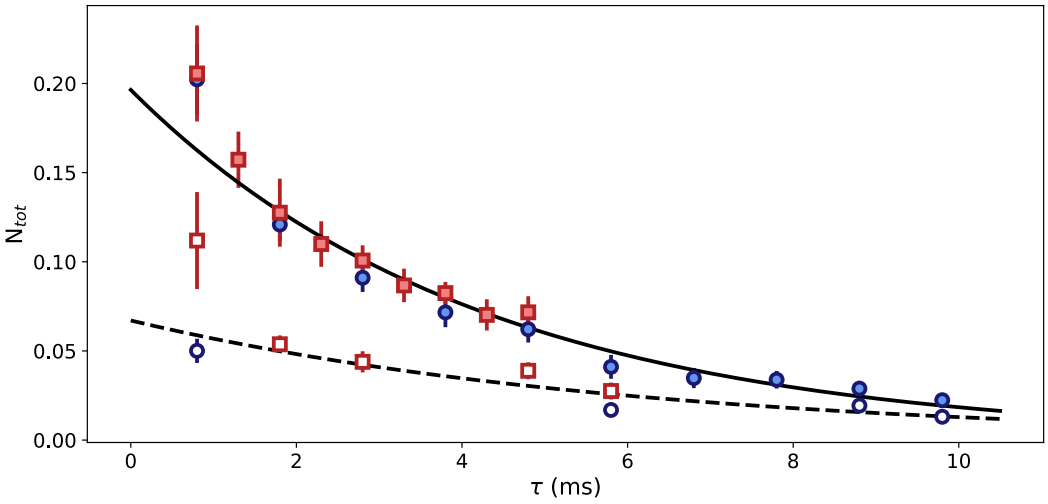

FIGURE V.15 Total population of $|50c\rangle$ before the MW_P probe pulse for trapped (blue circles) and untrapped (red rectangles) atoms. The line is an exponential fit. Full symbols correspond to an average atom number $\bar{N}$. Open symbols correspond to measurements with about $\bar{N}/2$ atoms.

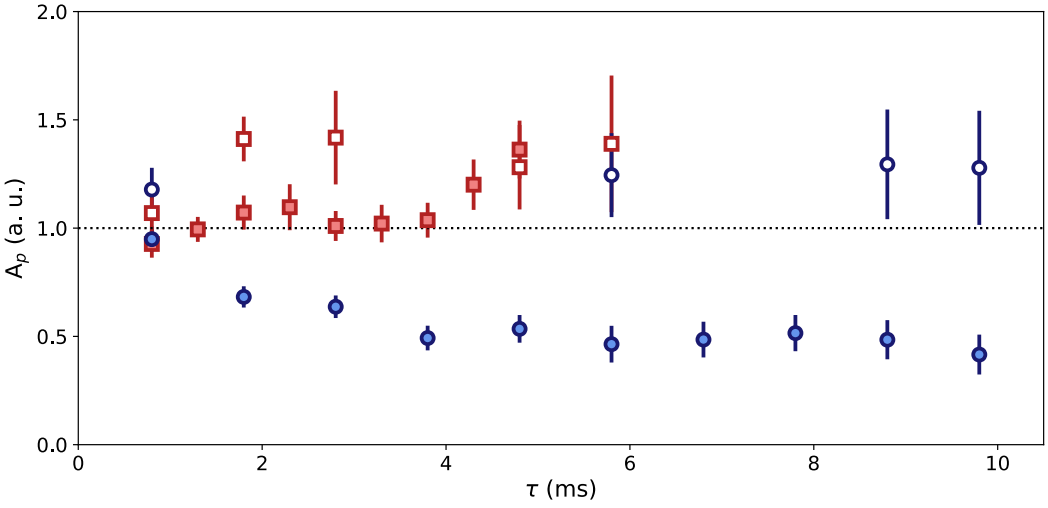

FIGURE V.16 Integrated area A_p of the MW_P probe spectrum for trapped (blue) and untrapped (red) atoms. Full symbols correspond to the measurements in Figures V.14 and V.15, for an average atom number $\bar{N}$. Open symbols correspond to measurements with about $\bar{N}/2$ atoms.

For the lowest atom number, the integrated area of the MW line A_p is nearly constant for untrapped (red open squares) and trapped (blue open circles) atoms, revealing that the trapping light does not affect the circular Rydberg level purity. For the highest atom number, A_p is also constant in the untrapped case (solid red squares) but decays rapidly (within 4 ms) to about half of its initial value for trapped atoms (solid blue circles). Once more, this effect is explained by the fact that, in a 1D-tube, the probability that two atoms come close enough to collide is larger than in free space.

V.3.4 Trap frequency

An important parameter to be determined is the mechanical oscillation frequency of the cRy atoms in the trap [91]. To measure it, an oscillating cloud of atoms is created by excitation in the inner slope of the LG trap. By turning off the trap at variable times, we expect the fast atoms to be ejected and their spatial location to depend on the trap frequency producing a measurable signal.

The timing of the experiment is shown in Figure V.17. To start the oscillation, we place the trapping beam on z_{LG} =12 µm and set the two-photon detuning to $\delta = 2.1$ MHz to excite atoms in the inner slope of the trap. In this way, the Rydberg atoms are excited at a position where the light-shift is half of its maximal value. These excitation conditions correspond to the calculation for the atomic distribution that we show in Figure V.10 (b). As before, the LG beam is on for 15 µs during Rydberg excitation. After preparation of the circular states, we switch the trap on at time $t = 0$. Under the influence of the LG confining-potential, the atoms start an oscillation mainly along the z-axis.

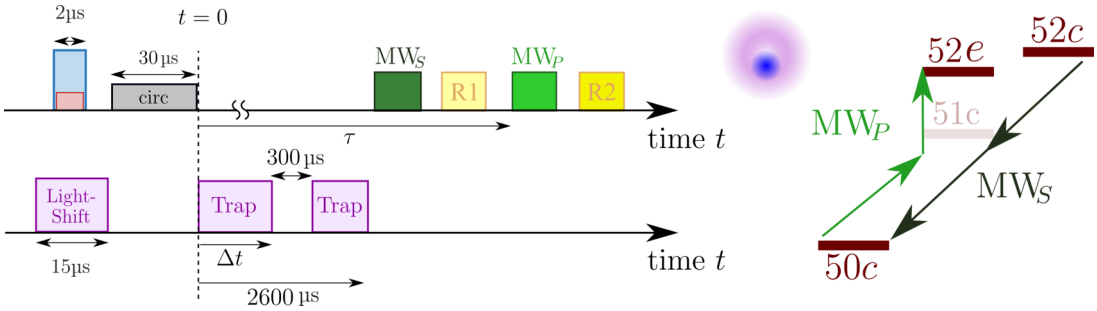

FIGURE V.17 Timing for the oscillation frequency measurement (not to scale).

In order to probe this oscillation, we turn off the LG beam for 300 µs after a variable waiting time Δt. Depending upon their velocity at time Δt, the atoms can either fly away from the trapping region or not. The 'slow' atoms are recaptured until 2.6 ms have passed, while the fast ones move away from the trap. The 300 µs duration of free evolution is long enough to allow the fast atoms to escape while they are at maximal speed, but short enough to recapture the ones moving at the lowest speeds. The recapture probability is lowest when the atoms are released while they speed through the bottom of the trap. Thus, the recapture probability oscillates at twice the trapping frequency.

We finally perform the detection sequence as above, setting MW_P at resonance with the $|50c\rangle$ to $|52e^-\rangle$ transition for the atoms at the center of the trap. The duration

$T - \Delta t$ is chosen long enough so that the atoms flying away in the electric field gradient are impervious to MW$_P$. The maximal speed of the atoms is calculated to be 18.6 cm/s, and considering the $\partial_z F = 0.56$ V/cm^2 gradient, the expected Stark shift is 2.8 MHz. Consequently, only atoms that are recaptured are successfully transferred to state $|52e^-\rangle$ while atoms flying away at different speeds are gradually detuned. The MW$_P$ pulse thus addresses *only* the atoms that remained trapped and measures the recapture probability.

In Figure V.18, we plot the number of atoms N_{52e} detected in state $|52e^-\rangle$ as a function of Δt. The damping in the blue signal is caused by a dephasing of the atomic oscillations. A perfectly harmonic trap would provide an oscillation period that is independent of the initial conditions. Thus, this damping is a signature of the trap anharmonicity and strongly depends on the trap imperfections. The dashed line is a fit to the data using a damped sinus. The angular frequency of the oscillation and the (Gaussian) damping time constant are fitted to be $2\pi \times (2.7 \pm 0.1)$ kHz and (882 ± 364) µs. The trap frequency is then measured to be $2\pi \times (1.35 \pm 0.05)$ kHz.

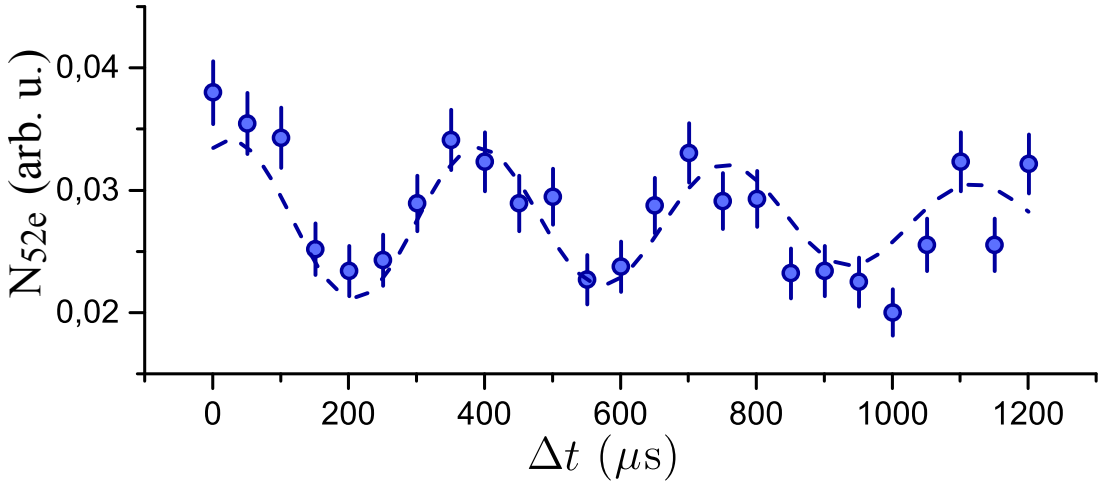

FIGURE V.18 Trap frequency measurement. Number of atoms N_{52e}, transferred to state $|52e^-\rangle$ state, as a function of time Δt during which the trap is switched off.

A posterior analysis stage provides evidence that the oscillation frequency can also be measured from the total number of atoms detected in $|50c\rangle$. The upper sketch in Figure V.19 (a) shows the evolution of a cRy in the trap as they oscillate. The vertical dashed lines mark the time corresponding to the sketched snapshots. In Figure V.19 (b), we reproduce the data in Figure V.18, and in (c), we plot the number of atoms N_{50c} detected in state $|50c\rangle$ (c, red dots) as a function of Δt. The oscillation is at the trap frequency and it is not appreciably damped (c). We understand our experimental result by noting that the atoms leave upwards in z once per period, where they reach an area of low detection efficiency. When they leave the trap downwards, they reach a high detection efficiency area. In 2.6 ms, they are estimated to fly a maximal distance of about ±480 µm. They sense a detection efficiency that produces a ∼25% of modulation on the oscillating signal.[6]

[6]We confirm the spatially varying detection efficiency by preparing, on purpose, the cRy atoms in the outer slope of the 1064 nm beam and expelling the atoms either downwards or upwards.

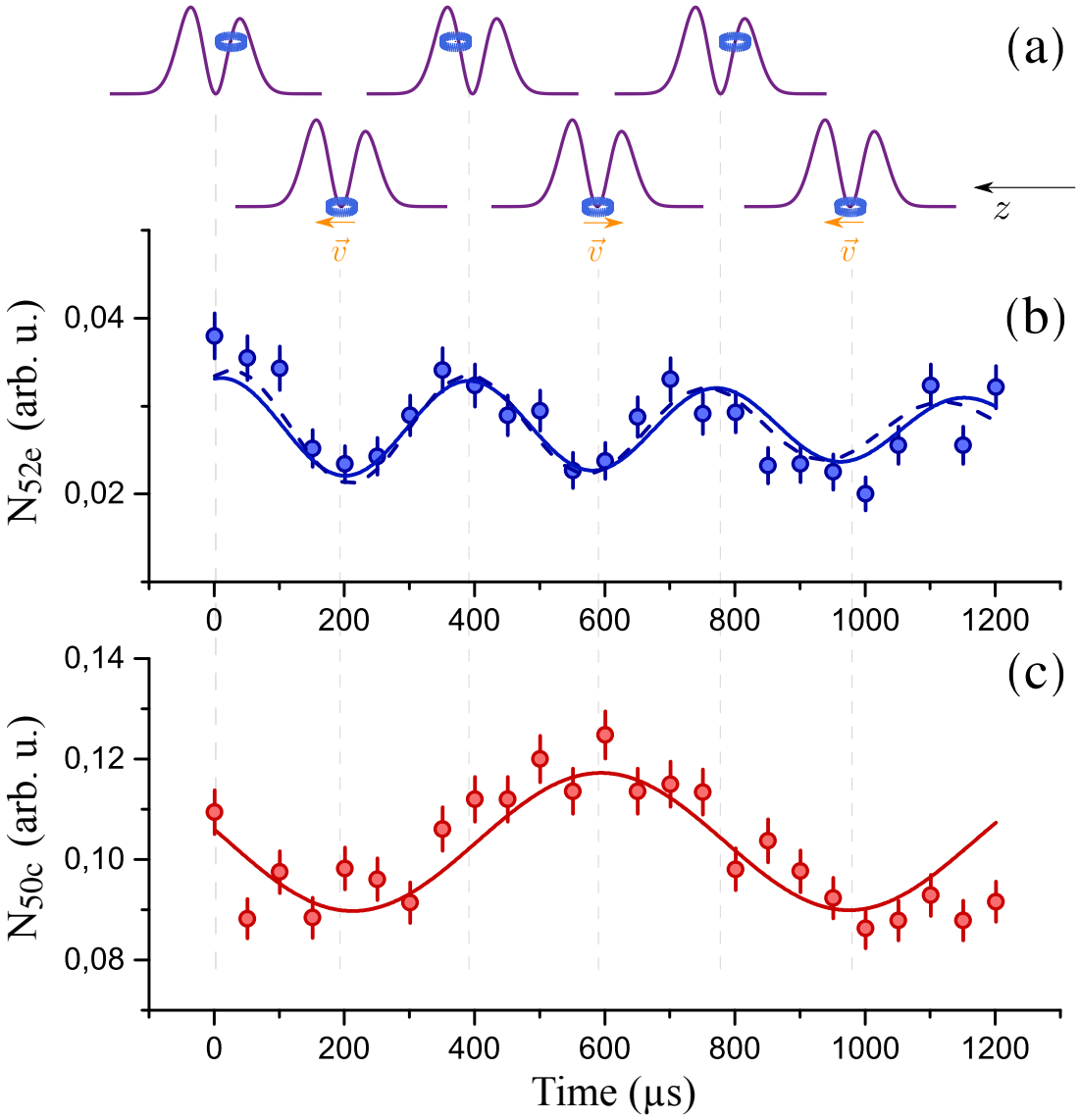

FIGURE V.19 Trap frequency measurement. (a) The top sketch shows a cRy atom oscillating in the LG trap. (b) Number of atoms, number of $|52e^-\rangle$ atoms detected. (c) Number of atoms, number of $|50c\rangle$ atoms detected. The lines are damped sinusoidal fits to the data.

We fit both signals in Figure V.19 by damped sinuses imposing the constraint that the N_{52e} signal oscillates at exactly two times the frequency of the N_{50c} signal. The phases of both signals are also constrained to be relatively shifted by $\pi/2$ as prescribed by their physical interpretation. The joint fit (solid lines) gives an angular trap frequency of $2\pi \times (1.31 \pm 0.06)$ kHz. The damping time of the fits are independent. We find that the damping for N_{50c} is negligible and that is of (1.1 ± 0.8) ms for N_{52e}. The dashed blue line in Figure V.19 (b) is the independent fit of the data also found in Figure V.18.

A Monte-Carlo simulation for the oscillation.

We reproduce the behavior of the atoms in the trap through numerical Monte-Carlo simulations. We model the trap by a 2D LG ponderomotive potential and input, as simulation parameters, the results of the fit to the data in Figure V.8. We calculate 500 atomic trajectories in the trap, with random initial positions that follow a Gaussian distribution in position, centered on ($y_{LG} = 0, z_{LG} = 12$µm) and with a width of 5 µm (see Figure V.8 (b)). The initial velocities of the atoms are randomly taken according to a Maxwell-Boltzmann distribution with a temperature of 13 µK. We then perform a discrete-time integration of the equations of motion. After the total 2.6 ms evolution, we count the fraction of atoms still within the trapping region ($\frac{y^2}{w_y^2} + \frac{z^2}{w_z^2} \leq 2$). The result of this simulation is plotted in Figure V.20. The data is fitted by a damped sinus and we find an oscillation frequency of (1.14 ± 0.01) kHz.

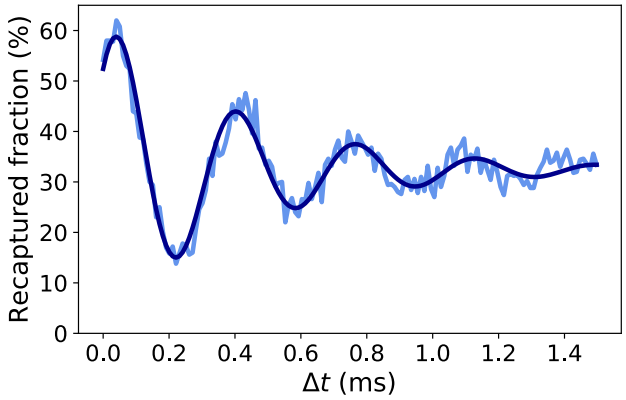

FIGURE V.20 Monte-Carlo simulation of the atomic motion in the trap. The solid dark-blue line is a damped sinusoidal fit to the simulated data (light-blue line).

We understand the difference with respect to the experimentally measured frequency by realizing that our trap profiling techniques where done at high light-shift. This approach makes our trap reconstruction sensitive to the height of the light barrier (the trap depth), but not to the structure of the trap around its center (the harmonic part). This may explain why the estimate from the Monte-Carlo simulation using the *in-situ* beam reconstruction is only in fair agreement with the oscillation frequency measurements.

We note that the damping rate of the Monte-Carlo simulation is (480±10) µs and it is faster than that of the data. This can be explained by noting that the *in-situ* reconstruction method is probably smoothing out fast variations of the trap intensity, which could account for anharmonicites and modify the damping of the oscillation. Thus, the numerical trap reconstruction may be biased.

V.3.5 Atomic coherence test

Finally, we check the coherence of the trapped circular atoms. We record, without applied field gradients, the spectrum of the $|50c\rangle$ to $|52c\rangle$ transition driven by a 215 µs microwave pulse. Figure V.21 shows the spectra obtained for untrapped (red squares)

and trapped (blue circles) atoms. The red dots are shifted upwards numerically for the purpose of this exposition. Ideally, the line is expected to have the same linewidth with and without the trap. A broadening in the presence of the trap would imply that the trap itself provides a decoherence mechanism that is absent in free space. The FWHM of Gaussian fit to the data (solid lines in Figure V.21) for untrapped and trapped atoms are respectively (5.8 ± 0.2) kHz and (5.7 ± 0.2) kHz. We thus observe, up to 200 Hz, no effect of the trapping on the transition coherence, as is expected for the ponderomotive trapping of cRy atoms. The spectrum linewidth is then determined in both cases by magnetic field noise.

We observe a $\sim$730 Hz lineshift between the two situations, compatible with a 1 mV/cm electric field drift over the one-hour data acquisition time, but no broadening.

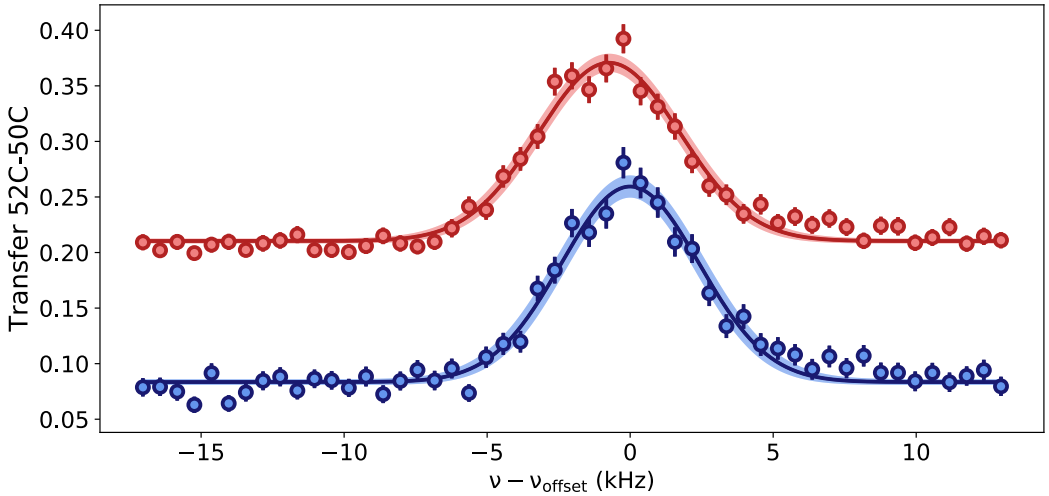

FIGURE V.21 Atomic coherence test. Microwave spectrum of the two-photon $|50c\rangle$ to $|52c\rangle$ transition for trapped (blue circles) and untrapped (red rectangles) atoms (statistical error bars) with and off-set of 49.639071 GHz. The red points have been shifted upwards for clarity.

V.4 Conclusion

We have demonstrated laser trapping of circular Rydberg atoms in two dimensions, for up to 10 ms. Since all high-angular-momentum states are efficiently trapped, the selection pulse and the ionization ramp allow us to specifically probe the trapping of atoms in the $|52c\rangle$ state. This timescale is currently limited only by the atomic lifetime in a finite-temperature environment.

We have characterized the trapping potential by making use of low-angular-momentum Rydberg atoms. This has proven to be a practical tool for these type of experiments, giving one the possibility to measure the trap profile inside the vacuum chamber. The successful implementation of the SLM to manipulate the trapping laser beam opens short-term perspectives to generalize the experiment to multiple traps.

We have verified that the ponderomotive potential does not affect the trapping lifetime as was expected from the estimated photoionization rates for circular levels, thus proving that the ponderomotive trapping is ideal for the exotic cRy states. Also, the coherence properties of the atoms are preserved in the trap, proving that, up to 200 Hz, the trap is level-independent.

Conclusion

In this work, we studied the properties of cold circular Rydberg atoms in a cryogenic environment. We addressed the proposal of a cRy atom based quantum simulator, the preparation of cold circular Rydberg atoms in a cryostat, and their laser trapping.

We prepared a cold atom cloud of Rubidium inside a Helium-4 cryostat (Chapter III). Large optical windows allowed for laser access and for the manipulation of the cold atoms. We implemented a laser excitation scheme to access Rydberg levels and we circularized them in place. The lifetime of the $|52c\rangle$ state was measured to be (3.7 ± 0.1) ms and it was limited by the black-body radiation that entered through the windows into the cold core of the experiment (Chapter IV). We mitigated the effect by reducing the effective aperture of the windows using copper irises thermalized to 4 K, and by installing MW absorber in the cold walls of the chamber. In future studies, the room temperature thermal radiation could be further reduced by using a thin layer of Indium tin oxide (ITO) on the windows. This oxide is transparent in the optical domain and near infrared, and acts like a metallic mirror at longer wavelengths, thus efficiently blocking the noxious 300 K thermal MW radiation. We note that the lifetime measurement of the cRy states can be extended to build an *in situ* atomic MW probe. One can directly measure the rates and deduce the MW mode structure from first principles. This could be of use to map the non-trivial effect of the surrounding electrodes on the electromagnetic environment. Alternatively, in a well-know mode structure, the approach can be used to directly measure the absolute MW temperature. This could be an important tool for metrology, particularly in the field of lattice atomic MW clocks, in which the black-body radiation induced shifts significantly contribute to the uncertainty budget.

The experiments done in this work are important steps towards the long-term goal of a cRy atom quantum simulator (Chapter II). In the mid-term, applications to quantum simulation and metrology could be pursued. The laser trapping of cRy atoms (Chapter V) could be extended to CQED applications, where one could use atoms trapped inside a high-finesse superconducting cavity [206, 207] to explore new regimes. Metrology could benefit from circular atoms trapped close to surfaces or close to nano structures to map the electric or magnetic field distribution beyond the standard quantum limit [106, 107].

The short-term perspectives include the implementation of optical tweezers in our experiment. An artist view of the future setup including Laguerre-Gauss tweezers is shown in Figure Conc.1 (a). In Figure Conc.1 (b), we show the experimental setup that will host the next generation of experiments. A sapphire cube will be used as a holder for a packed electrode structure and in-vacuum lenses, encapsulating a cold Rydberg atom cloud. The sapphire provides good electrical insulation, but allows for

the thermalization of the components thanks to its good thermal conductance. A pair of ITO coated lenses of a 12.5 mm diameter and 15 mm of focal length will be used to trap and image the atoms. We show only one of the lenses (blue) in Figure Conc.1 (b). The ITO metallic character allows us to use a lens close to the Rydberg atoms as an electrode and it naturally avoids the accumulation of charges along with the associated electric gradient drifts. Four 45° cylindrical apertures in the yz plane permit the access of a pair of cooling beams. Two larger apertures along the x direction allow for a third laser cooling beam and the exit of the ions after field-ionization.

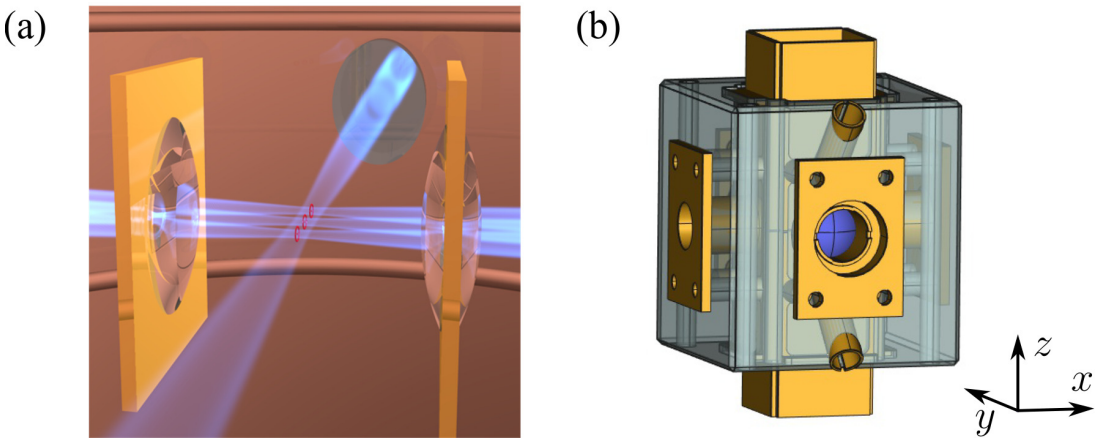

FIGURE CONC.1 (a) An artist view of the future experimental setup. In (b), a technical representation of the sapphire cube holding the gold coated electrode structure and the large numerical aperture lenses.

We will now outline some perspectives that one could explore in the years to come with this platform.

Two-dimensional arrays: expanding the Hilbert space

The perspectives provided by this new setup include the extension of the trapping potential to a two-dimensional array of traps.

Advances towards these new goals are already on their way in our group. Preliminary beam shaping experiments were done in an optical setup using a 810 nm laser, an SLM, a focusing lens with a 1 m focus, and a beam profiler camera (3.45 µm pixels). In Figure Conc.2, we show a few two-dimensional patterns we are able to produce. The long focal distance chosen permits a good resolution in the reconstruction of the beam profile. A feedback loop between the beam profiler camera and the SLM implements an automatic correction of aberrations and experimental imperfections. A modified Gerchberg-Saxton algorithm iteration provides the corrected phase mask at each step until convergence. The intensity profiles in Figure Conc.2 correspond to a 4×4 array of Gaussian beams (a), a LG_{01} beam array (b), and an array of three-dimensional Bottle beam (Bob) traps [132] (c). In Figure Conc.2 (d), we show a 10×10 Gaussian array of traps with a remarkable intensity uniformity of 0.6%. The replacement of the 1 m focal length lens by a high-numerical aperture aspherical lens with a shorter focal distance is not expected to qualitatively modify the optimization process. In the actual cube

experiment, using the second high-numerical aperture lens (not shown) will allow the recovery of the trapping light to implement the corrections.

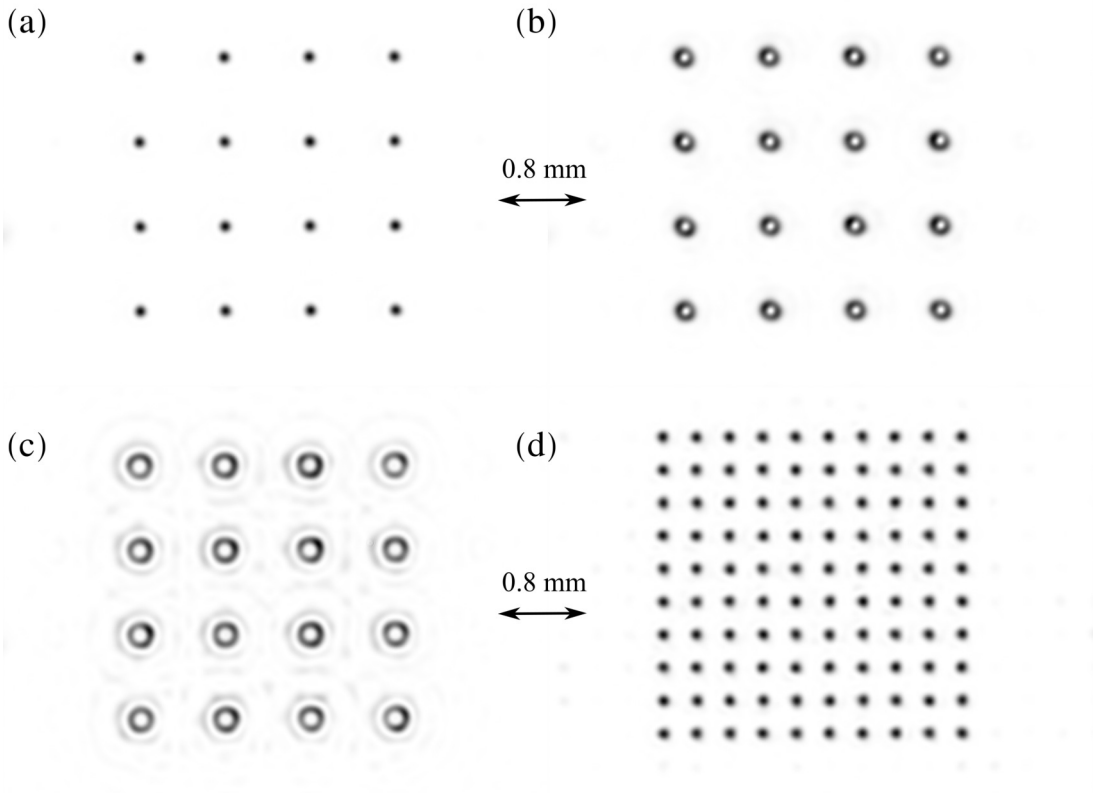

FIGURE CONC.2 Two-dimensional 4×4 arrays of Gaussians (a), LG_{01} (b), and Bob traps (c). In (d), we show an array of 10×10 Gaussian beams which are optimized to an intensity spread of 0.6% intensity.

Generalizing our simulator to a two-dimensional lattice opens the possibility of interesting quantum simulations. In general, in two-dimensional spin-1/2 lattices, finding the ground state is already challenging. The angular dependence of the van der Waals potential provides an additional degree of freedom that could be used to study topological phases of matter [102]. An intermediate step could be the study of two parallel linear chains of long lived cRy two-level atoms. This configuration can be mapped to a single linear spin-1 chain where finding the ground state is already numerically challenging. The relevant observables in these two-dimensional arrays depend on the problem to be addressed. The single cRy atom expulsion guided by a light tube as discussed in Chapter II may not be the ideal detection method in two dimensions. Instead, level selective de-circularization, combined with site addressed photoionization of the low-angular-momentum states, could be a promising road for detection. Preliminary experiments were carried out in the current setup. Two-photon Rabi and Ramsey oscillations were observed in between the $|50c\rangle$ and $|52c\rangle$ levels without field ionization. We selectively decircularized level $|52c\rangle$ into $|52F\rangle$ and measured photionization ion counts produced by the 1064 nm laser. This technique, combined with site resolved laser focusing, would directly lead to an efficient detection method in the new setup.

Note that a gold capacitive structure inhibiting the spontaneous emission (see Figure II.1) is no longer compatible with optical tweezers entering from the side due to their strong divergence. Instead, spontaneous emission for the cRy atoms trapped in tweezers could be provided by either a single mirror or a transparent ITO-coated capacitor. The laser incidence should then be normal to the flat surface. The strong divergence of the beam would allow one to trap the atoms a few hundred microns away from the surface of the inhibiting structure without damaging it. For the same reason, standing wave interference effects can be neglected due to the large intensity difference between the focus and the reflected wave. Also note that the effect of a spontaneous emission inhibiting structure varies in a typical lengthscale of a few millimeters for the MW transitions involved. This would make it possible to trap extended (disordered) arrays of atoms with a few tens of micrometers spread in their position without losing their enhanced lifetime.

Another trapping method: threading an atom with light

A variation of the ponderomotive trapping could be used to trap cRy atoms. The large circular electron orbit could in principle be 'threaded' by a Gaussian beam to produce tight 3D traps. We show the trapping scheme in Figure Conc.3 (a).

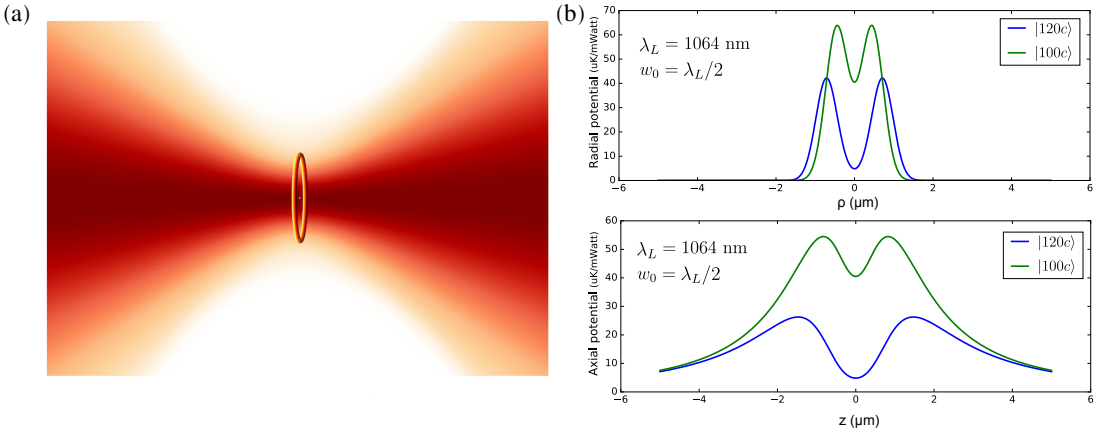

FIGURE CONC.3 A Rydberg belt for a light waist. (a) The trapping scheme. For large enough circular orbits, the trap is confining the atom in 3D. Otherwise the beam is a 2D radial trap and an anti-trap in the axial direction. In (b), we show the ponderomotive energy landscape for two large n circular atoms.

In general, the ponderomotive potential is computed by explicitly taking an average over the electron orbital. We compute the 3D trapping potential for the cRy atom by integrating a Gaussian beam profile over the semi-classical Bohr orbit[7] as (see eq.(II.17))

$$\mathcal{E}(\rho,z) = \frac{1}{2\pi}\int_0^{2\pi} d\theta \frac{q_e^2}{2m_e\epsilon_0 c}\frac{\lambda_L^2}{(2\pi c)^2}\frac{2\mathcal{P}_0}{\pi w^2(z)}\exp\{-\frac{2}{w^2(z)}[(x_n+x_\rho)^2+(y_n+y_\rho)^2]\}$$

[7]We have verified the validity of the approximation using numerical integration over the actual wave function (see Appendices).

where λ_L is the trapping light wavelength, $\mathcal{P}_0$ is the laser power, $x_n = n^2 a_0 \cos\theta$ and $y_n = n^2 a_0 \sin\theta$ are the cRy electron coordinates with respect to the atomic core, $\rho = \sqrt{x_\rho^2 + y_\rho^2}$ is atomic core distance to the beam axis, z is the position of the core (and of the electron) along the laser propagation axis, and $w(z) = w_0\sqrt{1 + (z/z_R)^2}$ is the Gaussian waist of the laser beam. We take the beam to be diffraction limited to (NA$= n_0 \sin\theta \sim 0.5$)

$$d = 2w_0 = \frac{\lambda_L}{2n_0 \sin\theta} \sim \lambda_L.$$

The trapping condition can be derived ($\partial_{r_n}\mathcal{E}\big|_{z=0,\rho=0} > 0$) to be[8]

$$2r_n > \lambda_L/\sqrt{2},$$

and it can be interpreted to mean that the Bohr atom needs to be big enough to fit a photon (of size $\sim \lambda_L$) inside its diameter. The trapping frequency in the axial direction is given by

$$\omega_z^2 = \frac{q_e^2}{m_e \epsilon_0 c}\frac{\lambda_L^2}{(2\pi c)^2}\frac{2\mathcal{P}_0}{\pi w_0^2}\frac{(2r_n^2 - w_0^2)e^{-2r_n^2/w_0^2}}{z_R^2 w_0^2 m_{\mathrm{Rb}}}.$$

In Table Conc.1, we give the wavelength range that allows the trapping of circular level $|nc\rangle$.[9] Note that, in contrast with Bob traps [132], if the circular orbit is 'too small' the focus point of the Gaussian is anti-trapping in the z direction ($\omega_z^2 < 0$). In Figure Conc.3 (b), we plot the radial and the axial potential for a $n = 100$ and $n = 120$ cRy states under the constrain of keeping the 1064 nm wavelength laser as the trapping beam. [10]

$\lvert nc\rangle$	λ_L ($n_0 \sin\theta = 0.5$)
$\lvert 50c\rangle$	<374 nm
$\lvert 60c\rangle$	<538 nm
$\lvert 70c\rangle$	<733 nm
$\lvert 80c\rangle$	<957 nm
$\lvert 90c\rangle$	<1212 nm

TABLE CONC.1 For a given NA, the trapping wavelength needed to thread different circular atoms.

On the one hand, the trapping relies in the electron charge de-localization in the circular Rydberg orbitals.[11] On the other hand, the trap is expected to work for

[8] This limit is not fundamental. The diffraction limit reads: $2r_n > \lambda_L/2\sqrt{2}n_0 \sin\theta$.

[9] Note that the Rubidium core is actually anti-trapped in this configuration. But being 1.6 hundred thousand times heavier than the electron, we neglect the effect.

[10] We note that plug-and-play commercial lasers are available from 200 nm to 300 nm with powers ranging from a few hundred milliwatts to a few Watts. For the most constraining atomic state on Table Conc.1 ($|50c\rangle$), one can get a $\sim$ 20 µK/mW trap if operating at 250 nm diffraction limited to NA=0.5. The trap frequency is computed to be $\omega_z/\sqrt{\mathcal{P}_0} \sim 2\pi\times 2.1$ MHz$/\sqrt{\mathrm{W}}$ for Rubidium. We note that this wavelength is used to excite Calcium Rydberg ions and that $m_{\mathrm{Ca}} \lesssim m_{\mathrm{Rb}}/2$.

[11] Note that this is a kind of trap that relies on the specific geometry of the electron orbital.

any superposition of circular Rydberg atoms fulfilling the trapping condition. This includes the $|nc\rangle + |(n+1)c\rangle$ 'planetary atom' superposition (see Figure I.1). In the semi-classical picture, the potential is provided by the time average of the GHz rotation of the localized electron around the core.

The tight confinement (submicrometer) of the atoms in this trap can be considered an asset, but it also implies a constraint in the initial position of the atom. It may be possible to use the same Gaussian beam that provides the circular atom trap as a conventional dipole trap for the ground state atom. This single beam trapping both the ground state atom and the circular state, may allow for the experimental realization. Note that low-angular-momentum Rydberg atoms are anti-trapped and, thus, fast circularization (~ 0.5 µs) and cold atoms (~ 50 µK) would be a requirement to avoid the laser missing the needle-eye.[12] Another problem that one would need to face is the fact that the longitudinal confinement of the ground state atoms in the dipole trap is of the order of the cRy trap extension. This uncertainty in the initial longitudinal position of the atom would probably lead to a reduced efficiency in the preparation of trapped cRy atoms. This could be mitigated by high-laser intensity during the ground-state trapping and colder atoms.

One could also consider using the Rubidium Rydberg excitation beam (at 420-480 nm) to provide the circular atom trapping. Using a blue beam with a shorter wavelength would relax the constraint on the principal quantum number n and would enable exciting and trapping the $|60c\rangle$ state with the same laser. In Figure Conc.4, we show the ponderomotive energy landscape for a few circular states for a beam of 420 nm wavelength focused down to the diffraction limit (NA=0.5). The corresponding axial trapping frequency for $|60c\rangle$ ($|80c\rangle$) is computed to be $\omega_z/\sqrt{\mathcal{P}_0} \sim 2\pi\times 1.2$ MHz$/\sqrt{\text{W}}$ ($2\pi\times 0.53$ MHz$/\sqrt{\text{W}}$).[13]

We note that, in these conditions, the electron is trapped in a high-intensity area. This makes the negligible photoionization rate of circular atoms an important asset. Also note that Compton elastic scattering may limit the coherence of the trapped cRy atom. We can make a back-of-the-envelope calculation to evaluate the magnitude of the process. We pessimistically assume that, as soon as an electron-photon scattering occurs, the cRy state is lost. Using the Thompson diffusion model to compute the non-relativistic scattering cross section of a free electron and the Gaussian beam intensity at distance r_n from the beam axis, we found the state lifetime associated to this process to be > 2.6 s/mWatt for state $|60c\rangle$ and > 85 s/mWatt for state $|80c\rangle$.

As a final comment, we note that, so far, we have discussed a parameter regime where the circular Rydberg electron acts as a tight belt to the Gaussian hyperboloid, but another configuration is in principle reachable. In Figure Conc.4, we show that for 420 nm and $n = 100$, the condition $2r_n \gg \lambda_L/\sqrt{2}$ is fulfilled and that the atom finds itself in a cylindrical 'box trap' ($\omega_z \to 0$): the atom is essentially free until the electron ring finds the hard inner light thread. In these conditions the electron is permanently in the dark. The trap would then be dominated by anharmonicities and Compton elastic scattering would not be a limiting factor (the estimation yields 10^{10} s/mWatt for state $|100c\rangle$).

[12] Note that a few mW will produce a negligible amount of photionization during a few microseconds.

[13] Considering state $|60c\rangle$, a 10 mW beam of 420 nm wavelength provides a trap frequency of $\omega_z = 2\pi\times 120$ kHz and a trap depth of about 100 µK. The spatial confinement is to a few hundred nanometers.

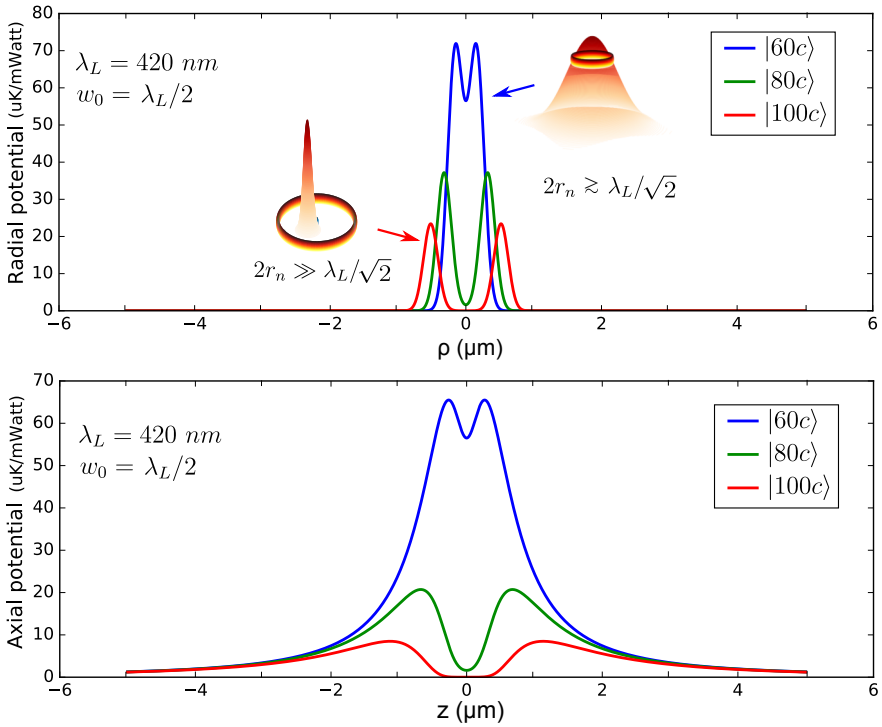

FIGURE CONC.4 The Rydberg excitation laser beam can also be used to provide the trapping. For large atoms and tight focused lasers, the cRy is 'canned' in a cylindrical volume.

Coupling to phonons: a van der Waals spin-boson model

Another interesting way to expand the Hilbert space of quantum simulations with cRy atoms is to include the motional degrees of freedom of the atoms in the description. One could decide to allow phonon excitations in the chain and, in this way opening a big Hilbert space with only a few atoms in a linear array. Using 'strong' interactions and 'weak traps' the spin exchange efficiently couples to the motional modes changing the dynamics of the system. Under these conditions, computing the evolution of a four or five atom chain is classically hard, but the physical realization could be within reach in the future. The model could be used to study a transition from Markovian to non-Markovian entanglement induced decoherence in the nearest neighbour regime. Simple analytical expressions can be derived for the two-atom case in harmonic traps (of frequency ω_x), where one finds hints of the physical effects that one could explore: Assuming that one can cool down the atoms to the ground state, the initial state can be written as $|\psi(0)\rangle = |48c, 50c\rangle_s|0,0\rangle_x$. Here, the first ket on the right-hand side stands for the spin degree of freedom and the second ket stands for the motional ground state of both atoms. For small oscillations with respect to the interatomic distance R [96, 108], one can show that the state will evolve into an entangled state in the form

$$|\psi(t)\rangle = \frac{1}{\sqrt{2}}\left(|+\rangle_s|\Xi^+(t)\rangle_x + |-\rangle_s|\Xi^-(t)\rangle_x\right),$$

where $|\Xi^\pm(t)\rangle_x$ is the two-oscillator state[14] and $|\pm\rangle_s \sim |48c, 50c\rangle \pm |50c, 48c\rangle$ are the

[14]The two-atom system evolves into a two-oscillator Schröndinger-cat state where the pair of atoms

spin eigenvalues of the van der Waals interaction. The reduced density matrix for the spin is obtained by taking the partial trace over the motional degree of freedom. In the $\{|+\rangle_s, |-\rangle_s\}$ basis, the partial density matrix reads

$$\hat{\rho}_s = \mathrm{Tr}_x(|\psi(t)\rangle\langle\psi(t)|) = \frac{1}{2}\begin{pmatrix} 1 & \Lambda e^{i4Jt} \\ \Lambda e^{-i4Jt} & 1 \end{pmatrix},$$

where $J = A_6/2R^6$ is the the spin exchange coupling (see eq.(II.6)) and the coherence $\Lambda(t) = |\langle\Xi^+(t)|\Xi^-(t)\rangle|$ is a measure of the entanglement between the spin and the motion of the atoms. The spin oscillations will then have a contrast given by $\Lambda^2 = e^{-8(J\eta/\omega_x)^2(1+\cos\omega_x t)}$, where we have introduced an analog to the Lamb-Dicke parameter for ion traps $\eta = 6/R\sqrt{\hbar/2\omega_x m_{\mathrm{Rb}}}$.[15] The phonon modes in a two-atom system, acting like a non-Markovian environment, induce an entanglement oscillation that modulates the spin coherence at the trap frequency ω_x. In Figure Conc.5 (a), we show the periodic contrast revivals. In Figure Conc.5 (b), we show the minimal contrast Λ_m^2 as a function of the inter-atomic distance R for a few trap frequencies and $A_6 = h \times 1$ GHzμm^6. At 5 μm the spin coupling constant is $J = h \times 32$ kHz. Including more atoms in the chain, which can be considered as an environment in themselves, would introduce more accessible motional modes and modify the entanglement dynamics. This could lead to studies complementing those already being carried out in other platforms.

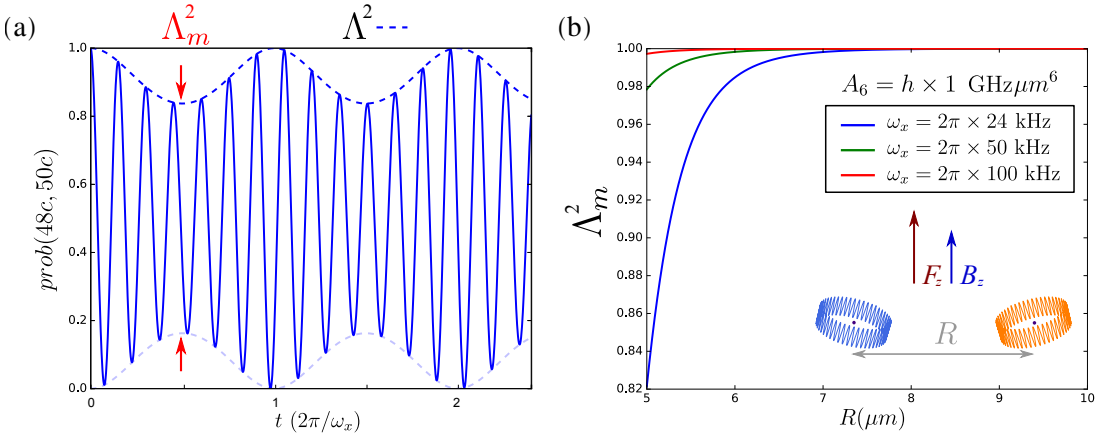

FIGURE CONC.5 In (a), we show the entanglement oscillation between the phonons and the spins. In (b), we show the minimal contrast Λ_m^2 for the spin oscillation as a function of distance.

The diverse behaviours one could access in a cRy based simulator as one tunes the different experimental parameters (dimensionlaity, principal quantum number n, the directing fields, the interatomic distance, the trap frequency, the geometry, etc.) make this platform interesting.

is in a superposition of classical coherent states $|\pm\alpha, \mp\alpha\rangle_x$.

[15] Here, the frequency $J\eta \propto 1/R^7$ is the Rabi frequency for the spin-phonon coupling.

Appendices

Appendix A

Stochastic treatment of dephasing

In this appendix, we discuss a model to quantitatively analyse the coherence properties of single qubits. We focus on the free induction decay (Ramsey) and on the spin-echo sequence. We treat the phase of a qubit superposition as a random variable and we integrate the stochastic equations that determine its statistical properties [208]. This analysis allows us to transform the measurable coherence properties of the quantum state into the noise parameters directly affecting the qubits [199]. Also, the analysis provides an efficient way to reconstruct the noise spectrum in the experiment.

In the second part of this appendix we develop the calculations for three examples.

A.1 A general dephasing process

Consider an ensemble of N qubits that we label with the letter j. At time $t = 0$, all are prepared in the same state superposition that we label $|\psi_j(0)\rangle = \frac{1}{\sqrt{2}}(|\uparrow\rangle + |\downarrow\rangle)$. Consider also that, at $t > 0$, a noise process starts, resulting in the accumulation of a relative stochastic phase $\varphi_j(t)$. The purity ($\gamma(t)$ =Tr$[(\sum_j^N |\psi_j(t)\rangle\langle\psi_j(t)|/N)^2]$) of the ensemble is set to degrade and here we work out a model to describe the state evolution. This purity is a direct measure of the contrast ($C(t) = \gamma(t)$) of the quantum interference terms that one can measure.

We now write the phase of the superposition for the jth trajectory as

$$|\psi_j(t)\rangle = \frac{1}{\sqrt{2}}(|\uparrow\rangle + e^{-i\varphi_j(t)}|\downarrow\rangle).$$

We write the phase as given by an integral of the energy difference between the two states $E_\downarrow(t) - E_\uparrow(t) = \hbar\Delta_j(t)$:

$$\varphi_j(t) = \int_0^t \Delta_j(t)dt.$$

One can compute the purity to be

$$\gamma(t) = \mathbf{Re}\{\langle e^{i\varphi_j}\rangle_j\},$$

where the angle brackets ($\langle\cdot\rangle_j$) stands for the average over the noise realizations (the different qubits). The calculation of this mean value can be done straightforwardly. Assuming that the phase is Normally distributed (Gaussian noise, $\varphi_j(t) \sim$ Normal$(0, \sigma_\varphi^2(t))$),

one can write

$$\langle e^{i\varphi_j}\rangle_j = \sum_n^{\infty} \frac{1}{n!}\langle (i\varphi_j)^n\rangle_j.$$

and make use of the identity $\langle (i\varphi_j)^n\rangle_j = (-1)^k \frac{(2k)!}{2^k k!}\sigma_\varphi^{2k}$. Note that the sum only runs over $n = 2k$ since the odd moments are zero. The expression for the purity then reads

$$\boxed{\gamma(t) = e^{-\frac{\sigma_\varphi^2(t)}{2}}}$$

The contrast drop of the coherences (dephasing) as a function of time depends on the specificities of the noise model used. One can readily express the noise variance as a function of the noise autocorrelation, as

$$\sigma_\varphi^2(t) = \int_0^t dt_1 \int_0^t dt_2 \langle \Delta_j(t_1)\Delta_j(t_2)\rangle_j.$$

A general way to construct different types of Gaussian noise is to filter a Gaussian white noise $W_j(t)$

$$\Delta_j(t) = \int_{-\infty}^{t} W_j(t') g_{\tau_\varphi}(t'-t)dt'$$

where $g_{\tau_\varphi}(t'-t)$ is the noise filter function. The stochastic process $W_j(t)$ is completely defined by $\langle W_j(t)\rangle_j = 0$ and $\langle W_j(t_1)W_j(t_2)\rangle_j = D_\varphi \delta(t_1 - t_2)$. The noise filter function g_{τ_φ} is a normalized function ($\int_{-\infty}^{t} g_{\tau_\varphi}(x)dx = 1$) that depends on a single parameter: the correlation time τ_φ. Note that we have imposed causality by including the integration limit t in the argument of $g_{\tau_\varphi}(t'-t)$. Finally, the variance of the phase random variable reads

$$\boxed{\sigma_\varphi^2(t) = D_\varphi \int_0^t dt_1 \int_0^t dt_2 \beta_{\tau_\varphi}(t_1 - t_2),} \tag{A.1}$$

where β_{τ_φ} is the autocorrelation function of the filter function $g_{\tau_\varphi}(x)$.

The phase evolution can be modified by introducing a π-rotation of the qubits on the Bloch sphere. This is known as spin-echo technique. By applying the π-pulse at time t_π, and assuming an infinitely short and perfect pulse, the phase undergoes the transformation $\varphi \to -\varphi + \pi$. The time evolving phase for $t > t_\pi$, which we denote now with a tilde, reads

$$\varphi_j(t) \to \tilde{\varphi}_j(t) = -\int_0^{t_\pi} \Delta_j(t')dt' + \pi + \int_{t_\pi}^{t} \Delta_j(t')dt'.$$

The variance reads

$$\sigma_{\tilde{\varphi}}^2 = \left(\int_0^{t_\pi}\int_0^{t_\pi} dt_1 dt_2 + \int_{t_\pi}^{t}\int_{t_\pi}^{t} dt_1 dt_2 - 2\int_0^{t_\pi} dt_1 \int_{t_\pi}^{t} dt_2 \right) \langle \Delta_j(t_1)\Delta_j(t_2)\rangle_j.$$

and simplifies to

$$\boxed{\sigma_{\tilde{\varphi}}^2 = D_\varphi \left(\int_0^{t_\pi} \int_0^{t_\pi} dt_1 dt_2 + \int_{t_\pi}^{t} \int_{t_\pi}^{t} dt_1 dt_2 - 2 \int_0^{t_\pi} dt_1 \int_{t_\pi}^{t} dt_2 \right) \beta_{\tau_\varphi}(t_1 - t_2).} \quad \text{(A.2)}$$

From eq.(A.1) (Ramsey) and eq.(A.2) (spin-echo) note that D_φ is only a scaling factor and plays no role in the functional form of the phase diffusion.

A.2 Three examples

Here, we first develop a minimalist example to show evidence for some general properties of stochastic phase diffusion. This minimalist model cannot be written as filtered Gaussian white noise and lays beyond the theory in the first section of this appendix. Secondly, we discuss the details of the calculation for a more realistic Lorentzian noise that we use to analyze that data discussed in Chapter IV. The last example is that of a Gaussian spectrum for the noise. These two last examples are completely encompassed by the theory from the previous section and they can be taken as an illustration of the general procedure.

A.2.1 A minimalist model

We now consider a model with the minimal ingredients to explain two decoherence time constants T_2^* and T_2. With this purpose, we include a fully reversible noise (static gradients) and a completely irreversible noise (white noise).

A.2.1.1 Slow noise (reversible)

Here we consider the case in which each qubit has its own precession frequency, constant in time. The decoherence (purity drop as time elapses) arises from the average of the oscillations at different frequencies. Atom j has frequency ω_j. The variance of that frequency is $\sigma_\omega^2 = \langle \omega_j^2 \rangle_j$ (center at zero $\langle \omega_j \rangle_j = 0$, corresponding to an interaction representation).[1] The phase variance reads

$$\varphi_j(t) = \int_0^t \omega_j dt = \omega_j t$$

$$\sigma_\varphi^2(t) = \sigma_\omega^2 t^2.$$

A.2.1.2 Fast (uncorrelated) noise (irreversible)

Now consider a Gaussian white noise contribution to the phase diffusion $W_j(t)$. The phase accumulation in these conditions reads

$$\varphi_j(t) = \int_0^t W_j(s) ds$$

[1] If instead of purely DC noise one considers a sinusoidal noise with a frequency much smaller than any other process in the experiment, the general argument still holds. Note that the contribution of a sinusoidal noise at a very low frequency will have a bi-modal distribution.

$$\langle\varphi_j^2(t)\rangle_j = \int_0^t ds \int_0^t ds' \langle W_j(s)W_j(s')\rangle_j$$

$$\sigma_\varphi^2(t) = \langle\varphi_j^2(t)\rangle_j = D_\varphi t.$$

A.2.1.3 The variance during the free induction decay (Ramsey)

Considering a process with a slow and a fast noise contribution, the qubit energy reads $\Delta_j(t) = \omega_j + W_j(t)$ and the variance is then computed to be

$$\boxed{\sigma_\varphi^2(t) = \sigma_\omega^2 t^2 + D_\varphi t.}$$

A.2.1.4 Spin-echo

We turn to compute the phase variance after the π-pulse. The phase random variable for $t < t_\pi$ reads

$$\varphi_j(t) = \int_0^t \omega_j + W_j(t)dt.$$

Knowing that an ideal π-pulse transforms the phase as $\varphi \to -\varphi + \pi$, one can write

$$\tilde{\varphi}_j(t) = -\int_0^{t_\pi} (\omega_j + W_j(t))dt + \pi + \int_{t_\pi}^t (\omega_j + W_j(t))dt.$$

The variance is then $\sigma_{\tilde{\varphi}}^2(t) = \langle\tilde{\varphi}_j^2(t)\rangle_j - \langle\tilde{\varphi}_j(t)\rangle_j^2$. One has

$$\tilde{\varphi}_j^2(t) = \pi^2 + [-\int_0^{t_\pi} (\omega_j + W_j(t))dt]^2 + [\int_{t_\pi}^t (\omega_j + W_j(t))dt]^2$$

$$-2\int_0^{t_\pi} (\omega_j + W_j(t))dt \times \int_{t_\pi}^t (\omega_j + W_j(s))ds + ...$$

$$\tilde{\varphi}_j^2(t) = \pi^2 + [\int_0^{t_\pi} \omega_j dt]^2 + [\int_0^{t_\pi} W_j(t)dt]^2 + [\int_{t_\pi}^t \omega_j dt]^2 + [\int_{t_\pi}^t W_j(t)dt]^2$$

$$-2\omega_j^2 t_\pi(t - t_\pi) + ...$$

where '...' stand for terms that are either linear in W_j or in ω_j and will go to zero after averaging: $\langle\omega_j W_j\rangle_j = \langle\omega_j\rangle_j\langle W_j\rangle_j = 0$. One then gets

$$\langle\tilde{\varphi}_j^2(t)\rangle_j = \pi^2 + \sigma_\omega^2 t_\pi^2 + D_\varphi t_\pi + \sigma_\omega^2(t - t_\pi)^2 + D_\varphi(t - t_\pi) - 2\sigma_\omega^2 t_\pi(t - t_\pi)$$

That finally simplifies to

$$\boxed{\sigma_\varphi^2(t) = \sigma_\omega^2(t - 2t_\pi)^2 + D_\varphi t.}$$

Where the DC component of the phase accumulation $\sigma_\omega^2(t-2t_\pi)^2$ is perfectly cancelled at time $2t_\pi$ and the phase accumulation due to the fast noise $D_\varphi t$ is unaffected by the π-pulse.

The maximal contrast for $t > t_\pi$ can be found analytically to be

$$t_E = \begin{cases} t_\pi & t_\pi < \frac{D_\varphi}{2\sigma_\omega^2} \\ 2t_\pi - \frac{D_\varphi}{2\sigma_\omega^2} & t_\pi > \frac{D_\varphi}{2\sigma_\omega^2}. \end{cases}$$

A.2.1.5 Observations

We make the following observations.

i. If one performs the π-pulse too early ($t_\pi < \frac{D_\varphi}{2\sigma_\omega^2}$), then the contrast will continue to decrease. This is easy to understand: for $t < \frac{D_\varphi}{2\sigma_\omega^2}$ the irreversible term (linear in time, see Figure A.1 (a)) dominates over the reversible phase accumulation term (quadratic in time) and, thus, the contrast drop cannot be reversed. For longer times the quadratic term dominates over the linear term and the oscillation has a revival. The time of the maximum echo contrast after the π-pulse as a function of t_π is plotted in Figure A.1 (b).

ii. Note that, by taking the derivative with respect to t_π (for $t_\pi > \frac{D_\varphi}{2\sigma_\omega^2}$), fixing $t = t_0$, and equating to zero, one can find the value of t_π that maximizes the contrast at any given t_0. We then have that $\partial_{t_\pi}\sigma_{\tilde{\varphi}}^2(t=t_0) = 0$ implies

$$\boxed{t_\pi = t_0/2,}$$

and, thus, to have the optimal contrast at a given t_0, one needs to perform the π-pulse at $t_0/2$.

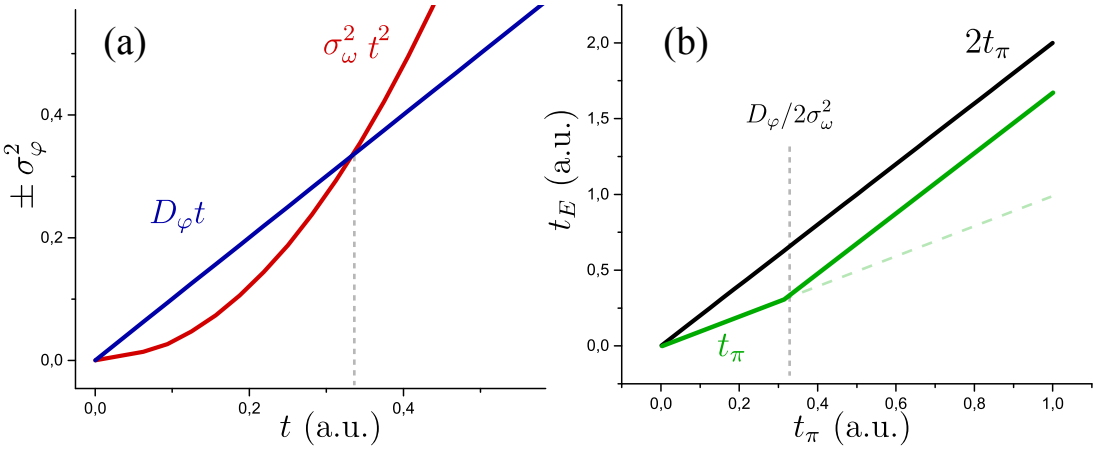

FIGURE A.1 (a) Reversible (red) and irreversible (blue) contributions to the phase diffusion. (b) The echo revival time (green) as a function of t_π. The black line corresponds to the line with slope 2. The revival time shows a sharp slope change that happens at the time where the dephasing character changes from irreversible to reversible.

A.2.2 Lorentzian noise spectrum: our experimental situation

We model our data (see Chapter IV) by temporal noise with a Lorentzian spectrum. No static gradients are required to explain our experimental observations. This kind of noise model is physically relevant as it arises from the natural band-pass in the standard experimental setup. Imposing a Lorentzian spectrum on the energy time dependence $\hbar\Delta_j(t)$ by taking Gaussian white noise and filtering it with an exponential function, one has

$$\Delta_j(t) = \int_{-\infty}^{t} W_j(\tau)\frac{e^{\frac{\tau-t}{\tau_\varphi}}}{\tau_\varphi}d\tau. \tag{A.3}$$

At each time t, the phase is $\varphi_j(t) = \int_0^t \Delta_j(t_1)dt_1$ and its moments are calculated as follows:

$$\langle\varphi_j(t)\rangle_j = 0.$$

$$\langle\varphi_j^2(t)\rangle_j = \langle\int_0^t dt_1\int_0^t dt_2\Delta_j\left(t_1\right)\Delta_j\left(t_2\right)\rangle_j,$$

$$\langle\varphi_j^2\rangle_j = \left(\frac{1}{\tau_\varphi}\right)^2\int_0^t dt_1\int_0^t dt_2\int_{-\infty}^{t_1} d\tau_1\int_{-\infty}^{t_2} d\tau_2 e^{\frac{\tau_1+\tau_2-t_1-t_2}{\tau_\varphi}}\langle W_j\left(\tau_1\right)W_j\left(\tau_2\right)\rangle_j. \tag{A.4}$$

Using explicitly that

$$\langle W_j(\tau_1)W_j(\tau_2)\rangle_j = D_\varphi\delta(\tau_1-\tau_2), \tag{A.5}$$

one can readily compute the variance $\sigma_\varphi^2 = \langle\varphi_j(t)\rangle_j^2$ as

$$\sigma_\varphi^2(t) = D_\varphi\left(\frac{1}{\tau_\varphi}\right)^2\left(\int_0^t dt_2\int_0^{t_2} dt_1\int_{-\infty}^{t_1} d\tau_1 e^{\frac{2\tau_1-t_1-t_2}{\tau_\varphi}} + \int_0^t dt_2\int_{t_2}^t dt_1\int_{-\infty}^{t_2} d\tau_2 e^{\frac{2\tau_2-t_1-t_2}{\tau_\varphi}}\right).$$

$$\sigma_\varphi^2(t) = \frac{D_\varphi}{2\tau_\varphi}\left(\int_0^t dt_2\int_0^{t_2} dt_1 e^{\frac{t_1-t_2}{\tau_\varphi}} + \int_0^t dt_2\int_{t_2}^t dt_1 e^{\frac{t_2-t_1}{\tau_\varphi}}\right)$$

$$\sigma_\varphi^2(t) = \frac{D_\varphi}{2}\left(\int_0^t dt_2\left(1-e^{\frac{-t_2}{\tau_\varphi}}\right) - \int_0^t dt_2\left(e^{\frac{t_2-t}{\tau_\varphi}}-1\right)\right)$$

$$\sigma_\varphi^2(t) = \frac{D_\varphi}{2}\left(\left(t+\tau_\varphi\left(e^{\frac{-t}{\tau_\varphi}}-1\right)\right) - \tau_\varphi\left(1-e^{\frac{-t}{\tau_\varphi}}\right)+t\right)$$

$$\boxed{\sigma_\varphi^2 = D_\varphi(t+\tau_\varphi(e^{-\frac{t}{\tau_\varphi}}-1)).}$$

A.2.2.1 Observations

We make the following observations.

i. At long times ($t \gg \tau_\varphi$), the variance time dependence becomes linear and reminds us of a 'random walk'

$$\sigma_\varphi^2(t) \sim D_\varphi t.$$

The energy undergoes a Wiener process, and is ruled by a Brownian diffusion equation.

ii. Our experimental situation: At short times ($t \ll \tau_\varphi$), the variance grows quadratically and reminds us of a 'free expansion'

$$\sigma_\varphi^2(t) \sim D_\varphi \frac{t^2}{2\tau_\varphi}.$$

iii. The term, $\tau_\varphi(e^{-\frac{t}{\tau_\varphi}} - 1)$, is negative and 'slows down' decoherence. This exponential memory acts like a low-pass filter and reminds us of an electric or magnetic 'discharge' affecting the coherence. In the limit of infinite memory, decoherence is stopped completely as $\tau_\varphi \to \infty$, $\sigma_\varphi^2 \to 0$, which is the result of a flat average on white noise.

A.2.2.2 Phase variance during the spin-echo in the case of Lorentzian noise

If a perfect π-pulse is done at $t = t_\pi$, the subsequent phase is (the tilde in $\tilde{\varphi}$ denotes the phase variable after the π pulse $t > t_\pi$):

$$\tilde{\varphi}_j(t) = -\int_0^{t_\pi} \Delta_j(t)dt + \pi + \int_{t_\pi}^{t} \Delta_j(t)dt.$$

the mean value is $\langle\tilde{\varphi}_j(t)\rangle_j = \pi$ and the second moment is calculated in the same manner as before:

$$\langle\tilde{\varphi}_j^2(t)\rangle_j = \pi^2 + \langle(\int_0^{t_\pi} \Delta_j(t)dt)^2\rangle_j + \langle(\int_{t_\pi}^{t} \Delta_j(t)dt)^2\rangle_j +$$

$$-2\langle\int_{t_\pi}^{t} \Delta_j(t_1)dt_1 \int_0^{t_\pi} \Delta_j(t_2)dt_2\rangle_j + 2\pi\langle\int_{t_\pi}^{t} \Delta_j(t)dt\rangle_j - 2\pi\langle\int_0^{t_\pi} \Delta_j(t)dt\rangle_j.$$

$$\langle\tilde{\varphi}_j^2(t)\rangle_j = \pi^2 + \int_0^{t_\pi}\int_0^{t_\pi} \langle\Delta_j(t_1)\Delta_j(t_2)\rangle_j dt_1 dt_2 + \int_{t_\pi}^{t}\int_{t_\pi}^{t} \langle\Delta_j(t_1)\Delta_j(t_2)\rangle_j dt_1 dt_2 +$$

$$-2\int_{t_\pi}^{t} dt_1 \int_0^{t_\pi} dt_2 \langle\Delta_j(t_1)\Delta_j(t_2)\rangle_j + 2\pi\int_{t_\pi}^{t} \langle\Delta_j(t)\rangle_j dt - 2\pi\int_0^{t_\pi} \langle\Delta_j(t)\rangle_j dt.$$

Now using that $\langle \Delta_j(t) \rangle_j = 0$

$$\langle \tilde{\varphi}_j^2(t) \rangle_j = \pi^2 + \int_0^{t_\pi} \int_0^{t_\pi} \langle \Delta_j(t_1)\Delta_j(t_2) \rangle_j dt_1 dt_2 + \int_{t_\pi}^{t} \int_{t_\pi}^{t} \langle \Delta_j(t_1)\Delta_j(t_2) \rangle_j dt_1 dt_2 +$$

$$-2 \int_{t_\pi}^{t} dt_1 \int_0^{t_\pi} dt_2 \langle \Delta_j(t_1)\Delta_j(t_2) \rangle_j,$$

to finally build $\sigma_{\tilde{\varphi}}^2 = \langle \tilde{\varphi}_j^2(t) \rangle_j - \langle \tilde{\varphi}_j(t) \rangle_j^2$

$$\sigma_{\tilde{\varphi}}^2 = \int_0^{t_\pi} \int_0^{t_\pi} \langle \Delta_j(t_1)\Delta_j(t_2) \rangle_j dt_1 dt_2 +$$

$$+ \int_{t_\pi}^{t} \int_{t_\pi}^{t} \langle \Delta_j(t_1)\Delta_j(t_2) \rangle_j dt_1 dt_2 +$$

$$-2 \int_{t_\pi}^{t} dt_1 \int_0^{t_\pi} dt_2 \langle \Delta_j(t_1)\Delta_j(t_2) \rangle_j.$$

The first two integrals are almost identical. They are related by the variable substitution $t \to (t - t_\pi)$. They correspond to the direct phase accumulation before and after the π-pulse. The third term is a 'delayed auto-correlation' and can be considered as a measure of the time symmetry of the noise with respect to t_π. The direct integration reads

$$\boxed{\sigma_{\tilde{\varphi}}^2 / D_\varphi = t_\pi + \tau_\varphi (e^{-\frac{t_\pi}{\tau_\varphi}} - 1) + (t - t_\pi) + \tau_\varphi (e^{-\frac{t - t_\pi}{\tau_\varphi}} - 1) + \tau_\varphi [e^{\frac{t_\pi}{\tau_\varphi}} - 1][e^{\frac{-t}{\tau_\varphi}} - e^{\frac{-t_\pi}{\tau_\varphi}}].}$$

Note that the last term is negative.

A.2.2.3 Observations

We make the following observations.

i. The maximal contrast for the spin-echo sequences is obtained at ($\partial_t \sigma_{\tilde{\varphi}}^2 |_{t=t_E} = 0$, see Chapter IV)

$$t_E = \tau_\varphi \ln(2e^{t_\pi / \tau_\varphi} - 1).$$

One can show that, in general, $t_E < 2t_\pi$. Also note that, in the limit $\tau_\varphi \gg t_\pi$, one gets $t_E \sim 2t_\pi$. In Figure A.2 (a), we plot the phase variance (blue) as a function of time for a π-pulse performed at $t_\pi = 0.2 \times \tau_\varphi$. In green, we schematically show the quantum oscillation: the contrast is large when the phase variance is small. In (b), we plot the revival time for the echo oscillation, also as a function of t_π. In Figure A.2 (c), we see that the difference between the contrast at t_E and at $2t_\pi$ can be large. For the purpose of this example, we take $D_\varphi = 1/\tau_\varphi$: the error turns out to be of 40% by the time the revival contrast is 40% of the initial contrast.

ii. The revival echo oscillations all have the same Ramsey envelope. First, note that, by fixing $t_\pi = 0$ in eq.(A.2.2.2) (Echo), we recover eq.(A.2.2) (Ramsey). To see

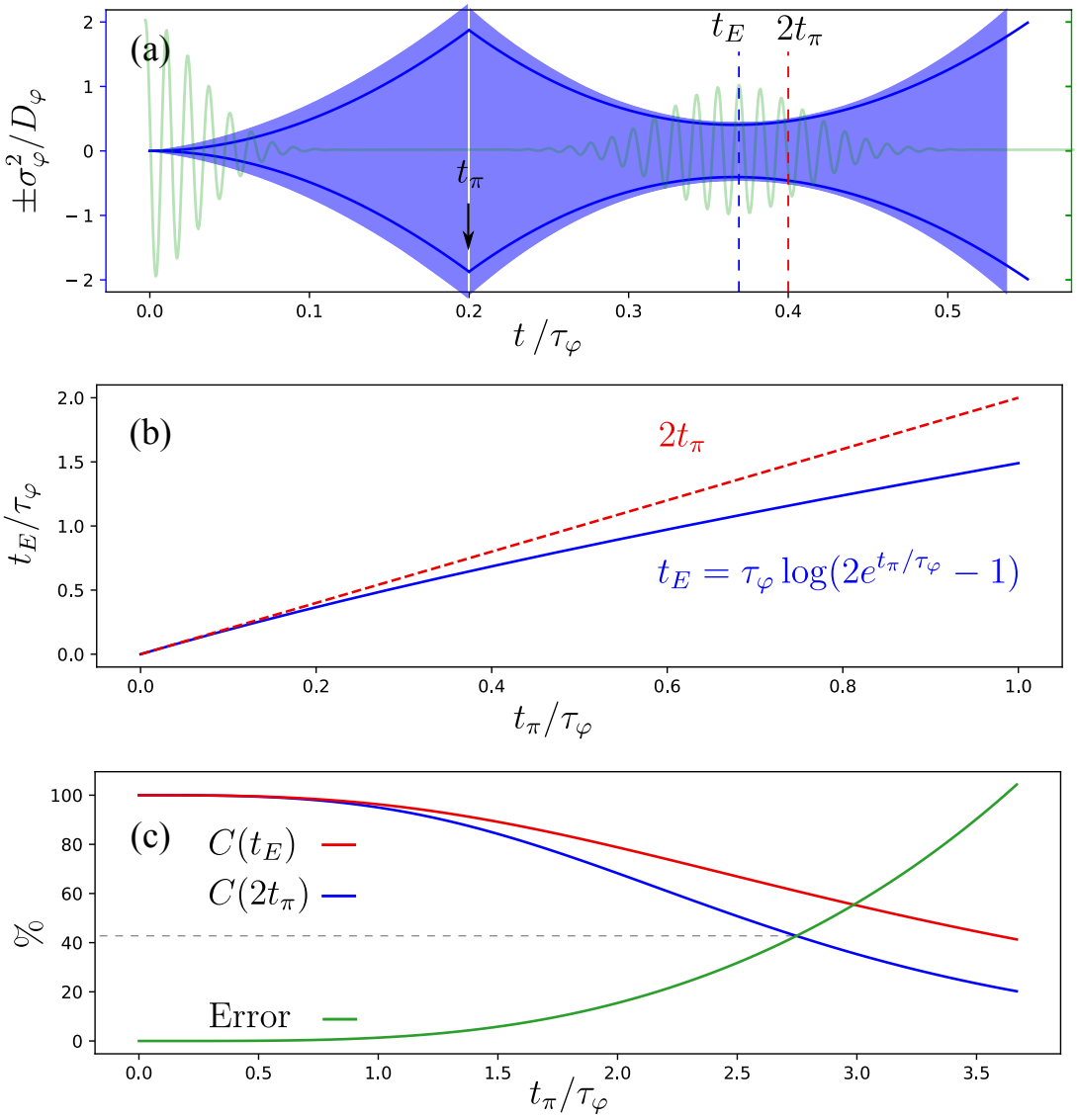

FIGURE A.2 Spin-focusing. In (a), we plot $\pm\sigma_\varphi^2(t)/D_\varphi$ (blue) as a function of time. The oscillation of the population is plotted in green. We see how the phase random variable, which is initially well defined $\sigma_\varphi^2(0) = 0$, diffuses. A π-pulse applied at $t_\pi = 0.2 \times \tau_\varphi$ reverts the phase diffusion and refocuses the random variable at $t_E < 2t_\pi$. In (b), we show the echo (revival) time as a function of t_π. In (c), we show the contrasts (the purity) of the spin systems at t_E (red) and at $2t_\pi$ (blue) as a function of t_π. The contrast for a fixed t_π is largest at t_E.

that the envelope is the same, we verify that the derivatives to all orders at $t = t_E$ are independent of t_π. We have

$$\partial_t^2 \sigma_{\tilde{\varphi}}^2 = \frac{D_\varphi e^{-\frac{t}{\tau_\varphi}}}{\tau_\varphi}(2e^{\frac{t_\pi}{\tau_\varphi}} - 1).$$

Evaluating in t_E, we get

$$\frac{D_\varphi e^{-\ln(2e^{\frac{t_\pi}{\tau_\varphi}}-1)}}{\tau_\varphi}(2e^{\frac{t_\pi}{\tau_\varphi}}-1)=\frac{D_\varphi}{\tau_\varphi}.$$

For $l \geq 2$, we have that $\partial_t^l \sigma_\varphi^2|_{t_E} = -\frac{D_\varphi}{(-\tau_\varphi)^{(l-1)}}$ (independent of t_π).

iii. The maximum contrast at a given time t_0 is obtained by applying the π pulse at $t_\pi = t_0/2$. This is derived from the condition $\partial_{t_\pi}\sigma_{\vec{\varphi}}^2(t=t_0)=0$.

A.2.2.4 Fluctuation-dissipation relations: noise autocorrelation, noise spectrum and noise energy

The noise autocorrelation function reads

$$\beta_{\tau_\varphi}(t_1-t_2)=\langle\Delta_j(t_1)\Delta_j(t_2)\rangle_j=\frac{D_\varphi}{2\tau_\varphi}e^{-\frac{|t_1-t_2|}{\tau_\varphi}}.$$

For sufficiently long times T, one can define the variance for the noise as

$$\sigma_\Delta^2=\int_0^T\langle\Delta_j^2(t)\rangle_j dt/T.$$

We then get that $\sigma_\Delta^2=\beta_{\tau_\varphi}(0)=D_\varphi/2\tau_\varphi$. To compute the noise energy E_ξ, we need to compute the power spectrum

$$F[\beta_{\tau_\varphi}](\omega)=\frac{D_\varphi}{(2\pi\tau_\varphi)^2}\frac{1}{\omega^2+(\frac{1}{2\pi\tau_\varphi})^2},$$

and integrate it over all the frequencies to get

$$E_\xi=\int_{-\infty}^{\infty}F[\beta_{\tau_\varphi}](\omega)d\omega=\frac{D_\varphi}{2\tau_\varphi}.$$

Here we find a manifestation of the Wiener–Khintchine theorem.[2] Out of direct computation, we find Fluctuation(D_φ)-Dissipation(T_2^*) relations for the Lorentzian noise we have modeled. They read

$$\boxed{E_\xi=\sigma_\Delta^2=\frac{D_\varphi}{2\tau_\varphi}=(1/T_2^*)^2.}$$

The noise energy E_ξ, the diffusion constant over the correlation time $D_\varphi/2\tau_\varphi$, and the noise variance σ_Δ^2 are equivalent representations of the fluctuations. The Ramsey time T_2^* (see Chapter IV) represents the dissipation here.

A.2.2.5 The phase random variable is normally distributed

For completeness, and because our discussion is based on the fact that the phase random variable φ_j is normally distributed, we present a sketch of the proof here. The proof starts with the realization that

[2]The theorem states that $\lim_{t\to\infty}\int_0^T\langle\Delta_j(t)^2\rangle_j dt/T=\int_{-\infty}^{\infty}F[\beta_{\tau_\varphi}](\omega)d\omega$. Or, more precisely, that $\int_{-\infty}^{\infty}\Delta_j(t)^2dt=\int_{-\infty}^{\infty}F[\int_{-\infty}^{\infty}dt\Delta_j(t)\Delta_j(t+\tau)](\omega)d\omega$. The equivalence comes from the time invariance of the noise, the linearity of $\langle\cdot\rangle_j$ and from the fact that $\beta_{\tau_\varphi}(\tau)$ depends only on the time difference τ.

$$\varphi_j(t) = \int_0^t \Delta_j(t)dt = \int_0^t dt \int_{-\infty}^t d\tau W_j(\tau) \frac{e^{\frac{\tau-t}{\tau_\varphi}}}{\tau_\varphi}$$

is a 'sum of Gaussians' (W_j). The central limit theorem (CLT) then ensures its normal character, and gives the correct analytical formula for its variance in terms of W_j.

Explicitly, one can write[3] the Riemann sum for the noise as

$$\Delta_j(t) = \sum_{n=-\infty}^{N=t/d\tau} W_j(nd\tau) \frac{e^{\frac{nd\tau-t}{\tau_\varphi}}}{\tau_\varphi} d\tau.$$

For the sake of the argument, we will take $W_j(nd\tau)$ to have a standard deviation A_0. Then, $\Delta_j(t)$ is a sum of normal random variables with standard deviation $\sigma_n = A_0 \frac{e^{\frac{nd\tau-t}{\tau_\varphi}}}{\tau_\varphi} d\tau$, so, after the CLT, its variance can be computed as

$$\sigma_\Delta^2 = \sum_n \sigma_n^2.$$

In the limit $d\tau \to 0$, one needs to take $(A_0 * d\tau)^2 = D_\varphi d\tau$ to again get an expression linear in $d\tau$.[4] One can take the limit on the Riemann sum to get back an integral.

$$\sigma_\Delta^2 = D_\varphi \int_{-\infty}^t \frac{e^{2\frac{\tau-t}{\tau_\varphi}}}{\tau_\varphi^2} d\tau.$$

The same argument can be practiced again to deduce the normal character of $\varphi_j(t)$, starting from the normal character of $\Delta_j(t)$. This proves the Normal character of the phase random variable. One can recover the expression previously derived for σ_φ^2 following this approach.

A.2.3 Gaussian noise spectrum

The last noise model we will explore is that having Gaussian correlation. A description involving a Gaussian cut-off in the noise spectrum arises if one takes

$$g_{\tau_\varphi}(\tau - t) = e^{-\frac{(\tau-t)^2}{\tau_\varphi^2}} / \tau_\varphi \sqrt{\pi}$$

and

$$\Delta_j(t) = \int_{-\infty}^t W_j(\tau) g_{\tau_\varphi}(\tau - t) d\tau.$$

The calculation can be carried out analytically in terms of the Error function (Erf[x]).

The phase variance after the echo pulse reads

$$\sigma_{\bar{\varphi}}^2 \pi / D_\varphi = -3\tau_\varphi - \tau_\varphi e^{-t^2/\tau_\varphi^2} + 2\tau_\varphi e^{-(t-t_\pi)^2/\tau_\varphi^2} + 2\tau_\varphi e^{-t_\pi^2/\tau_\varphi^2} +$$

[3] The proof is analogous to that proving Itō's Isometry.

[4] This is the standard limit in Brownian motion. Here, instead of the mean free path l and the collision time $d\tau$ going to zero ($l^2/d\tau = D = cte$ as both $l, d\tau \to 0$), we have a diverging noise amplitude A_0 during an infinitesimal amount of time so that $A_0^2 d\tau \to cte$.

$$+\sqrt{\pi}\; t\; \mathrm{Erfi}[t/\tau_\varphi] + 2\sqrt{\pi}\; (t-t_\pi)\; \mathrm{Erfi}[(t-t_\pi)/\tau_\varphi] + 2\sqrt{\pi}\; t_\pi\; \mathrm{Erfi}[t_\pi/\tau_\varphi],$$

where $\mathrm{Erfi}[x]$ is the imaginary part of the error function defined as $\mathrm{Erfi}[x] = \mathrm{Erf}[ix]/i$.

The peak of the revival oscillation will appear at t_E satisfying

$$\partial_t \sigma^2_{\tilde{\varphi}}\Big|_{t_E} \propto 2\;\mathrm{Erfi}\left[\frac{t_E - t_\pi}{\tau_\varphi}\right] - \mathrm{Erfi}\left[\frac{t_E}{\tau_\varphi}\right] = 0.$$

Taking $\mathrm{Erfi}[x] \sim 2x/\sqrt{\pi}$, under the condition $t_E, t_\pi \ll \tau_\varphi$, one gets $t_E \sim 2t_\pi$. In general, one has $t_E < 2t_\pi$ for the non-linear expression.

Appendix B

Correlation of the noise parameters

By very general arguments, the 'revival time' $t_E < 2t_\pi$ for a spin-echo sequence is not only a sensitive observable to the noise correlation time τ_φ, but it is also independent of the noise amplitude D_φ. The contrast drop (which for our experiment is $T_2^* \sim 35$ µs and $T_2 \sim 270$ µs) only depends on a combination of these two parameters, making their individual determination difficult. Time-domain spin-echo spectroscopy gives one access to direct information on the correlation time of the noise which is absent in standard frequency-domain spin-echo spectroscopy.

B.1 Identification of the parameter dependence

The coherence measurements we have performed (Chapter IV) depend on the noise in our setup and the qubits can be considered as a probe to determine its characteristics. Nonetheless, the effect of the independent noise parameters D_φ (noise amplitud) and τ_φ (noise correlation time) on the coherence drop is highly correlated. In Figure B.1, we present an alternative way to analyze the data. In Figure B.1 (a), we plot the result of performing different model fits (eq.(IV.9)) on the oscillations data points in Figure IV.17. The empty blue dot with error bars in both directions corresponds to the fits shown in Figure IV.17, where both τ_φ and D_φ are free. The other blue dots are obtained by artificially fixing the parameter τ_φ and allowing the fitting algorithm to fit D_φ. The red dots in Figure B.1 (a) correspond to the reduced χ^2 of the fit. It varies only slightly over one order of magnitude in the numerical variation of τ_φ. In Figure B.1 (b), we plot $1/D_\varphi$ versus $1/\tau_\varphi^2$. The linear fit corresponds to the identification of the combination D_φ/τ_φ^2 as the relevant parameter to explain the data. The shaded band represents the 95% confidence region for the fit. We then claim that the fitting procedure gives a reliable value for any function of this quantity, in particular (assuming $T_2 \ll \tau_\varphi$, see Chapter IV) $T_2 = \sqrt[3]{\ln(2) \times 24\tau_\varphi^2/D_\varphi}$.

B.2 Information from time-domain spectroscopy

Assuming a Lorentzian spectrum for the noise, the coherence oscillations studied in Chapter IV yield noise parameters $D_\varphi \sim 3.8 \times 10^6$ s^{-1} and $\tau_\varphi \sim 2.1$ ms. Under these conditions, the coherent oscillations are measurable during a few hundred microseconds

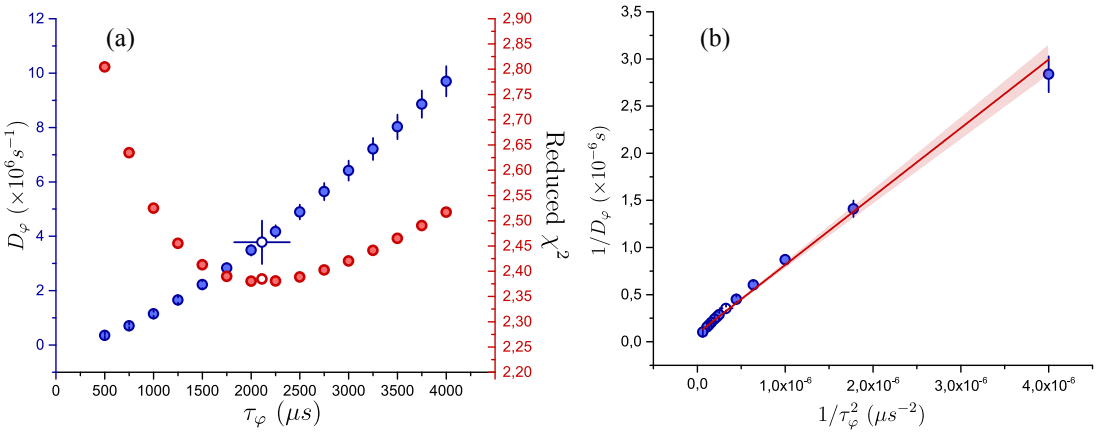

FIGURE B.1 In (a), we show the strong correlation in between D_φ and τ_φ (blue dots). The red dots are the error of the fit achieved by fixing τ_φ. In (b), we plot the fit result $1/D_\varphi$ against $1/\tau_\varphi^2$. The correlation is linear.

($T_2 \ll \tau_\varphi$), and one can approximate the expressions derived in Chapter IV and in Appendix A for the Ramsey contrast, the spin-echo contrast and the revival time as,

$$C_{\text{Ramsey}}(\tau_{1,2}) = e^{-D_\varphi\left(\tau_{1,2}+\tau_\varphi(e^{-\tau_{1,2}/\tau_\varphi}-1)\right)} \tag{B.1}$$

$$= e^{-\tau_{1,2}^2 D_\varphi/4\tau_\varphi} + \mathcal{O}_{\text{Ramsey}}\left(\frac{\tau_{1,2}^3 D_\varphi}{12\tau_\varphi^2}\right), \tag{B.2}$$

$$C_{\text{spin-echo}}(t_E) = e^{-D_\varphi(t_E/2-\tau_\varphi \tanh(t_E/2\tau_\varphi))} \tag{B.3}$$

$$= e^{-t_E^3 \frac{D_\varphi}{24\tau_\varphi^2}} + \mathcal{O}_{\text{s-e}}\left(\frac{t_E^5 D_\varphi}{240\tau_\varphi^4}\right), \quad \text{and} \tag{B.4}$$

$$t_E(t_\pi) = \tau_\varphi \ln(2e^{t_\pi/\tau_\varphi} - 1) \tag{B.5}$$

$$\sim 2t_\pi + \mathcal{O}_{\text{Revival}}\left(\frac{t_\pi^2}{\tau_\varphi}\right). \tag{B.6}$$

The errors we accept in doing these approximations in our experimental situation are

$$\mathcal{O}_{\text{Ramsey}}\left(\tau_{1,2} = T_2^*\right) \sim 0.3\%, \tag{B.7}$$

$$\mathcal{O}_{\text{s-e}}\left(t_E = T_2\right) \sim 0.1\%, \quad \text{and} \tag{B.8}$$

$$\mathcal{O}_{\text{Revival}}\left(t_\pi = 200\ \mu s\right)/2t_\pi \sim 5\%. \tag{B.9}$$

In Figure B.2 (a), we show an echo oscillation. The solid green line is the fit of a

sinus with an envelope given by the model expression eq.(B.1). The red dashed line corresponds to a Gaussian envelope for comparison and it corresponds to neglecting the error in eq.(B.2). Note that, in our experimental situation, one cannot confidently distinguish between a Gaussian envelope for the Ramsey signal and that of the full analytic expression. In Figure B.2 (b), we show a fit to the revival oscillation contrast. The green line is a fit of the full analytical model eq.(B.3), where we have allowed for a multiplicative constant to account for the reduced initial contrast. The red dashed line corresponds to a fit with cubic expression eq.(B.4) to the same data points.[1] Note that, once again, one cannot distinguish confidently between the full analytical expression and the approximation here either.

In Figure B.2 (c), we show a fit (green line) to the experimentally determined t_E using expression eq.(B.5). Note that, remarkably, the determination of the revival time is very well differentiated from the approximate expression suggested by eq.(B.6), which is parameter independent.

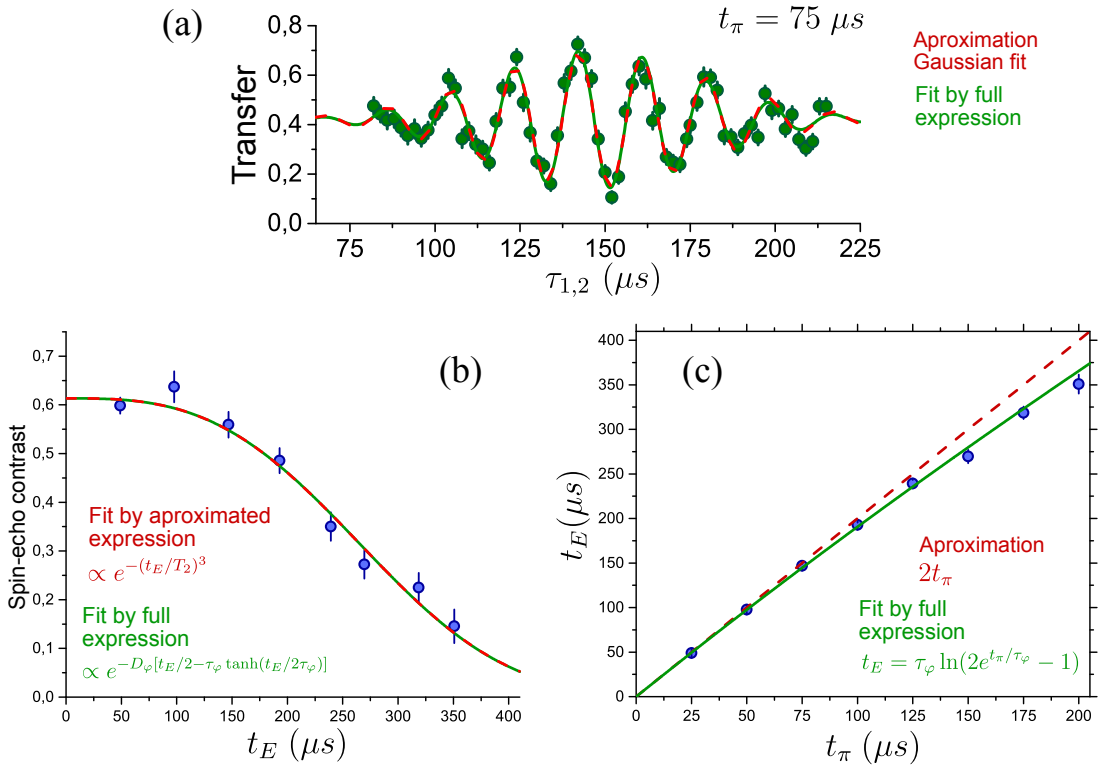

FIGURE B.2 Analysis of echo data. The red dashed lines are the first non-trivial terms of the approximation. The green curves are fits taking into account the full analytic expressions. In (a), we show a revival oscillation presented in Chapter IV. The red dashed line is a Gaussian fit (the same as in Figure IV.15). The solid green line corresponds to a global fit of the model, done simultaneously to all data shown in Figure IV.17. In (b), we show the contrast drop as a function of time. The solid green line is the fit of eq.(B.3) to the data points. The red dashed line corresponds to a fit inspired in eq.(B.4). In (c), the dashed line corresponds to the linear term in eq.(B.6). The green line is a fit of these data points using eq.(B.5).

[1] The blue line traced on Figure IV.16 (a) lies exactly over the plots in Figure B.2 (b).

Note that, for the Lorentzian noise model, both coherence times $T_2^* = \sqrt{2\tau_\varphi/D_\varphi}$ and $T_2 = \sqrt[3]{\ln(2) \times 24\tau_\varphi^2/D_\varphi}$ depend on a combination of the noise parameters, making their individual determination less precise. Also note that the function $t_E(t_\pi)$ is the only of the discussed observables that depends on a single one of the noise parameters (τ_φ), and that it is also 50 times more sensitive than the others (see eq.(B.8) and eq.(B.9)).[2]

From Figure B.2 (b) and (c), we extract the noise parameters to be $D_\varphi \sim (810 \pm 60) \times 10^3$ s^{-1} and $\tau_\varphi \sim (966 \pm 135)$ µs. Again, the irreversible coherence time is computed out of these two quantities to be $T_2 = (270 \pm 20)$ µs, as one would expect from Figure B.1 (b). On the other, hand we find $T_2^* = (48 \pm 5)$ µs.

B.3 Conclusion

The information on the noise one can get from spin-echo spectroscopy can be accessed in two non-equivalent ways, either by performing experiments in the time-domain or in the frequency-domain. We have performed time-domain spin-echo spectroscopy (Chapter IV). The procedure consists in applying a first $\pi/2$ Ramsey pulse at time $t = 0$, a π-pulse at time t_π and then a second $\pi/2$ Ramsey pulse delayed $\tau_{1,2}$ from the first one. For a fixed MW detuning and a fixed t_π one measures the contrast of the oscillations as a function of $\tau_{1,2}$. This is repeated for different t_π, to measure the maximal available contrast as a function of time. In the frequency-domain approach, the spin-echo spectroscopy is made using a fixed time delay $\tau_{1,2}$ between the two $\pi/2$ Ramsey pulses and scanning the detuning of the MW drive to measure the oscillation contrast. For this, the intermediate π-pulse is performed at $t_\pi = \tau_{1,2}/2$ to maximize the contrast at $\tau_{1,2}$. This is repeated for different $\tau_{1,2}$ to reproduce the contrast drop in time.

On the one hand, to the extent to which one can neglect the error in eq.(B.6), the two approaches are indeed equivalent. On the other hand, if the error in eq.(B.6) is measurable, one can get important information over the noise spectrum using the time-domain spectroscopy if one measures the full envelopes.

[2]Note that the independence of the revival time t_E on D_φ is a very general property independent of the Lorentzian model we study here. This independence is to be found in any noise that can be written as filtered white noise. See equations eq.(1) in Appendix A. The noise amplitude is a multiplicative constant that drops out of the equation when minimizing the variance to find the revival time.

Appendix C

Exact calculation of the ponderomotive potential

The integration on the Bohr orbit used (see Conclusion chapter) to estimate the energy landscape in optical traps for cRy atom remains an approximation. The full potential corresponds to the average of ponderomotive energy over the electron orbit. Here we develop the calculation for the Laguerre-Gauss (LG) traps and for the needle traps.

C.1 The LG trap

The full potential corresponds to the average of ponderomotive energy over the electron orbit and for an LG trap it reads

$$\mathcal{E}(x_c, y_c, z_c) = \iiint \sin(\theta_e) r_e^2 dr_e d\theta_e d\phi_e \, |\psi_{nc}(r_e, \theta_e, \phi_e)|^2$$

$$\times \frac{q_e^2}{2m_e\epsilon_0 c} \frac{\lambda_L^2}{(2\pi c)^2} \frac{4\mathcal{P}_0}{\pi w^4 (x_c + x_e)} [(z_e + z_c)^2 + (y_e + y_c)^2]$$

$$\times \exp\left\{ \frac{-2}{w^2(x_c + x_e)} [(z_e + z_c)^2 + (y_e + y_c)^2] \right\}, \tag{C.1}$$

where ψ_{nc} is the circular electron wavefunction (see Chapter I). The choice of axis is shown in Figure C.1 (a). The 'electron coordinates' (x_e, y_e, z_e) are given by the parametrization in spherical coordinates (r_e, θ_e, ϕ_e). The position of the core is given by (x_c, y_c, z_c). The LG beam is taken to propagate along the x-axis and is focused at $x = 0$. The plots in Figure C.1 corresponds to a LG_{01} at 1064 nm and focused to $w_0 = 7$ µm. The atom is taken to be in state $|50c\rangle$. The solid lines correspond to the wavefunction average of the potential. The dots correspond to the average over the one dimensional Bohr orbit, and the dashed line corresponds to the approximation of having a point like atom i.e. neglecting its finite size, see Chapter II. The red dots correspond to a core displacement in the plane of the orbit (y) and the blue dots correspond to a core displacement along the quantization axis (z). We see the Bohr orbit remains an excellent approximation.

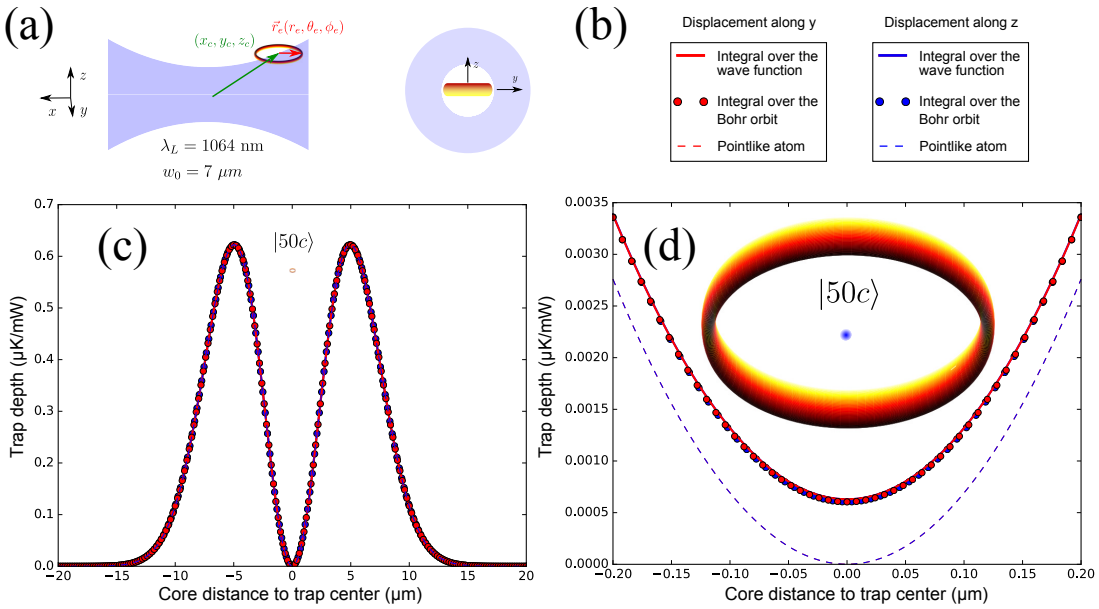

FIGURE C.1 (a) Choice of axis and of the coordinate system. (b) Labels for both plots. The blue shade represents the LG profile. (c) and (d) Ponderomotive energy landscape for a cRy in a LG trap. The energy is computed by the exact formula (solid lines, wavefunction average), under the approximation induced by the Bohr atom picture (dots, see Conclusion chapter), and by neglecting the size of the atom (dashed lines). In red, we show displacements along the y direction. In blue, we show displacements along the z direction. (c) Full landscape. (d) Zoom-in to the center of the trap. The atomic orbital is drawn to scale in (c), and (d).

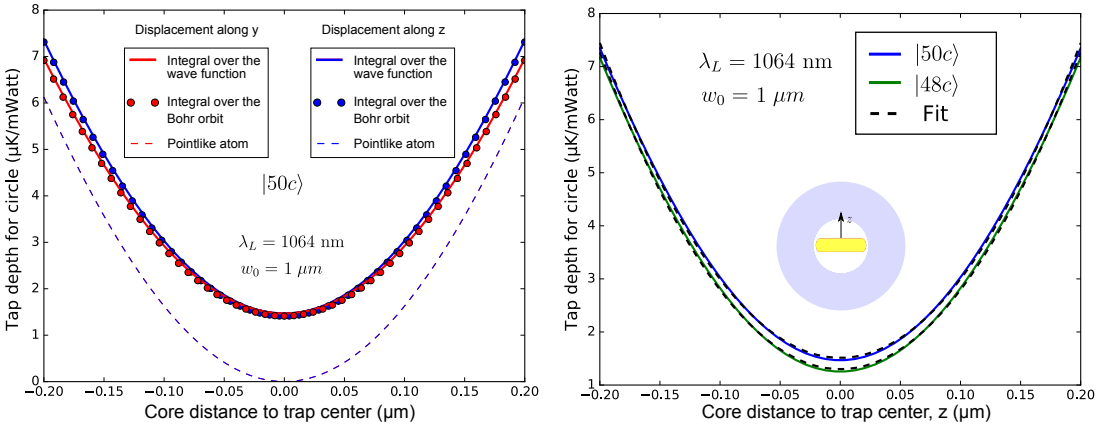

FIGURE C.2 Strongly focalized LG beam ($w_0 = 1$ μm). (a) Quasi-harmonic potentials along the y (red) and z (blue) directions for state $|50c\rangle$. The solid lines correspond to the full wavefunction average of the potential. The dots correspond to the Bohr orbit approximation and the dashed lines correspond to the point-like atom picture. (b) Potential along the z direction for states $|48c\rangle$ and $|50c\rangle$. The blue ring represents the LG profile.

In Figure C.2, we instead take $w_0 = 1$ µm. This condition corresponds to individual LG tweezers for a cRy atom (see Conclusion chapter). We see that the geometry of the atom plays a role and causes a small difference in the oscillation frequency depending on the orientation of the orbit. By fitting the energies in Figure C.2 (a), we get $\omega_{z,50c}/\sqrt{\mathcal{P}_0} = 2\pi \times 815$ kHz$/\sqrt{\text{W}}$ and $\omega_{y,50c}/\sqrt{\mathcal{P}_0} = 2\pi \times 790$ kHz$/\sqrt{\text{W}}$. The tight confinement also induces a state dependent oscillation frequency. For state $|48c\rangle$ (see Figure C.2 (b)), we fit an oscillation frequency of $\omega_{z,48c}/\sqrt{\mathcal{P}_0} = 2\pi \times 822$ kHz$/\sqrt{\text{W}}$ along the z direction. The trap is almost state-independent (see eq.(II.20)) even for strongly focused beams.

C.2 The Needle trap

For the circular atom trap discussed in the Conclusion chapter, the Needle trap, we compare the approximated potential calculated over the Bohr orbit with the full average over the 'toroidal' wavefunction in Figure C.3.

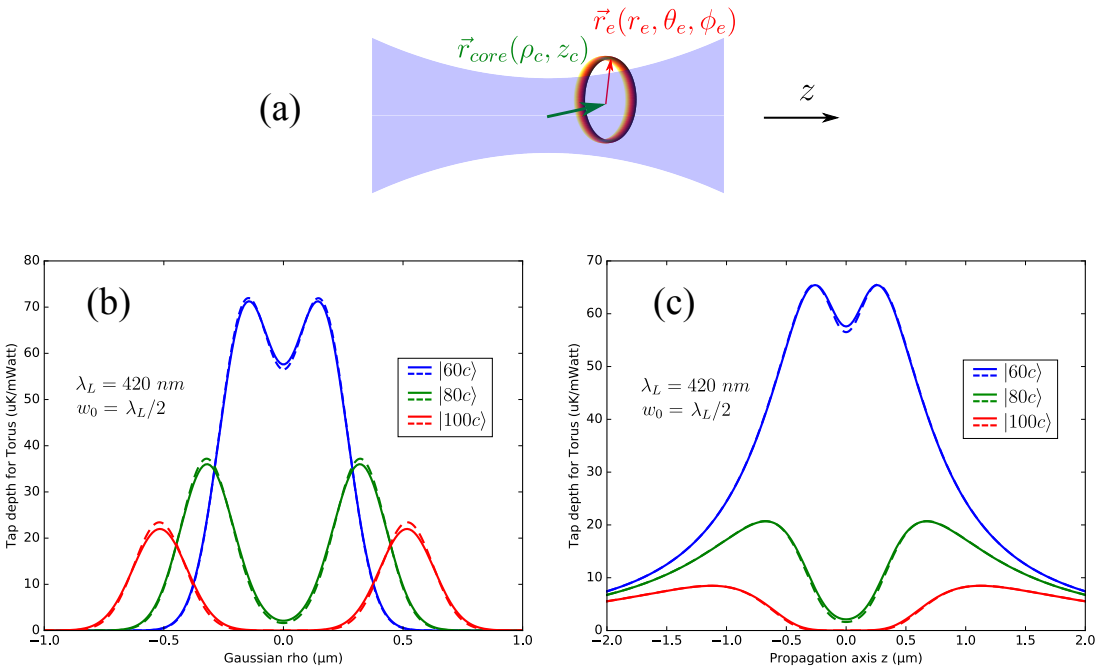

FIGURE C.3 Energy landscape of a cRy atom threaded by a Gaussian beam (NA=0.5). (a) Choice of coordinate system. (b) Radial potential. (c) Longitudinal potential. The dashed line corresponds to approximating the electron orbital by the associated Bohr orbit. The solid line corresponds to the computation using the exact analytic cRy atom wavefunction.

The exact analytically potential reads

$$\mathcal{E}(\rho_c, z_c) = \iiint \sin(\theta_e) r_e^2 dr_e d\theta_e d\phi_e \; |\psi_{nc}(r_e, \theta_e, \phi_e)|^2$$

$$\times \frac{q_e^2}{2m_e\epsilon_0 c} \frac{\lambda_L^2}{(2\pi c)^2} \frac{2\mathcal{P}_0}{\pi w^2(z_c + z_e)} \exp\left\{ \frac{-2}{w^2(z_c + z_e)} [(x_e + x_c)^2 + (y_e + y_c)^2] \right\}, \quad \text{(C.2)}$$

where the notation is analogous to that in eq.(C.1) and the Gaussian beam is taken to propagate along the z-axis, focused at $z = 0$. The variable $\rho_c^2 = x_c^2 + y_c^2$ is introduced to make the cylindrical symmetry of the problem explicit. We reproduce the approximated landscape (dashed lines, integration over the Bohr circular orbit, see Conclusion chapter) in Figure C.3. The solid lines correspond to the full wavefunction average in eq.(C.2).

The Bohr orbit remains a good approximation to compute the ponderomotive energy even in these extreme focalization conditions.

Bibliography

[1] E. T. Jaynes. *Probability Theory: The Logic of Science*. Vol. 1. Cambridge University press, 2003. ISBN: 9780521592710.

[2] A. Terenin and D. Draper. *Cox's Theorem and the Jaynesian Interpretation of Probability*. 2015. arXiv: 1507.06597 [math.ST].

[3] G. Birkhof and J. V. Neumann. "The Logic of Quantum Mechanics". In: *The Annals of Mathematics*. 2 (37 1936), pp. 823–824.

[4] I. Buluta and F. Nori. "Quantum Simulators". In: *Science* 326.5949 (2009), pp. 108–111. ISSN: 0036-8075.

[5] S. Lloyd. "Universal Quantum Simulators". In: *Science* 273.5278 (1996), pp. 1073–1078. ISSN: 0036-8075.

[6] R. Feynman. "Simulating Physics with Computers". In: *Int. J. of Theor. Phys.* 21 (1982), pp. 467–488.

[7] I. M. Georgescu, S. Ashhab, and F. Nori. "Quantum simulation". In: *Rev. Mod. Phys.* 86 (1 2014), pp. 153–185.

[8] M. Kjaergaard et al. "Superconducting Qubits: Current State of Play". In: *Annual Review of Condensed Matter Physics* 11.1 (2019). ISSN: 1947-5462.

[9] J. Preskill. "Quantum Computing in the NISQ era and beyond". In: *Quantum* 2 (2018), p. 79. ISSN: 2521-327X.

[10] D. Vion et al. "Manipulating the Quantum State of an Electrical Circuit". In: *Science* 296.5569 (2002), pp. 886–889. ISSN: 0036-8075.

[11] P. Krantz et al. "A quantum engineer's guide to superconducting qubits". In: *Applied Physics Reviews* 6.2 (2019), p. 021318. ISSN: 1931-9401.

[12] A. A. Houck et al. "Controlling the Spontaneous Emission of a Superconducting Transmon Qubit". In: *Physical Review Letters* 101.8 (2008). ISSN: 1079-7114.

[13] A. Wallraff et al. "Strong coupling of a single photon to a superconducting qubit using circuit quantum electrodynamics". In: *Nature* 431.7005 (2004), pp. 162–167.

[14] R. J. Schoelkopf and S. M. Girvin. "Wiring up quantum systems". In: *Nature* 451.7179 (2008), pp. 664–669.

[15] R. K. Gainutdinov et al. "Dressing of superconducting qubits by their interaction with a low frequency photon reservoir". In: *Journal of Physics: Conference Series* 1283 (2019), p. 012004.

[16] M. H. Devoret and R. J. Schoelkopf. "Superconducting Circuits for Quantum Information: An Outlook". In: *Science* 339.6124 (2013), pp. 1169–1174. ISSN: 0036-8075.

[17] P. V. Klimov et al. "Fluctuations of Energy-Relaxation Times in Superconducting Qubits". In: *Phys. Rev. Lett.* 121 (9 2018), p. 090502.

[18] C. Eichler et al. "Exploring Interacting Quantum Many-Body Systems by Experimentally Creating Continuous Matrix Product States in Superconducting Circuits". In: *Phys. Rev. X* 5 (4 2015), p. 041044.

[19] C. Neill et al. "Ergodic dynamics and thermalization in an isolated quantum system". In: *Nature Physics* 12.11 (2016), pp. 1037–1041.

[20] Z. K. Minev et al. "To catch and reverse a quantum jump mid-flight". In: *Nature* 570.7760 (2019), 200–204. ISSN: 1476-4687.

[21] R. Barends et al. "Digital quantum simulation of fermionic models with a superconducting circuit". In: *Nature Communications* 6.1 (2015), p. 7654.

[22] R. Barends et al. "Digitized adiabatic quantum computing with a superconducting circuit". In: *Nature* 534.7606 (2016), 222–226. ISSN: 1476-4687.

[23] Y. Salathé et al. "Digital Quantum Simulation of Spin Models with Circuit Quantum Electrodynamics". In: *Phys. Rev. X* 5 (2 2015), p. 021027.

[24] P. Roushan et al. "Chiral ground-state currents of interacting photons in a synthetic magnetic field". In: *Nature Physics* 13.2 (2017), pp. 146–151.

[25] F. Arute et al. "Quantum supremacy using a programmable superconducting processor". In: *Nature* 574.7779 (2019), pp. 505–510.

[26] T. Albash et al. "Reexamining classical and quantum models for the D-Wave One processor". In: *The European Physical Journal Special Topics* 224.1 (2015), pp. 111–129.

[27] P. Hauke et al. *Perspectives of quantum annealing: Methods and implementations*. 2019. arXiv: 1903.06559 [quant-ph].

[28] M. Fitzpatrick et al. "Observation of a Dissipative Phase Transition in a One-Dimensional Circuit QED Lattice". In: *Phys. Rev. X* 7 (1 2017), p. 011016.

[29] S. Boixo et al. "Evidence for quantum annealing with more than one hundred qubits". In: *Nature Physics* 10.3 (2014), pp. 218–224.

[30] B. Heim et al. "Quantum versus classical annealing of Ising spin glasses". In: *Science* 348.6231 (2015), pp. 215–217. ISSN: 0036-8075.

[31] T. Albash et al. "Reexamination of the evidence for entanglement in a quantum annealer". In: *Physical Review A* 92.6 (2015). ISSN: 1094-1622.

[32] J. I. Cirac and P. Zoller. "Quantum Computations with Cold Trapped Ions". In: *Phys. Rev. Lett.* 74 (20 1995), pp. 4091–4094.

[33] P. W. Shor. "Polynomial-Time Algorithms for Prime Factorization and Discrete Logarithms on a Quantum Computer". In: *SIAM Journal on Computing* 26.5 (1997), 1484–1509. ISSN: 1095-7111.

[34] W. Neuhauser et al. "Localized visible Ba^+ mono-ion oscillator". In: *Phys. Rev. A* 22 (3 1980), pp. 1137–1140.

[35] D. J. Wineland. "Nobel Lecture: Superposition, entanglement, and raising Schrödinger's cat". In: *Rev. Mod. Phys.* 85 (3 2013), pp. 1103–1114.

[36] J. C. Bergquist et al. "Observation of Quantum Jumps in a Single Atom". In: *Phys. Rev. Lett.* 57 (14 1986), pp. 1699–1702.

[37] W. M. Itano et al. "Quantum projection noise: Population fluctuations in two-level systems". In: *Phys. Rev. A* 47 (5 1993), pp. 3554–3570.

[38] S. M. Brewer et al. "$^{27}Al^+$ Quantum-Logic Clock with a Systematic Uncertainty below 10^{-18}". In: *Phys. Rev. Lett.* 123 (3 2019), p. 033201.

[39] P. Jurcevic et al. "Quasiparticle engineering and entanglement propagation in a quantum many-body system". In: *Nature* 511.7508 (2014), pp. 202–205.

[40] R. Blatt and C. F. Roos. "Quantum simulations with trapped ions". In: *Nature Physics* 8.4 (2012), pp. 277–284.

[41] I. Arrazola et al. "Digital-Analog Quantum Simulation of Spin Models in Trapped Ions". In: *Scientific Reports* 6.1 (2016), p. 30534.

[42] C. D. Bruzewicz et al. "Trapped-ion quantum computing: Progress and challenges". In: *Applied Physics Reviews* 6.2 (2019), p. 021314. ISSN: 1931-9401.

[43] T. P. Harty et al. "High-Fidelity Preparation, Gates, Memory, and Readout of a Trapped-Ion Quantum Bit". In: *Phys. Rev. Lett.* 113 (22 2014), p. 220501.

[44] Y. Wang et al. "Single-qubit quantum memory exceeding ten-minute coherence time". In: *Nature Photonics* 11.10 (2017), 646–650. ISSN: 1749-4893.

[45] E. A. Martinez et al. "Real-time dynamics of lattice gauge theories with a few-qubit quantum computer". In: *Nature* 534.7608 (2016), 516–519. ISSN: 1476-4687.

[46] T. Monz et al. "Realization of a scalable Shor algorithm". In: *Science* 351.6277 (2016), pp. 1068–1070. ISSN: 0036-8075.

[47] G Pagano et al. "Cryogenic trapped-ion system for large scale quantum simulation". In: *Quantum Science and Technology* 4.1 (2018), p. 014004. ISSN: 2058-9565.

[48] C. D. Bruzewicz et al. "Scalable loading of a two-dimensional trapped-ion array". In: *Nature Communications* 7.1 (2016), p. 13005.

[49] J. W. Britton et al. "Engineered two-dimensional Ising interactions in a trapped-ion quantum simulator with hundreds of spins". In: *Nature* 484.7395 (2012), 489–492. ISSN: 1476-4687.

[50] K. Kim et al. "Entanglement and Tunable Spin-Spin Couplings between Trapped Ions Using Multiple Transverse Modes". In: *Phys. Rev. Lett.* 103 (12 2009), p. 120502.

[51] R. Islam et al. "Emergence and Frustration of Magnetism with Variable-Range Interactions in a Quantum Simulator". In: *Science* 340.6132 (2013), pp. 583–587. ISSN: 0036-8075.

[52] C. Senko et al. “Realization of a Quantum Integer-Spin Chain with Controllable Interactions”. In: *Phys. Rev. X* 5 (2 2015), p. 021026.

[53] P. Jurcevic et al. “Spectroscopy of Interacting Quasiparticles in Trapped Ions”. In: *Phys. Rev. Lett.* 115 (10 2015), p. 100501.

[54] J. Smith et al. “Many-body localization in a quantum simulator with programmable random disorder”. In: *Nature Physics* 12.10 (2016), 907–911. ISSN: 1745-2481.

[55] J. G. Bohnet et al. “Quantum spin dynamics and entanglement generation with hundreds of trapped ions”. In: *Science* 352.6291 (2016), pp. 1297–1301. ISSN: 0036-8075.

[56] I. Bloch, J. Dalibard, and W. Zwerger. “Many-body physics with ultracold gases”. In: *Reviews of Modern Physics* 80.3 (2008), 885–964. ISSN: 1539-0756.

[57] M. Lewenstein et al. “Ultracold atomic gases in optical lattices: mimicking condensed matter physics and beyond”. In: *Advances in Physics* 56.2 (2007), 243–379. ISSN: 1460-6976.

[58] I. Bloch, J. Dalibard, and S. Nascimbène. “Quantum simulations with ultracold quantum gases”. In: *Nature Physics* 8.4 (2012), pp. 267–276.

[59] R. Grimm, M. Weidemüller, and Y. B. Ovchinnikov. *Optical dipole traps for neutral atoms*. 1999. arXiv: physics/9902072 [physics.atom-ph].

[60] C. Gross and I. Bloch. “Quantum simulations with ultracold atoms in optical lattices”. In: *Science* 357.6355 (2017), pp. 995–1001. ISSN: 0036-8075.

[61] M. Greiner et al. “Quantum phase transition from a superfluid to a Mott insulator in a gas of ultracold atoms”. In: *Nature* 415.6867 (2002), pp. 39–44.

[62] P. T. Brown et al. “Bad metallic transport in a cold atom Fermi-Hubbard system”. In: *Science* 363.6425 (2019), pp. 379–382. ISSN: 0036-8075.

[63] L. Sanchez-Palencia and M. Lewenstein. “Disordered quantum gases under control”. In: *Nature Physics* 6.2 (2010), pp. 87–95.

[64] M. Schreiber et al. “Observation of many-body localization of interacting fermions in a quasirandom optical lattice”. In: *Science* 349.6250 (2015), pp. 842–845. ISSN: 0036-8075.

[65] J. F. Sherson et al. “Single-atom-resolved fluorescence imaging of an atomic Mott insulator”. In: *Nature* 467.7311 (2010), pp. 68–72.

[66] W. S. Bakr et al. “Probing the Superfluid–to–Mott Insulator Transition at the Single-Atom Level”. In: *Science* 329.5991 (2010), pp. 547–550. ISSN: 0036-8075.

[67] E. Haller et al. “Single-atom imaging of fermions in a quantum-gas microscope”. In: *Nature Physics* 11.9 (2015), pp. 738–742.

[68] M. F. Parsons et al. “Site-resolved measurement of the spin-correlation function in the Fermi-Hubbard model”. In: *Science* 353.6305 (2016), pp. 1253–1256. ISSN: 0036-8075.

[69] M. Boll et al. “Spin- and density-resolved microscopy of antiferromagnetic correlations in Fermi-Hubbard chains”. In: *Science* 353.6305 (2016), pp. 1257–1260. ISSN: 0036-8075.

[70] J. Vijayan et al. *Time-Resolved Observation of Spin-Charge Deconfinement in Fermionic Hubbard Chains*. 2019. arXiv: 1905.13638 [cond-mat.quant-gas].

[71] O. M. Auslaender et al. "Spin-Charge Separation and Localization in One Dimension". In: *Science* 308.5718 (2005), pp. 88–92. ISSN: 0036-8075.

[72] C. Kim et al. "Observation of Spin-Charge Separation in One-Dimensional $SrCuO_2$". In: *Phys. Rev. Lett.* 77 (19 1996), pp. 4054–4057.

[73] J. Koepsell et al. "Imaging magnetic polarons in the doped Fermi–Hubbard model". In: *Nature* 572.7769 (2019), pp. 358–362.

[74] P. A. Lee, N. Nagaosa, and X.-G. Wen. *Doping a Mott Insulator: Physics of High Temperature Superconductivity*. 2004. arXiv: cond-mat/0410445 [cond-mat.str-el].

[75] A. M. Kaufman et al. "Quantum thermalization through entanglement in an isolated many-body system". In: *Science* 353.6301 (2016), pp. 794–800. ISSN: 0036-8075.

[76] J.-y. Choi et al. "Exploring the many-body localization transition in two dimensions". In: *Science* 352.6293 (2016), pp. 1547–1552. ISSN: 0036-8075.

[77] N. Goldman, J. C. Budich, and P. Zoller. "Topological quantum matter with ultracold gases in optical lattices". In: *Nature Physics* 12.7 (2016), pp. 639–645.

[78] H. Lignier et al. "Dynamical Control of Matter-Wave Tunneling in Periodic Potentials". In: *Phys. Rev. Lett.* 99 (22 2007), p. 220403.

[79] F. Gerbier and J. Dalibard. "Gauge fields for ultracold atoms in optical superlattices". In: *New Journal of Physics* 12.3 (2010), p. 033007.

[80] B. K. Stuhl et al. "Visualizing edge states with an atomic Bose gas in the quantum Hall regime". In: *Science* 349.6255 (2015), pp. 1514–1518. ISSN: 0036-8075.

[81] M. Mancini et al. "Observation of chiral edge states with neutral fermions in synthetic Hall ribbons". In: *Science* 349.6255 (2015), pp. 1510–1513. ISSN: 0036-8075.

[82] M. E. Tai et al. "Microscopy of the interacting Harper–Hofstadter model in the two-body limit". In: *Nature* 546.7659 (2017), pp. 519–523.

[83] O. Romero-Isart et al. "Superconducting Vortex Lattices for Ultracold Atoms". In: *Phys. Rev. Lett.* 111 (14 2013), p. 145304.

[84] A. González-Tudela et al. "Subwavelength vacuum lattices and atom–atom interactions in two-dimensional photonic crystals". In: *Nature Photonics* 9.5 (2015), 320–325. ISSN: 1749-4893.

[85] S. Baier et al. "Extended Bose-Hubbard models with ultracold magnetic atoms". In: *Science* 352.6282 (2016), pp. 201–205. ISSN: 0036-8075.

[86] T Lahaye et al. "The physics of dipolar bosonic quantum gases". In: *Reports on Progress in Physics* 72.12 (2009), p. 126401. ISSN: 1361-6633.

[87] C. S. Adams, J. D. Pritchard, and J. P. Shaffer. "Rydberg atom quantum technologies". In: *Journal of Physics B: Atomic, Molecular and Optical Physics* 53.1 (2019), p. 012002.

[88] T. F. Gallagher. "Rydberg Atoms". In: *Rep. Prog. Phys* 51 (1988), p. 143.

[89] L. S. Theis et al. "High-fidelity Rydberg-blockade entangling gate using shaped, analytic pulses". In: *Physical Review A* 94.3 (2016). ISSN: 2469-9934.

[90] H. Weimer et al. "A Rydberg quantum simulator". In: *Nature Physics* 6.5 (2010), pp. 382–388.

[91] F. Nogrette et al. "Single-Atom Trapping in Holographic 2D Arrays of Microtraps with Arbitrary Geometries". In: *Physical Review X* 4.2 (2014). ISSN: 2160-3308.

[92] D. Barredo et al. "Demonstration of a Strong Rydberg Blockade in Three-Atom Systems with Anisotropic Interactions". In: *Physical Review Letters* 112.18 (2014). ISSN: 1079-7114.

[93] M. D. Lukin et al. "Dipole Blockade and Quantum Information Processing in Mesoscopic Atomic Ensembles". In: *Phys. Rev. Lett.* 87 (3 2001), p. 037901.

[94] S. de Léséleuc et al. "Optical Control of the Resonant Dipole-Dipole Interaction between Rydberg Atoms". In: *Phys. Rev. Lett.* 119 (5 2017), p. 053202.

[95] S. Ravets et al. "Measurement of the angular dependence of the dipole-dipole interaction between two individual Rydberg atoms at a Förster resonance". In: *Phys. Rev. A* 92 (2 2015), p. 020701.

[96] N. Than-Long. "Study of Dipole-Dipole Interaction between Rydberg Atoms: Toward Quantum Simulation with Rydberg Atoms". en. In: (2016).

[97] A. Osterwalder and F. Merkt. "Using High Rydberg States as Electric Field Sensors". In: *Phys. Rev. Lett.* 82 (9 1999), pp. 1831–1834.

[98] M. Peper et al. "Magic Rydberg-Rydberg transitions in electric fields". In: *Phys. Rev. A* 100 (3 2019), p. 032512.

[99] V. Lienhard et al. "Observing the Space- and Time-Dependent Growth of Correlations in Dynamically Tuned Synthetic Ising Models with Antiferromagnetic Interactions". In: *Phys. Rev. X* 8 (2 2018), p. 021070.

[100] H. Bernien et al. "Probing many-body dynamics on a 51-atom quantum simulator". In: *Nature* 551.7682 (2017), pp. 579–584.

[101] H. Pichler et al. *Quantum Optimization for Maximum Independent Set Using Rydberg Atom Arrays*. 2018. arXiv: 1808.10816 [quant-ph].

[102] S. de Léséleuc et al. "Observation of a symmetry-protected topological phase of interacting bosons with Rydberg atoms". In: *Science* 365.6455 (2019), 775–780. ISSN: 1095-9203.

[103] J. Zeiher et al. "Many-body interferometry of a Rydberg-dressed spin lattice". In: *Nature Physics* 12.12 (2016), 1095–1099. ISSN: 1745-2481.

[104] E. A. Goldschmidt et al. "Anomalous Broadening in Driven Dissipative Rydberg Systems". In: *Phys. Rev. Lett.* 116 (11 2016), p. 113001.

[105] S. Haroche. "Nobel Lecture: Controlling photons in a box and exploring the quantum to classical boundary". In: *Reviews of Modern Physics* 85.3 (2013), pp. 1083–1102.

[106] A. Facon et al. "A sensitive electrometer based on a Rydberg atom in a Schrödinger-cat state". In: *Nature* 535 (2016), p. 262.

[107] E. K. Dietsche et al. "High-Sensitivity Magnetometry with a Single Atom in a Superposition of Two Circular Rydberg States". en. In: *Nature Physics* 15.4 (2019), pp. 326–329. ISSN: 1745-2473, 1745-2481.

[108] T. L. Nguyen et al. "Towards Quantum Simulation with Circular Rydberg Atoms". In: *Phys. Rev. X* 8 (1 2018), p. 011032.

[109] R. G. Hulet, E. S. Hilfer, and D. Kleppner. "Inhibited Spontaneous Emission by a Rydberg Atom". In: *Phys. Rev. Lett.* 55 (1985), p. 2137.

[110] M. Saffman and T. G. Walker. "Analysis of a quantum logic device based on dipole-dipole interactions of optically trapped Rydberg atoms". In: *Phys. Rev. A* 72 (2 2005), p. 022347.

[111] M. Brune and D. Papoular. *Evaporative cooling to a Rydberg crystal close to its ground state*. 2019. arXiv: 1909.02367 [cond-mat.quant-gas].

[112] A. Ramos, K. Moore, and G. Raithel. "Measuring the Rydberg constant using circular Rydberg atoms in an intensity-modulated optical lattice". In: *Physical Review A* 96.3 (2017). ISSN: 2469-9934.

[113] F. Merkt. "Molecules in high Rydberg states". In: *Annual Review of Physical Chemistry* 48.1 (1997). PMID: 15012453, pp. 675–709.

[114] C. Fey, F. Hummel, and P. Schmelcher. "Ultralong-range Rydberg molecules". In: *Molecular Physics* (2019), 1–15. ISSN: 1362-3028.

[115] T. Thiele et al. "Imaging electric fields in the vicinity of cryogenic surfaces using Rydberg atoms". In: *Physical Review A* 92.6 (2015). ISSN: 1094-1622.

[116] T. Thiele et al. "Manipulating Rydberg atoms close to surfaces at cryogenic temperatures". In: *Physical Review A* 90.1 (2014). ISSN: 1094-1622.

[117] J. D. Carter, O. Cherry, and J. D. D. Martin. "Electric-field sensing near the surface microstructure of an atom chip using cold Rydberg atoms". In: *Physical Review A* 86.5 (2012). ISSN: 1094-1622.

[118] A. Reinhard et al. "Rydberg-Rydberg Collisions: Resonant Enhancement of State Mixing and Penning Ionization". In: *Phys. Rev. Lett.* 100 (12 2008), p. 123007.

[119] Z.-X. Gong et al. *Steady-state superradiance with Rydberg polaritons*. 2016. arXiv: 1611.00797 [quant-ph].

[120] Y. Xue et al. "Rydberg electromagnetically induced transparency in a large Hilbert space". In: *Phys. Rev. A* 99 (5 2019), p. 053426.

[121] V. Zhelyazkova et al. "Fluorescence-lifetime-limited trapping of Rydberg helium atoms on a chip". In: *Molecular Physics* 117.21 (2019), pp. 2980–2989.

[122] J.-H. Choi et al. "Magnetic Trapping of Long-Lived Cold Rydberg Atoms". In: *Phys. Rev. Lett.* 95 (24 2005), p. 243001.

[123] T. Pohl, H. Sadeghpour, and P. Schmelcher. "Cold and ultracold Rydberg atoms in strong magnetic fields". In: *Physics Reports* 484.6 (2009), 181–229. ISSN: 0370-1573.

[124] E. Vliegen et al. "Stark deceleration and trapping of hydrogen Rydberg atoms". In: *Phys. Rev. A* 76 (2 2007), p. 023405.

[125] S. D. Hogan and F. Merkt. "Demonstration of Three-Dimensional Electrostatic Trapping of State-Selected Rydberg Atoms". In: *Phys. Rev. Lett.* 100 (4 2008), p. 043001.

[126] S. Zhang, F. Robicheaux, and M. Saffman. "Magic-wavelength optical traps for Rydberg atoms". In: *Phys. Rev. A* 84 (4 2011), p. 043408.

[127] S. K. Dutta et al. "Ponderomotive Optical Lattice for Rydberg Atoms". In: *Phys. Rev. Lett.* 85 (26 2000), pp. 5551–5554.

[128] S. E. Anderson, K. C. Younge, and G. Raithel. "Trapping Rydberg Atoms in an Optical Lattice". In: *Phys. Rev. Lett.* 107 (26 2011), p. 263001.

[129] K. C. Younge, S. E. Anderson, and G. Raithel. "Rydberg-atom trajectories in a ponderomotive optical lattice". In: *New Journal of Physics* 12.11 (2010), p. 113036.

[130] D. A. Anderson et al. "Production and trapping of cold circular Rydberg atoms". In: *Phys. Rev. A* 88 (3 2013), p. 031401.

[131] D Delande and J. C Gay. "A New Method for Producing Circular Rydberg States". In: *Europhysics Letters (EPL)* 5.4 (1988), pp. 303–308.

[132] D. Barredo et al. "Three-Dimensional Trapping of Individual Rydberg Atoms in Ponderomotive Bottle Beam Traps". In: *arXiv:1908.00853* (2019).

[133] T. Nirrengarten et al. "Realization of a Superconducting Atom Chip". In: *Physical Review Letters* 97.20 (2006). ISSN: 1079-7114.

[134] G. Nogues et al. "Effect of vortices on the spin-flip lifetime of atoms in superconducting atom-chips". In: *EPL (Europhysics Letters)* 87.1 (2009), p. 13002.

[135] J. Mozley et al. "Trapping and coherent manipulation of a Rydberg atom on amicrofabricated device: a proposal". In: *The European Physical Journal D - Atomic, Molecular, Optical and Plasma Physics* 35.1 (2005), pp. 43–57. ISSN: 1434-6079.

[136] C. H. Hermann Avigliano. "Towards deterministic preparation of single Rydberg atoms and applications to quantum information processing". Theses. Université Pierre et Marie Curie - Paris VI, 2014.

[137] C. Roux et al. "Bose-Einstein condensation on a superconducting atom chip". In: *EPL (Europhysics Letters)* 81.5 (2008), p. 56004.

[138] C. Hermann-Avigliano et al. "Long coherence times for Rydberg qubits on a superconducting atom chip". In: *Phys. Rev. A* 90 (4 2014), p. 040502.

[139] R. Celistrino Teixeira. "Mechanical effects of dipolar interaction of Rydberg atoms probed by microwave spectroscopy". Theses. Université Pierre et Marie Curie, 2014.

[140] R. G. Cortiñas et al. *Laser Trapping of Circular Rydberg Atoms*. 2019. arXiv: 1911.02316 [physics.atom-ph].

[141] S. Haroche and J.-M. Raimond. *Exploring the Quantum: Atoms, Cavities and Photons*. Oxford University Press, 2006.

[142] S. Haroche. "Courses in the Collège de France". In: *Collège de France* (2004-2015).

[143] C. Sayrin et al. "Real-time quantum feedback prepares and stabilizes photon number states". In: *Nature* 477 (2011), p. 73.

[144] S. Gleyzes et al. "Quantum jumps of light recording the birth and death of a photon in a cavity". In: *Nature* 446 (2007), p. 297.

[145] A. Signoles et al. "Coherent Transfer between Low-Angular-Momentum and Circular Rydberg States". In: *Phys. Rev. Lett.* 118 (25 2017), p. 253603.

[146] S. Patsch et al. "Fast and accurate circularization of a Rydberg atom". In: *Phys. Rev. A* 97 (5 2018), p. 053418.

[147] C. Cohen-Tannoudji, B. Diu, and F. Laloë. *Quantum Mechanics*. New York: Wiley, 1977.

[148] J. J. Sakurai. *Modern Quantum Mechanics*. New York: Addison Wesley, 1994.

[149] K. Afrousheh et al. "Determination of the ^{85}Rb ng-series quantum defect by electric-field-induced resonant energy transfer between cold Rydberg atoms". In: *Phys. Rev. A* 74 (6 2006), p. 062712.

[150] W. Li et al. "Millimeter-wave spectroscopy of cold Rb Rydberg atoms in a magneto-optical trap: Quantum defects of the ns, np, and nd series". In: *Phys. Rev. A* 67 (5 2003), p. 052502.

[151] J. Han et al. "Rb nf quantum defects from millimeter-wave spectroscopy of cold ^{85}Rb Rydberg atoms". In: *Phys. Rev. A* 74 (5 2006), p. 054502.

[152] S. Haroche and J.-M. Raimond. "Bohr's Legacy in Cavity QED". In: *Niels Bohr, 1913-2013: Poincaré Seminar 2013*. Ed. by O. Darrigol et al. Cham: Springer International Publishing, 2016, pp. 103–146. ISBN: 978-3-319-14316-3.

[153] J. D. Jackson. *Classical Electrodynamics*. 2nd ed. New York: Wiley, 1975.

[154] J. Dalibard, J. Dupont-Roc, and C. Cohen-Tannoudji. "Vacuum fluctuations and radiation reaction : identification of their respective contributions". In: *Journal de Physique* 43.11 (1982), pp. 1617–1638.

[155] T. Giamarchi. *Quantum Physics in One Dimension*. illustrated edition. The international series of monographs on physics 121. Clarendon; Oxford University Press, 2004. ISBN: 0198525001.

[156] M. Müller et al. "Engineered Open Systems and Quantum Simulations with Atoms and Ions". In: *Advances in Atomic, Molecular, and Optical Physics, Volume 61*. Ed. by E. A. Paul Berman and C. Lin. Academic Press, 2012, pp. 1 –80.

[157] B. d'Espagnat. *Foundations of Quantum Mechanics*. New York: Academic Press, 1971.

[158] G. S. Joyce. "Classical Heisenberg Model". In: *Phys. Rev.* 155 (2 1967), pp. 478–491.

[159] M. Kenzelmann et al. "Order-to-disorder transition in the XY-like quantum magnet Cs_2CoCl_4 induced by noncommuting applied fields". In: *Phys. Rev. B* 65 (14 2002), p. 144432.

[160] O. Breunig et al. "Spin-$\frac{1}{2}$ XXZ Chain System Cs_2CoCl_4 in a Transverse Magnetic Field". In: *Phys. Rev. Lett.* 111 (18 2013), p. 187202.

[161] B. Grenier et al. "Longitudinal and Transverse Zeeman Ladders in the Ising-Like Chain Antiferromagnet $BaCo_2V_2O_8$". In: *Phys. Rev. Lett.* 114 (1 2015), p. 017201.

[162] D. V. Dmitriev et al. "One-dimensional anisotropic Heisenberg model in the transverse magnetic field". In: *Journal of Experimental and Theoretical Physics* 95.3 (2002), pp. 538–549. ISSN: 1090-6509.

[163] C. N. Yang and C. P. Yang. "One-Dimensional Chain of Anisotropic Spin-Spin Interactions. I. Proof of Bethe's Hypothesis for Ground State in a Finite System". In: *Phys. Rev.* 150 (1 1966), pp. 321–327.

[164] C. N. Yang and C. P. Yang. "One-Dimensional Chain of Anisotropic Spin-Spin Interactions. II. Properties of the Ground-State Energy Per Lattice Site for an Infinite System". In: *Phys. Rev.* 150 (1 1966), pp. 327–339.

[165] V. L. Pokrovsky and A. L. Talapov. "Ground State, Spectrum, and Phase Diagram of Two-Dimensional Incommensurate Crystals". In: *Phys. Rev. Lett.* 42 (1 1979), pp. 65–67.

[166] H. J. Schulz. "Critical behavior of commensurate-incommensurate phase transitions in two dimensions". In: *Phys. Rev. B* 22 (11 1980), pp. 5274–5277.

[167] Y. Hieida, K. Okunishi, and Y. Akutsu. "Anisotropic antiferromagnetic spin chains in a transverse field: Reentrant behavior of the staggered magnetization". In: *Phys. Rev. B* 64 (22 2001), p. 224422.

[168] E. Barouch and B. M. McCoy. "Statistical Mechanics of the *XY* Model. II. Spin-Correlation Functions". In: *Phys. Rev. A* 3 (2 1971), pp. 786–804.

[169] P. Pfeuty. "The one-dimensional Ising model with a transverse field". In: *Annals of Physics* 57.1 (1970), pp. 79 –90. ISSN: 0003-4916.

[170] S. R. White. "Density matrix formulation for quantum renormalization groups". In: *Phys. Rev. Lett.* 69 (19 1992), pp. 2863–2866.

[171] U. Schollwöck. "The density-matrix renormalization group". In: *Rev. Mod. Phys.* 77 (1 2005), pp. 259–315.

[172] *ITensor*. 2016. URL: http://itensor.org/.

[173] U. Schollwöck. "The density-matrix renormalization group in the age of matrix product states". In: *Annals of Physics* 326.1 (2011). January 2011 Special Issue, pp. 96 –192. ISSN: 0003-4916.

[174] G. Müller and R. E. Shrock. "Implications of direct-product ground states in the one-dimensional quantum XYZ and XY spin chains". In: *Phys. Rev. B* 32 (9 1985), pp. 5845–5850.

[175] R. Grimm, M. Weidemüller, and Y. B. Ovchinnikov. "Destruction of Long-Range Order in One-Dimensional and Two-Dimensional Systems Having a Continuous Symmetry Group I. Classical Systems". In: Sov. Phys. JETP 32, 493 (1971) 42 (2000), pp. 95 –170.

[176] J. M. Kosterlitz and D. J. Thouless. "Ordering, metastability and phase transitions in two-dimensional systems". In: *Journal of Physics C: Solid State Physics* 6.7 (1973), pp. 1181–1203.

[177] J. M. Kosterlitz. "The critical properties of the two-dimensional xy model". In: *Journal of Physics C: Solid State Physics* 7.6 (1974), pp. 1046–1060.

[178] P. Calabrese and J. Cardy. "Entanglement entropy and quantum field theory". In: *Journal of Statistical Mechanics: Theory and Experiment* 2004.06 (2004), P06002.

[179] P. Calabrese and J. Cardy. "Entanglement entropy and conformal field theory". In: *Journal of Physics A: Mathematical and Theoretical* 42.50 (2009), p. 504005.

[180] D. Barredo et al. "Synthetic three-dimensional atomic structures assembled atom by atom". In: *Nature* 561.7721 (2018), pp. 79–82.

[181] W. Jhe et al. "Suppression of Spontaneous Emission Decay at Optical Frequencies: Test of Vacuum-Field Anisotropy in Confined Space". In: *Phys. Rev. Lett.* 58 (1987), p. 666.

[182] A. Aspect and J. Dalibard. "Measurement of the atom-wall interaction: from London to Casimir-Polder". In: 42.50 (2002), p. 504005.

[183] E. A. Hinds. "Cavity Quantum Electrodynamics". In: *Advances in Atomic and Molecular Physics*. Ed. by D. Bates and B. Bederson. Vol. 28. San Diego: Academic Press, 1990, p. 237.

[184] S. Haroche, J.-M. Raimond, and M. Brune. "Works of the CQED group of the ENS vol. I and II". In: *Advances in Atomic and Molecular Physics*. Vol. 28. ENS: Academic Press, 1990.

[185] E. M. Purcell. "Spontaneous Emission Probabilities at Radio Frequencies". In: *Phys. Rev.* 69 (1946), p. 681.

[186] J. Dalibard. "Lectures at the Collège de France". In: *https://www.college-de-france.fr/site/jean-dalibard/index.htm*. Paris: Collège de France, 2015.

[187] T. L. Nguyen. "Study of dipole-dipole interaction between Rydberg atoms - Toward quantum simulation with Rydberg atoms". Theses. Université Pierre et Marie Curie UPMC Paris VI, 2016.

[188] M. Gross and S. Haroche. "Superradiance: An essay on the theory of collective spontaneous emission". In: *Physics Reports* 93.5 (1982), pp. 301 –396. ISSN: 0370-1573.

[189] S. E. Anderson. "Trapping Rydberg Atoms in Ponderomotive Optical Lattices". Theses. The University of Michigan, 2014.

[190] P. Cheinet. "Conception and realisation of a cold atom gravimeter". Theses. Université Pierre et Marie Curie - Paris VI, 2006.

[191] N. V. Smith. "Optical Constants of Rubidium and Cesium from 0.5 to 4.0 eV". In: *Phys. Rev. B* 2 (8 1970), pp. 2840–2848.

[192] R. C. Teixeira et al. "Microwaves Probe Dipole Blockade and van der Waals Forces in a Cold Rydberg Gas". In: *Phys. Rev. Lett.* 115 (1 2015), p. 013001.

[193] D. Steck. *Spectroscopic data, Rubidium 87 D Line Data*. 2019. URL: https://steck.us/alkalidata/rubidium87numbers.pdf (visited on 09/30/2019).

[194] J. Venzke et al. “Angular momentum distribution in Rydberg states excited by a strong laser pulse”. In: *Phys. Rev. A* 98 (4 2018), p. 043434.

[195] R. G. Hulet and D. Kleppner. “Rydberg Atoms in "Circular" States”. In: *Phys. Rev. Lett.* 51 (16 1983), pp. 1430–1433.

[196] I. Ushijima et al. “Cryogenic optical lattice clocks”. In: *Nature Photonics* 9.3 (2015), pp. 185–189.

[197] V. D. Ovsiannikov, A. Derevianko, and K. Gibble. “Rydberg Spectroscopy in an Optical Lattice: Blackbody Thermometry for Atomic Clocks”. In: *Phys. Rev. Lett.* 107 (9 2011), p. 093003.

[198] M. J. Martin. “Quantum Metrology and Many-Body Physics: Pushing the Frontier of the Optical Lattice Clock”. PhD thesis. University of Colorado, 2013.

[199] W. Oliver. *Quantum information processing: Lecture notes of the 44th IFF spring school*. 2013. URL: http://equs.mit.edu/wp-content/uploads/2016/11/SC_qubits_Oliver_IFF_Spring_School_20140330.pdf (visited on 01/01/2020).

[200] J. R. Klauder and P. W. Anderson. “Spectral Diffusion Decay in Spin Resonance Experiments”. In: *Phys. Rev.* 125 (3 1962), pp. 912–932.

[201] J. W. Goodman. *Introduction to Fourier Optics*. 2nd ed. McGraw-Hill series in electrical and computer engineering. McGraw-Hill, 1996. ISBN: 0070242542.

[202] M. Born et al. *Principles of Optics: Electromagnetic Theory of Propagation, Interference and Diffraction of Light*. 7th ed. Cambridge University Press, 1999.

[203] E. Hecht. *Optics*. Pearson education. Addison-Wesley, 2002. ISBN: 9780321188786.

[204] A. E. Siegman. *Lasers*. University Science Books, 1986.

[205] M. S. Safronova, C. J. Williams, and C. W. Clark. “Relativistic Many-Body Calculations of Electric-Dipole Matrix Elements, Lifetimes, and Polarizabilities in Rubidium”. In: *Phys. Rev. A* 69 (2004), p. 022509.

[206] F. Assémat. “Manipulating quantum states of light with a single Rydberg atom”. Theses. Sorbonne Université, 2019.

[207] S. D. Hogan et al. “Driving Rydberg-Rydberg Transitions from a Coplanar Microwave Waveguide”. In: *Phys. Rev. Lett.* 108 (6 2012), p. 063004.

[208] J. R. Klauder and P. W. Anderson. “Spectral Diffusion Decay in Spin Resonance Experiments”. In: *Phys. Rev.* 125 (3 1962), pp. 912–932.

RÉSUMÉ

Nous proposons un nouveau paradigme pour la simulation quantique de chaines de spin-1/2, basés sur des atomes de Rydberg circulaires piégés par laser. Leur longue durée de vie intrinsèque, combinée à l'inhibition de leur émission spontanée micro-onde et leur photoionisation négligeable rendent réalistes des temps de simulation à l'échelle de la minute. Cette nouvelle plateforme offre une grande flexibilité et permettra d'explorer de nouveaux regimes de simulation. Le simulateur proposé modélise un Hamiltonien XXZ à spin 1/2, les couplages entre plus proches voisins pouvant aller jusqu'à quelques dizaines de kilohertz. Tous les paramètres du modèle peuvent être réglés dynamiquement à volonté, ce qui permet d'accéder à un large éventail de systèmes simulés. Ainsi, l'évolution du système peut être suivie sur des temps suffisamment long pour permettre la préparation adiabatique depuis l'état fondamental ainsi que l'étude de la thermalisation et du désordre.
Cette thèse est un premier pas vers la mise en oeuvre de ce schéma de simulation quantique. (i) Nous démontrons la préparation d'états de Rydberg circulaires à partir d'atomes refroidis par laser dans un environnement cryogénique 4.2 K avec accès optiques. Leur durée de vie révèle une température effective du corps noir micro-ondes de 11±2 K. (ii) Nous évaluons le temps de cohérence pour un seul qubit (268±5 µs), et la durée de vie (3.7±0.1 ms). (iii) Enfin nous démontrons le piégeage par laser d'atomes de Rydberg circulaires prouvant leur photoionisation négligeable sur de nombreux temps de vie à la échèle de 10 ms.

MOTS CLÉS

atomes de Rydberg, atomes froids, simulation quantique, interaction dipolaire, atomes circulaires, spectroscopie microonde.

ABSTRACT

We propose a new paradigm for quantum simulation of spin-1/2 arrays, providing unprecedented flexibility and allowing one to explore domains that remain unexplored, based on laser-trapped circular Rydberg atoms. The long intrinsic atomic lifetimes, combined with the inhibition of their microwave spontaneous emission and their negligible photoionisation, make operation in the minute range realistic. The proposed simulator realizes an XXZ spin-1/2 Hamiltonian, with nearest-neighbour couplings ranging from a few to tens of kilohertz. All the model parameters can be dynamically tuned at will, making a large range of simulations accessible. Thus, the system evolution can be followed long enough to be relevant for ground-state adiabatic preparation and for the study of thermalization and disorder.
In this thesis, as a first step towards the implementation of this quantum simulation scheme, we (i) demonstrate the preparation of cold circular Rydberg states in a 4.2 K cryogenic environment with optical access out of a cold atom cloud. Their lifetime reveals an effective microwave black-body temperature of 11±2 K. We (ii) assess the single qubit coherence time (268±5 µs) and lifetime (3.7±1 ms), and, finally, we (iii) demonstrate the laser trapping of circular Rydberg atoms to prove their negligible photoionisation at the timescale of 10 ms.

KEYWORDS

Rydberg atoms, cold atoms, quantum simulation, dipolar interactions, circular atoms, microwave spectroscopy.